Universität Bremen

EUROPROX

How magnetics and granulometry of continental margin sediments reflect terrestrial and marine environments of South America and West Africa

Dissertation for the doctoral degree in natural sciences

(Dr. rer. nat.)

at the Faculty of Geosciences of the Bremen University

submitted by

Sebastian Razik

08. September 2014

1st referee: Prof. Dr. Tilo von Dobeneck, Bremen University

2nd referee: Dr. Cristiano M. Chiessi, São Paulo University

This cumulative doctoral thesis is the outcome of the research project III-13b, 40500245 of the International Graduate College ‘Proxies in Earth History – EUROPROX’. The studies contained within this thesis were carried out from August 2009 to August 2014 at the Faculty of Geosciences (Bremen University) and at the Instituto de Geociências (Universidade de São Paulo, Brazil) during a stay abroad of three months.

Summary

Marine sediments act globally as natural archives for various environmental conditions. In particular, continental margins are simultaneously supplied by terrigenous clastic, as well as by biogenic marine sediments. Thus, investigations of continental margin deposits reveal insights about both, prevalent climatic conditions on land with impacts on terrestrial sediment sources and sediment transport paths, as well as about marine environments linked to ocean-wide current systems. In this context, the western South Atlantic as well as the eastern North Atlantic, being sensitive to climate change, constitute scientifically rewarding sites. The continental margins of SE South America (ca. 20°–55° S) and NW Africa (i.e., 14°–17° N) obtain sediments from various terrestrial sources, each conveying specific magnetic mineral assemblages due to existent source-rock petrology and respective climatic and weathering conditions. The delivered fluvial and eolian continental margin sediments are distributed by ocean currents, which are also under influence of the South American Monsoon System (SAMS) and the Southern Westerly Wind Belt (SWWB), as well as under the influence of the northeasterly trade and the easterly Harmattan winds in the realm of NW Africa.

The amount of available rock-magnetic studies in the realm of SE South America is very limited and 'non-magnetic' provenance studies are mainly restricted to regional areas. Hence, one aim of this thesis is the delineation of terrigenous sediment provinces at the majority of the SE South American continental margin and the identification of corresponding terrestrial sources mainly based on sedimentary magnetic properties. Since original terrestrial source-rock signatures (i.e., magnetic and clastic grain size) may be overprinted during sediment transport, paleoclimatic and paleoceanographic processes must be considered in studies of marine sediments. Thus, for the first time, past interactions of the SAMS and the SWWB are taken into joint consideration with respect to their impacts on the surface-ocean circulation. A further aim of the thesis is the investigation of benthic environmental conditions at the South Brazilian continental slope and of the Brazil Current hydrodynamics. In this way, links shall be revealed towards the Atlantic Meridional Overturning Circulation (AMOC). Another study was carried out off NW Africa with the focus on magnetic properties of individual grain-size fractions and with the target to detect multiple terrestrial sources, as well as different transport mechanisms.

To reach these aims, a series of well established and modified enviromagnetic approaches was performed and specified with respect to the different emphases. Sets of rock and enviromagnetic parameters were used in combination with clastic grain-size distributions, major-element concentrations, planktic and benthic foraminiferal assemblages, as well as stable isotope signatures obtained from surface and down-core sediment samples. Hereby, multivariate methods as fuzzy c-means cluster analysis and non-linear mapping were used to facilitate and to strengthen the multiparametric environmental interpretations.

Off SE South America, three major sediment provinces were delineated: (i) tropically weathered clayey silts of the Plata Drainage Basin (PDB; high proportion of fine magnetite) distributed with the Plata Plume Water up to SE Brazil (~24° S); (ii) Pampean loessoidal sand (high proportion of hematite

and goethite) recently delivered to the Pampean shelf mainly by coastal wave erosion. Relict Pampean sediments are admixed to PDB sediments on the slope off SE Brazil; and (iii) contouritic sand (high proportions of coarse magnetite) of the Pampean slope originally delivered by Colorado and Negro River meltwaters under deglacial sea-level lowstand conditions.

Based on the origin of sediments deposited in the vicinity of the Subtropical Shelf Front (STSF; off South Brazil), relative meridional positions of the STSF were delineated with further clues on over-regional climatic and hydrodynamic conditions: During the Late Glacial and the Early Holocene (14–8 cal kyr BP), the sediments mainly originated from the PDB. However, during the Mid Holocene (8–4 cal kyr BP) the deposits were dominated by Pampean sand. This sand transport occurred due to the intensified northward flow of the Subantarctic Shelf Water, which is reflected by high sedimentary abundances of Antarctic diatoms. This was enabled by the northward extension of the SWWB, leading to the northernmost STSF position of the last 14 cal kyr. During the Late Holocene (last 4 cal kyr), the STSF shifted southward to its modern position due to a strengthened SAMS, which is mirrored by a marked deposition of riverine silty clays from the PDB.

During the Last Deglaciation, the AMOC and related atmospheric circulation patterns underwent significant variations due to climatic impacts related to Heinrich Stadial 1 (HS1; ~16.8 cal kyr BP) and Antarctic Cold Reversal (ACR; 14.5–12.5 cal kyr BP) on the southern hemisphere (Bølling-Allerød on the northern hemisphere). This is mirrored by distinct environmental and hydrodynamic conditions associated to the Brazil Current. Thus, during the HS1, the lowered South Atlantic Central Water ventilation (e.g., decreased BFOI values and increased clay contents) hints at weakened Antarctic Intermediate Water formation occurring simultaneously with the smallest Antarctic sea-ice extension up to this time. The set-in of the AMOC at 16–15.4 cal kyr BP weakened the Brazil Current again, while the reaction was opposed during the set-in of the Agulhas Leakage (15.4–15 cal kyr BP).

Off NW Africa, the joint consideration of whole sediment and magnetic mineral grain-size distributions allows to address several important issues: (i) distinction of two eolian sediment fractions (trade and Harmattan winds), as well as of one fluvial fraction (Senegal River); (ii) identification of three terrestrial sediment sources: southern Sahara and Sahel dust (high proportions of hematite and coarse magnetite), dust from Senegalese coastal dunes (intermediate magnetic mineral proportions), and soils from the upper reaches of the Senegal River (high proportion of fine magnetite). These sources show changes in their dominance with respect to the arid conditions of HS1 and the humid conditions of the Mid Holocene. This study reveals that the performed grain-size specific enviromagnetic approach is sensitive and efficient for provenance studies in regions with multiple sediment sources, as well as different sediment transport mechanisms. This approach and the multi-proxy methods performed in this thesis have a large potential to answer challenging questions with respect to terrestrial, limnic, fluvial and marine environments worldwide.

Zusammenfassung

Marine Sedimente stellen weltweit natürliche Archive für diverse Umweltbedingungen dar. Insbesondere sind es die Kontinentalränder, welche gleichzeitig mit terrigenen klastischen, als auch mit biogenen marinen Sedimenten versorgt werden. Somit liefern Untersuchungen von Kontinentalhangablagerungen sowohl Einblicke in vorherrschende terrestrische Klimabedingungen mit Auswirkungen auf Sedimentquellen und Transportwege, als auch in marine Umweltbedingungen mit Verbindung zu ozeanweiten Strömungssystemen. In diesem Zusammenhang stellen der westliche Südatlantik, als auch der östliche Nordatlantik wissenschaftlich lohnende Untersuchungsgebiete dar, da sie sensitiv auf Klimaveränderungen reagieren. Die Kontinentalränder von SO-Südamerika (ca. 20°–55° S) und NW-Afrika (sprich 14°–17° N) werden durch diverse terrestrische Sedimentquellen beliefert, wobei jede von ihnen, bedingt durch Gesteinspetrologie und klimaabhängige Verwitterungsprozesse, spezifische magnetische Mineralvergesellschaftungen aufweist. Die angelieferten fluvialen und äolischen Schelf- und Hangsedimente werden durch Ozeanströmungen verteilt, welche jeweils unter dem Einfluss des Südamerikanischen Monsunsystems (SAMS) und des Südlichen Westwindgürtels (SWWB), bzw. hinsichtlich NW-Afrika unter dem Einfluss der nordöstlichen Passatwinde und des östlichen Harmattans, stehen.

Die Anzahl der vorhandenen gesteinsmagnetischen Studien im Bereich von SO-Südamerika ist sehr eingeschränkt und die wenigen vorhandenen ‚nicht-magnetischen' Provenienzstudien hinsichtlich terrigener Sedimente sind zumeist auf regionale Bereiche dieses Kontinentalrandes beschränkt. Ein Ziel dieser Doktorarbeit ist die Identifizierung terrigener Sedimentprovinzen auf dem Großteil des Kontinentalhanges von SO-Südamerika, sowie ihre Zuordnung zu terrestrischen Quellen hauptsächlich basierend auf magnetischen Eigenschaften. Da ursprüngliche Signaturen terrestrischer Ausgangsgesteine (sprich, die magnetische und klastische Korngröße) durch den Sedimenttransport überprägt werden können, müssen paläoklimatische und paläoozeanographische Prozesse bei Studien mariner Sedimente berücksichtigt werden. Somit werden das erste Mal überhaupt das SAMS und der SWWB, im Hinblick auf deren Auswirkungen auf die Ozeanoberflächenzirkulation vor SO-Südamerika, gemeinsam betrachtet. Ein weiteres Ziel dieser Arbeit besteht darin, die benthischen Umweltbedingungen am Kontinentalhang vor Südbrasilien als auch die Hydrodynamik des Brasilstroms zu betrachten. Diese weisen das Potenzial auf, Einblicke in die Atlantische Meridionale Umwälzungszirkulation (AMOC) zu gewähren. Eine weitere Studie basierend auf magnetischen Eigenschaften individueller Korngrößenfraktionen wurde vor NW-Afrika durchgeführt, um dort mehrere terrestrische Sedimentquellen als auch Transportmechanismen zu ermitteln.

Um die erwähnten Ziele zu erreichen, wurde eine Serie an bewährten und modifizierten umweltmagnetischen Analysen durchgeführt und im Hinblick auf unterschiedliche Schwerpunktsetzungen präzisiert. Datensätze mit gesteins- und umweltmagnetischen Parametern wurden in Kombination mit klastischen Korngrößenverteilungen, Hauptelement-Konzentrationen, planktischen und benthischen Foraminiferenvergesellschaftungen als auch stabilen Isotopen aus Oberflächensediment- und Sedimentkern-Proben verwendet. Dabei wurden multivariate Methoden wie ‚fuzzy c-means cluster analysis' und ‚non-linear mapping' eingesetzt, um multiparametrische Interpretationen hinsichtlich wirkender Umweltbedingungen zu erleichtern und zu unterstützen.

Vor SO-Südamerika wurden drei Sedimentprovinzen ausgemacht: (i) tropisch verwitterte tonige Silte des Plata-Einzugsgebietes (PDB; hoher Anteil feinen Magnetits), welche mit dem Platawasser (PPW) bis nach SO-Brasilien (~24° S) verteilt werden; (ii) pampeanischer lössoidaler Sand (hoher Hämatit- und Göthitan-

teil), gegenwärtig zum pampeanischen Kontinentalschelf hauptsächlich durch Küstenerosion angeliefert. Reliktäre pampeanische Sedimente werden auf dem SO-brasilianischen Kontinentalhang rezenten PDB-Sedimenten beigemischt; und (iii) Konturitsand (hoher Anteil groben Magnetits) auf dem pampeanischen Kontinentalhang ursprünglich angeliefert durch die deglazialen Schmelzwässer der Colorado und Negro Flüsse während Meeresspiegel-Tiefstände.

Basierend auf dem Ursprung der in der Nähe der Subtropischen Schelffront (STSF; vor Südbrasilien) abgelagerten Sedimente, wurden relative meridionale Positionen der STSF umrissen und weitere Rückschlüsse auf überregionale klimatische und hydrodynamische Bedingungen ermöglicht: Während des Spätglazials und des Frühholozäns (14–8 cal kyr BP) entstammten die Sedimente hauptsächlich dem PDB. Während des Mittelholozäns (8–4 cal kyr BP) wurden die Ablagerungen jedoch durch pampeanischen Sand dominiert. Der Sandtransport erfolgte mit dem verstärkten, nordwärts fließenden Subantarktischen Schelfwasser (SASW), was erhöhte Häufigkeiten an antarktischen Diatomeen belegen. Dies wurde durch die nordwärts gerichtete Expansion des SWWB ermöglicht, was in der nördlichsten Position der STSF innerhalb der letzten 14 cal kyr BP resultiert. Während des Spätholozäns (letzten 4 cal kyr) verschob sich die STSF weiter südwärts bis zur heutigen Lage bedingt durch ein verstärktes SAMS, was durch die ausgeprägte Ablagerung fluviatiler siltiger PDB-Tone belegt wird.

Während des Letzten Deglazials unterlagen die AMOC und die mit ihr verbundenen atmosphärischen Zirkulationsmuster, bedingt durch klimatische Auswirkungen des Heinrichstadials (HS1; ~16.8 cal kyr BP) und des Antarktischen Kälteumschwungs (ACR; 14.5–12.5 cal kyr BP) auf der südlichen Hemisphäre (Bølling-Allerød auf der nördlichen), signifikanten Veränderungen. Dies wird durch ausgeprägte hydrodynamische Zustände und Umweltbedingungen in Verbindung mit dem Brasilstrom widergespiegelt. Folglich weist die im HS1 abgeschwächte Durchlüftung des Südatlantischen Zentralwassers (z.B. niedrigere BFOI-Werte sowie geringerer Tongehalt) auf eine Bildungsverminderung des Antarktischen Zwischenwassers hin, was mit der bis dahin geringsten Ausdehnung der antarktischen Meereisdecke zusammenfällt. Das Wiedereinsetzen der AMOC um 16–15.4 cal kyr BP schwächte erneut den Brasilstrom, wobei eine gegenläufige Reaktion während des Wiedereinsetzens der Agulhas Leckage (15.4–15 cal kyr BP) erfolgte.

Vor NW-Afrika ermöglicht die gemeinsame Betrachtung der Gesamtsediment- und Magnetomineral-Korngrößenverteilungen das Angehen einiger wichtiger Sachverhalte: (i) Abgrenzung zweier äolischer Sedimentfraktionen (Passat- und Harmattanwinde) als auch einer fluvialen Fraktion (Senegalfluss); (ii) Identifizierung dreier terrestrischer Sedimentquellen: südlicher Sahara- und Sahelstaub (hoher Anteil an Hämatit und groben Magnetit), Staub von senegalesischen Küstendünen (intermediäre Mineralproportionen) und Böden vom Oberlauf des Senegalflusses (hoher Feinmagnetitanteil). Diese Quellen zeigen Veränderungen in ihrer Dominanz, welche durch die ariden Bedingungen des HS1 und die humiden Bedingungen des Mittleren Holozäns hervorgerufen werden. Diese Studie beleuchtet, dass der korngrößenspezifische magnetische Ansatz, hinsichtlich Provenienzstudien in Regionen mit mehreren Sedimentquellen als auch unterschiedlichen Sedimenttransportmechanismen, sensitiv und effizient ist. Dieser Ansatz und die Multiproxy-Methoden, welche innerhalb dieser Doktorarbeit durchgeführt wurden, besitzen ein großes Potenzial, um anspruchsvolle Fragen bezüglich terrestrischer, limnischer, fluvialer und mariner Umweltbedingungen weltweit zu beantworten.

Declaration

Name: Sebastian Razik

Address: Brommystraße 20, 27570 Bremerhaven

Herewith I declare that

I. this document and the accompanying data has been composed by myself, and describes my own work;

II. material from the published or unpublished work of others, which is referred to in the dissertation, is credited to the author in the text;

III. this work has not been submitted for any other degree.

Bremen, 08. September 2014

.....

Sebastian Razik

(Signature)

"He who knows nothing, loves nothing. He who can do nothing understands nothing. He who understands nothing is worthless. But he who understands also loves, notices, sees… The more knowledge is inherent in a thing, the greater the love… Anyone who imagines that all fruits ripen at the same time as the strawberries knows nothing about grapes."

— Paracelsus

Table of contents

Chapter 1: Introduction

1.1. Preamble

The Earth is a complex and dynamic system since its conditions change permanently with time and space. In particular, the Earth's surface is under the influence of all subsystems (lithosphere, hydrosphere, cryosphere, atmosphere, and biosphere) interacting with each other (Fig. 1.1) (e.g., Ruddiman, 2001; Press and Siever, 2003; Wefer, 2010). The intercoupled subsystems lead to changes in dimensions ranging from minerals to continents. These changes take place during time periods of decades up to millions of years involving the climate, sea-level fluctuations and the evolution of life. The energy sources for these natural dynamics are present above and below the Earth's surface. Exogenous processes, like the atmospheric and hydrospheric cycles (incl. sediment transport), weathering, erosion and sedimentation, are primarily ruled by the sun and the tides. Endogenous processes, like movement of lithospheric plates, mountain uplift, volcanism and earthquakes, are controlled by heat transport between the Earth's core and the surface.

As it is the nature of the humankind to realize many of these processes within the span of a person's life, the humankind has probably always wondered about the reason and cause for the perceptible processes in the nature and thus for the own roots. The raised questions consequently brought out the established geology of the last centuries and the modern geosciences, which are the only sciences concerned in the first case with the phenomenon 'time'. However, recently the modern man changes his environment with drastic effects on the balance of all life on the Earth: Agriculture and settlement moving more sediment than rivers; industrial combustion of fossil fuels leading to climate warming; release of genetically manipulated organism and radioactive substances into the environment;

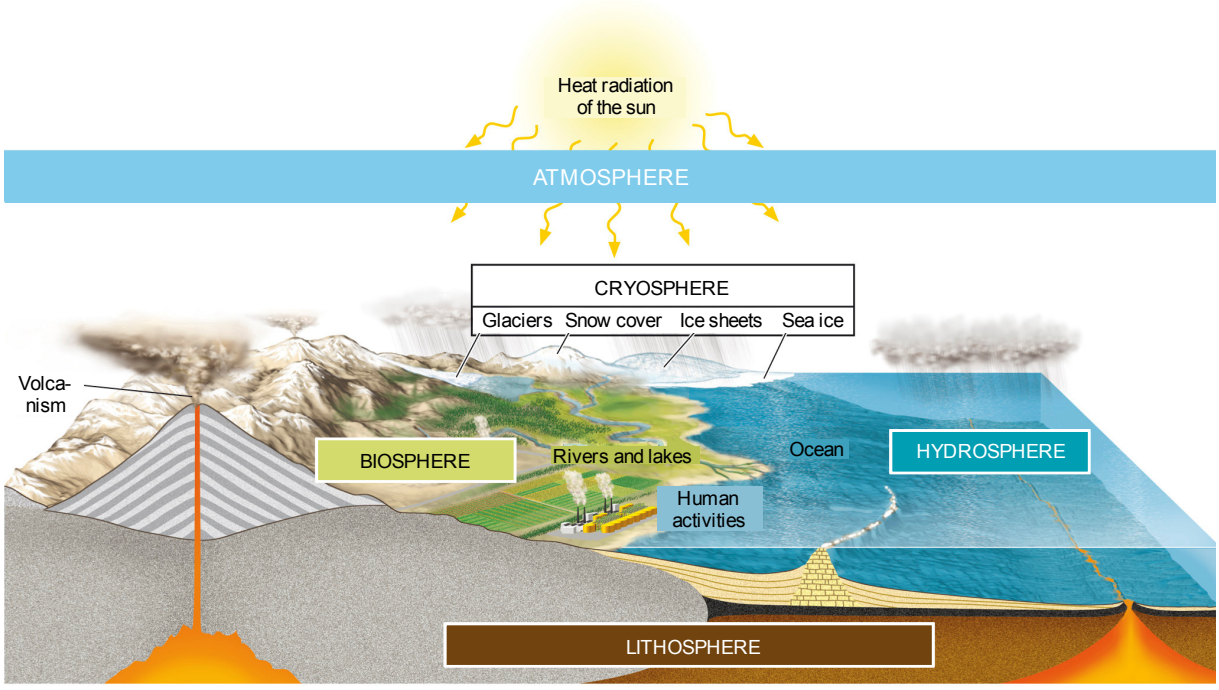

Fig. 1.1. The Earth's interacting subsystems: Lithosphere, hydrosphere, cryosphere, atmosphere, and biosphere (adapted from Grotzinger et al., 2008).

contamination of waters by waste etc. (e.g., Dietrich et al., 1975; Ott, 1988; Ruddiman, 2001; Stocker et al., 2013). Consequently, the geosciences do not only focus on the past, but develop required predictions for the Earth's future with respect to all concurring subsystems, while these revealed 'answers' are today likely more crucial than during any other time of the human history. Nevertheless, the past natural processes (e.g., large-scale variations of ocean-current systems due to abrupt changes of climate and deep-water formation in the realm of the North Atlantic; Stocker et al., 2013) have to be better known with the aim to enable a more robust understanding of naturally and anthropogenically induced environmental changes. This is essential for drawing-up adequate guidance for policy makers *and* for consideration of the recognized nexus on an active daily basis. Thus, geoscientific investigations may contribute to the comprehension, how to sustainably coexist in and with nature.

Marine deposits constitute the most far-reaching natural archives for environmental conditions, comprising millions of years (e.g., Wefer et al., 1996). Although sediments deposited in the marine realm have different origins (e.g., biogenic, hydrothermal, cosmogenic), the major sediment proportion on continental margins (85–95%) is derived from the continents (Fig. 1.2) (Dietrich et al., 1975; Milliman and Meade, 1983; Ott, 1988; Syvitski et al., 2003). Terrigenous sediments are created by physical, as well as by chemical weathering of igneous, metamorphic, and sedimentary rocks. These sediments are mainly transported to the ocean by rivers with an estimated load of ~12 km^3 yr^{-1} (Dietrich et al., 1975; Milliman and Meade, 1983; Ott, 1988; Syvitski et al., 2003). While the largest amount of these sediments is trapped on the continental shelves, only a minor amount constituted by fine sediments reaches the deep ocean at 5000 m water depth (e.g., Hill et al., 2007). Terrigenous sediments are also transported by winds over large distances (e.g., Koopmann, 1981; Sarnthein et al., 1981; Middleton and Goudie, 2001; Stuut et al., 2005), like the Saharan dust over the Atlantic towards the Caribbean (Prospero et al, 1981; Middleton, 1985; Swap et al., 1996). Glacio-marine deposits, like

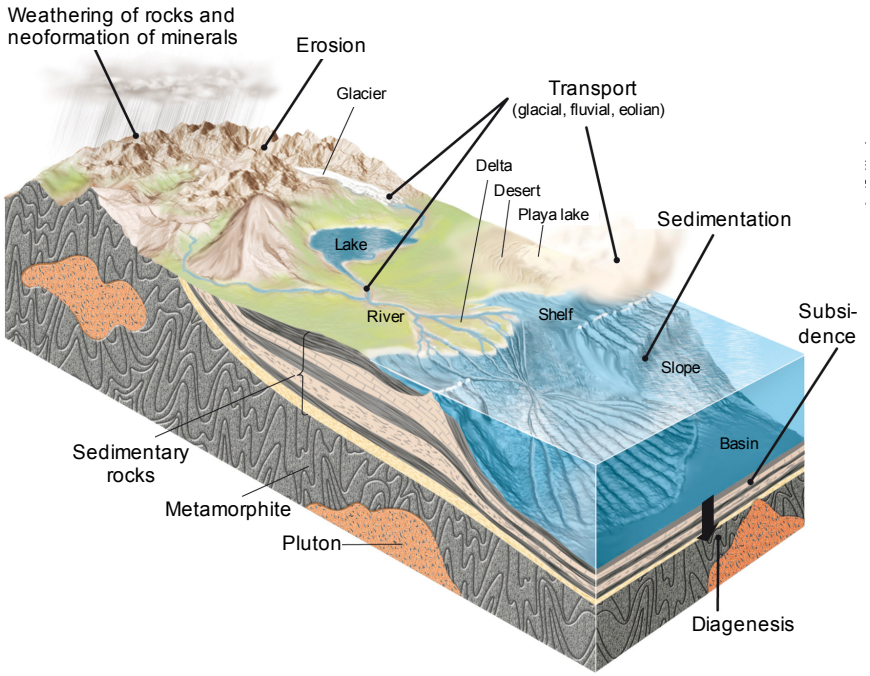

Fig. 1.2. Processes affecting the sediments at the Earth surface (adapted from Grotzinger et al., 2008).

ice-rafted debris (IRD), is another supplier of terrigenous material transported by glaciers from polar to sub-polar regions. This sediment deposition is most expressed during deglacial phases and characterized by the deposition of heterogeneous and poorly sorted grain-size distributions of angular particles (e.g., Bischof, 2000).

Among the geoscientific methods, environmental magnetism is capable to detect environmental changes in an exceptionally broad range of natural realms, ranging from terrestrial over fluvial and limnic to marine (e.g., Thompson and Oldfield, 1986; Dunlop and Özdemir, 2001; Evans and Heller, 2003). All of these realms show magnetic mineral assemblages of various origins (e.g., eolian, fluvial or biogenic) reflecting different sources and climates. Although magnetic Fe-oxide, Fe-hydroxide, and Fe-sulfide minerals are relatively low in species number and concentration in natural soils and sediments (e.g., Kämpf and Schwertmann, 1983; Schwertmann and Taylor, 1989), even trace contents (ppm) can be quantified. Based on the distinct properties of magnetic minerals (mineralogy, concentration, and grain size) found in continental margin sediments, enviromagnetism is suitable to link terrestrial climatic to marine hydrodynamic conditions (e.g., Thompson and Oldfield, 1986; Dunlop and Özdemir, 2001; Evans and Heller, 2003 and references therein). A range of sensitive sedimentary parameters can successfully be used to (1) distinguish between terrigenous sediment source areas, (2) identify transport processes, i.e. pathways of eolian, fluvial, as well as marine sediments, and (3) detect authigenic iron (Fe) minerals formed by biomineralization, abiotic precipitation and diagenetic processes. Enviromagnetism combined with other methods like sedimentology has an even larger potential to reveal interactions of the Earth's subsystems with influence on the sediment composition and its properties (e.g., Liu et al., 2012). The joint consideration of these methods yields more robust and generally valid explanations for processes, which would not be possible by performing solely one of these methods.

1.2. Magnetic minerals, their properties, and their origin

1.2.1. Major magnetic minerals

The most abundant magnetic minerals in nature can be divided into two groups; the Fe-(hydr)oxides and the Fe-sulfides (e.g., Thompson and Oldfield, 1986; Frederichs et al., 1999; Dunlop and Özdemir, 2001; Evans and Heller, 2003; Tauxe, 2005; Liu et al., 2012). However, the Fe-(hydr)oxides have by far the largest impact on the magnetic properties of natural materials. Fe-cations within the crystal lattice of Fe-(hydr)oxides are very often substituted by cations of other elements. The most important substitute is titanium (Ti). In nature, Fe and Ti constitute a continuous solid solution series (Fig. 1.3), generally displayed in the ternary phase diagram of FeO (wüstite) – Fe_2O_3 (hematite) – TiO_2 (rutile). From the magnetic point of view, the two important solution series are the 'Ti-magnetites' and the 'Ti-hematites'. Both series contain different proportions of Fe- and Ti-cations and can be differentiated by investigations of their specific thermoremanent magnetizations. Since this thesis is focused on room-temperature magnetic properties, the Fe-Ti-oxide solid solution series is simplified to magnetite (maghemite) and hematite, being the most common magnetic forms in natural sediments.

Magnetite (Fe_3O_4; Fig. 1.4a) is the most magnetic and a very abundant natural mineral that is almost omnipresent in soils and marine sediments, being also vastly found in igneous, metamorphic and sedimentary rocks, which act as primary sources. Magnetite has a spinel (cubic center-faced) crystal structure. The unit cell has eight tetrahedral sites (Fe^{3+}) and sixteen octahedral sites (50% Fe^{3+} and 50% Fe^{2+}). Magnetite occurring as fine particles is characterized by a distinct black color.

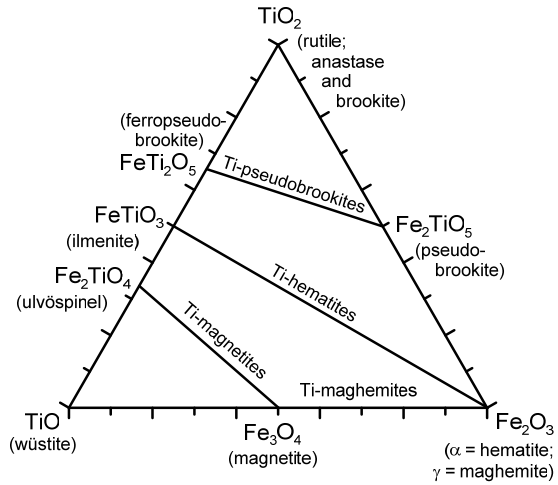

Fig. 1.3. Ternary phase diagram of iron (Fe) and titanium (Ti) oxides displaying the solid solution series (adapted from Evans and Heller, 2001).

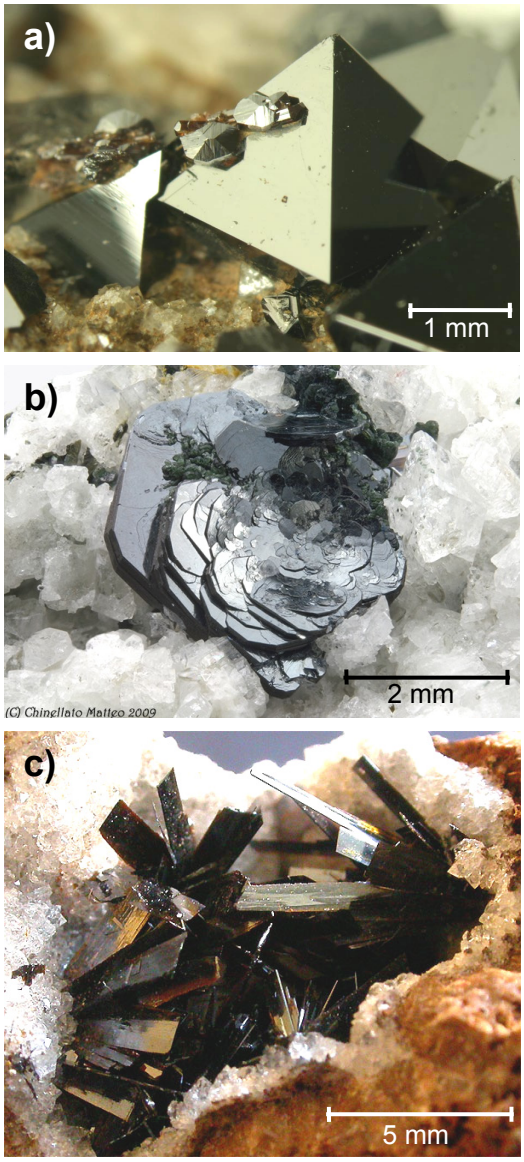

Fig. 1.4. Major magnetic minerals: (a) euhedral magnetite (Wallis, Switzerland – ©Dominik Schläfli); (b) euhedral hematite platelets (Bolzano, South Tirol – ©Matteo Chinellato); and (c) assemblage of goethite minerals (Indre, France – ©Peter Haas) (all pictures from www.mineralienatlas.de)

Hematite (αFe_2O_3; Fig. 1.4b) is a significant magnetic mineral found in oxidized igneous rocks and sediments formed under oxidizing environmental conditions. Hematite has a corundum-like (rhombohedral-hexagonal) crystal structure. It is constituted by tetrahedral Fe-O_3-Fe units. Each unit's Fe-ion pair is coupled by anti-parallel spin moments due to exchange interaction through the Fe-O-triplets.

Maghemite (γFe_2O_3) is a cation-deficient spinel. As it shows the crystal structure of magnetite, its magnetic properties are very similar. Maghemite is an oxidized form of magnetite (Fig. 1.3), thus its stoichiometry resembles that of hematite. A possible cation-deficient (square '□' marked) structural formula of maghemite is $Fe^{3+}[Fe^{3+}_{5/3}\square_{1/3}]O_4$. Maghemite is less stable than magnetite or hematite and is often transformed to hematite under oxidizing environmental conditions.

Goethite (αFeOOH; Fig. 1.4c) is often found as a stable weathering product in soils under humid climatic conditions. Its crystal structure is orthorhombic, which often shows cation-deficient disorder. Goethite is characterized by prominent reddish to brownish yellow.

Iron sulfides, besides the Fe-(hydr)oxides, are the second most abundant magnetic minerals. Pyrrhotite (FeS) is the most magnetic Fe-sulfide. However, when its monoclinic crystal lattice is perfect, it shows no

magnetization. Magnetization is enabled by vacancy ordering, which leads to stoichiometries of Fe_7S_8 to Fe_9S_{10}. As pyrrhotite is a semi-stable mineral, it is often transformed to the magnetic greigite (Fe_3S_4) and later on can be replaced by the also magnetic pyrite (FeS_2) e.g., under reducing conditions due to high organic matter content (Fig. 1.5). High organic matter contents of marine sediments are usually caused by high primary bioproductivity coupled with slow bottom-water circulation and thus low oxygenation rates. Since Fe-sulfides have often a diagenetic origin, they are therefore treated as 'secondary' magnetic minerals.

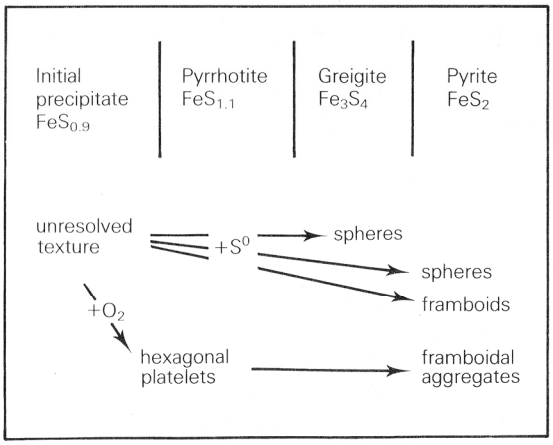

Fig. 1.5. Transformation of various sedimentary iron sulfides due to sulfurization reactions (from Thompson and Oldfield, 1986).

1.2.2. Origin of major magnetic minerals

Igneous rocks are the main natural sources for magnetic minerals contained in sediments deposited on the continent and in the marine realm (e.g., Rumble, 1976; Thompson and Oldfield, 1986; Frederichs et al., 1999; Dunlop and Özdemir, 2001; Evans and Heller, 2003; Tauxe, 2005; Liu et al., 2012). These minerals can be initially present as fine grains in lava outflows, pyroclastic clouds and ashes. Below the surface, magnetic minerals slowly crystallize in coarse-grained plutonic rocks. In many igneous rocks, magnetite is euhedral as it is one of the first crystals to be formed. However, it can also occur as small anhedral grains embedded in a siliceous matrix, when it crystallizes as one of the last minerals. Hematite is less common in igneous rocks and occurs mainly as fine grains. Pyrrhotite and goethite are uncommon in igneous rocks.

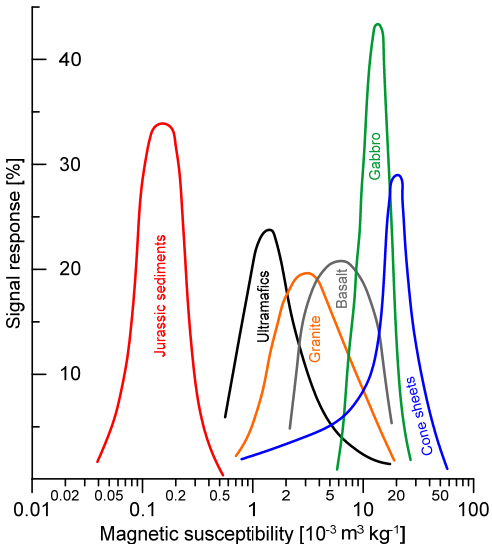

Fig. 1.6. Relative concentrations of magnetic minerals in main terrigenous source rocks, displayed by means of magnetic susceptibility values. Increasing values mirror higher concentrations of all magnetic minerals (redrawn from Thompson and Oldfield, 1986).

Basalt, as a mafic rock, is characterized by its dark mineral assemblage (e.g., feldspars and pyroxene). It contains one of the highest Fe-oxide concentrations (2–6%) of all igneous rocks (Fig. 1.6). Many continental basalts have passed high-temperature (>600°C) oxidation, which may have altered the original magnetic mineral content acquired during crystallization from the magma. High-temperature oxidation progressively alters Ti-magnetite to magnetite and ilmenite, then to Ti-hematite and rutile and finally to pseudobrookite (Fig. 1.3). Ti-maghemites can exsolve at temperatures of 400–600°C. High-temperature oxidation is usually related to volatile accumulation, which is prevalent in subaerially extruded lava flows.

Gabbro has the same petrology as basalt. However, as it is a plutonic rock, it has passed a slow cooling process and is thus characterized by large (Ti)-magnetite minerals. (Ti)-hematite can be found in weathered gabbros as a 'secondary' mineral (Fig. 1.6).

Granite is a plutonic rock containing a felsic (bright) and coarse mineral assemblage (quartz, feldspar, and muscovite). The Fe-oxide concentrations are lower than those of basalts and gabbros (Fig. 1.6). The most important magnetic phase is made up by (Ti)-hematite, being less Ti-rich than that of mafic rocks.

Metamorphic rocks can also provide magnetic minerals. However, low-grade metamorphosis (green-schist facies) mainly destroys all primary Fe-oxide minerals and may contain pyrite. Neoformation of large and pure magnetite, as well as hematite grains can proceed during high-grade metamorphosis (granulite facies).

Magnetosomes are the most abundant magnetic particles of non-igneous (non-clastic) origin. They are chains composed of individual fine magnetite particles, which were produced by magnetotactic bacteria. Magnetosomes are omnipresent in marine sediments and have specific magnetic properties, which can provide a significant contribution to the sedimentary bulk-magnetic signal. This is often detectable in areas of high nutrient input and high sedimentation rates (e.g., off river mouths and in upwelling areas) creating favorable conditions for living magnetotactic bacteria, while preventing relict magnetosomes from dissolution due to rapid burial. However, in regions of large terrestrial sediment input (i.e., at continental margins) or under reductive sedimentary conditions, magnetosomes play a minor role with respect to the sedimentary bulk-magnetic signal, but have always to be considered as a potential biogenic source.

1.2.3. Basic magnetic properties

All materials are magnetic, thus they can be differentiated and classed by rock and environmental magnetism in a qualitative and a quantitative way. The materials can be classified as diamagnetic, paramagnetic, ferromagnetic, ferrimagnetic, and antiferromagnetic (Fig. 1.7) (e.g., Thompson and Oldfield, 1986; Frederichs et al., 1999; Dunlop and Özdemir, 2001; Evans and Heller, 2003; Tauxe, 2005; Liu et al., 2012 and references therein).

Diamagnetism is the weakest of all magnetic properties. It is caused by the interaction of the applied magnetic field with the electron orbital motion of the investigated material. The measurable result is a weak negative magnetization, while strong magnetic fields can even repel diamagnets. In absence of the external magnetic field, the material's magnetization vanishes. The spin magnetic moments of electrons do not contribute to the magnetization here. This is due to the paired spin motion of all available electrons. Most abundant natural diamagnets are calcium carbonate ($CaCO_3$), feldspars, clastic (quartz) and biogenic (radiolarians and diatoms) silica (SiO_3), as well as water. Diamagnetism is detectable by low negative magnetic susceptibility values.

Paramagnetism arises when a material contains individual molecules, atoms or ions with a permanent elementary magnetic dipole moment. The latter aligns parallel to the direction of an applied magnetic field, which results in a weak positive magnetization. Thus, paramagnets are attracted by

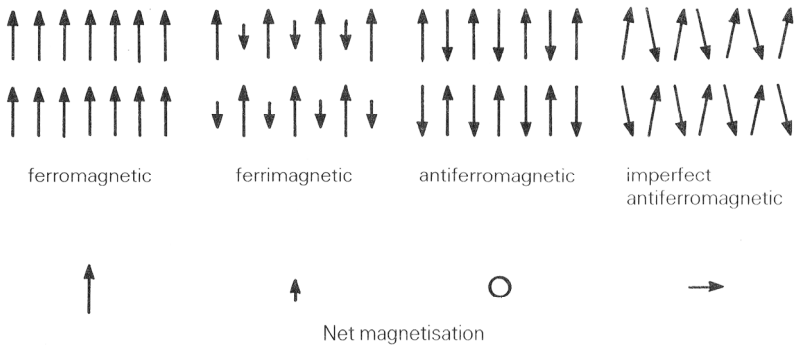

Fig. 1.7. Types of magnetization due to different arrangements of electron magnetic moments found in natural materials (from Thompson and Oldfield, 1986).

magnetic fields. As soon as the external magnetic field is shut off, this magnetization is lost due to thermal dissipation. Natural paramagnetic minerals are olivine, pyroxene, garnet, biotite, pyrite, as well as Fe- and Mn-bearing carbonates. Paramagnetism is generally caused by the deficient fill of the inner electron shells of ions like Mn^{2+}, Fe^{2+} and Fe^{3+}. This results in unpaired electrons with free spin magnetic moments. Paramagnetism contributes in a relatively weak positive way to magnetic susceptibility.

Ferromagnetism is defined by materials, which are capable to carry a strong remanent magnetization in the absence of an applied magnetic field. This ferromagnetic behavior is observed below the so-called 'Curie temperature', which is specific for each material. Above this temperature, the material's ferromagnetic ordering breaks down due to thermal energy and shows paramagnetic behavior. Ferromagnetism arises from exchange interactions among magnetic groups within a material. Within one group, all elementary magnetic moments of adjacent electrons are aligned parallel to each other by quantum mechanical effects (Fig. 1.7). Thus, ferromagnets obtain the strongest magnetization of all materials. The most common ferromagnets are iron, cobalt and nickel. However, in the Earth crust they are rarely found in their metallic form and if present, they are usually of cosmic origin. Ferromagnetism is distinguished by the highest susceptibility and magnetic remanence values.

Ferrimagnetism is similar to ferromagnetism as ferrimagnetic materials carry remanent magnetization below the 'Curie temperature' or the 'Néel temperature' and are paramagnetic above these. Ferrimagnets are mainly Fe-oxides with a spinel crystal structure (close-packed face-centered cubic). Their crystal structure is characterized by two lattice planes with anti-parallel magnetization (Fig. 1.7). However, one of the sub-lattices shows weaker electron magnetic moments than the other, which results in a net bulk magnetization of the material. The imbalance between the lattice planes is caused by different ionic populations or by crystallographic dissimilarities. The most important and common ferrimagnets are magnetite and maghemite.

Antiferromagnetism is characterized by identical antiparallel magnetic moments between two lattice planes. Thus, the net bulk magnetization of the material is zero below the 'Néel temperature'. Net bulk magnetization ('parasitic ferromagnetism') can be obtained (Fig. 1.7), when the ordering of the two lattice planes to each other is imperfect due to impurities (substitutes) or lattice defects, as well as due to spin canting of electron moments. The most important antiferromagnetic minerals are hematite and

goethite. The contribution of antiferromagnets to susceptibility and to remanent magnetization is smaller than of ferro- and ferrimagnets. With respect to susceptibility, it is larger than that of paramagnets, however.

1.2.4. Magnetogranulometry

Besides the magnetomineralogy, the grain size of magnetic minerals has a significant influence on the respective magnetic properties (Fig. 1.8) (e.g., Thompson and Oldfield, 1986; Frederichs et al., 1999; Dunlop and Özdemir, 2001; Evans and Heller, 2003; Tauxe, 2005; Liu et al., 2012; Hatfield, 2014 and references therein). This is due to the arrangement of magnetic domains within an individual ferrimagnetic or imperfect antiferromagnetic grain (Fig. 1.9a). Each magnetic domain is defined as a certain region with a distinct direction of spontaneous magnetization. Considering all magnetic domains of a grain, the net spontaneous magnetization can be zero, resulting in externally no detectable magnetization. These domains are separated by 'Bloch walls' (Fig. 1.9b). The emergence of single domains surrounded by Bloch walls within a grain is due to an advantageous balance between all spontaneous magnetizations, aiming at the lowest possible net energetic state. The lowermost energetic state of a magnetite grain is mostly attained at a domain size of ~1 µm.

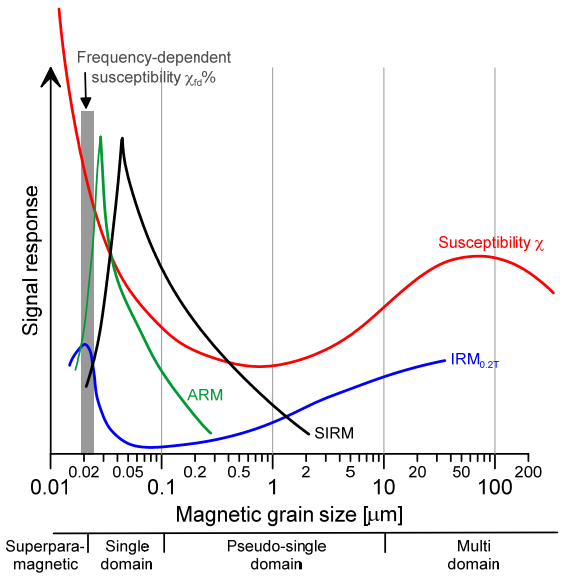

Fig. 1.8. Room-temperature rock and enviromagnetic parameters displayed versus magnetic grain size and domain state: magnetic mass susceptibility χ, frequency-dependent susceptibility χ_{fd}%, isothermal remanent magnetization acquired at 0.2 T direct fields ($IRM_{0.2T}$), saturation IRM (SIRM), anhysteretic remanent magnetization (ARM) acquired at alternating fields (redrawn from Crockford and Willett, 1997).

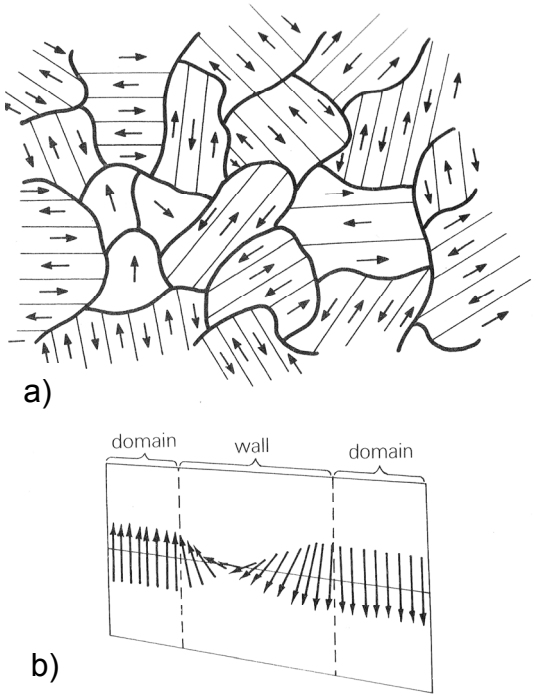

Fig. 1.9. (a) Magnetic domain arrangements in polycrystalline grains and (b) progressive rotation by 180° of electron spins through a domain (Bloch) wall during remagnetization (from Thompson and Oldfield, 1986).

Multi-domain (MD) behavior is typical for magnetite grains with a diameter of >10 µm (Fig. 1.8). Under applied magnetic fields of adequate strength, these grains obtain a net field-parallel magnetization by shifting of the Bloch walls (Fig. 1.9b). In this way, domains with an initial field-parallel magnetization grow at the cost of domains with other directions of magnetization. The grain reaches magnetic saturation, when all electron magnetic moments are aligned

parallel to the applied field. When the applied field is removed, some Bloch walls may return to their initial positions. However, some of them are 'trapped' and the grain attains a new energetic balance, a relatively 'soft' ('viscous') MD remanent magnetization. MD grains have a significant contribution to magnetic remanence acquired at 0.2 T magnetic fields (Fig. 1.8).

Single-domain (SD) behavior is fundamentally different from MD behavior, as movements of Bloch walls are of no relevance here. SD grains of pure magnetite have diameters of 20–100 nm (Fig. 1.8), while each SD grain is composed of exactly one magnetic domain (visualized by one single arrow in Fig. 1.9a,b). Under applied magnetic fields, the SD grain has only two possible magnetic states, a field-parallel or anti-parallel one. For this reason, SD grains carry the highest remanent magnetizations (i.e., saturation remanent magnetization; SIRM, Fig. 1.8), while the SD grains require higher field strengths for remagnetization than MD grains.

Superparamagnetic (SP) behavior of magnetite grains is restricted to diameters of <20 nm (Fig. 1.8). These grains are not capable to obtain a remanent magnetization at room temperature. As soon as there is no applied magnetic field, thermal dissipation exaggerates the electron magnetic moments of these ultra-fine grains. Nevertheless, superparamagnets have the largest contribution to magnetic susceptibility and frequency-dependent susceptibility (Fig. 1.8). Thus, superparamagnetism shows certain parametric parallels to paramagnetism. However, the effect of superparamagnetic materials is much stronger.

Magnetic grains with diameters between 0.1 and 10 µm are named '***pseudo-single domain***' (PSD) particles (Fig. 1.8). This PSD range is a transition zone between SD and MD grains, rather than a range defined by an independent magnetic behavior: Each of the PSD grains contains more than one magnetic domain. However, they show net magnetic behavior more similar to SD than to MD grains. With respect to magnetogranulometry, the focus is mainly set on magnetite as hematite (and other magnetic minerals) has larger SD-MD transition sizes, mainly due to significantly lower SIRM. For example, MD behavior of hematite requires grain-sizes >100 µm, which are very rare in marine sediments. Thus, sedimentary hematite can be generally treated as SD particles.

1.2.5. Environmental factors influencing sedimentary magnetic signatures

As the Earth's surface is exposed to atmospheric processes, to colonization by plants and to weathering, as well as to soil formation, initial magnetic properties (magnetomineralogy and magnetogranulometry) of source rocks can be affected by various processes of dilution, transport or transformation (e.g., Thompson and Oldfield, 1986; Frederichs et al., 1999; Dunlop and Özdemir, 2001; Evans and Heller, 2003; Tauxe, 2005; Liu et al., 2012; Hatfield, 2014 and references therein). Here, the most prevalent influences are listed:

Chemical transformation of magnetic minerals occurs mainly during tropical (humid) weathering and soil formation, which can lead to conversion of Fe-bearing paramagnetic minerals to ferri- and antiferromagnets. However, also transformation from one ferrimagnet (or antiferromagnet) to another can happen, as well as a reversal from ferri- to paramagnets (e.g., pyrite). These transformations are explained by the following causalities: As igneous source rocks contain lots of Fe^{2+} within silicates, hydrolytic and oxidative weathering releases these ions as Fe^{3+} with low solubility. This process leads

to precipitation of Fe-oxides and Fe-hydroxides. Subsequent suboxic or anoxic conditions may reduce sedimentary Fe^{3+} to the more soluble Fe^{2+}, which is often diluted by water and precipitates at other localities. These chemical reactions are significantly dependent on soil pH, E_H, temperature, organic matter concentration and the soil's ability to retain moisture (most expressed within clays), as well as on the climate in general. 'Primary' magnetite contained in igneous rocks is consequently weathered to 'secondary' pedogenic hematite and goethite. Hematite is mainly restricted to well-aerated soils with a rapid decomposition of organic matter, which are exposed to high temperatures and affected by intermittently dry and wet seasons (e.g., Kämpf and Schwertmann, 1983; Schwertmann and Taylor, 1989). Igneous rocks containing preferably primary hematite are mainly weathered to secondary goethite under cooler and moister conditions.

Physical comminution takes place due to physical weathering during sediment transport by rivers, winds and glaciers. Changes in the clastic grain size of the crushed material can also have an impact on magnetic parameters, if also the magnetic grain size is affected.

Transport and deposition can affect the clastic and the magnetic grain size. Fluvial, eolian and ocean current transport leads to grain-size sorting due to different transport velocities. In this way, different transport paths and modes are distinguishable from each other. However, it has to be considered that measured magnetic properties of the deposited sediment may therefore also differ from the primary source-rock signatures.

Concentration and dilution of magnetic minerals is caused by various processes without alteration of the primary magnetic mineralogy. Usually, primary Fe-oxides are more resistant towards weathering than other minerals (e.g., feldspars, mica, and clay minerals) and thus can be enriched in the upper soil layers. In contrast, sedimentary concentrations of terrigenous magnetic minerals can also be lowered due to simultaneous deposition of organic matter, $CaCO_3$ and SiO_3 (organic silica and detrital quartz).

Physical comminution, transport, and deposition, as well as concentration, and dilution jointly influence the magnetic properties of sediments. These affecting factors can be differentiated, which is the discipline of environmental magnetism. As these controlling factors are governed by environmental conditions, conclusions can be also drawn about climate change or different paleoceanographic states based on magnetic investigations of sediments. Due to these impacts on magnetic properties, primary magnetic Fe-oxide assemblages (and thus source rocks) can be differentiated from secondary pedogenic magnetic Fe-(hydr)oxides by their magnetogranulometry, as a first indicator. In particular, secondary magnetite and maghemite exclusively occur within the SP grain-size range, while the primary magnetite grains occur also as SD and MD particles. Dilutional effects on magnetic signatures of ferri- and antiferromagnets due to admixing of diamagnetic or paramagnetic material can be avoided, when concentration-independent interparametric ratios are considered. Further support for distinction between environmental processes can be achieved by clastic grain-size parameters: Magnetogranulometry is not directly (linearly) linked to the clastic grain size, as e.g. fine hematite can occur as coating on sand grains and ultra-fine magnetite can be incorporated in agglutinating benthic foraminifera shells or quartz particles of different diameters. Thus, specific magnetic grain sizes (or

relation between magnetic and clastic grain size) may still reveal the original magnetic source-rock signature in spite of clastic grain-size sorting during transport.

1.3. Clastic grain-size parameters and sediment transport

Terrigenous sediments are transported to the continental shelves of the investigated areas off SE South America and NW Africa mainly by rivers (e.g., Plata River of South America and the Senegal River of Africa) (Barusseau et al., 1988; Violante and Parker, 2004; Nizou et al., 2010; Lantzsch et al., 2014). Fluvial sediment load reaching the ocean is primarily restricted to clays and silts (Milliman and Meade, 1983; Ott, 1988; Syvitski et al., 2003). Continuous and dominant deposition of eolian material in the marine realm is mainly detectable in regions with minor fluvial sediment input (e.g., off Patagonia and the Pampas, as well as to the west of the Sahara) (e.g., Sarnthein et al., 1981; Gaiero et al., 2003; Stuut et al., 2005; Itambi et al., 2009; Just et al., 2012). In addition, coastal wave erosion plays a significant role as deliverer of sandy detritus (e.g., Swift and Palmer, 1978; Potter, 1984, 1986). Sediment transport and thus the respective distribution patterns on the shelf are governed by different factors (e.g., McCave, 1972; Hill et al., 2007): (1) the origin and the amount of available material; (2) the atmospheric circulation systems; and (3) the ocean-circulation patterns (in combination with trans- and regressional cycles of the sea level). Further sediment transport over the shelf towards the slope takes place in three ways: by (i) advection due to shelf-water currents; (ii) diffusion due to storm events; and (iii) dense suspension flows driven by gravity, generating nepheloid layers between water masses of different densities due to the contained sediment load. Subsequent sediment distribution at the slope is governed by (iv) gravity (e.g., turbidites or debris flows) and, if present, by (v) western boundary currents. The latter show surface-water velocities of 10–50 cm s^{-1} (Palma et al., 2004, 2008) with velocities of ~20 cm s^{-1} over ground off SE South America (Gwilliam et al., 1997; Vivier and Provost, 1999) and generate large-scale elongated contouritic sand and silt deposits (e.g., Hernández-Molina et al., 2010; Rebesco et al., 2014 and references therein).

Fluvial, eolian and ocean-current transport with respect to amount and transport energy is mirrored by the grain-size distributions and other granulometric parameters (e.g., Ott, 1988; Tucker, 1996). The ***grain size*** found at continental margins ranges from gravel (63–2 mm) via sand (2 mm–63 µm) to silt (63–2 µm) and clay (<2 µm). Since sediments are mainly available as mixtures, their compositions can be best visualized by cumulative grain-size distribution curves, or by volume and weight frequencies of the respective grain-size fractions (Fig. 1.10a). If no grain-size fraction reaches >50%, the two most dominant fractions are used to define the general sediment composition (e.g., 'silty clay' or 'sandy silt'). All other granulometric parameters are usually derived from the cumulative grain-size curve (Fig. 1.10a). The ***sorting*** (σ_ϕ) of the sediment (Fig. 1.10b) is represented by the curve's width, which is comparable to the standard deviation in statistics. Well sorted sediments yield a small σ_ϕ value and conversely for poorly sorted sediments. The ***kurtosis*** describes the steepness of the curve's peak with respect to the spreading of the entire distribution curve (Fig. 1.10b). The ***skewness*** is a measure for the symmetry of the curve (Fig. 1.10c), which reaches 0 in the case of perfect symmetry. The ***median*** can always be used as a representative value for a grain-size distribution, as it provides a certain grain-size above and below which 50% of the sediment is found (Fig. 10c). The ***mean value***

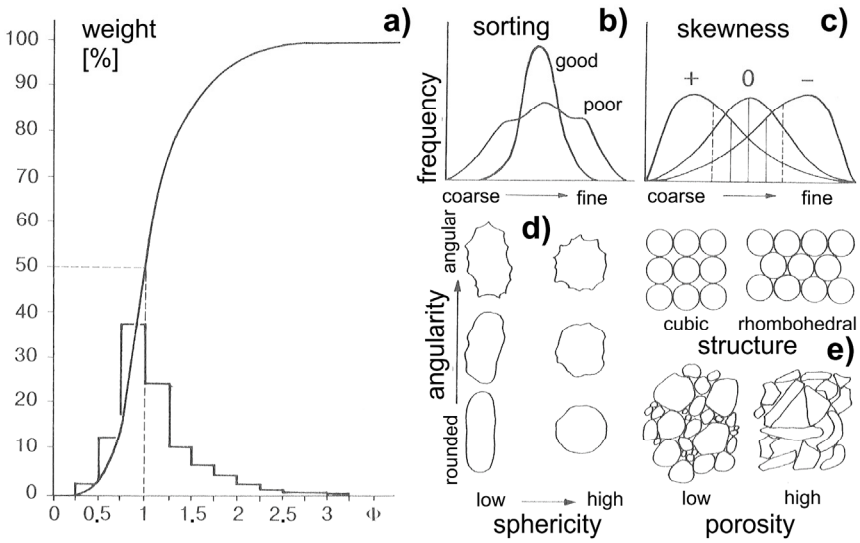

Fig. 1.10. Sediment properties: (a) Grain-size distribution as cumulative curve and histogram; (b) Quality of sediment sorting; (c) Skewness – the central distribution is symmetric, the others show dominance of coarse or of fine particles; (d) Angularity and sphericity of individual grains; and (e) Structure and porosity of sediments and sedimentary rocks (adapted from Ott, 1988).

resembles the grain-size average only when the grain-size distribution is symmetrical (Fig. 10c). In addition, the ***angularity*** (Fig. 1.10d) presents another possibility to differentiate transport processes due to the shape of individual particles (e.g., fluvial sediment particles are rounded, while IRD is mainly composed of angular particles). As different grain-size distributions have an influence on the sediment ***structure*** and ***porosity*** (Fig. 1.10e), the latter also bear information about transport and depositional conditions which cannot be derived solely from grain-size parameters (e.g., settling in calm water leads to deposition of hetergenous particles creating more compact packages, while strong currents cause deposition of homogenous particles, which increases porosity).

Sediment particles carried by ocean currents can be transported over a range of distances. The time to reach the ocean floor is thus dependent on the grain-size, the mineral density, and the depth of the water column (bathymetry). Hence, at the continental slope in water depths of ~1000 m, clay and silt need months to decades to reach the ground (e.g., Ott, 1988; Tucker, 1996). Most of these fine particles reach the ocean floor significantly faster as they are incorporated into larger aggregates (fecal pellets) created by suspension feeders (e.g., Dietrich et al., 1975; Koopmann, 1981 and references therein; Ott, 1988 and references therein). However, sufficiently high water velocity at the sea floor can resuspend already settled particles. These are usually further transported by creeping (i.e., as bed load) and saltation. The most popular way to make a first approximation about water velocities, which can erode, transport or deposit particles of

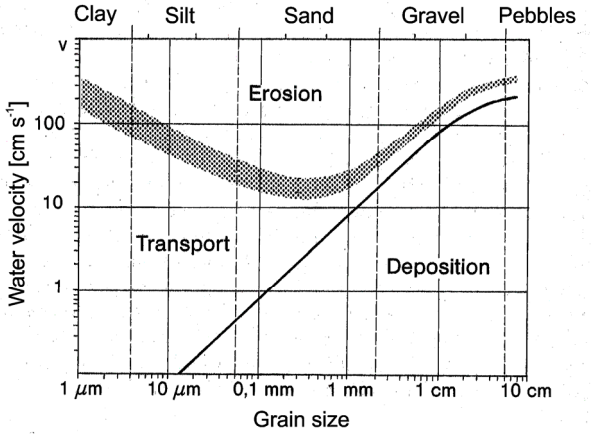

Fig. 1.11. Hjulstrøm diagram displaying sediment dynamics with respect to fresh-water velocities (1 m above ground) and eroded, transported or deposited quartz patricles of various diameters. The boundaries between clay, silt, sand, gravel, and pebbles are marked by dashed vertical lines. Subdivision in fine, middle, and coarse fractions is visualized by minor tick marks at the top of the diagram (adapted from Ott, 1988).

a certain grain size, is by using the 'Hjulstrøm diagram' (Fig. 1.11). As this curve was compiled for fresh water under room-temperature conditions and for water velocities measured 1 m above the ground, the relation between water velocity and grain size will differ for deep-ocean currents acting directly at the ground. Hence, in the marine realm this curve has a rather qualitative than a quantitative meaning. A more precise method to reveal erosion, transport and deposition of particles with different diameters was demonstrated by Soulsby and Whitehouse (1997). They published non-dimensional diagrams for horizontal and sloping beds, as well as for wave and current motions. In particular, the contained Shields and Soulsby curves display relations between the non-dimensional grain size and the non-dimensional threshold value of the 'Shields parameter' (proportional to the bed shear stress). In this way, forces acting directly on grains of certain diameters and densities can be calculated using the underlying formulas. They precisely reveal shear forces and thus water velocities required for each of the above mentioned sedimentary processes.

1.4. Objectives and thesis outline

The continental margins of SE South America (ca. 20°–55° S) and NW Africa (here, 14°–17° N) are challenging regions from the geoscientific point of view, as they are sensitive to climate change. Both continental margins obtain sediments from various terrestrial sources, each conveying specific magnetic mineral assemblages due to existent source-rock petrology and respective climatic and weathering conditions (e.g., Koopmann, 1981; Gaiero et al., 2003; Nizou et al., 2010; Lantzsch et al., 2014). The delivered fluvial and eolian shelf and slope sediments are distributed by ocean currents, which are under influence of the South American Monsoon System (SAMS) and the Southern Westerly Wind Belt (SWWB) (Palma et al., 2004, 2008), as well as under the influence of the northeasterly trade and the easterly Harmattan winds, respectively (Hagen, 2001; Stramma et al., 2005). Thus, these sediment distribution patterns may mirror likewise atmospheric and hydrographic circulation patterns, which are strongly dependent on the climate and its variation with time.

The amount of available rock and enviromagnetic studies in the realm of SE South America is fairly limited (e.g., Schmidt et al., 1999; Orgeira et al., 2003; Garming et al., 2007; Mathias et al., 2014), being often focused on soil weathering or post-depositional diagenetic processes of Fe-oxides (e.g., Allan et al., 1989; Garming et al., 2005). The few available magnetic-based provenance studies are mainly limited to regional areas of this continental margin and unable to compare major terrestrial sediment sources with each other. In spite of other studies aimed at identifying the terrestrial sources and related transport paths (e.g., Urien and Ewing, 1974; Martins et al., 2005; Campos et al., 2008; Corrêa et al., 2008; Mahiques et al., 2008; Gyllencreutz et al., 2010; Nagai et al., 2013), which cover a broad range of geoscientific methods (granulometry, stable isotope geochemistry, heavy and clay mineral analysis), there remain many open questions and even controversies concerning the shelf transport of relict sands, as well as of recent fluvial slits and clays. In addition, paleoclimatic studies in the realm of South America were concerned either with the temporal and spatial variations of the SAMS (Behling, 1997; Cruz et al., 2005; Wang et al., 2006, 2007) or of the SWWB (e.g., Kilian and Lamy, 2012 and references therein). However, so far there are no paleoclimatic studies taking both atmospheric circulation systems into joint consideration.

In contrast, in the realm of NW Africa, the magnetic properties of terrestrial source sediments are much better investigated (e.g., Lyons et al., 2010, 2012), as well as those of the marine deposits (e.g., Itambi et al., 2009; Just et al., 2012). Also the fluvial and eolian transport mechanisms are well understood (e.g., Koopmann, 1981; Nicholson, 2009; Nizou et al., 2010). This makes this site suited for investigations with the aim to fathom the potential of magnetic approaches on a grain-size specific basis, being so far rarely applied to such complex marine sedimentary environments. Prior to the consideration of issues related to sediment provenance and paleoclimate, the following general questions arise with respect to the used sedimentary parameters:

- How sensitive are magnetic properties for delineation of terrigenous sediment provinces on the investigated continental margins with respect to source-rock signatures and to particular weathering (climatic) conditions?
- In which way do clastic grain-size distributions help to distinguish between source- and transport-related sedimentary signatures?
- To which extent are bulk-sediment properties – in combination with major-element and stable-isotope signatures, as well as benthic and planktonic data – capable to reveal differences between eolian, fluvial and ocean-current transports and to detect temporal changes in transport intensities?
- What is the additional gain of information revealed by enviromagnetic investigations on a grain-size specific basis if compared with bulk-magnetic studies?

Are the above questions satisfactorily solved, one can prompt more far-reaching questions:

- What is the extent of the specific terrigenous sediment provinces on the investigated continental margins?
- Which are the main fluvial and eolian sediment contributors to these shelves and slopes, and where are the primary magnetic minerals derived from?
- How did each of the involved atmospheric and marine circulations systems vary with time due to climate change since the Last Glacial Maximum (the last ~19 kyr) and what was their joint influence on environmental processes on a continental and global scale?

These above mentioned issues are addressed in the individual studies of this thesis. Nevertheless, each of the studies has its own specific emphasis on provenance, paleoclimate, and paleoceanography, or methodology.

Chapter 2: Interaction of the South American Monsoon System and the Southern Westerly Wind Belt during the last 14 kyr

In this published paper, bulk-magnetic properties together with clastic grain-size distributions, dry-bulk porosities, major-element signatures, $CaCO_3$-concentrations, and abundances of siliceous diatoms are investigated. They are obtained from a sediment core recovered from the continental slope of South Brazil. This study aims to differentiate between sediments derived from the Plata River and those from

the Argentinean continental shelf. Based on distinct sediment properties, it is envisaged to reveal sediment transport intensities and latitudinal extents of different shelf waters with respect to the last 14 cal kyr. The superordinate task is to make points on the SAMS and the SWWB, as well as on their joint impact on the surface-ocean circulation of the western South Atlantic.

Chapter 3: Paleoenvironmental evolution and hydrodynamics of the Rio Grande Cone: Insights from benthic foraminiferal and terrigenous granulometric properties from Last Deglacial sediments off South Brazil

This manuscript in preparation deals with the same site as the study mentioned above. However, the focus is on benthic environmental and slope hydrodynamic conditions of the Brazil Current with respect to the Last Deglaciation (19–14 cal kyr BP). For this reason, benthic foraminiferal assemblages, organic matter and $CaCO_3$ concentrations, as well as major-element, stable-isotope signatures and clastic granulometric parameters were investigated. As the Brazil Current is linked to the Atlantic Meridional Overturning Circulation (AMOC), its intensity changes can give clues on essential climatic and oceanographic conditions and interacting processes at global scales; i.e., relation to the Heinrich Stadial 1 (HS1; ~16.8 cal kyr BP) and the Antarctic Cold Reversal / Bølling-Allerød (14.5–12.5 cal kyr BP) at the southern / northern hemisphere, respectively.

Chapter 4: Identification of terrigenous sediment provinces at the continental margin of SE South America

This manuscript under revision displays a provenance study of surface sediments from the SE South American continental margin. Established multivariate analyses like fuzzy c-means cluster analysis and non-linear mapping are used to delineate terrigenous sediment provinces based on concentration-independent interparametric ratios (magnetic and major-element signatures). By means of distinct concentration-independent magnetomineralogical and magnetogranulometric input-parameters, it is aimed at differentiating between source-rock signatures (e.g., the Plata Drainage Basin or the Pampas) and those imprinted by sediment transport dynamics (i.e., grain-size sorting, mineral enrichment or depletion). In this way, discovering of recent and past erosional, as well as eolian and fluvial sediment-delivery mechanisms proves to be possible.

Chapter 5: How environmental magnetism can enhance the interpretational value of grain-size analysis: A time-slice study on sediment export to the NW African margin in Heinrich Stadial 1 and Mid Holocene

This published paper describes the outcomes of an enviromagnetic study of individual (sieved and settled) grain-size fractions of continental slope sediments derived from off NW Africa. By testing a grain-size specific rock-magnetic approach in a glacial arid and a post-glacial humid climate, the aim is to resolve the impacts of individual sediment sources (e.g., coastal dunes versus southern Sahel Zone), as well as of various transport systems (i.e., the trade winds, the Harmattan winds, and the Senegal River). In particular, it is examined whether or not magnetic particles are being enriched or depleted in specific grain-size ranges by these aforementioned factors. It is also tested whether or not the grain sizes of magnetic particles co-vary with clastic grain size and, if so, how strong this link is for

various magnetic mineral associations and provenances. Further paleoclimatic information is derived from the preservation of fine magnetic particles, while pinpointing magnetite dissolution throughout the clastic grain-size range.

1.5. References

Allan, J.E.M., Coey, J.M.D., Sander, I.S., Schwertmann, U., Friedrich, G., Wiechowski, A., 1989. An occurrence of a fully-oxidized natural titanomaghemite in basalt. Mineralogical Magazine 53, 299–304.

Barusseau, J.P., Giresse, P., Faure, H., Lézine, A.M., Masse, J.P., 1988. Marine sedimentary environments on some parts of the tropical and equatorial Atlantic margins of Africa during the Late Quaternary. Continental Shelf Research 8, 1–21.

Behling, H., 1997. Late Quaternary vegetation, climate and fire history of the Araucaria forest and campos region from Serra Campos Gerais, Paraná State (South Brazil). Review of Palaeobotany and Palynology 97, 109–121.

Bischof, J., 2000. Ice drift, ocean circulation and climate change. Springer – Praxis Publishing, 215 p.

Campos, E.J.D., Mulkherjee, S., Piola, A.R., de Carvalho, F.M.S., 2008. A note on a mineralogical analysis of the sediments associated with the Plata River and Patos Lagoon outflows. Continental Shelf Research 28, 1687–1691.

Corrêa, I.C.S., Ayoup-Zouain, R.N., Weschenfelder, J., Tomazelli, L.J., 2008. Áreas fontes dos minerais pesados e sua distribução sobra a plataforma continental sul-brasileira, uruguaya e norte-argentina. Revista Pesquisas em Geosciências 35, 137–150.

Crockford, R.H., Willett, I.R., 1997. The magnetic properties of a stratigraphic section of a sedimentary soil in New South Wales, Australia. CSIRO Technical Report 22/97 (part 1 of 3), CSIRO Land and Water, Canberra, 31 p. (and appendix).

Cruz, F.W., Burns, S.J., Karmann, I., Sharp, W.D., Vuille, M., Cardoso, A.O., Ferrari, J.A., Dias, P.L.S., Viana, O., 2005. Insolation-driven changes in atmospheric circulation over the past 116,000 years in subtropical Brazil. Nature 434, 63–65.

Dietrich, G., Kalle, K., Krauss, W., Siedler, G., 1975. Allgemeine Meereskunde: Eine Einführung in die Ozeanographie, 593 p.

Dunlop, D.J., Özdemir, Ö., 2001. Rock Magnetism: Fundamentals and Frontiers (Cambridge Studies in Magnetism). Cambridge University Press, 573 p.

Evans, M.E., Heller, F., 2003. Environmental magnetism - principles and applications of enviromagnetics. Academic Press, Amsterdam, 299 p.

Frederichs, T., Bleil, U., Däumler, K., von Dobeneck, T., Schmidt, A.M., 1999. The magnetic view on the marine paleoenvironment: parameters, techniques and potentials of rock magnetic studies as a key to paleoclimatic and paleoceanographic changes. In: Fischer, G., Wefer, G. (Eds.), Use of Proxies in Paleoceanography. Springer Berlin Heidelberg, pp. 575–599.

Gaiero, D.M., Probst, J.-L., Depetris, P.J., Bidart, S.M., Leleyter, L., 2003. Iron and other transition metals in Patagonian riverborne and windborne materials: Geochemical control and transport to the southern South Atlantic Ocean. Geochimica et Cosmochimica Acta 67, 3603–3623.

Garming, J.F.L., Bleil, U., Riedinger, N., 2005. Alteration of magnetic mineralogy at the sulfate–methane transition: analysis of sediments from the Argentine continental slope. Physics of the Earth and Planetary Interiors 151, 290–308.

Garming, J.F.L., von Dobeneck, T., Franke, C., Bleil, U., 2007. Low-temperature partial magnetic self-reversal in marine sediments by magnetostatic interaction of titanomagnetite and titanohematite intergrowths. Geophysical Journal International 170, 1067–1075.

Grotzinger, J., Jordan, T.H., Press, F., Siever, R., 2008. Allgemeine Geologie. Spektrum Akademischer Verlag, 736 p.

Gwilliam, C.S., Coward, A.C., de Cuevas, B.A., Webb, D.J., Rourke, E., Thompson, S.R., Döös, K., 1997. The OCCAM Global Ocean Model. In: García, F.G., Cisneros, G., Fernández, A.E, Álvarez, R. (Eds.), Numerical Simulations in the Environmental and Earth Sciences: Proceedings of the Second UNAM-CRAY Supercomputing Conference. Cambridge University Press, pp. 24–30.

Gyllencreutz, R., Mahiques, M.M., Alves, D.V.P., Wainer, I.K.C., 2010. Mid- to late-Holocene paleoceanographic changes on the southeastern Brazilian shelf based on grain size records. The Holocene 20, 863–875.

Hagen, E., 2001. Northwest African upwelling scenario. Oceanologica Acta 24 – Supplement, 113–128.

Hatfield, R.G., 2014. Particle size-specific magnetic measurements as a tool for enhancing our understanding of the bulk magnetic properties of sediments. Minerals 4, 758–787.

Hernández-Molina, F.J., Paterlini, M., Somoza, L., Violante, R., Arecco, M.A., De Isasi, M., Rebesco, M., Uenzelmann-Neben, G., Neben, S., Marshall, P., 2010. Giant mounded drifts in the Argentine Continental Margin: origins, and global implications for the history of thermohaline circulation. Marine and Petroleum Geology 27, 1508–1530.

Hill, P.S., Fox, J.M., Crockett, J.S., Curran, K.J., Friedrichs, C.T., Geyer, W.R., Milligan, T.G., Ogston, A.S., Puig,P., Scully, M.E., Traykovski, P.A., Wheatcroft, R.A., 2007. Sediment delivery to the seabed on continental margins. Continental-Margin Sedimentation: From Sediment Transport to Sequence Stratigraphy. IAP Special Publication 37, 49–100.

Itambi, A.C., von Dobeneck, T., Mulitza, S., Bickert, T., Heslop, D., 2009. Millennial-scale northwest African droughts related to Heinrich events and Dansgaard-Oeschger cycles: Evidence in marine sediments from offshore Senegal. Paleoceanography 24, 1205–1220.

Just, J., Dekkers, M.J., von Dobeneck, T., van Hoesel, A., Bickert, T., 2012. Signatures and significance of aeolian, fluvial, bacterial and diagenetic magnetic mineral fractions in Late Quaternary marine sediments off Gambia, NW Africa, Geochemistry, Geophysics, Geosystems 13, Q0AO02, 23 p.

Kämpf, N., Schwertmann, U., 1983. Goethite and hematite in a climosequence in southern Brazil and their application in classification of kaolinitic soils. Geoderma 29, 27–39.

Kilian, R., Lamy, F., 2012. A review of Glacial and Holocene paleoclimate records from southernmost Patagonia (49–55° S). Quaternary Science Reviews 53, 1–23.

Koopmann, B. 1981. Sedimentation von Saharastaub im subtropischen Nordatlantik während der letzten 25.000 Jahre. “Meteor”-Forschungs-Ergebnisse Reihe C, 35: 23–59.

Lantzsch, H., Hanebuth, T.J.J., Chiessi, C.M., Schwenk, T., Violante, R.A., 2014. The high-supply, current-dominated continental margin of southeastern South America during the late Quaternary. Quaternary Research 81, 339–354.

Liu, Q.S., Roberts, A.P., Larrasoaña, J.C., Banerjee, S.K., Guyodo, Y., Tauxe, L., Oldfield, F., 2012. Environmental magnetism: Principles and applications. Reviews of Geophysics 50, RG4002, 1–50.

Lyons, R., Oldfield, F., Williams, E., 2010. Mineral magnetic properties of surface soils and sands across four North African transects and links to climatic gradients. Geochemistry Geophysics Geosystems 11, Q08023, 22 pp.

Lyons, R., Oldfield, F., Williams, E., 2012. The possible role of magnetic measurements in the discrimination of Sahara/Sahel dust sources. Earth Surface Processes and Landforms 37, 594–606.

Mahiques, M.M., Tassinari, C.C.G., Marcolini, S., Violante, R.A., Figueira, R.C.L., Silveira, I.C.A., Burone, L., Sousa, S.H.M., 2008. Nd and Pb isotope signatures on the southeastern South American upper margin: Implications for sediment transport and source rocks. Marine Geology 250, 51–63.

Martins, L.R., Urien, C.M., Martins, I.R., 2005. Gênese dos sedimentos da plataforma continental atlântica entre o Rio Grande do Sul (Brasil) e Tierra del Fuego (Argentina). Gravel 3, 85–102.

Mathias, G.L., Nagai, R.H., Trindade, R.I., de Mahiques, M.M., 2014. Magnetic fingerprint of the late Holocene inception of the Río de la Plata plume onto the southeast Brazilian shelf. Palaeogeography, Palaeoclimatology, Palaeoecology 415, 183–196.

McCave, I.N., 1972. Transport and escape of fine-grained sediment from shelf areas. In: Swift, D.J.P., Duane, D.P., Pilkey, O.H. (Eds.), Shelf Sedimentation Transport: Process and Pattern. Dowden, Hutchinson and Ross Incorporated, Stroudsburg Pennsylvania, pp. 225–248.

Middleton, N.J., 1985. Effect of drought on dust production in the Sahel. Nature 316, 431-434.

Middleton, N.J., Goudie, A.S., 2001. Saharan dust: sources and trajectories. Transactions of the Institute of British Geographers 26, 165–181.

Milliman, J.D., Meade, R.H., 1983. World-wide delivery of river sediment to the oceans. The Journal of Geology, 1–21.

Nagai, R.H., Ferreira, P.A.L., Mulkherjee, S., Martins, M.V., Figueira, R.C.L., Sousa, S.H.M., Mahiques, M.M., 2013. Hydrodynamic controls on the distribution of surface sediments from the southeast South American continental shelf between 23° S and 38° S. Continental Shelf Research 89, 51–60.

Nicholson, N., Flohn, H., 1980. African environmental and climatic changes and the general atmospheric circulation in Late Pleistocene and Holocene. Climatic Change 2, 313–348.

Nizou, J., Hanebuth, T.J.J., Heslop, D., Schwenk, T., Palamenghi, L., Stuut, J.-B., Henrich, R., 2010. The Senegal River mud belt: A high-resolution archive of paleoclimatic change and coastal evolution. Marine Geology 278, 150–164.

Orgeira, M.J., Walther, A.M., Tofalo, R.O., Vásquez, C., Berquó, T., Favier Dobois, C., Bohnel, H., 2003. Environmental magnetism in fluvial and loessic Holocene sediments and paleosols from the Chacopampean plain (Argentina). Journal of South American Earth Sciences 16, 259–274.

Ott, J., 1988. Meereskunde – Einführung in die Geographie und Biologie der Ozeane. Stuttgart, Ulmer, 386 p.

Palma, E.D., Matano, R.P., Piola, A.R. , 2004. A numerical study of the Southwestern Atlantic Shelf circulation: Barotropic response to tidal and wind forcing. Journal of Geophysical Research: Oceans (1978–2012) 109, 1–17.

Palma, E.D., Matano, R.P., Piola, A.R., 2008. A numerical study of the southwestern Atlantic shelf circulation: Stratified ocean response to local and offshore forcing. Journal of Geophysical Research 113, C11010.

Potter, P. E., 1984. South American modern beach sand and plate tectonics. Nature 311, 645–648.

Potter, P. E., 1986. South America and a few grains of sand: Part 1, beach sands. Journal of Geology 94, 301–319.

Press, F., Siever, R., 2003. Allgemeine Geologie. Spektrum, Akademischer Verlag, 723 p.

Prospero, J.M., Glaccum, R.A., Nees, R.T., 1981. Atmospheric transport of soil dust from Africa to South America. Nature 289, 570–572.

Rebesco, M., Hernández-Molina, F.J., van Rooij, D., Wåhlin, A., 2014. Contourites and associated sediments controlled by deep-water circulation processes: State-of-the-art and future considerations. Marine Geology 352, 111–154.

Ruddiman, W.F., 2001. Earth's Climate: past and future. Macmillan, 465 p.

Sarnthein, M., Tetzlaff, G., Koopmann, B., Wolter, K., Pfaumann, U., 1981. Glacial and interglacial wind regimes over the eastern subtropical Atlantic and North-West Africa. Nature 293, 193–196.

Schmidt, A.M., von Dobeneck, T., Bleil, U., 1999. Magnetic characterization of Holocene sedimentation in the South Atlantic. Paleoceanography 14, 465–481.

Schwertmann, U., Taylor, R.M., 1989. Iron Oxides. In: Dixon, J.B., Weed, S.B., Dinauer, R.C. (Eds), Minerals in soil environments. Soil Scientific Society of America, pp. 379–435.

Soulsby, R.L., Whitehouse, R.J.S., 1997. Threshold of sediment motion in coastal environments. In: Pacific Coasts and Ports' 97: Proceedings of the 13th Australasian Coastal and Ocean Engineering Conference and the 6th Australasian Port and Harbour Conference; Volume 1. Centre for Advanced Engineering, University of Canterbury, 145 p.

Stocker, T.F., Qin, D., Plattner, G.K., Tignor, M., Allen, S.K., Boschung, J., Nauels, A., Xia, Y., Bex, V., Midgley, P.M., 2013. Climate change 2013: The physical science basis. Intergovernmental Panel on Climate Change, Working Group I Contribution to the IPCC Fifth Assessment Report (AR5). Cambridge University Press, New York, 1535 p.

Stramma, L., Hüttl, S., Schafstall, J., 2005. Water masses and currents in the upper tropical northeast Atlantic off northwest Africa. Journal of Geophysical Research 110, C12006, 18 pp.

Stuut, J.-B., Zabel, M., Ratmeyer, V., Helmke, P., Schefuß, E., Lavik, G., Schneider, R., 2005. Provenance of present-day eolian dust collected off NW Africa. Journal of Geophysical Research 110, D04202, 14 pp.

Swap, R., Ulanski, S., Cobbett, M., Garstang, M., 1996. Temporal and spatial characteristics of Saharan dust outbreaks. Journal of Geophysical Research 101, 4205–4220.

Swift, D.J., Palmer, H.D., 1978. Coastal sedimentation. Dowden, Hutchinson and Ross, Stroudsburg Pennsylvania, 339 p.

Syvitski, J.P., Peckham, S.D., Hilberman, R., Mulder, T., 2003. Predicting the terrestrial flux of sediment to the global ocean: a planetary perspective. Sedimentary Geology 162, 5–24.

Tauxe, L., 2005. Lectures in paleomagnetism.

Thompson, R., Oldfield, F., 1986. Environmental magnetism. Allen and Unwin London, 227 p.

Tucker, M. 1996. Methoden der Sedimentologie. Ferdinand Enke Verlag, Stuttgart, 366 p.

Urien, C.M., Ewing, M., 1974. Recent sediments and environment of southern Brazil, Uruguay, Buenos Aires, and Rio Negro continental shelf. In: Burk, C.A., Drake, C.L., (Eds.), The Geology of Continental Margins. Springer, Berlin, pp.157–177.

Violante, R.A., Parker, G., 2004. The post-last glacial maximum transgression in the de la Plata River and adjacent inner continental shelf, Argentina. Quaternary International 114, 167–181.

Vivier, F., Provost, C., 1999. Direct velocity measurements in the Malvinas Current. Journal of Geophysical Research 104, 21,083–21,103.

Wang, X., Auler, A.S., Edwards, R.L., Cheng, H., Ito, E., Solheid, M., 2006. Interhemispheric anti-phasing of rainfall during the last glacial period. Quaternary Science Reviews 25, 3391–3403.

Wang, X., Auler, A.S., Edwards, R.L., Cheng, H., Ito, E., Wang, Y., Kong, X., Solheid, M., 2007. Millennial-scale precipitation changes in southern Brazil over the past 90,000 years. Geophysical Research Letters 34, L23701.

Wefer, G., 2010. Dynamische Erde – Zukunftsaufgaben der Geowissenschaften. Strategieschrift der DFG-Senatskommission für die Geowissenschaftliche Gemeinschaftsforschung. Online-Version, 367 p.

Wefer, G., Berger, W.H., Siedler, G., Webb, D.J., (Eds.) 1996. The South Atlantic: Present and Past circulation. Springer Verlag 644 p.

Chapter 2: Interaction of the South American Monsoon System and the Southern Westerly Wind Belt during the last 14 kyr

Sebastian Razik [a], Cristiano M. Chiessi [b,1], Oscar E. Romero [a,2] and Tilo von Dobeneck [a,b]

[a] Department of Geosciences, University of Bremen, Klagenfurter Straße, D-28359 Bremen, Germany

[b] MARUM – Center for Marine Environmental Sciences, University of Bremen, Leobener Straße, D-28359 Bremen, Germany

[1] Now at: School of Arts, Sciences and Humanities, University of São Paulo, Av. Arlindo Bettio 1000, CEP03828-000 São Paulo, SP, Brazil

[2] Now at: Instituto Andaluz de Ciencias de la Tierra, Universidad de Granada, Av. de las Palmeras 4, 18100 Armilla-Granada, Spain

Palaeogeography, Palaeoclimatology, Palaeoecology 374 (2013) 28–40
(reprinted with permission from Elsevier)

2.1. Abstract

Surface currents and sediment distribution of the SE South American upper continental margin are under the influence of the South American Monsoon System (SAMS) and the Southern Westerly Wind Belt (SWWB). Both climatic systems determine the meridional position of the Subtropical Shelf Front (STSF) and probably also of the Brazil-Malvinas Confluence (BMC). We reconstruct the changing impact of the SAMS and the SWWB on sediment composition at the upper Rio Grande Cone off southern Brazil during the last 14 cal kyr BP combining sedimentological, geochemical, micro-paleontological and rock-magnetic proxies of marine sediment core GeoB 6211-2. Sharp reciprocal changes in ferri- and paramagnetic mineral content and prominent grain-size shifts give strong clues to systematic source changes and transport modes of these mostly terrigenous sediments. Our interpretations support the assumption that the SAMS over SE South America was weaker than today during most of the Late Glacial and entire Early Holocene, while the SWWB was contracted to more southern latitudes, resembling modern austral summer-like conditions. In consequence, the STSF and the BMC were driven to more southern positions than today's, favoring the deposition of Fe-rich but weakly magnetic La Plata River silts at the Rio Grande Cone. During the Mid Holocene, the northern boundary of the SWWB migrated northward, while the STSF reached its northernmost position of the last 14 cal kyr BP and the BMC most likely arrived at its modern position. This shift enabled the transport of Antarctic diatoms and more strongly magnetic Argentinean shelf sands to the Rio Grande Cone, while sediment contributions from the La Plata River became less important. During the Late Holocene, the modern El Niño Southern Oscillation set in and the SAMS and the austral tradewinds intensified, causing a southward shift of the STSF to its modern position. This reinforced a significant deposition of La Plata River silts at the Rio Grande Cone. These higher magnetic silts with intermediate Fe contents mirror the modern more humid terrestrial climatic conditions over SE South America.

2.2. Introduction

The SE South American continental margin (ca. 22°–55° S) is under influence of tropical and extratropical climatic and oceanographic regimes (Fig. 2.1). Its northern sector (22°–38° S) is affected by the warm southward-flowing Brazil Current and its southern sector (38°–55° S) by the cold northward-flowing Malvinas Current (Palma et al., 2008). Both currents meet and merge in the Brazil-Malvinas Confluence (BMC) at ~38° S. As a continuation of the BMC on the shelf, the Subtropical Shelf Front (STSF) divides cold and fresh Subantarctic Shelf Waters from warm and saline Subtropical Shelf Waters (Piola et al., 2000). From landside, the La Plata Drainage Basin (LPDB) releases large amounts of freshwater and sediments through the La Plata Estuary into this complex shelf system. The northeastward-directed Brazilian Coastal Current carries this Plata Plume Water at the inner continental shelf along Uruguay and towards SE Brazil (Souza and Robinson, 2004). This near-surface flow displays high seasonal and interannual variability (Piola et al., 2005). Models and observations indicate that during austral summer the buoyant upper layer flows more southwestward and the low salinity Plata Plume Water is constrained south of 32° S (Piola et al., 2000; Palma et al., 2008). At interannual time scales the plume's northeastward spreading is also modulated by alongshore southwesterly winds, being most extreme during La Niña events. In contrast, although El Niño peaks are associated with largest river outflows, the plume spreading is limited by anomalously strong northeasterly winds (Piola et al., 2005).

Several sediment-based paleostudies have recently provided clues on the past extent of these water masses off SE South America. A multi-proxy approach of Mahiques et al. (2009) was able to show changes in the northward reach of the Plata Plume Water on the inner shelf off SE Brazil. They explained a low terrigenous sediment input between 5.2 and 3.0 cal kyr BP by weaker southwesterly winds driven by the Southern Westerly Wind Belt (SWWB) and by lower humidity in SE South America. Higher terrigenous input was observed after 3.0 cal kyr BP and linked to the development of the modern South American Monsoon System (SAMS) and the La Plata River discharge. While Mahiques et al. (2009) were only mentioning sediments originating from the LPDB, Gyllencreutz et al. (2010) assumed the Argentinean shelf as provenance for anomalously sandy sediments deposited at the South Brazilian shelf between 7.0 and 5.0 cal kyr BP. According to their view, the termination of this sediment flux was caused by an intensified Plata Plume Water outflow, creating a barrier for the Subantarctic Shelf Water off the La Plata Estuary; evidently, these two interpretations are in conflict. In addition to the latter two studies dealing with shelf processes, Laprida et al. (2011) were able to reconstruct latitudinal changes in the paleoposition of the BMC during MIS 6 and 8 based on planktonic foraminifera. However, it is not known to date, if and how far the STSF and the BMC shifted during the Holocene. Our study seeks for evidence of postglacial shifts in the STSF position and tries to answer the question whether only LPDB sediments or also Argentinean shelf sediments reached latitudes north of 38° S during the last 14 cal kyr. We investigate multi-proxy source and transport signatures of postglacial terrigenous sediments off South Brazil and use their records to reconstruct Holocene sediment dynamics and oceanographic variations at the SE South American upper continental margin. An intensification of the SAMS during the Holocene

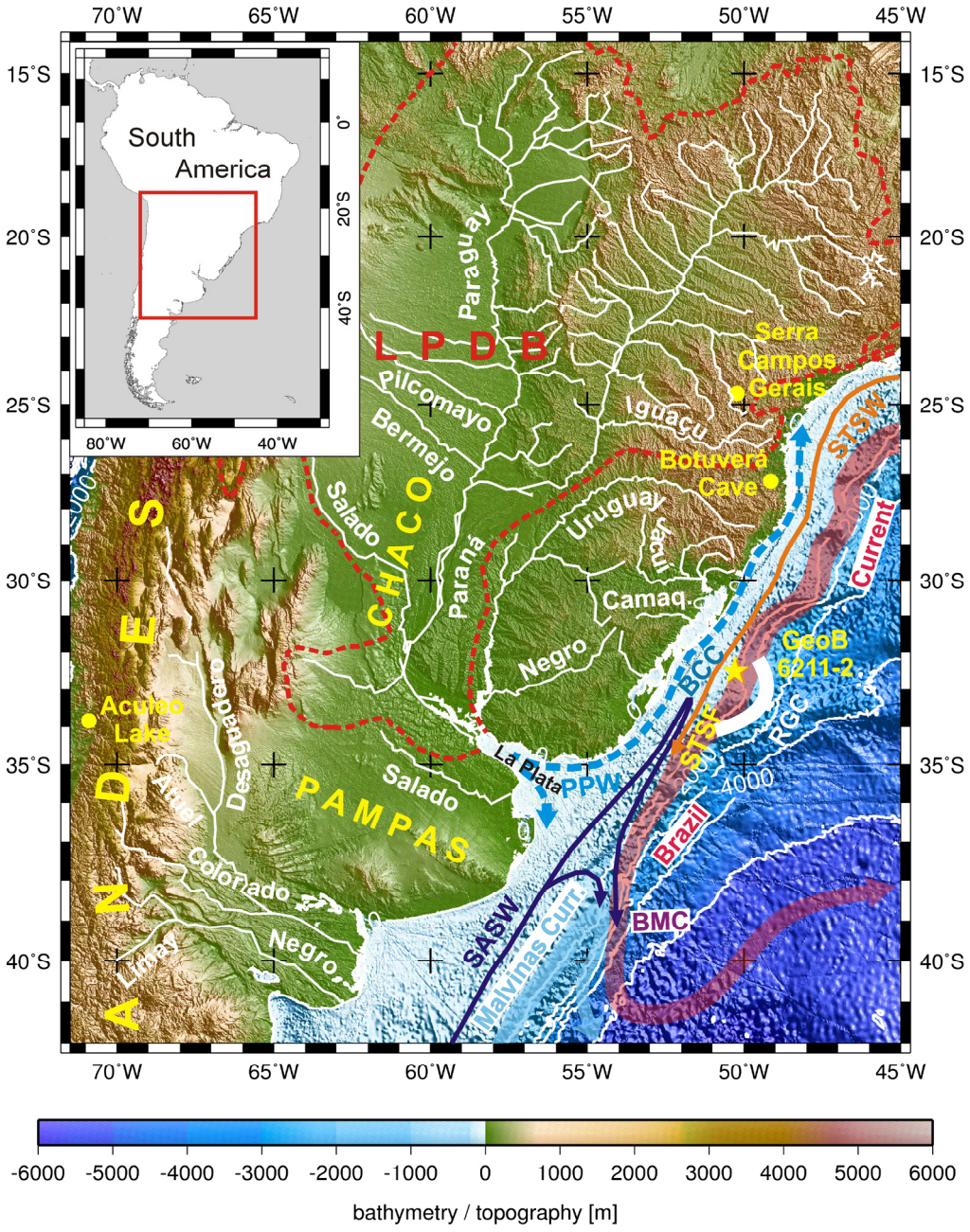

Fig. 2.1. Study area at the continental margin of SE South America showing the location of gravity core GeoB 6211-2 (yellow star) at the Rio Grande Cone (RGC, marked as thick white contour line). On land, the main geographic features and rivers (white lines) are shown with locations of sites cited in this study (yellow dots). Contour currents (transparent, thick arrows) are imposed after the GEBCO bathymetry (0.5 min grid). The Subantarctic Shelf Water (SASW) and the Subtropical Shelf Water (STSW) are marked as thin, opaque arrows. The Plata Plume Water (PPW) together with the Brazilian Coastal Current (BCC) is displayed as a dashed blue line. The Brazil and the Malvinas Currents encounter each other in the Brazil-Malvinas Confluence (BMC) (oceanography after Piola et al., 2008). The location of the investigation area (red square) in respect to South America is inserted in the upper left corner of the figure.

has been made responsible for precipitation changes over SE South America by several studies (e.g., Behling, 1997; Cruz et al., 2005). Other authors have noted a strengthening and northward expansion of the SWWB over the same period (e.g., Jenny et al., 2003; Lamy et al., 2010). Obviously, the interaction of tropical and extratropical climate systems of SE South America and their joint impact on the western subtropical South Atlantic have not yet been

taken into closer conjunction. We address these paleoclimatic issues from a multi-proxy perspective combining and co-interpreting sedimentological, micropaleontological, geochemical and rock-magnetic data of a 14 ka marine sediment series collected off South Brazil (Fig. 2.1).

2.3. Environmental and geological settings

2.3.1. Climate systems of SE South America

2.3.1.1. South American Monsoon System (SAMS)

The SAMS is driven by tropical temperature and pressure gradients between ocean and land and strongly controls the seasonal precipitation changes on the continent. Monthly precipitation over the eastern LPDB can be one order of magnitude higher (Fig. 2.2a) during austral summer than during austral winter (Fig. 2.2b). Exceptional features of the SAMS are its precipitation impact also on subtropical areas and smaller directional change between summer and winter winds of below 120°, which is the typical angular change of most monsoonal winds (Zhou and Lau, 1998). During austral summer, the Intertropical Convergence Zones of the Atlantic and Pacific migrate southward. Simultaneously, the major heating zone over South America shifts toward the subtropics and the thermal low-pressure cell over the Chaco Plains intensifies (Fig. 2.1). This increases the pressure gradient between the NW African high- and the South American low-pressure zones and intensifies the boreal northeasterly tradewinds, enabling them to cross over the equator and to transport moisture toward the Amazon Basin (Fig. 2.2a) (Vera et al., 2006). There, the tradewinds become channeled between the eastern flank of the Andes and the western flank of the Brazilian Highlands (Fig. 2.1), intensifying the South American Low-

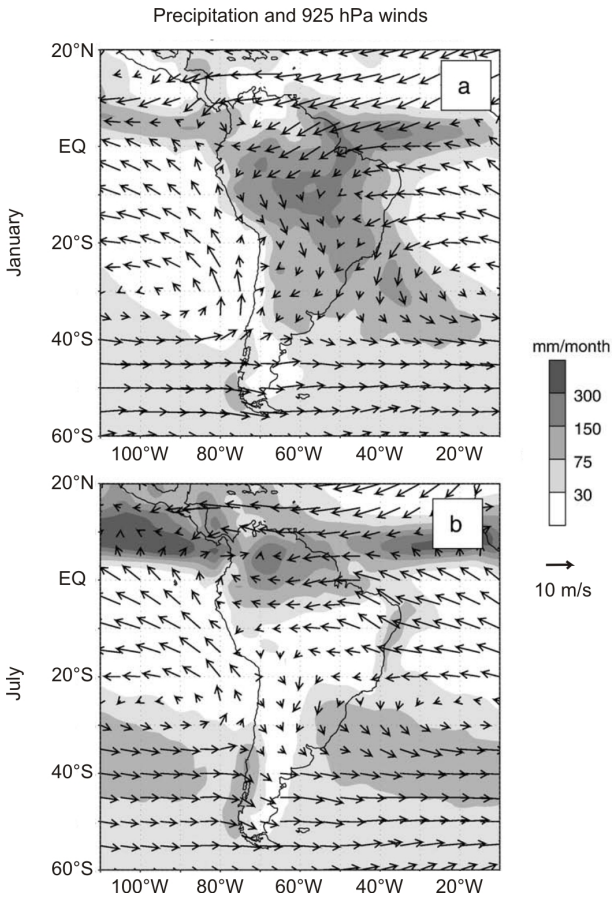

Fig. 2.2. Long-term mean precipitation for (a) January and (b) July. The precipitation is shown as shading and wind vectors at 925 hPa as arrows (arranged from Garreaud et al., 2009; with permission from Elsevier).

Level Jet and transporting moisture towards SE Brazil. By anti-clockwise rotation of the South Atlantic high-pressure cell, the austral tradewinds also carry moisture from the tropical Atlantic southwestward along the Brazilian coast. Both winds contribute to the high convective variability of the South Atlantic Convergence Zone during austral summer and to seasonal peak precipitation over the eastern LPDB as well as over the western subtropical South Atlantic (Fig. 2.2a) (Zhou and Lau, 1998; Seluchi and Marengo, 2000; Marengo et al., 2004; Vera et al., 2006; Garreaud et al., 2009).

2.3.1.2. Southern Westerly Wind Belt (SWWB)

The SWWB has a dominant whole-year influence at mid latitudes (40°–60° S) (Fig. 2.2) and is responsible for high precipitation at the western

flank of the Andes (Garreaud et al., 2009), which act as a topographic barrier. Daily changes in pressure and precipitation are related to the migration of dynamic cyclones and anticyclones created by a meandering high-level jet stream. Anticyclones generated west of the Andes produce southerly to southwesterly cold air incursions on the coast of SE South America, which are particularly frequent during austral winter (Pezza and Ambrizzi, 2005). During austral summer, the SWWB contracts to the south and shows highest annual wind velocities, which remain however restricted to the core zone (50°–55° S) (Garreaud et al., 2009). During austral winter, the wind velocities in the core zone decrease as the SWWB extends northward to ~30° S. During this migration, the anticyclones pick-up moisture from local air masses and generate precipitation along the coast of SE South America up to SE Brazil by creating tropospheric instabilities (Pezza and Ambrizzi, 2005; Garreaud et al., 2009).

2.3.2. Hydrology and petrology of the La Plata Drainage Basin (LPDB)

The LPDB (Fig. 2.1) is the second largest drainage basin of South America (3.2×10^6 km^2) with a modern water discharge averaging 21×10^3 m^3 s^{-1} (Berbery and Barros, 2002). The La Plata River discharges some 130×10^6 t yr^{-1} of suspended sediment load to the estuary (Depetris and Griffin, 1968; Depetris et al., 2003; Amsler and Drago, 2009). The LPDB is divided into three main subbasins, the Uruguay River (0.4×10^6 km^2), the Paraguay River (1.1×10^6 km^2) and the Paraná River (1.7×10^6 km^2) (Laborde, 1997). The Uruguay River subbasin covers 13% of the LPDB and contributes 22% of the runoff, eroding tholeiitic basalts, sedimentary rocks and alluvial deposits. The Paraguay River subbasin makes up 34% of the LPDB area, adds ~16% to the total runoff (Depetris and Griffin, 1968; Depetris et al., 2003; Amsler and Drago, 2009) and consists of sedimentary deposits and metamorphic rocks. The Bermejo River is the main sediment contributor to the Paraguay subbasin due to its steep topographic gradient through unconsolidated Chaco Plain sedimentary deposits (Orfeo and Stevaux, 2002). As these sediments contain primarily diamagnetic quartz and feldspars (Zárate, 2003) they should have very limited influence on the rock-magnetic properties of the LPDB sediments (Evans and Heller, 2003; Dunlop and Özdemir, 2001). The Paraná River subbasin (53% of the LPDB area) is the largest contributor of freshwater (56%) to the La Plata Estuary (Laborde, 1997; Berbery and Barros, 2002; Pasquini and Depetris, 2007). Within this subbasin, sedimentary rocks, flood basalts and intrusive rocks crop out (Peate, 1997), while the latter two generally show highest ferrimagnetic Fe-(Ti)-oxide concentrations of all natural rocks (Rumble, 1976; Evans and Heller, 2003). Due to an intense weathering of mainly basic source rocks (Allan et al., 1989), these relatively weathering-resistant primary magnetic minerals are common as remaining individual particles in subtropical and tropical soils of SE South America (Schwertmann and Taylor, 1989). Because of their source geology, river-bed morphology and water discharge, the upper Paraná River and the Uruguay River (Fig. 2.1) carry the highest magnetic mineral loads within the LPDB (Allan et al., 1989; Schwertmann and Taylor, 1989; Campos et al, 2008).

2.3.3. Hydrography of the western South Atlantic margin

In the northern sector (22°–36° S) of the SE South American continental margin the low-salinity Plata Plume Water (Fig. 2.1) is transported from the La Plata Estuary northeastward

along the inner shelf by the Brazilian Coastal Current, which is driven by southerly to southwesterly winds (Piola et al., 2000, 2005; Möller et al., 2008). The Plata Plume Water mainly consists of La Plata River water and a small discharge from the Patos Lagoon (30°–33° S), while riverine runoff between 22° and 34° S is very minor under modern conditions (Campos et al., 2008; Corrêa et al., 2008). The Plata Plume Water frequently reaches 24° S during austral fall and winter (Piola et al., 2008; Palma et al., 2008) and sporadically flows as far as 22° S (Stevenson et al., 1998). This northward penetration of the Plata Plume Water is primarily controlled by the intensity of southerly winds and just secondarily by continental runoff (Piola et al., 2000). On the mid shelf Subtropical Shelf Water, formed by mixing of Tropical Water with South Atlantic Central Water and subordinately with Plata Plume Water, streams southward (Palma et al., 2008). Large parts of the outer shelf and slope are mainly under influence of the southward-flowing Brazil Current, which merges with the equally southward-flowing Intermediate Western Boundary Current transporting recirculated Antarctic Intermediate Water at the mid slope (Stramma and Peterson, 1989; Boebel et al., 1999; Palma et al., 2008).

The southern sector (>36° S) of the continental shelf is overflown by the cold Subantarctic Shelf Water (Fig. 2.1), which originates from water masses entering the Atlantic via the Drake Passage at ~55° S and mixing with local coastal freshwater inputs along its way (Palma et al., 2008). The outer continental shelf and slope are influenced by the Subantarctic Water, which is driven northeastward by the Malvinas Current (Palma et al., 2008). The Subantarctic Shelf Water encounters the southward-flowing Subtropical Shelf Water at the north-south-oriented STSF located between 32° and 34° S (Piola et al., 2000, 2005; Möller et al., 2008). The STSF is created by the dynamic effect of an arrested topographic wave (Csanady, 1978), which is set up by a cross-shelf pressure gradient imposed by the Malvinas Current several hundred km further south (Palma et al., 2008).

2.3.4. Sedimentology of the SE South American upper continental margin

Along the inner shelf (0–50 m water depth) of the northern sector (28°–36° S) siliciclastic sands constitute ~50% of the surface sediment (Urien and Ewing, 1974). Silts from the Plata Plume Water (Fig. 2.1) are deposited at the modern mid shelf (50–100 m water depth). On the outer shelf (100–160 m water depth), again mainly sands are found and make up to 75% of the total sediment (Urien and Ewing, 1974). In contrast, postglacial deposits at the outer shelf of the Rio Grande Cone (31°–34° S) are described as coarse silts or even finer sediments (Urien and Ewing, 1974) turning into silty to clayey muds at its upper continental slope (Frenz et al., 2003). The continental shelf is dissected by paleochannels starting at the La Plata Estuary and leading to the northeast (Laborde, 1997; Martins and Coutinho, 1981; Violante and Parker, 2004). These paleochannels are believed to be past continuations of the La Plata River during periods of sea-level low stands and are nowadays partially filled with LPDB sediments (Urien and Ewing, 1974; Martins and Coutinho, 1981; Campos et al., 2008). All these paleochannels recently carry the Plata Plume Water down to the mid shelf (Urien and Ewing, 1974) and the Subantarctic Shelf Water at their deeper parts (Piola et al., 2008). Further, the STSF is thought to be a major export path of shelf waters to the slope region (Piola et al., 2008) and thus, channelized off-shelf transport of LPDB

sediments to the Rio Grande Cone is realized under modern sea-level high stand conditions.

The inner La Plata Estuary is covered with sands (Urien and Ewing, 1974; Laborde, 1997; Violante and Parker, 2004 and references therein). Its middle sector contains the finest sediments, ranging from silty clays to clayey silts. In the outer estuary, the deposits coarsen again to sands.

Around 65% of the continental shelf of the southern sector (>36° S) are covered with fine sands (Urien and Ewing, 1974; Parker et al., 1997). Minor contents of very fine and medium sand and occasionally even gravel and mud are observed in the vicinity of the La Plata Estuary. All these sands contain a high concentration of igneous detritus (Potter, 1984, 1986) and were mainly deposited as coastline sediments under sea-level low stands, being later reworked by coastal processes under a predominantly northward alongshore transport. Sediments with similar grain-size distributions and petrological characteristics are also found onshore in the southern Pampas as loessoidal sands (Zárate and Blasi, 1993; Zárate, 2003) transported by westerly winds to the Argentinean continental shelf (Pierce and Siegel, 1979; Gaiero et al., 2003). The loessoidal and fluvial sands of the Colorado River originate from the Andean Cordillera between 32° and 42° S (Zárate and Blasi, 1993), where basic and intermediate effusive rocks, as well as felsic intrusive and eruptive bodies are extensively exposed (Deruelle, 1982; Drake et al., 1982). Such volcanic rocks contain significant amounts of magnetic minerals (Rumble, 1976).

2.4. Materials

2.4.1. Location and lithology of core GeoB 6211-2

This study presents multi-proxy records of the marine gravity core GeoB 6211-2, which was collected during the RV Meteor cruise M46/2 at the upper continental margin of the Rio Grande Cone off southern Brazil (32° 30.31' S; 50° 14.56' W) from a water depth of 657 m (Fig. 2.1) (Schulz et al., 2001). The surface sediments at the core site are composed of silty to clayey muds (Frenz et al., 2003) being transported from the La Plata Estuary with the Plata Plume Water and the underlying Subantarctic Shelf Water along the shelf to the STSF. As the STSF is thought to be a major export path of shelf waters to the slope region (Piola et al., 2008), the present-day location of the STSF likely provides a direct route of LPDB sediments to the Rio Grande Cone. Hence, this core location is very sensitive to climate-driven changes in sediment dynamics. In contrast to other sites in this region (Frenz et al., 2003), this core shows an exceptionally good carbonate preservation, allowing the establishment of a carbonate-based ^{14}C AMS age-depth model.

The seemingly continuous and undisturbed gravity core is 7.74 m long and reaches the Last Glacial Maximum at its base (Chiessi et al., 2008). Here, we focus on the last 14 cal kyr BP (uppermost 123 cm) which show near-constant sedimentation rates of ~9 cm kyr^{-1} (Fig. 2.3). The section deposited before 14 cal kyr BP is not shown here, as sedimentation rates change significantly due to sea-level related effects, altering the distance between the coastline and our core site with time. Between 123 and 76 cm, the core is composed of light reddish, slightly laminated silty muds. The upper 76 cm consist of olive-gray clayey to fine sandy muds. The

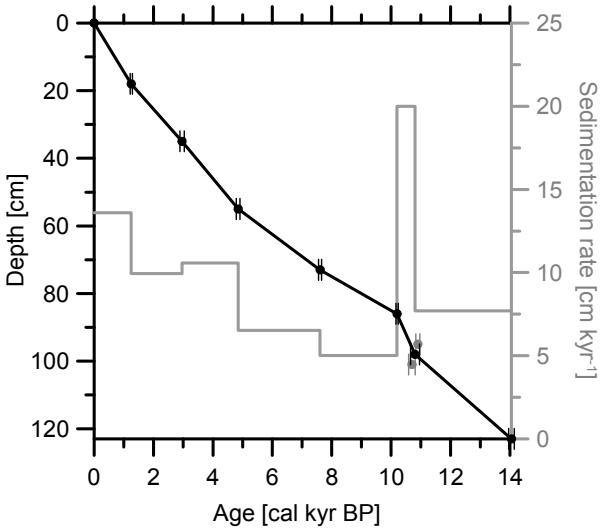

Fig. 2.3. Improved age-depth model (black) and sedimentation rate (gray) based on eight ^{14}C-ages for the upper 123 cm of the sediment core GeoB6211-2 (see first version in Chiessi et al., 2008). The data was obtained from shallow-dwelling planktonic foraminifera *Globigerinoides ruber* (pink and white) and *Globigerinoides sacculifer*. The two ages in grey overlap each other in the one sigma range and were used to calculate an average value (Table 2.1).

uppermost sediments of the core resemble the grain sizes of the surface sediments investigated by Urien and Ewing (1974) at the Rio Grande Cone. Since the outer and inner continental shelf mainly contain coarser sediments being deficient in the fine fraction (Frenz et al., 2003), we assume that our sediment core fits in a regional context and is therefore representative for the sediment dynamics at the Rio Grande Cone.

2.4.2. Calibrated ^{14}C age-depth model

The age-depth model for the upper 123 cm of sediment core GeoB 6211-2 is based on eight ^{14}C AMS ages of the shallow-dwelling planktonic foraminifera *Globigerinoides ruber* (pink and white) and *Globigerinoides sacculifer* (Fig. 2.3, Table 2.1). Three ^{14}C AMS ages were previously published by Chiessi et al. (2008) and five additional ages are reported here for the first time. One of the samples was measured at the *National Ocean Sciences Accelerator Mass Spectrometry Facility at Woods Hole (USA)*, the other four at the *Leibniz-Laboratory for Radiometric Dating and Stable Isotope Research at Kiel (Germany)*. The software CALIB v. 6.0 (Stuiver and Reimer, 1993) and the Marine09 calibration curve of Reimer et al. (2009) were used to calibrate raw ^{14}C ages. These calibrated ages were linearly interpolated to generate the final age-depth model. An extrapolation of the two youngest calibrated ^{14}C ages yields ~0 cal kyr BP for the core-top (Table 2.1). The age at the core depth of 98 cm was obtained by linear interpolation between two measured ^{14}C values at 95 and 101 cm, overlapping each other in the one-sigma range. No regional deviation from the global reservoir age is assumed due to the distance of the core location to upwelling zones. The database compiled by Reimer and Reimer (2001) provides no marine-reservoir correction data for our study area.

2.5. Methods

2.5.1. Clastic grain-size distribution

To determine the grain-size distribution of the terrigenous sediment fraction, organic carbon, calcium carbonate ($CaCO_3$) and biogenic opal were chemically removed. Samples of 2–4 g were consecutively treated with 10 ml H_2O_2 (35%$_{v/v}$), 10 ml HCl (10%$_{v/v}$) and 6 g NaOH-pellets in 100 ml aquatic solutions as described by Mulitza et al. (2008). Between every chemical reaction, samples were washed with demineralized water. To avoid aggregate formation of clay minerals, ~300 mg of $Na_4P_2O_7 \cdot 10(H_2O)$ was added to the sediment solutions before analysis.

The grain-size analyses were performed using a BECKMANN-COULTER LS200 laser particle sizer coupled to a water demineralization and degassing device at the *MARUM – Center for*

Table 2.1

Accelerator mass spectrometry (AMS) radiocarbon dates and calibrated ages used in the age-depth model of sediment core GeoB6211-2.

Lab ID	Core depth [cm]	AMS radiocarbon age ±1σ error[a] [^{14}C yr BP]	Calibrated ages [cal kyr BP]	1σ calibrated age range [cal kyr BP]	Additional ages used in the age model
	1				Modern[b]
KIA30528[c]	18	1685 ± 30	1.25	1.22 - 1.28	
KIA35166	35	3170 ± 40	2.96	2.89 - 3.03	
KIA35165	55	4625 ± 45	4.85	4.80 - 4.90	
KIA30527[c]	73	7145 ± 55	7.61	7.57 - 7.66	
NOSAMS75186	86	9370 ± 40	10.20	10.15 - 10.25	
KIA35163	95	9920 ± 70	10.90	10.75 - 11.00	
	98				10.80[d]
KIA35162	101	9810 ± 110	10.70	10.55 - 10.85	
KIA30526[c]	123	12600 ± 70	14.05	13.95 - 14.15	

[a] Raw radiocarbon dates.
[b] Extrapolation of the calibrated ^{14}C ages at 18 and 35 cm core depth results in an age close to 0 cal kyr BP for the core top and allows assigning a modern age to the uppermost centimeters of the core sequence.
[c] Chiessi et al. (2008).
[d] Interpolated value between the ^{14}C ages at 95 and 101 cm depth.

Marine Environmental Sciences in Bremen (Germany). The grain-size detection range of this equipment is specified as 0.04–2000 µm, but due to the pre-treatment of the sediment and its settling properties, only distributions of particles ≥2 µm are reliable, while finer fractions have to be considered with care. To process the data, the BECKMANN-COULTER Particle Characterization software v. 3.01 was used.

2.5.2. Diatom counts

The samples for diatom analysis were prepared following the method proposed by Schrader and Gersonde (1978). Qualitative and quantitative analyses were performed at 1000× magnification using a Zeiss-Axioscope BX41 with phase-contrast illumination at the *Instituto Andaluz de Ciencias de la Tierra (Granada, Spain)*. Counts were carried out on permanent slides of acid-cleaned material (Mountex mounting medium). Several traverses across the cover-slip were examined, depending on microorganism abundances. At least two cover slips per sample were scanned in this way. Diatom counting of replicate slides indicates that the analytical error of the concentration estimates is ≤15%. The counting procedure and definition of counting units for diatoms to the lowest possible taxonomic level followed those of Schrader and Gersonde (1978).

2.5.3. Major-element concentrations

To obtain major-element intensities along the whole sedimentary sequence, the split core was analyzed at the *MARUM in Bremen (Germany)* with an Avaatech X-Ray Fluorescence (XRF) core scanner operating at 10 kV, following the procedure described by Richter et al. (2006). XRF spectra were recorded every 0.5 cm for 30 s, each time covering an area of 0.4 cm^2

(0.4 cm along and 1.0 cm across-core). Before and after analysis, the instrument was calibrated using a set of pressed powder standards with a standard deviation of <5%, following the method described by Jansen et al. (1998). Processing of the XRF spectra was done with the WinAxil and WinBatch software packages.

Core-scanner element intensities were converted to relative concentrations based on powder XRF analyses obtained for 22 discrete samples at 5 cm intervals. Before measurement, the samples (~4 g each) were freeze-dried, pulverized and loosely packed into plastic sample holders with bottoms of Ultralene® X-ray transmission foil. Powder XRF analyses were performed with an energy dispersive polarization SPECTRO XEPOS XRF analyzer at the *MARUM in Bremen (Germany)*, as described in Wien et al. (2005) and Tjallingii et al. (2007). The system was operated with the SPECTRO X-Lab Pro v. 2.4 software (Schramm and Heckel, 1998) and calibrated with the certified standard reference material MAG-1 (Govindaraju, 1994). Fe and Ca analyses of MAG-1 standards during the measuring period differed less than 3% from the expected published values (Govindaraju, 1994). The log-ratio approach of Weltje and Tjallingii (2008) was used to calibrate core-scanner XRF intensities to element concentrations from powder analyses. This approach is based on linear calibration equations and takes into account changes in water content as well as matrix-related effects. The calibration showed a goodness-of-fit of $R^2 = 0.97$ ($Q = 0.006$) with Ca as common log-ratio denominator. All Fe concentrations are displayed as calibrated and carbonate-free values (Fe_{cf}).

2.5.4. Magnetic susceptibility

Magnetic volume susceptibility was measured on archive core halves at the *Paleomagnetic Laboratory of Bremen University (Germany)* at 1 cm spacing using an automated BARTINGTON MS2 unit with a spot F-type sensor with operating frequency of 0.58 kHz enabling 2 mm penetration. Susceptibility measurements were also made on discrete 6.2 cm^3 cube samples every 5 cm using a bulk B-type sensor. The resolution of both sensors was set to 1.0×10^{-6} SI. Susceptibility values were corrected for diamagnetic effects of water and $CaCO_3$ and adjusted for bulk sediment porosity. The resulting data is displayed as carbonate-free mass susceptibilities χ_{cf} following the nomenclature by Bleil and Dobeneck (2003). χ_{cf} quantifies the relative ferrimagnetic mineral content of the terrigenous sediment fraction. The required porosity data (Müller, 2004a) was only available at 5 cm spacing and had to be linearly interpolated to 1 cm intervals. $CaCO_3$ measurements (Müller, 2004b) were used to transform the Ca counts of the XRF core scanner acquired at 0.5 cm intervals into $CaCO_3$ weight percentages.

2.5.5. Magnetic remanence

The artificial Isothermal Remanent Magnetization (IRM) was measured on 6.2 cm^3 cube samples every 5 cm using an automated 2G ENTERPRISES 755R DC cryogenic pass-through magnetometer at the *Paleomagnetic Laboratory of Bremen University (Germany).* The sensitivity of this equipment is 1.0×10^{-9} emu (0.1613 µA m^{-1} for sample of 6.2 cm^3) as specified by the producer. IRM was acquired over 24 steps from 0 to 700 mT in an internal pulse coil and over 6 more steps up to 2.63 T in an external pulse coil. The IRM at the maximum field of 2.63 T is defined here as Saturation Isothermal Remanent Magnetization (SIRM). Volume-specific bulk SIRMs were corrected for $CaCO_3$ content and porosity and are presented as mass-specific carbonate-free $SIRM_{cf}$. IRM-based parameters

and spectra are considered as the most indicative and practical environmental magnetic data to assess the concentration and mineralogy of the ferrimagnetic mineral assemblage of natural sediments (Robinson, 1986; Bloemendal et al., 1988; Larrasoaña et al., 2003).

2.6. Results

The new analytical results of this sediment core study have been compiled together with paleoclimatic and paleoceanographic proxies from previous studies for subsequent correlation and interpretation (Fig. 2.4 and Table 2.2). The graph is divided into three phases based on characteristics of the proxy-signals, these phases correspond to (i) the Late Glacial (LG; 14–11.7 cal kyr BP) and Early Holocene (EH; 11.7–8 cal kyr BP), hereafter addressed in combination (LG-EH) due to similar proxy trends in our sediment core, (ii) the Mid Holocene (MH; 8–4 cal kyr BP) and (iii) the Late Holocene (LH; 4–0 cal kyr BP). These substages follow Lamy et al. (2010).

Median clastic grain size (Fig. 2.4a and Fig. 2.5 for entire distribution) ranges between 6 and 9 µm during the LG-EH (14–10 cal kyr BP). During the MH (8.2–4 cal kyr BP), much coarser values between 23 and ~40 µm are observed. During the early LH (4–3 cal kyr BP) the median grain-size returns to its previous low values, where it remains throughout the LH.

Sediment porosity (Fig. 2.4b; Müller, 2004a) varies between 65 and 70% during the LG-EH, reaches a minimum of almost 60% during the MH and increases from 60 to 80% during the LH. These trends seem to be related to both grain-size effects and compaction.

$CaCO_3$ concentrations are low (~2%$_{w/w}$) during the LG-EH (Fig. 2.3c; Müller, 2004b). They show a rapid increase around 8.4 cal kyr BP to ~8%$_{w/w}$ where they stay during the MH to decrease to the modern values of ~5%$_{w/w}$ during the LH.

Abundances of Antarctic diatoms (Fig. 2.4d) are used as a proxy for Subantarctic Shelf Water (Romero and Hensen, 2002). During the LG-EH, Antarctic diatom abundances are rather low (0–20%). Very high MH numbers (50–80%) drop subsequently to values below 10% during the LH in high similarity to the median grain-size trend (Fig. 2.4a).

Fe_{cf} concentrations (Fig. 2.4e) vary around 42 g kg^{-1} during the LG-EH. At ~8.4 cal kyr BP, the values drop to ~30 g kg^{-1} and stay low during the entire MH. Since 3 cal kyr BP, there is a distinct increase towards a maximum value of 47 g kg^{-1} at the core-top.

Carbonate-free mass-specific susceptibility χ_{cf} shows values around 125 × 10^{-8} m^3 kg^{-1} during the LG-EH (Fig. 2.4f). A peak at ~13 cal kyr BP (dark blue curve) is not taken into account here, since it is based on a single thin sediment lens, which the discrete samples do not show (bright blue curve). At 8.4 cal kyr BP, χ_{cf} increases slightly toward stable MH values of ~150 × 10^{-8} m^3 kg^{-1}. During the LH (especially since 2 cal kyr BP), a continuous increase toward the modern maximum values of ~280 × 10^{-8} m^3 kg^{-1} is observed. This parameter primarily accounts for the concentration of ferrimagnetic Fe-(Ti)-oxides and, to far smaller degree, for paramagnetic Fe-sulfides (e.g., pyrite) as well as for Fe-bearing clay minerals (e.g., illite, smectite, and chlorite) in the terrigenous sediment fraction (Evans and Heller, 2003).

The carbonate-free mass-specific $SIRM_{cf}$ (Fig. 2.4g) shows the lowest values (5.2–5.8 A m^2 kg^{-1}) during the LG-EH (14–10 cal kyr BP). After a sudden rise between 10 and

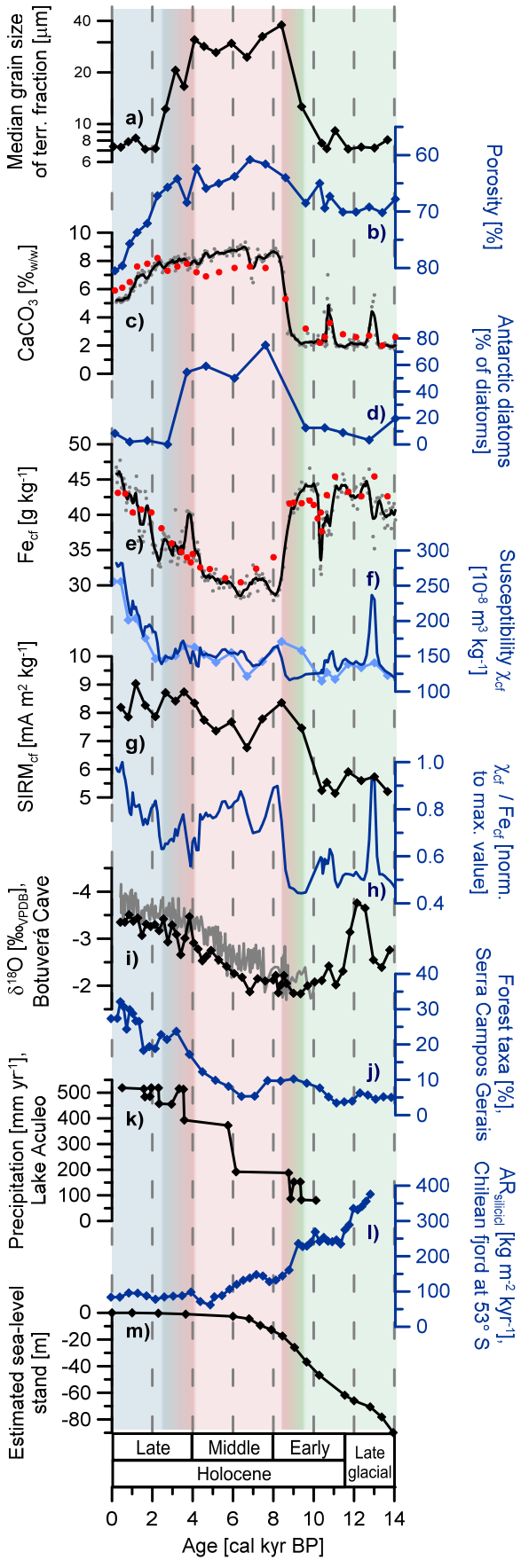

8 cal kyr BP, $SIRM_{cf}$ values remain high until present. The range of values is relatively broad during the MH (6.6–8.5 A m^2 kg^{-1}) and LH (7.6–9.1 A m^2 kg^{-1}) but always remains significantly above the LG-EH values. $SIRM_{cf}$ quantifies relative concentrations of primary ferrimagnetic Fe-(Ti)-oxides in the terrigenous fraction (Evans and Heller, 2003; Dunlop and Özdemir, 2001).

During the LG-EH, normalized χ_{cf} / Fe_{cf} values (Fig. 2.4h) range between 0.45 and 0.6 (not including the peak at 13 cal kyr BP for the earlier mentioned reasons) and rise to 0.7–0.9 at the onset of the MH. At the transition from the MH to

Fig. 2.4. Compilation of proxy records published (a–h) and cited (i–m) in this study; (a) median grain size of the clastic sediment fraction, (b) bulk porosity used for correction of the rock-magnetic parameters (note reversed y-axis; Müller, 2004a), (c) $CaCO_3$ contents (Müller, 2004b; red circles) and calibrated Ca intensities (gray dots, black line represents a 5-point running average), (d) abundance of Antarctic diatoms, (e) Fe_{cf} concentrations from powder samples (red circles) and calibrated Fe_{cf} intensities (gray dots, black line represents a 5-point running average), (f) susceptibility χ_{cf} measured along core every 1 cm (dark blue curve) and on distinct samples of 6.2 cm^3 at 5 cm interval (bright blue curve), (g) Saturation Isothermal Remanent Magnetization ($SIRM_{cf}$), (h) χ_{cf} / Fe_{cf} normalized to maximum value), (i) $\delta^{18}O$ of Botuverá Cave stalagmites, SE Brazil, for the last 14 cal kyr BP (black curve, Wang et al., 2007) and a higher resolved curve reaching 10 cal kyr BP (Wang et al., 2006) (note reversed y-axis, lower values are indicative for more humid conditions), (j) forest taxa abundance in Serra Campos Gerais, SE Brazil (Behling, 1997) using updated calibrated ^{14}C age-depth model (pers. com.), (k) modeled annual precipitation over Aculeo Lake, Central Chile (Jenny et al., 2003), (l) accumulation rate of siliciclastic deposits from a Chilean fjord at ~53° S (Lamy et al., 2010), (m) estimated sea-level curve (Lambeck and Chappell, 2001, updated 2007). Bright background colors mark the three phases with similar environmental signals; dark background colors mark their transitions.

Table 2.2

General trends of parameters presented in Fig. 2.4 together with our own and cited paleointerpretations.

Paleo-interpretation	Region	Changes in	Late Holocene	Middle Holocene	Early Holocene	Late Glacial
			0 - 2.5	4.0 - 5.5 - 8.4		9.5 - 14.0
New records by this study	Rio Grande Cone off southern Brazil	Clastic grain size	-	++		-
		Antarctic diatom abundance	-	++		-
		$CaCO_3$ concentration	+	++		-
		Fe_{cf} concentration	+	-		++
		Susceptibility χ_{cf}	++	+		-
		$SIRM_{cf}$	++	+		--
		χ_{cf} / Fe_{cf}	++	+		-
Cited records	Serra Campos Gerais Bog[a]	Forest taxa abundance	++	+	-	-
	Botuverá Cave[b]	$\delta^{18}O$	-	+		+
	Aculeo Lake[c]	Precipitation	++	+		-
	Chilean Fjord at 53° S[d]	Accumulation rate of siliciclastics	-	-	+	++
	Global[e]	Sea-level stand	+	+		--
Precipitation	Eastern La Plata Drainage Basin	South American Monsoon System	++	+	-	-
River runoff	La Plata Drainage Basin	La Plata River	++	+	-	-
Water masses	Shelf off Uruguay and South Brazil	Plata Plume Water	++	+	-	+
	Shelf off SE and South Brazil	Subtropical Shelf Water	+	-		+
	Shelf off Argentina	Subantarctic Shelf Water	+	++		-
Wind	Northward extension (33°-40° S)	Southern Westerlies	↑↑	↑	↓	↓↓
	Core zone (50°-55° S)		-	-	+	++
Main source for magnetic minerals	Eastern La Plata Drainage Basin	Brazilian flood basalts	++	-	--	+
	Argentinean continental shelf	Andean igneous rocks (32°-42° S)	-	++		-

related to paleoclimate and paleoceanography

related to paleoceanography (mainly sediment dynamics)

related to paleoclimate (mainly precipitation)

++ very high

+ high

- low

-- very low

↑ north

↓ south

the LH, the ratio slightly drops to ~0.55 and then rises gradually throughout the LH reaching 1.0 at the core-top. The χ_{cf} / Fe_{cf} ratio depends on the concentration relation of ferrimagnetic and paramagnetic Fe-bearing minerals. Since no relevant diagenetic magnetite dissolution could be detected as indicated by the continuously high magnetogranulometric ratios ARM / IRM and SIRM / χ (not shown here), χ_{cf} / Fe_{cf} can be interpreted as a magneto-petrological marker for changes in sediment source and weathering conditions.

2.7. Discussion

In combination with previously published regional paleoenvironmental proxy records, our data confirms and provides new clues on the interaction between the SAMS and the SWWB as well as on the surface-ocean circulation at the western South Atlantic (Table 2.2). During the last decades, a large amount of paleostudies has been made in the LPDB and the mid-latitude Andes focusing on the SAMS and the SWWB, respectively. In regard to the paleoclimate over

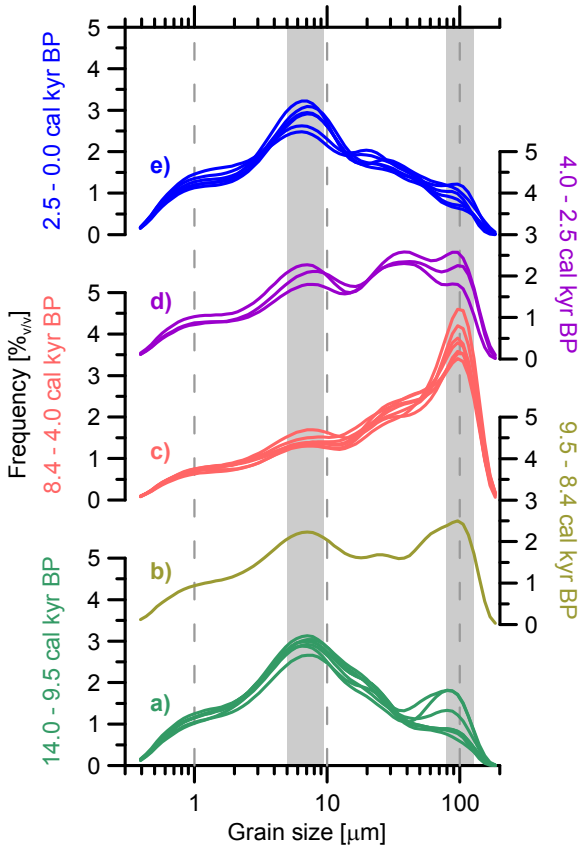

Fig. 2.5. Grain-size distributions of the terrigenous fraction shown in colors corresponding to the background colors in Fig. 2.4 for: (a) Late Glacial and Early Holocene (c) Mid Holocene (e) Late Holocene as well as (b,d) for the transitions between the three main phases. Distinguishable distribution modes are highlighted by gray bars.

the LPDB, the most studies show a more arid climate during the LG-EH and MH with increased precipitation during the LH if compared to the modern conditions (e.g., Behling, 1995; Behling et al., 1997; Behling et al., 2001; Cruz et al., 2005; Wang et al., 2006, 2007; Zech et al., 2009; Behling and Safford, 2010; Whitney et al., 2011).

Although there are some studies, which show just opposite signals during the MH in particular, they display rather more local than regional paleoclimatic conditions (e.g., Ledru, 1993). Also the spacious study of Stevaux (2000) based on fluvial sedimentary facies in the LPDB yields hints for a more humid MH. However, this interpretation was made on a fluvial sedimentary facies with deficient Mid Holocene age constraints.

Also the various interpretations of the paleointensity, paleoposition and seasonality of the SWWB may differ from each other due to varying geographic locations of the investigated sites. Thus, sites at the leeside of the Andes show more local climatic conditions than being representative for a large-scale behavior of the SWWB (e.g., Wagner et al., 2007). This difficulty was mentioned in the study of Lamy et al. (2010) and was discussed in detail in the review of Kilian and Lamy (2012). However, it is well established that the SWWB northern boundary started to migrate northward (Jenny at al., 2003; Lamy et al., 2010) with a simultaneous increase in precipitation between the northern (Jenny et al., 2003) and the southern (Villa-Martínez and Moreno, 2007) boundaries of the SWWB at last since the mid of the MH.

In our study, sediment core GeoB6211-2 covers essentially three phases with distinct paleoenvironmental characteristics (Figs. 2.4 and 2.5) over the last 14 cal kyr. The transitions between these phases correlate with the beginnings of the Mid and Late Holocene. The first transition around 8.4 cal kyr BP is rather sharp in most parameters (e.g., Fig. 2.4a,d–h), whereas the second shows a gradual change between 4 and 3 cal kyr BP (e.g., Fig. 2.4a,e–h).

In further paragraphs, the paleoclimatic interpretations of our study are shown in comparison with foregoing investigations of Wang et al. (2006, 2007; Fig. 2.4i) and Behling (1997; Fig. 2.4j). These studies are located in the Paraná River subbasin, which drains the largest amount of precipitation in the LPDB. The studies cover the entire last 14 kyr in a high temporal resolution, being representative for the SAMS paleoprecipitation in the entire LPDB. On the other side, our interpretations about the SWWB paleointensity during the last 14 kyr are shown in

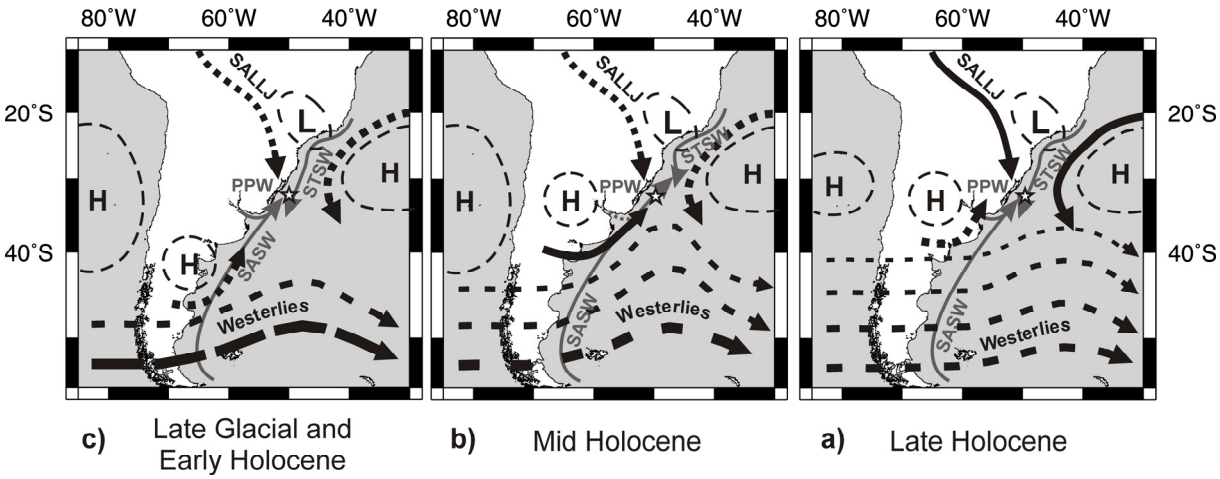

Fig. 2.6. Postulated changes in intensity and trajectory of low-level winds (thick black arrows) and continental shelf waters (thin gray arrows) at southern South America are shown schematically for the (a) Late Glacial and Early Holocene, (b) Mid Holocene and (c) Late Holocene. Displayed are the shelf waters with direct influence on the core site (white star): Plata Plume Water (PPW), Subantarctic Shelf Water (SASW) and Subtropical Shelf Water (STSW). The Subtropical Shelf Front (STSF) is situated between the arrowheads of the PPW / SASW and STSW. Dominant winds during each phase are shown as solid arrows, minor ones as dashed arrows (SALLJ; South American Low Level Jet).

joint consideration with the studies of Jenny et al. (2003; Fig. 2.4k) and Lamy et al. (2010; Fig. 2.4l). Both studies explain best the connections between the paleolocality of the SWWB's core zone and the northward extension of its northern boundary

2.7.1. Late Glacial and Early Holocene

During the LG-EH, the SAMS was significantly weaker over the eastern LPDB (Fig. 2.6a) as compared to modern climate (Garreaud et al., 2009). This was mainly an effect of lower austral summer insolation (Cruz et al., 2005) as recorded at Botuverá Cave (Figs. 2.1 and 2.4i) (e.g. Cruz et al., 2005; Wang et al., 2006, 2007) and Serra Campos Gerais (Figs. 2.1 and 2.4j) (Behling, 1997). During the Younger Dryas (12.8–11.5 cal kyr BP) anomalously humid conditions prevailed in this area (e.g., Wang et al., 2006, 2007). The paleoclimatic signal of the Younger Dryas is not evident at our core site, suggesting it had little impact on the sediment dynamics of the terrigenous fraction at the western South Atlantic margin.

During the LG-EH, the northern boundary of the SWWB was shifted towards its core zone (50°–55° S, Fig. 2.6a) which was further south than under modern conditions, as suggested by a record from a Chilean fjord at 53° S (Fig. 2.4l) (Lamy et al., 2010) and from low precipitation at Aculeo Lake at ca. 34° S (Fig. 2.4k) (Jenny et al., 2003). This lake is located at the modern position of the northern SWWB boundary during austral winter (Fig. 2.1). Although short-term variations of paleohumidity and paleotemperature in the Andes at ~33° S during the period from 14 to 11 cal kyr BP are seen and related to short-term strengthening of the SWWB (Lamy et al., 1999 and references therein), the SWWB seems to be restricted to more southerly latitudes during the LG-EH period. The authors argue with a lower temperature gradient between the warming austral mid latitudes (South Atlantic and SE Pacific) and still relatively cool eastern Pacific tropics (Lamy et al., 2010).

A weak more southerly SWWB during the LG-EH (Fig. 2.6a) should entail an equally more southern position of the STSF and probably also of the BMC. A weaker Malvinas Current as

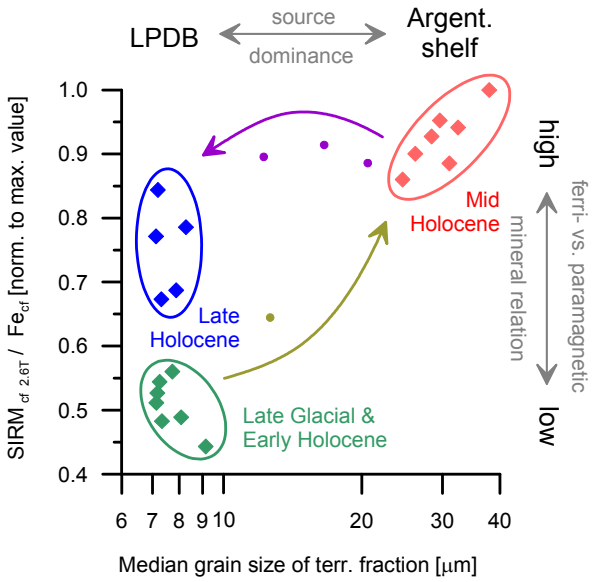

Fig. 2.7. Sedimentological, geochemical and rock-magnetic parameters displaying variations of sediment characteristics based on changes in the dominance of provenance (Argentinean continental shelf versus La Plata Drainage Basin (LPDB)) and concentration of primary ferrimagnetic Fe-(Ti)-oxides in connection to climatic conditions and sediment dynamics at the continental shelf.

compared to modern conditions, being triggered by the SWWB, is in accordance with atmospheric and oceanographic model runs by Sijp and England (2008). The model results distinguish between modern and Last Glacial Maximum conditions, while a southward shift of the SWWB is followed by a southward shift of the Malvinas Current. In consequence, the upper continental margin off Uruguay and South Brazil must have been under a stronger influence of the Subtropical Shelf Water during the LG-EH (Fig. 2.6a). Despite a weak SAMS and lower precipitation over the eastern LPDB (Fig. 2.4i,j) as compared to the present (e.g., Behling, 1997; Cruz et al., 2005; Wang et al., 2006, 2007), there was a significant deposition of LPDB sediments at the Rio Grande Cone (Fig. 2.4a, 2.4d–h). The relatively fine clastic sediments with a main modal value of ~6 µm (Figs. 2.5a and 2.7) resemble modern surface sediments (Figs. 2.5e and 2.7) (Urien and Ewing, 1974; Frenz et al., 2003), which clearly originate from the LPDB (Campos et al., 2008; Corrêa et al., 2008; Mahiques et al., 2008). These sediments were mainly transported from the La Plata Estuary to the Rio Grande Cone together with the Plata Plume Water, first in paleochannels and later gravitationally off-shelf (Fig. 2.1). Flood basalts of the eastern LPDB made up the dominant source for magnetic minerals (Allan et al., 1989; Schwertmann and Taylor, 1989; Campos et al., 2008).

According to Toldo et al. (2000) and Weschenfelder et al. (2008) the Jacuí and Camaquã Rivers (Fig. 2.1) delivered a significantly higher amount of sediments to the western South Atlantic before sea level (Fig. 2.4m) reached a modern stand at ~8 kyr BP. A large sector of the Jacuí and Camaquã Rivers' drainage basin also contains tholeiitic basalts and metamorphic units (Philipp and Machado, 2005). These rivers are thus strong candidates for additional, more proximal sediment supply to the Rio Grande Cone during the LG-EH.

The weaker monsoonal precipitation over the eastern LPDB (Fig. 2.4i,j) and therefore a less intense chemical weathering of LPDB sediments is possibly seen at our core site by the deposition of a high proportion of secondary paramagnetic minerals (Fig. 2.7, low $SIRM_{cf}$ / Fe_{cf} ratios). Fe-bearing clay minerals like kaolinite (Fe-substituted during chemical weathering of igneous rocks), smectites (e.g., nontronite) and illite are common paramagnets in the surface sediments of the SE South American continental margin, being transported from the LPDB (Campos et al., 2008). Since these clay minerals are more prone towards chemical weathering than primary Fe-oxides, weaker chemical weathering favors their relative increase in abundance as compared to the abundance of the

last ones and therefore increases the Fe_{cf} values. Additionally, lower runoff should result in less energetic and therefore weaker transport of the heavy ferrimagnetic Fe-(Ti)-oxide mineral grains in the LPDB, leaving magnetically enriched river bed and bank sediments unaffected and lowering the $SIRM_{cf}$ values at our core site. Siliciclastic minerals such as paramagnetic clay minerals can be transported in suspension over long distances due to their oblique shape and lower density as well as their shorter residence time in the sediment bed (Gallaway et al., 2012).

2.7.2. Mid Holocene

During the MH, the temperature gradient between mid and tropical latitudes of the eastern South Pacific was rising (Lamy et al., 2010). Higher austral summer insolations increased the sea-surface temperatures in the eastern subtropical Pacific (Lamy et al., 2010) strengthening the SWWB and shifting its northern boundary northward (Fig. 2.6b), as seen in the mounting precipitation at Aculeo Lake (Fig. 2.4k) and lower SWWB activity in the core zone (Fig. 2.4l). The SE Pacific high-pressure cell remained strong and reached relatively far south, preventing the SWWB from extending further north (Lamy et al., 2010). An intensified SE Pacific high-pressure cell together with a strong SWWB increased the frequency and intensity of anticyclones migrating to the NE along the leeside of the Andean Cordillera (Pezza and Ambrizzi, 2005). This situation produced more frequent southwesterly to southerly air incursions along the coast of SE South America, driving the Subantarctic Shelf Water and the Plata Plume Water further to the north as compared to the LG-EH. The stronger SWWB also intensified the flow of the Malvinas Current and shifted the STSF and probably also the BMC to the north (Fig. 2.6b). This scenario is in agreement with the atmospheric and oceanographic model runs of Sijp and England (2008), which show a strengthening of the Malvinas Current in dependence of the strengthened SWWB during the Last Glacial Maximum. The flow of the Subantarctic Shelf Water is likely additionally intensified by a broadening shelf due to sea level rise (Fig. 2.4m). During the MH, the STSF must have been permanently or seasonally located to the north of our core site (Fig. 2.6b), enabling remobilized sandy sediments from the Argentinean shelf to be transported with the Subantarctic Shelf Water toward the upper continental margin of southern Brazil. The deposition of Argentinean shelf sediments might also have become dominant during the MH due to sea-level high stand of up to 6 m above the modern one (Angulo et al., 2006). Such conditions would have trapped LPDB sediments in the La Plata Estuary (Violante and Parker, 2004).

The strong influence of the Subantarctic Shelf Water at the Uruguayan and South Brazilian upper continental margin during the MH can be seen by a significant increase in the abundance of Antarctic diatoms (Fig. 2.4d) and bioproductivity (Fig. 2.4c) due to higher availability of nutrients in respect to the warm and saline Subtropical Shelf Water. Much coarser sediments (grain-size peak around 100 µm; Figs. 2.4c and 2.7) than during the LG-EH were now deposited at the Rio Grande Cone. Following the nondimensional Shields curve improved by Soulsby and Whitehouse (1997), bottom current velocities between 1.1 and 1.3 cm s^{-1} (friction threshold velocities for water temperatures between 20° and 0° C, respectively) are needed to transport quartz grains with a diameter of 100 µm. Palma et al. (2008) modeled modern current velocities of at least 50 cm s^{-1} in a water depth of 15 m at the northeastern Argentinean continental shelf, off the La Plata Estuary and off Uruguay. Bottom

current velocities of ~20 cm s^{-1} at the whole outer SE South American continental shelf are provided by the OCCAM Global Model (Gwilliam et al., 1997) and were directly measured by Vivier and Provost (1999) at the Argentinean upper continental margin in water depths between 300 and 500 m, around 100 m above the ground. In these water depths, the current velocities can seasonally even reach 40 cm s^{-1} (Vivier and Provost, 1999) and are able to enter the shelf (Piola et al., 2010). Thus, existing bottom current velocities are not only capable to transport 100 µm quartz particles, but are even sufficient to erode fine quartz sand with magnetic inclusions, being easily able to transport silt sized Fe-(Ti)-oxide grains in suspension.

Indeed, the MH sediments at the Rio Grande Cone show a stronger ferrimagnetic signal (Figs. 2.4f,g,h and 2.7), while total Fe_{cf} concentrations (Fig. 2.4e) decrease significantly compared to the LG-EH. We explain this apparent paradox by far higher ferrimagnetic contributions by Fe-(Ti)-oxides as seen in the magnetic signals (Figs. 2.4h and 2.7) and a much lower content in paramagnetic Fe-bearing clay minerals (e.g., illite, smectite) as seen in total Fe_{cf} content (Fig. 2.4e). The magnetic dominance of primary ferrimagnetic Fe-(Ti)-oxides over pedogenic Fe species calls for a magnetically richer sediment source than the LPDB, which was the dominant source during the LG-EH (Fig. 2.7). The closest available source for sediments with such magnetic properties and characteristic grain size of 100 µm is the Argentinean continental margin (Urien and Ewing, 1974; Frenz et al., 2003) with its igneous detritus of Andean origin (Mahiques et al., 2008). The Argentinean continental shelf can hence be treated as an independent sedimentary province with vastly different rock-magnetic characteristics compared to the LPDB sediments, which is in agreement with foregoing isotopic, heavy mineral and clay mineral studies (Campos et al., 2008; Corrêa et al., 2008; Mahiques et al., 2008).

Uruguayan and Brazilian coastal sands can be ruled out as a relevant sediment source during the MH, since they are mainly composed of diamagnetic quartz and feldspars (Potter, 1984, 1986). The Uruguayan and South Brazilian Highlands can also be excluded as potential sediment sources due to sea-level rise during the EH and part of the MH (Angulo et al., 2006) trapping most sediments of the Jacuí and Camaquã Rivers in the Patos Lagoon, dramatically increasing sedimentation rates there (e.g., Toldo et al., 2000). The LPDB can also be ruled out as major sediment source during the MH. The observed grain-size coarsening during the MH (Fig. 2.4a) would have to be related with a strong velocity increase of the Brazilian Coastal Current. If the Brazilian Coastal Current were able to deposit sand at our core site, the finer fractions would have been transported further to the northeast. Such grain-size sorting of magnetic minerals from a constant sediment source would cause a decrease in susceptibility (Fig. 2.4e) and SIRM (Fig. 2.4g) during the MH, since the magnetite content of marine sediments is generally much higher in the silt and clay fractions (Dunlop and Özdemir, 2001; Liu et al, 2004). This postulated effect is in obvious conflict with the enhanced ferrimagnetic mineral contents during the MH (Fig. 2.7).

2.7.3. Late Holocene

During the LH, the SE Pacific high-pressure cell became weaker (Fig. 2.6c) and the northern boundary of the SWWB was able to migrate further north to its modern location (Jenny at al., 2003; Lamy et al., 2010). In consequence, the precipitation at Aculeo Lake has reached its highest level throughout the last 10 kyr

(Fig. 2.4k). Simultaneously, the precipitations at the SWWB core zone experienced their lowest intensity of the last 14 kyr (Fig. 2.4l) (Lamy et al., 1999 and references therein; Lamy et al., 2010). At the western South Atlantic margin, the STSF has migrated back south (Fig. 2.6c) due to a stronger southward flow of the Subtropical Shelf Water (Fig. 2.4d) driven by more intense austral (here northeasterly) tradewinds, in response to a strengthened and southward shifted South Atlantic high-pressure cell (Höflich, 1984; Lima et al., 1996; Garreaud et al., 2009).

The climatic (Fig. 2.4i,j) and oceanographic (Fig. 2.4d) changes between 4 and 3 cal kyr BP were induced by the highest Holocene austral summer insolation followed by an intensification of the SAMS over SE South America and the onset of the modern El Niño Southern Oscillation (ENSO) (e.g., Moy et al., 2002; Rein et al., 2005). Effects of increasing precipitation over SE South America are already detectable since ~6 cal kyr BP (e.g., by increasing sedimentation rates, Fig. 2.3), but become more evident between 4 and 2.5 cal kyr BP, with continuous increase in SAMS intensity until present (Fig. 2.4i,j) (e.g., Behling, 1997; Wang et al., 2006, 2007; Chiessi et al., 2010).

The pronounced SAMS over SE South America during the LH (Fig. 2.4i,j) is mirrored in the regained deposition of LPDB sediments at the Rio Grande Cone, while no significant deposition of Argentinean shelf sediments is observed after ~4 cal kyr BP (Figs. 2.5c,e and 2.7). The LPDB sediments are transported with the Plata Plume Water and the underlying Subantarctic Shelf Water from the La Plata Estuary northeastward along the SE South American continental shelf to the STSF (Piola et al., 2000, 2005; Möller et al., 2008). As the STSF is thought to be a major export path of shelf waters to the slope region (Piola et al., 2008), the present-day location of the STSF likely provides a direct route of LPDB sediments to the Rio Grande Cone. The Plata Plume Water also delivers high amounts of nutrients and compensates the southward retreated Subantarctic Shelf Water (Fig. 2.4d), while the LH bioproductivity (Fig. 2.4c) remains comparable to that during the MH. The sediments deposited during the LH have a very similar grain-size mode as those deposited during the LG-EH (Fig. 2.5a,e). During the LH and likewise the LG-EH, the main source for sedimentary magnetic minerals was therefore the flood basalts of the eastern LPDB. Nevertheless, there is a prominent difference in the magnetic assemblages of both periods (Fig. 2.7). The higher χ_{cf} and $SIRM_{cf}$ (Fig. 2.4f,g) of LH sediments point towards higher concentrations of primary Fe-(Ti)-oxides in relation to secondary Fe-bearing clay minerals than during the LG-EH (Fig. 2.7). This difference is thought to be caused by more humid climatic conditions within the LPDB (e.g., Behling, 1997; Wang et al., 2006, 2007) since at least 2.5 cal kyr BP (Fig. 2.4i,j). The increased humidity accelerates chemical weathering of silicates and their dissolution, while the more weathering-resistant Fe-(Ti)-minerals are indirectly enriched in the sediments and can be eroded from river bed and banks by higher runoff and related flood events (Fig. 2.7).

2.8. Conclusions

Our study stresses the importance of taking tropical and extratropical climate elements jointly into consideration. We assessed the interaction of the South American Monsoon System (SAMS) and the Southern Westerly Wind Belt (SWWB) during the last 14 cal kyr BP based on multi-proxy analyses performed in a sediment core collected in the western South Atlantic. During

the Late Glacial and Early Holocene (~14–8 cal kyr BP; except Younger Dryas), the SAMS was weaker than today due to lower austral summer insolation. The SWWB was contracted to more southern latitudes in response to a smaller temperature gradient between mid and tropical latitudes in the eastern South Pacific. Thereby, the Brazil-Malvinas Confluence (BMC) and the Subtropical Shelf Front (STSF) were located more to the south than today (derived from low carbonate concentrations in our core that reflect a relatively low paleoproductivity, being typical for the nutrient-poor Subtropical Shelf Water). During this period the Rio Grande Cone served as a sea-level low stand deposition center for fine sediments from the La Plata, Jacuí and Camaquã Rivers. This was deduced from a silty high-iron low-susceptibility low-remanence magnetogranulometric fingerprint, pointing to a less humid catchment if compared to modern conditions.

During the Mid Holocene (~8–4 cal kyr BP), the SWWB strengthened and extended further north due to a rising temperature gradient in the eastern South Pacific, caused by enhancing austral summer insolation. This northward shift of the wind regime strengthened the Malvinas Current, leading to a meridional displacement of the BMC and the related STSF to their northernmost positions during the last 14 cal kyr (deduced from higher Antarctic diatom abundances and carbonate contents in our core due to increased paleoproductivity triggered by the northward extension of the nutrient-rich Subantarctic Shelf Water). This, in combination with a broadened continental shelf due to sea-level rise enabled remobilized coarser and magnetically stronger Argentinean shelf sediments to dominate the deposition at the Rio Grande Cone. The Argentinean shelf provenance could be defined by a sandy low-iron intermediate-susceptibility intermediate-remanence magnetogranulometric fingerprint.

In the Late Holocene (since ~4 cal kyr BP), the SAMS intensified over SE South America, while El Niño Southern Oscillation (ENSO) variability also increased significantly. Both features (in particular during the more frequent El Niño events) generated higher precipitation over the La Plata Drainage Basin (LPDB) and enhanced sediment export to the western South Atlantic. The SAMS and the related austral tradewinds were intensified by the highest austral summer insolation, typical of the Late Holocene. This strengthened the flow of the warm and saline Subtropical Shelf Water and caused a southward shift of the STSF (recorded by a decrease in the concentration of Antarctic diatoms), with possibly a minor effect on the BMC, while deposition of Argentinean continental shelf sediments significantly decreased at the Rio Grande Cone. The substitution of the Argentinean shelf by the LPDB, as the main source of terrigenous sediments to the Rio Grande Cone, was determined by a silty intermediate-iron high-susceptibility high-remanence magnetogranulometric fingerprint, revealing modern humid conditions over the LPDB.

2.9. Acknowledgements

Constructive comments by two anonymous referees greatly improved the paper. We acknowledge the help of Inka Meyer for guidance during grain-size analyses. We thank James A. Collins for improving the English and Alberto R. Piola for the helpful remarks on the regional oceanography. We are grateful to the Institute of Geosciences, University of São Paulo, to have enabled a three-months stay abroad to S.R. for fruitful discussions on the results. Financial support for this survey was provided by the DFG through the European Graduate College EUROPROX to S.R., by FAPESP grants 2010/09983-9 and 2011/50394-0 to C.M.C. as well as partially by the Spanish Council of Scientific Research (CSIC) to O.E.R. Data presented in this study are available at the PANGAEA database (http://www.pangaea.de).

2.10. References

Allan, J.E.M., Coey, J.M.D., Sander, I.S., Schwertmann, U., Friedrich, G., Wiechowski, A., 1989. An occurrence of a fully-oxidized natural titanomaghemite in basalt. Mineralogical Magazine 53, 299–304.

Amsler, M.L., Drago, E.C., 2009. A review of the suspended sediment budget at the confluence of the Paraná and Paraguay Rivers. Hydrological Processes 23, 3230–3235.

Angulo, R.J., Lessa, G.C., Souza, M.C., 2006. A critical review of mid- to late-Holocene sea-level fluctuations on the eastern Brazilian coastline. Quaternary Science Reviews 25, 486–506.

Behling, H., 1995. Investigation into the Late Pleistocene and Holocene history of vegetation and climate in Santa Catarina (S Brazil). Vegetation History and Archaeobotany 4, 127-152.

Behling, H., 1997. Late Quaternary vegetation, climate and fire history of the Araucaria forest and campos region from Serra Campos Gerais, Paraná State (South Brazil). Review of Palaeobotany and Palynology 97, 109–121.

Behling, H., Safford, H.D., 2010. Late-glacial and Holocene vegetation, climate and fire dynamics in the Serra dos Órgãos, Rio de Janeiro State, southeastern Brazil. Global Change Biology 16, 1661–1671.

Behling, H., Bauermann, S.G., Neves, P.C.P., 2001. Holocene environmental changes in São Francisco de Paula region, southern Brazil. Journal of South American Earth Sciences 14, 631–639.

Berbery, E.H., Barros, V.R., 2002. The hydrologic cycle of the La Plata Basin in South America. Journal of Hydrometeorology 3, 630–645.

Bleil, U., von Dobeneck, T., 2003. Late Quaternary terrigenous sedimentation in the western equatorial Atlantic – South American versus African provenance discriminated by magnetic mineral analysis. In: Wefer, G., Mulitza, S., Ratmeyer, V. (Eds.), The South Atlantic in the Late Quaternary; Reconstruction of Material Budgets and Current Systems. Springer-Verlag, Berlin-Heidelberg-New York-Tokyo, pp. 213–236.

Bloemendal, J., Lamb, B., King, J., 1988. Paleoenvironmental implications of rock-magnetic properties of late quaternary sediment cores from the eastern equatorial Atlantic. Paleoceanography 3, 61–87.

Boebel, O., Davis, R.E., Ollitrault, M., Peterson, R.G., Richardson, P.L., Schmid, C., Zenk, W., 1999. The intermediate depth circulation of the western South Atlantic. Geophysical Research Letters 26, 3329–3332.

Campos, E.J.D., Mulkherjee, S., Piola, A.R., de Carvalho, F.M.S., 2008. A note on a mineralogical analysis of the sediments associated with the Plata River and Patos Lagoon outflows. Continental Shelf Research 28, 1687–1691.

Chiessi, C.M., Mulitza, S., Paul, A., Pätzold, J., Groeneveld, J., Wefer, G., 2008. South Atlantic interocean exchange as the trigger for the Bølling warm event. Geology 36, 919–922.

Chiessi, C.M., Mulitza, S., Pätzold, J., Wefer, G., 2010. How different proxies record precipitation variability over southeastern South America. IOP Conf. Ser.: Earth and Environmental Science 9, 012007.

Corrêa, I.C.S., Ayoup-Zouain, R.N., Weschenfelder, J., Tomazelli, L.J., 2008. Áreas fontes dos minerais pesados e sua distribução sobra a plataforma continental sul-brasileira, uruguaya e norte-argentina. Revista Pesquisas em Geosciências 35, 137–150.

Cruz, F.W., Burns, S.J., Karmann, I., Sharp, W.D., Vuille, M., Cardoso, A.O., Ferrari, J.A., Dias, P.L.S., Viana, O., 2005. Insolation-driven changes in atmospheric circulation over the past 116,000 years in subtropical Brazil. Nature 434, 63–65.

Csanady, G.T., 1978. The arrested topographic wave. Journal of Physical Oceanography 8, 47–62.

Depetris, P.J., Griffin, J.J., 1968. Suspended load in the Río de la Plata Drainage Basin. Sedimentology 11, 53–60.

Depetris, P.J., Probst, J.-L., Pasquini, A.I., Gaiero, D.M., 2003. The geochemical characteristics of the Paraná River suspended sediment load: an initial assessment. Hydrological Processes 17, 1267–1277.

Deruelle, B., 1982. Petrology of the Plio-Quaternary volcanism of the South-Central and Meridional Andes. Journal of Volcanology and Geothermal Research 14, 77–124.

Drake, R., Vergara, M., Munizaga, F., Vicente, J.C., 1982. Geochronology of Mesozoic-Cenozoic magmatism in Central Chile, Lat. 31°-36°S. Earth Science Reviews 18, 353–363.

Dunlop, D.J., Özdemir, Ö., 2001. Rock Magnetism: Fundamentals and Frontiers (Cambridge Studies in Magnetism). Cambridge University Press, 573 p.

Evans, M.E., Heller, F., 2003. Environmental magnetism - principles and applications of enviromagnetics. Academic Press, Amsterdam, 299 p.

Frenz, M., Höppner, R., Stuut, J.-B.W., Wagner, T., Henrich, R., 2003. Surface sediment bulk geochemistry and grain-size composition related to the oceanic circulation along the South American continental margin in the Southwest Atlantic. In: Wefer, G., Mulitza, S., Ratmeyer, V., (Eds.), The South Atlantic in the Late Quaternary; Reconstruction of Material Budgets and Current Systems. Springer-Verlag, Berlin-Heidelberg-New York-Tokyo, pp. 347–373.

Gaiero, D.M., Probst, J.-L., Depetris, P.J., Bidart, S.M., Leleyter, L., 2003. Iron and other transition metals in Patagonian riverborne and windborne materials: Geochemical control and transport to the southern South Atlantic Ocean. Geochimica et Cosmochimica Acta 67, 3603–3623.

Gallaway, E., Trenhaile, A.S., Cioppa, M.T., Hatfield, R.G., 2012. Magnetic mineral transport and sorting in the swash-zone: northern Lake Erie, Canada. Sedimentology 59, 1718–1734.

Garreaud, R.D., Vuille, M., Compagnucci, R., Marengo, J., 2009. Present-day South American climate. Palaeogeography, Palaeoclimatology, Palaeoecology 281, 180–195.

Govindaraju, K., 1994. Compilation of working values and descriptions for geostandards. Geostandards Newsletter 18, 1–158.

Gwilliam, C.S., Coward, A.C., de Cuevas, B.A., Webb, D.J., Rourke, E., Thompson, S.R., Döös, K., 1997. The OCCAM Global Ocean Model. In: García, F.G., Cisneros, G., Fernández, A.E, Álvarez, R. (Eds.), Numerical Simulations in the Environmental and Earth Sciences: Proceedings of the Second UNAM-CRAY Supercomputing Conference. Cambridge University Press, pp. 24–30.

Gyllencreutz, R., Mahiques, M.M., Alves, D.V.P., Wainer, I.K.C., 2010. Mid- to late-Holocene paleoceanographic changes on the southeastern Brazilian shelf based on grain size records. The Holocene 20, 863–875.

Höflich, O., 1984. Climate in the South Atlantic. In: Van Loon, H. (Ed.), Climates of the Oceans. World Survey of Climatology 15, 1–132.

Jansen, J.H.F., Gaast, S.J.V., Koster, B., Vaars, A.J., 1998. CORTEX, a shipboard XRF-scanner for element analyses in split sediment cores. Marine Geology 151, 143–153.

Jenny, B., Wilhelm, D., Valero-Garcés, B.L., 2003. The southern Westerlies in Central Chile: Holocene precipitation estimates based on a water balance model for Laguna Aculeo (33°50'S). Climate Dynamics 20, 269–280.

Kilian, R., Frank Lamy, F., 2012. A review of Glacial and Holocene paleoclimate records from southernmost Patagonia (49–55° S). Quaternary Science Reviews 53, 1–23.

Laborde, J.L., 1997. Geomorphological and geological setting of the Río de la Plata. In: Wells, P.G., Daborn, G.R (Eds.), The Río de la Plata – An Environmental Overview. Dalhousie University, Halifax, pp. 1–16.

Lambeck, K., Chappell, J., 2001. Sea level change through the last glacial cycle. Science 292, 679–686.

Lamy, F., Hebbeln, D., Wefer, G., 1999. High-resolution marine record of climatic change in mid-latitude Chile during the last 28,000 years based on terrigenous sediment parameters. Quaternary Research 51, 83–93.

Lamy, F., Kilian, R., Arz, H.W., Francois, J.-P., Kaiser, J., Prange, M., Steinke, T., 2010. Holocene changes in the position and intensity of the southern westerly wind belt. Nature Geoscience 3, 695–699.

Laprida, C., Chapori, N.G., Chiessi, C.M., Violante, R.A., Watanabe, S., Totah, V., 2011. Middle Pleistocene sea surface temperature in the Brazil-Malvinas Confluence Zone: Paleoceanographic implications based on planktonic foraminifera. Micropaleontology 57, 183–195.

Larrasoaña, J.C., Roberts, A.P., Rohling, E.J., Winklhofer, M., Wehausen, R., 2003. Three million years of monsoon variability over the northern Sahara. Climate Dynamics 21, 689–698.

Ledru, M.P., 1993. Late Quaternary environmental and climatic changes in Central Brazil. Quaternary Research 9, 90–98.

Lima, I.D., García, C.A.E., Möller, O.O., 1996. Ocean surface processes on the southern Brazilian shelf: Characterization and seasonal variability. Continental Shelf Research 16, 1307–1317.

Liu, Q., Banerjee, S.K., Jackson, M.J., Maher, B.A., Pan, Y., Zhu, R., Deng, C., Chen, F., 2004. Grain sizes of susceptibility and anhysteretic remanent magnetization carriers in Chinese loess/paleosol sequences. Journal of Geophysical Research 109, B03101.

Mahiques, M.M., Tassinari, C.C.G., Marcolini, S., Violante, R.A., Figueira, R.C.L., Silveira, I.C.A., Burone, L., Sousa, S.H.M., 2008. Nd and Pb isotope signatures on the southeastern South American upper margin: Implications for sediment transport and source rocks. Marine Geology 250, 51–63.

Mahiques, M.M., Klein, I., Wainer, C., Burone, L., Nagai, R., Sousa, S.H.M., Figueira, R.C.L., Silveira, I.C.A., Bícego, M.C., Alves, D.P.V., Hammer, Ø. , 2009. A high-resolution Holocene record on the Southern Brazilian shelf: Paleoenvironmental implications. Quaternary International 206, 52–61.

Marengo, J.A., Soares, W.R., Saulo, C., Nicolini, M., 2004. Climatology of the low-level jet east of the Andes as derived from the NCEP–NCAR reanalyses: Characteristics and temporal variability. Journal of Climate 17, pp. 2261–2280.

Martins, L.R., Coutinho, P.N., 1981. The Brazilian continental margin. Earth Science Reviews 17, 87–107.

Möller, O.O., Piola, A.R., Freitas, A.C., Campos, E.J.D., 2008. The effects of river discharge and seasonal winds on the shelf off southeastern South America. Continental Shelf Research 28, 1607–1624.

Moy, C.M., Seltzer, G.O., Rodbell, D.T., Anderson, D.M., 2002. Variability of El Niño/Southern Oscillation activity at millennial timescales during the Holocene epoch. Nature 420, 162–164.

Mulitza, S., Prange, M., Stuut, J.-B., Zabel, M., von Dobeneck, T., Itambi, A.C., Nizou, J., Schulz, M., Wefer, G., 2008. Sahel megadroughts triggered by glacial slowdowns of Atlantic meridional overturning. Paleoceanography 23, PA4206.

Müller, P.J., 2004a. Density and water content of sediment core GeoB 6211-2. Department of Geosciences, University of Bremen, unpublished dataset #137022, doi:10.1594/PANGAEA.137022.

Müller, P.J., 2004b. Carbon and nitrogen data of sediment core GeoB 6211-2. Department of Geosciences, University of Bremen, unpublished dataset #137054, doi:10.1594/PANGAEA.137054.

Orfeo, O., Stevaux, J., 2002. Hydraulic and morphological characteristics of middle and upper reaches of the Paraná River (Argentina and Brazil). Geomorphology 44, 309–322.

Palma, E.D., Matano, R.P., Piola, A.R., 2008. A numerical study of the southwestern Atlantic shelf circulation: Stratified ocean response to local and offshore forcing. Journal of Geophysical Research 113, C11010.

Parker, G., Paterlini, C.M., Violante, R.A., 1997. El fondo marino. In: Boschi, E. (Ed.), El Mar argentino y sus Recursos Marinos. INIDEP, Mar del Plata 1, 65–87.

Pasquini, A.I., Depetris, P.J., 2007. Discharge trends and flow dynamics of South American rivers draining the southern Atlantic seaboard: An overview. Journal of Hydrology 333, 385–399.

Peate, D.W., 1997. The Paraná-Etendeka province. In: Mahoney, J.J., Coffin, M.F. (Eds.), Large Igneous Provinces. Continental, Oceanic, and Planetary Flood Volcanism. American Geophysical Union, pp. 217–245.

Pezza, A.B., Ambrizzi, T., 2005. Dynamical conditions and synoptic tracks associated with different kind of cold surges over tropical South America. International Journal of Climatology 25, 215–241.

Philipp, R.P., Machado, R., 2005. The Late Neoproterozoic granitoid magmatism of the Pelotas Batholith, southern Brazil. Journal of South American Earth Sciences 19, 461–478.

Pierce, J.W., Siegel, F.R., 1979. Suspended particulate matter on the southern Argentine shelf. Marine Geology 29, 73–91.

Piola, A.R., Campos, E.J.D., Möller, O.O., Charo, M., Martinez, C., 2000. Subtropical shelf front off eastern South America. Journal of Geophysical Research 105, 6565–6578.

Piola, A.R., Matano, R.P., Palma, E.D., Möller, O.O., Campos, E.J.D., 2005. The influence of the Plata River discharge on the western South Atlantic shelf. Geophysical Research Letters 32, L01603.

Piola, A.R., Möller, O.O., Guerrero, R.A., Campos, E.J.D., 2008. Variability of the subtropical shelf front off eastern South America: Winter 2003 and summer 2004. Continental Shelf Research 28, 1639–1648.

Piola, A.R., Avellaneda, N.M., Guerrero, R.A., Jardón, F.P., Palma, E.D., Romero, S.I., 2010. Malvinas-slope water intrusions on the northern Patagonia continental shelf. Ocean Sciences 6, 345–359.

Potter, P. E., 1984. South American modern beach sand and plate tectonics. Nature 311, 645–648.

Potter, P. E., 1986. South America and a few grains of sand: Part 1, beach sands. Journal of Geology 94, 301–319.

Reimer, P.J., Reimer, R.W., 2001. A marine reservoir correction database and on-line interface. Radiocarbon 43, 461–463.

Reimer, P.J., Baillie, M.G.L., Bard, E., Bayliss, A., Beck, J.W., Blackwell, P.G., Ramsey, C.B., Buck, C.E., Burr, G.S., Edwards, R.L., Friedrich, M., Grootes, P.M., Guilderson, T.P., Hajdas, I., Heaton, T.J., Hogg, A.G., Hughen, K.A., Kaiser, K.F., Kromer, B., McCormac, F.C., Manning, S.W., Reimer, R.W., Richards, D.A., Southon, J.R., Talamo, S., Turney, C.S.M., Plicht, J., Weyhenmeyer, C.E., 2009. IntCal09 and Marine09 radiocarbon age calibration curves, 0-50,000 years cal BP. Radiocarbon 51, 1111–1150.

Rein, B., Lückge, A., Reinhardt, L., Sirocko, F., Wolf, A., Dullo, W.-C., 2005. El Niño variability off Peru during the last 20,000 years. Paleoceanography 20, PA4003.

Richter, T.O., van der Gaast, S., Koster, B., Vaars, A., Gieles, R., de Stigter, H., de Haas, H., van Weering, T.C.E., 2006. The Avaatech XRF core scanner: technical description and applications of NE Atlantic sediments. In: Rothwell, R.G. (Ed.), New Techniques in Sediment Core Analysis. Special Publication 267. Geological Society, London, pp. 39–50.

Robinson, S.G., 1986. The late Pleistocene palaeoclimate record of North Atlantic deep-sea sediments revealed by mineral-magnetic measurements. Physics of Earth and Planetary Interiors 42, 22–47.

Romero, O., Hensen, C., 2002. Oceanographic control of biogenic opal and diatoms in surface sediments of the southwestern Atlantic. Marine Geology 186, 263–280.

Rumble, D., 1976. Oxide Minerals - Short Course Notes Volume 3. Mineralogical Society of America, 706 p.

Schrader, H., Gersonde, R., 1978. Diatoms and silicoflagellates. In: Zachariasse, W.J., Riedel, W.R., Sanfilippo, A., Schmidt, R.R., Brolsma, M.J., Schrader, H., Gersonde, R., Drooger, M.M., Broekman, J.A. (Eds.), Micropaleontological Counting Methods and Techniques – An Exercise on an Eight Meter Section of the Lower Pliocene of Capo Rosello, Sicily. Utrecht Micropaleontological Bulletins 17, 129–176.

Schramm, R., Heckel, J., 1998. Fast analysis of traces and major elements with ED (P)XRF using polarized X-rays: TURBOQUANT. Journal of Physics IV 8, 335–342.

Schulz, H.D., Ayres-Neto, A., Boetius, A., Enneking, K., Fabian, K., Feseker, T., Funk, J., Gorke, M., Heidersdorf, F., Hensen, C., Heuer, V., Hill, H.G., Hinrichs, S., Kasten, S., Klann, M., Souza, C.L., Briao, A.M., Meyer, S., Mulitza, S., Niebler, H.-S., Ochsenhirt, W.-T., Panteleit, B., Pfeifer, K., Schewe, F., Schwenk, T., Señorans, J.L., Siemer, S., Steinmetz, E., Wenzhöfer, F., 2001. Report and preliminary results of Meteor Cruise M46/2, Recife–Montevideo, 02.12.-29.12.1999. Berichte 174, Fachbereich Geowissenschaften, Universität Bremen vol. 01-1, 69 p.

Schwertmann, U., Taylor, R.M., 1989. Iron Oxides. In: Dixon, J.B., Weed, S.B., Dinauer, R.C. (Eds), Minerals in Soil Environments. 2nd ed. Madison, Wisconsin. Soil Science Society of America, pp. 379-439.

Seluchi, M. E., Marengo, J.A. 2000. Tropical-midlatitude exchange of air masses during summer and winter in South America: Climatic aspects and examples of intense events. International Journal of Climatology 20, pp. 1167–1190.

Sijp, W.P., England, M.H., 2008. The effect of a northward shift in the southern hemisphere Westerlies on the global ocean. Progress in Oceanography 79, 1–19.

Soulsby, R.L., Whitehouse, R.J.S., 1997. Threshold for sediment motion in coastal environments. Combined Australasian Coastal Engineering and Ports Conference, Christchurch, 149–154.

Souza, R.B., Robinson, I.S., 2004. Lagrangian and satellite observations of the Brazilian Coastal Current. Continental Shelf Research 24, 241– 262.

Stevaux, J.C., 2000. Climatic events during the Late Pleistocene and Holocene in the Upper Parana River: correlation with NE Argentina and South-Central Brazil. Quaternary International 72, 73–85.

Stevenson, M.R., Dias-Brito, D., Stech, J.L., Kampel, M., 1998. How do cold water biota arrive in a tropical bay near Rio de Janeiro, Brazil? Continental Shelf Research 18, 1595–1612.

Stramma, L., Peterson, R.G., 1989. The South Atlantic Current. Journal of Physical Oceanography 20, 846–859.

Stuiver, M., Reimer, P.J., 1993. Extended 14C database and revised CALIB 3.0 14C age calibration program. Radiocarbon 35, 215–230.

Tjallingii, R., Röhl, U., Kölling, M., Bickert, T., 2007. Influence of the water content on X-ray fluorescence core-scanning measurements in soft marine sediments. Geochemistry, Geophysics, Geosystems 8, Q02004.

Toldo, E.E., Dillenburg, S.R., Corrêa, I.C.S., Almeida, L.E.S.B., 2000. Holocene sedimentation in Lagoa dos Patos Lagoon, Rio Grande do Sul, Brazil. Journal of Coastal Research 16, 816–822.

Urien, C.M., Ewing, M., 1974. Recent sediments and environment of southern Brazil, Uruguay, Buenos Aires, and Rio Negro continental shelf. In: Burk, C.A., Drake, C.L., (Eds.), The Geology of Continental Margins. Springer, Berlin, pp.157–177.

Vera, C., Higgins, W., Amador, J., Ambrizzi, T., Garreaud, R., Gochis, D., Gutzler, D., Lettenmaier, D., Marengo, J., Mechoso, C.R., Nogues-Paegle, J., Silva-Dias, P.L., Zhang, C., 2006. Towards a unified view of the American Monsoon System. Journal of Climate 19, 4977–5000.

Villa-Martínez, R., Moreno, P.I., 2007. Pollen evidence for variations in the southern margin of the westerly winds in SW Patagonia over the last 12,600 years. Quaternary Research 68, 400–409.

Violante, R.A., Parker, G., 2004. The post-last glacial maximum transgression in the de la Plata River and adjacent inner continental shelf, Argentina. Quaternary International 114, 167–181.

Vivier, F., Provost, C., 1999. Direct velocity measurements in the Malvinas Current. Journal of Geophysical Research 104, 21,083–21,103.

Wagner, S., Widmann, M., Jones, J., Haberzettl, T., Lucke, A., Mayr, C., Ohlendorf, C., Schabitz, F., Zolitschka, B. 2007. Transient simulations, empirical reconstructions and forcing mechanisms for the Mid-holocene hydrological climate in southern Patagonia. Climate Dynamics 29, 333–355.

Wang, X., Auler, A.S., Edwards, R.L., Cheng, H., Ito, E., Solheid, M., 2006. Interhemispheric anti-phasing of rainfall during the last glacial period. Quaternary Science Reviews 25, 3391–3403.

Wang, X., Auler, A.S., Edwards, R.L., Cheng, H., Ito, E., Wang, Y., Kong, X., Solheid, M., 2007. Millennial-scale precipitation changes in southern Brazil over the past 90,000 years. Geophysical Research Letters 34, L23701.

Weltje, G.J., Tjallingii, R., 2008. Calibration of XRF core scanners for quantitative geochemical logging of sediment cores: Theory and application. Earth and Planetary Science Letters 274, 423–438.

Weschenfelder, J., Medeanic, S., Corrêa, I.C.S., Aliotta, S., 2008. Holocene paleoinlet of the Bojuru region, Lagoa dos Patos, southern Brazil. Journal of Coastal Research 24, 99–109.

Whitney, B.S., Mayle, F.E., Punyasena, S.W., Fitzpatrick, K.A., Burn, M.J., Guillen, R., Chavez, E., Mann, D., Pennington, R.T, Metcalfe, S.E., 2011. A 45 kyr palaeoclimate record from the lowland interior of tropical Suth America. Palaeogeography, Palaeoclimatology, Palaeoecology 307, 177–192.

Wien, K., Wissmann, D., Kölling, M., Schulz, H.D., 2005. Fast application of X-ray fluorescence spectrometry aboard ship: How good is the new portable Spectro Xepos analyser? Geo-Mar. Lett. 25, 248–264.Zárate, M.A., 2003. Loess of southern South America. Quaternary Science Reviews 22, 1987–2006.

Zárate, M.A. Blasi, A., 1993. Late Pleistocene-Holocene eolian deposits of the southern Buenos Aires Province, Argentina: A preliminary model. Quaternary International 17, 15–20.

Zech, W., Zech, M., Zech, R., Peinemann, N., Morrás, H.J.M., Moretti, L., Ogle, N., Kalim, R.M., Fuchs, M., Schad, P., Glaser, B., 2009. Late Quaternary palaeosol records from subtropical (38°S) to tropical (16°S) South America and palaeoclimatic implications. Quaternary International 196, 107–120.

Zhou, J., Lau, K.-M., 1998. Does a Monsoon Climate exist over South America? Journal of Climate 11, 1020–1040.

2.11. Scientific background and individual contributions

The work on the study 'Interaction of the South American Monsoon System and the Southern Westerly Wind Belt during the last 14 kyr' was launched during the second half of 2009, in a close cooperation with Dr. Cristiano M. Chiessi. This study builds upon foregoing insightful paleoceanographic studies performed during the PhD thesis of Dr. Cristiano M. Chiessi on the exceptional sediment core GeoB 6211-2 from the Rio Grande Cone off South Brazil. Some former aims concerning shelf-sediment dynamics based on electromagnetic profiling had to be replaced by down-core based paleoclimatic and paleoceanographic targets. This profound change of the focus was caused by the total loss of the 'GEM Shark' electromagnetic profiler during the RV Meteor cruise M78/3a in May 2009, leading to the absence of a suited electromagnetic data base. Thus, this unexpected drawback was the beginning of a new and fruitful challenge.

The design of the study was carried out by Sebastian Razik and Dr. Cristiano M. Chiessi. The sets of room-temperature rock and enviromagnetic parameters, as well as clastic grain-size data were provided by Sebastian Razik. Dr. Cristiano M. Chiessi provided ^{14}C-age data for the sediment core's age-depth model, which was supplemented by major-element data. Data on abundances of siliceous diatoms were contributed by Dr. Oscar E. Romero. Essential interpretation of the results was carried out by Sebastian Razik and Dr. Cristiano M. Chiessi. The paper was entirely written by Sebastian Razik with comments on the manuscript's shape and contents made by Dr. Cristiano M. Chiessi, Prof. Dr. Tilo von Dobeneck and Dr. Oscar E. Romero in order of significance.

Chapter 3: Paleoenvironmental evolution and hydrodynamics of the Rio Grande Cone: Insights from benthic foraminiferal and terrigenous granulometric properties from Last Deglacial sediments off South Brazil

Juliana Braga Silva [a], Cristiano M. Chiessi [b], Sebastian Razik [c] and Wania Duleba [b]

[a] Universidade de São Paulo, Instituto de Geociências, Rua do Lago, 562, Cidade Universitária, CEP05508-080 São Paulo SP, Brazil

[b] Escola de Artes, Ciências e Humanidades, Universidade de São Paulo, Av. Arlindo Béttio 1000, CEP03828-000 São Paulo SP, Brazil

[c] Department of Geosciences, University of Bremen, Klagenfurter Straße, 28359 Bremen, Germany

In preparation for Paleoceanography

3.1. Abstract

The Atlantic Meridional Overturning Circulation (AMOC) and related atmospheric circulation patterns underwent significant variations during the Last Deglaciation due to climatic impacts related to Heinrich Stadial 1 (~16.8 cal kyr BP) and Antarctic Cold Reversal (14.5–12.5 cal kyr BP) on the southern hemisphere (Bølling-Allerød on the northern). Although the paleoclimatic periods and their associated paleoenvironmental changes are well described in respect to the northern hemisphere, studies in the subtropical western Atlantic are fairly limited. In this context, benthic foraminiferal assemblages and granulometric parameters of the terrigenous sediment fraction were analyzed, which were deposited on the Rio Grande Cone off southern Brazil. Five distinct phases were identified and linked to changes in oceanic and atmospheric circulations. Phase 1 (19–18.6 cal kyr BP) was characterized by high sedimentation rates (~246 cm kyr^{-1}) with relatively sudden inputs of organic matter causing low sediment oxygenation. Phase 2 (18.6–17 cal kyr BP) is typical for high oxygenation and high hydrodynamic energies due to a strong Brazil Current caused by an almost collapsed AMOC. Accordingly to decreased (labile) organic matter contents, infaunal species became more dominant. Phase 3 (17–16 cal kyr BP) is characterized by weakening of the oxygenation and hydrodynamics, while infaunal species could populate exclusively shallow sedimentary habitats. This was caused by paleoclimatic changes in Antarctica at 17–16.2 cal kyr BP, which were accompanied by lowest sea-ice extension up to this time weakening the AAIW formation and causing lower SACW ventilation. This resulted in warmer and well-stratified bottom waters at the Rio Grande Cone. Phase 4 (16–14.7 cal kyr BP) shows low hydrodynamics and oxygenations due to restructuring of the AMOC during this pahse's first half. During the second half, stronger hydrodynamics and oxygenations could be observed due to the set-in of the Agulhas Leakage with effects on the Brazil Current. This led to a continuous increase of epifaunal-infaunal and epifaunal species at the water-sediment interface and shallower sediment depths. After 15 cal kyr BP, hydrodynamics and oxygenation weakened under the influence of a warmer and well-stratified Brazil Current. Phase 5 (14.7–14 cal kyr BP) shows the

lowest sedimentation rates (~8 cm kyr^{-1}) due to sea-level transgression. Weakening of hydrodynamics led to higher deposition of organic matter and to sedimentary FeS_2 enrichment, while epifaunal and infaunal species indicated reduced oxygenation of the sedimentary environment. This phase offers the lowest bottom-water temperatures at the Rio Grande Cone likely due to conditions related to the Antarctic Cold Reversal.

3.2. Introduction

The Late Pleistocene is mainly characterized by the environmental conditions of the Last Glacial Maximum (~20 cal kyr BP), where large glaciers covered the northern hemisphere's continents, and by its effects during deglaciation (e.g., Ruddiman and McIntyre, 1981; Hewitt, 2000; Dawson, 2013). After ~20 cal kyr BP the deglaciation set in, leading to ice-shield melting with impacts on the ocean circulation. The first ice-melting pulse during Heinrich Stadial 1 (HS1) at ~19 cal kyr BP caused weakening of the North Atlantic Deep Water (NADW) formation. The NADW formation remained reduced for ~4 kyr due to an intense desalination of ocean water and a respective decrease of its density (Stanford et al., 2011). In turn, this weakening led to initial attenuation of the Atlantic Meridional Overturning Circulation (AMOC) (Stanford et al., 2011), while it almost collapsed between 17.5 and 16.7 cal kyr BP. AMOC intensities could reach values comparable to modern ones between 15 and 14.6 cal kyr BP, as the boreal high-latitudinal fresh-water influx was reduced (Stanford et al., 2011). This last phase corresponds to the transition between the HS1 and the northern hemisphere period called the Bølling-Allerød (Lea et al., 2003; Rasmussen et al., 2006), as well as the Antarctic Cold Reversal (ACR) of the southern hemisphere (14.5–12.5 cal kyr BP) (Blunier et al., 1997; Stenni et al., 2001).

The HS1 variations in the AMOC and its associated atmospheric reorganizations directly affected the climate of the Atlantic's entire neighborhood (e.g., Lohmann, 2003; Pahnke et al., 2008). During such phases of weakened AMOC, interhemispheric transport of water masses occurred at lower bathymetric levels, especially in the western South Atlantic (Arz et al., 1999; Weldeab et al., 2006). The Intertropical Convergence Zone and the South Atlantic Convergence Zone migrated southwards, while the northeasterly trade winds strengthened (Cruz Jr. et al., 2006; Jaeschke et al., 2007). Simultaneously, the Brazil Current strengthened and the North Brazil Current weakened (Arz et al., 1999; Chiessi et al., 2009). Pahnke et al. (2008) noted a production increase of Antarctic Intermediate Water (AAIW) in the southeastern Pacific and in the western South Atlantic. These oceanographic changes influenced the position and the intensity of the marine primary productivity in the southwestern tropical Atlantic (Toledo et al., 2007).

During the transition between HS1 and ACR, the climate of the southern hemisphere cooled due to northward migration of the Subtropical Front and the concurrent northward expansion of cold waters from the Southern Ocean (Putman et al., 2010). Simultaneously, the Intertropical Convergence Zone and the South Atlantic Convergence Zone migrated northward, while the southeasterly trade winds and the AMOC strengthened. These factors created conditions initiating a stronger interhemispheric transport of water masses, which weakened the Brazil Current for the benefit of the North Brazil Current (Arz et al., 1999; Chiessi et al., 2009). As consequence, the spatial precipitation patterns and their intensities

changed over SE South America (Cruz Jr. et al., 2006; Jaeschke et al., 2007).

These atmospheric and oceanographic changes affected the Atlantic fauna (e.g., Cortese and Abelman, 2002; Toledo et al., 2007; Mangini et al., 2010). Benthic foraminifera are important compounds of the ocean floor meiofauna. As their assemblage distributions and respective characteristics are controlled by sedimentary conditions, as well as by physical and chemical properties of the overlying water masses (Schnitker, 1994; Mackensen et al., 1995; Schmiedl et al., 1997), they are among the most commonly used indicators of paleoceanographic changes (Sousa et al., 2006; De and Gupta, 2010). Two of these properties (i.e., the oxygen concentrations in the foraminiferal interstitials and marine bottom waters), as well as the organic matter (nutrition) flux to the ocean floor play a fundamental role in delineation of the benthic foraminiferal distributions (Sen Gupta et al., 1996; Den Dulk et al., 2000; Smart, 2008).

In this study, benthic foraminiferal assemblages (BFA) and granulometric properties of the terrigenous fraction are investigated, which were obtained from the sediment gravity core GeoB 6211-2. The core was recovered at the upper continental slope off South Brazil. As this core site has already provided interesting paleoclimatic and paleoceanographic findings for the last 14 cal kyr BP (Chiessi et al., 2008, 2009; Razik et al., 2013), our goal is to focus on the older part of this sedimentary sequence (19–14 cal kyr BP) and to determine in which way paleoenvironmental conditions varied at the Rio Grande Cone and if implications can be made on the entire AMOC. With this information, we hope to contribute to the scarce knowledge regarding the paleoenvironmental changes in the western South Atlantic in particular, and to contribute to a more robust overall understanding of the AMOC.

3.3. Regional setting

The Rio Grande Cone is a prominent semicircular submarine feature of quaternary age, extending from the shelf to the continental rise off South Brazil. The surface sediments of this sedimentary deposition center are predominantly composed of silty to clayey muds (Frenz et al., 2003; Castilho et al., 2009), originating from the Plata Drainage Basin and being transported from the Plata estuary with the Plata Plume Water and the underlying Subantarctic Shelf Water across the shelf to the study site.

Large-scale ocean circulation of the South Atlantic is formed by the subtropical gyre (Fig. 3.1a). At the western South Atlantic down to a water depth of ~1500 m (Fig. 3.1a), this circulation is composed of the following three main boundary currents: the Brazil Current, the Intermediate Western Boundary Current and the Malvinas Current (Silveira et al., 2000, 2004). The Brazil Current is found at depths of ~500 m with a maximum speed of 0.8 m s^{-1} at 31° S. It originates form latitudes south of 10° S and flows southward until it reaches the Subtropical Convergence Zone at 33°–38° S. At the Subtropical Convergence Zone (also termed Brazil-Malvinas Confluence), the Brazil Current converges with the northward-flowing Malvinas Current, while both become deflected eastward off the continental margin (Peterson and Stramma, 1991; Silveira et al., 2000) (Fig. 3.1a). Below the Brazil Current, the southward-flowing branch of the Intermediate Western Boundary Current carries water masses at sub-picnoclyne depths, reaching maximum speeds of ~0.3 m s^{-1} at 800 m around 23° S (Silveira et al., 2000; Silveira and Machado, 2004).

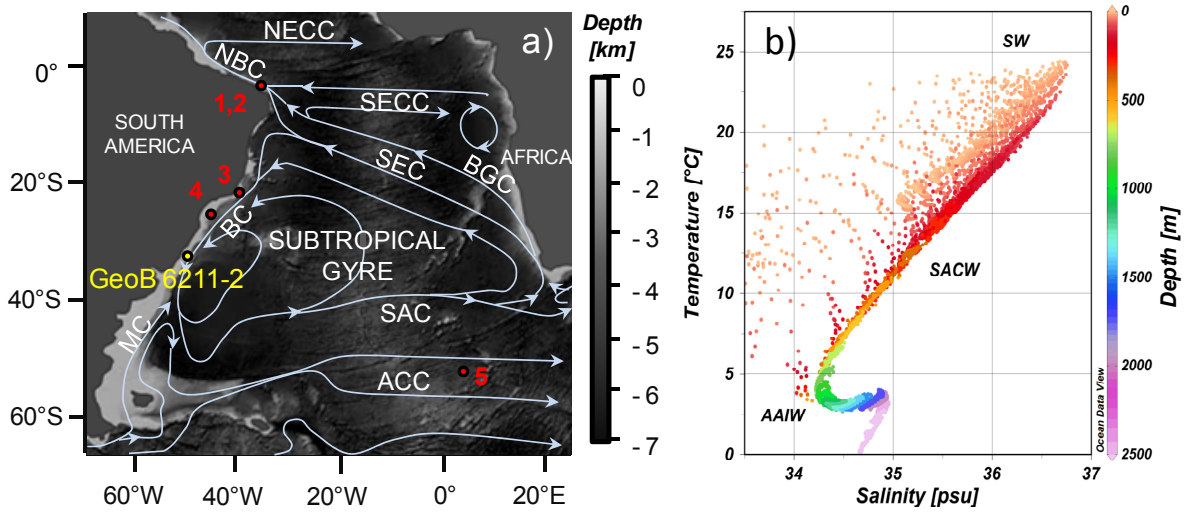

Fig. 3.1. Study area with the location of the investigated sediment core GeoB 6211-2. (a) Large scale circulation of the South Atlantic Ocean modified from Peterson and Stramma (1991: ACC – Antarctic Circumpolar Current; BC – Brazil Current; BGC – Benguela Current; MC – Malvinas Current; NBC – North Brazil Current; NECC – North Equatorial Counter Current; SAC – South Atlantic Current; SEC – South Equatorial Current; and SECC – South Equatorial Counter Current. Cited studies for environmental comparisons are presented as: **1.** GeoB 3129 / 3911 (Wedeab et al., 2006); **2.** GeoB 3910-2 (Jaeschke et al., 2007); **3.** GeoB 3202-1 (Arz et al., 1999); **4.** KNR159-5-36GGC (Pahnke et al., 2008); **5.** TN057-13 (Shemesh et al., 2002; Anderson et al., 2009). (b) Salinity vs. temperature vs. depth diagram at study site of GeoB 6211-2: AAIW – Antarctic Intermediate Water; SACW – South Atlantic Central Water; and SW – South Atlantic Surface Water.

Thus, the investigated core site at the Rio Grande Cone is under influence of the South Atlantic Central Water (SACW) and the Antarctic Intermediate Water (AAIW) (Fig. 3.1b). The SACW is composed of Light South Atlantic Central Water, the South Atlantic Subtropical Mode Water and the Subantarctic Mode Water (Stramma and England, 1999; Silveira et al., 2000; Donners et al., 2005), while it is driven by the southward-flowing Brazil Current from 22° S at depths between 150 m and the picnoclyne at 600–700 m. The SACW is characterized by temperatures of 6–20° C and salinities of 34.6–36.0 psu (Silveira et al., 2000). Currently, at water depths of 550 m around 32° S, contents of dissolved oxygen are ~4.6 ml l^{-1}, of nitrate ~20 µmol kg^{-1}, and of phosphate ~1.4 µmol kg^{-1} (Tsuchiya et al., 1994).

The AAIW flows below the SACW at sub-picnoclyne levels and reaches depths of up to 1400 m. The AAIW is formed in the eastern South Pacific and western South Atlantic sectors, in the realm of the Antarctic Circumpolar Current (Stramma and England, 1999; Silveira et al., 2000; Donners et al., 2005). At the western Atlantic margin around 28° S, it bifurcates and flows towards north and south. AAIW temperatures are between 2° and 6° C and salinities reach values of 34.2–34.6 psu (Silveira et al., 2000). Currently, at around 32° S and a depth of ~800 m, its content of dissolved oxygen is ~5.6 ml l^{-1}, of nitrate ~29 µmol kg^{-1}, and of phosphate ~1.8 µmol kg^{-1} (Tsuchiya et al., 1994).

3.4. Material and methods

3.4.1. Material

In this study, we investigate the marine gravity sediment core GeoB 6211-2, which was collected during the RV Meteor cruise M46/2 at the upper continental margin of the Rio Grande Cone off South Brazil (32° 30.31' S; 50° 14.56' W) from a water depth of 657 m (Schulz et al., 2001). The surface sediments at the core site are composed

of silty to clayey muds (Frenz et al., 2003; Castilho et al., 2009). In contrast to other sites off South Brazil and Uruguay (Frenz et al., 2003), this core shows an exceptionally good calcium-carbonate preservation, allowing the establishment of a ^{14}C AMS age-depth model.

The seemingly continuous and undisturbed gravity core is 7.74 m long and reaches the Last Glacial Maximum at its base (Chiessi et al., 2008, 2009). The core's uppermost sediments consist of olive-gray clayey to fine sandy muds, resembling the grain sizes of the surface sediments investigated by Frenz et al. (2003) at the Rio Grande Cone. Since the outer and inner continental shelf off South Brazil mainly contains coarser sediments being deficient in the fine fraction (Urien and Ewing, 1974), we assume that the investigated sediment core fits in a regional context and is therefore representative for the paleoenvironmental conditions at the Rio Grande Cone.

Here, we focus on the time sequence 19.1–13.9 cal kyr BP (123–573 cm), corresponding to the Last Deglaciation. The respective sediment is composed of light reddish, slightly laminated clayey silts. The age-depth model for the whole sediment core and the derived sedimentation rates (8–246 cm kyr^{-1}) used in this study (Fig. 3.2a) were obtained from Chiessi et al. (2008, 2009) and Razik et al. (2013).

3.4.2. Methods

3.4.2.1. Benthic Foraminiferal Assemblage analysis

BFAs were analyzed from 45 samples, which were taken every 10 cm core depth. One gram of dry sediment was removed from each sample and washed over a set of sieves with aperture sizes of 63 and 125 µm following Schröder et al. (1987). Material of both obtained grain-size fractions was dried and analyzed. More than 200 benthic foraminiferal tests were picked from each sample using a ZEISS STEMI SV11 microscope. Where necessary, the samples were quartered until the number of ~200 specimens was reached.

Scanning electron microscopy was performed to aid the taxonomic identification and visualization of the taphonomical processes, which cause test alteration. The picked specimens were identified using the procedures of Loeblich and Tappan (1964, 1988), Boltovskoy et al. (1980), and the World Modern Foraminifera Database. BFAs were subdivided according to their paleoenvironmental indications (e.g., Murray, 1991; Baas et al., 1998; Badawi et al., 2005; Duleba et al., 2005; Langezaal et al., 2006; Basak et al., 2009) and distinct microhabitats; i.e., into 'epifauna' living on ocean-floor sediments; 'infauna' living within ocean-floor sediments; and 'epifauna-infauna' capable of living in both environments. The taphonomical analyses classified the samples by their color and their fragmentation grades (Mayklem, 1967; Brett and Baird, 1986; Martin and Lidell, 1991; Duleba, 1994): 'white' without color alteration; 'golden' impregnated with iron sulfide (FeS_2); 'black' impregnated with iron monosulfide (FeS); and 'brownish' impregnated with lepidocrocite (γ-FeO(OH)). On the fragmentation scale, the samples were classified as: unidentifiable 'fragments'; 'partially fragmented' (classified at least at the genus level, but with some *post mortem* alteration such as abrasion, bioerosion, corrosion, and/or dissolution); or 'whole' with no *post mortem* alterations affecting the external structure.

The BFAs were grouped into categories defined as: 'dominant' representing >50% of the sample; 'subdominant' representing 25–49%; 'accessory'

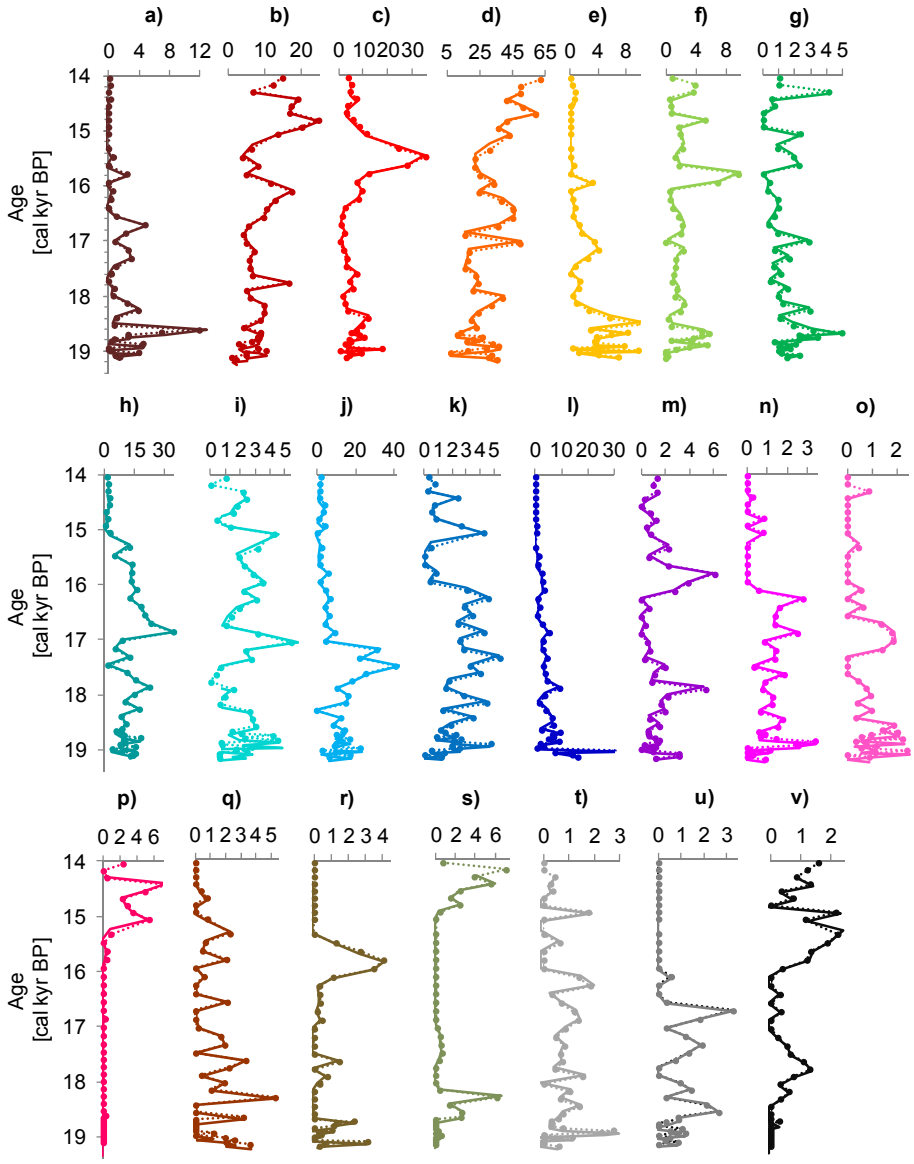

Fig. 3.2. Abundances of the main species found in the time sequence 19–14 cal kyr BP of the sediment core GeoB 6211-2. Dominant species are: (a) *Bolivininellina translucens*; (b) *Bulimina elongate*; (c) *Bulimina marginata*; (d) *Brizalina subaenariensis*; (e) *Fursenkoina pontoni*; (f) *Globobulimina pacifica*; (g) *Globocassidulina crassa*; (h) *Nonionella atlantica*; (i) *Nonionella opima*; (j) *Nonionoides grateloupi*; (k) *Quinqueloculina atlantica*; (l) *Rutherfordoides rotundiformis*; (m) *Uvigerina bifurcada*. Subdominant species are: (n) *Adelosina laevigata*; (o) *Buliminella elegantissima*; (p) *Cassidulinoides brasiliensis*; (q) *Fursenkoina sp.*; (r) *Melonis barleeanus*; (s) *Nonionellina labradorica*; (t) *Quinqueloculina milletti*; (u) *Stainforhia concave*; (v) *Uvigerina peregrina*. Data are displayed as dashed lines with dots. Three-point running averages are shown as solid lines.

representing 5–25%; and 'rare' being <5%. These relative abundances of 'dominant' and 'subdominant' species formed the numerical base for the statistical R-mode (species vs. species) cluster analysis. The Euclidean distance method and Ward's method (Everitt et al., 2011) were applied to the 22 most abundant species using Minitab 15 software for Windows.

For identification of BFA structure changes, the following parameters were calculated: density (number of specimens per 1 g dry sediment), the richness (number of species per specimen), the Jouli Evenness (J'; from Pielou, 1969) and the Shannon-Wiener (or -Weaver) Diversity indices (H'; from Shannon and Weaver, 1949). The BFA Rate index (BFAR, from Herguera and Berger, 1991) was calculated to determine whether

changes in sedimentation rates affect the test accumulation.

All obtained specimens were measured using AnaliSys software and the samples were grouped into fractions called 'small' (<125 µm), 'medium' (125–250 µm), 'large' (250–500 µm) and 'macro' (>500 µm) using the granulometric table of Wentworth (1922). In this way, juvenile forms could be excluded from paleoenvironmental interpretation.

3.4.2.2. Carbon isotope analysis

The $\delta^{13}C$ values were measured on specimens of *Globigerinoides ruber* (white, *stricto sensu*, 250–350 µm) using a Finnigan MAT 252 mass spectrometer equipped with an automatic carbonate preparation device at the *University of Bremen (Germany)*. The standard deviation of the laboratory standard was 0.05‰. The results are expressed as the ‰ deviation from the Vienna Pee Dee Belemnite (VPDB) standard, as calibrated by NBS 18, 19, and 20 standards.

3.4.2.3. Grain-size analysis of terrigenous fraction

The grain-size distributions of the terrigenous sediment fraction were detected by laser-particle sizing. Samples of 2–4 g were consecutively treated with 10 ml H_2O_2 (35%$_{v/v}$), 10 ml HCl (10%$_{v/v}$), and 6 g NaOH-pellets in 100 ml aquatic solutions as described by Mulitza et al. (2008), to chemically remove organic carbon, calcium carbonate ($CaCO_3$) and biogenic opal. Between every chemical reaction, samples were washed with demineralized water. To avoid aggregate formation of clay minerals, ~300 mg of $Na_4P_2O_7 \cdot 10(H_2O)$ were added to the sediment solutions before analysis.

The grain-size analyses were performed using a BECKMANN-COULTER LS200 laser particle sizer coupled to a water demineralization and degassing device at the *MARUM – Center for Marine Environmental Sciences in Bremen (Germany)*. The grain-size detection range of this equipment is specified as 0.04–2000 µm, but due to pre-treatment of the sediment and its settling properties, distributions of particles ≤2 µm should be considered with care. To process the data, the BECKMANN-COULTER Particle Characterization software v. 3.01 was used. Calculation of parameters derived from grain-size distributions (skewness, kurtosis, sorting, sortable silt, mean, median, mode value, and silt/clay) were performed after Tucker (1996) and McCave (2008).

3.5. Results

We identified 98 species of benthic foraminifera belonging to 49 different genera in the analyzed samples. Due to the broad range of species, we decided to show only the most dominant 22 species (Fig. 3.2a–v). In the following (Figs. 3.4–3.8), we present BFA cluster analysis and calculated parameters like $\delta^{13}C$, specimen density, as well as J' and H' indices. They were taken into joint consideration with paleoenvironmental indicators of microhabitat, oxygenation rate and organic matter (O.M.) accumulation in the sediments, as well as with morphometric characteristics and taphonomical features, respective color and fragmentation gradations. To strengthen the insights based on proxies representing the marine sediment fraction, we show granulometric properties of the terrigenous fraction (Fig. 3.9), which carry information about hydrodynamic energies of the bottom waters. This enables grouping of the investigated time sequence into five phases with respect to subsequent interpretation: (i) phase 1 at 19–18.6 cal kyr BP; (ii) phase 2 at 18.6–17 cal kyr BP; (iii) phase 3 at 17–16 cal kyr BP;

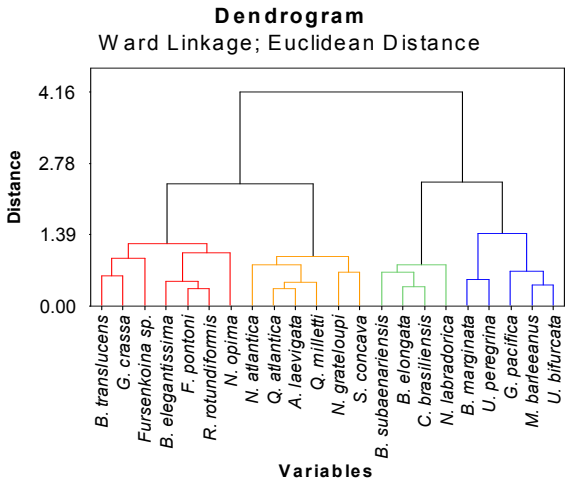

Fig. 3.3. Dendogram of statistical cluster R-mode analysis based on 22 main benthic foraminiferal species found in sediment core GeoB 6211-2 between 19 and 14 cal kyr BP.

(iv) phase 4 at 16–14.7 cal kyr BP; and (v) phase 5 after 14.7 cal kyr BP.

3.5.1. Identification of Benthic Foraminiferal Assemblages

Statistical R-mode cluster analysis of benthic foraminiferal species (Fig. 3.2) was performed to obtain an objective grouping of the most significant assemblages. The obtained results (Fig. 3.3) are divided into four distinct assemblages, which show different prevalence in dependence with time (Fig. 3.4; Table 3.1). Assemblage 1 is most dominant (30–50%) during phase 1 and it decreases until phase 5 (5–10%). Assemblage 2 is most dominant during phase 2 (30–50%), while its abundance decreases towards phase 1 (~5%). Assemblage 3 reaches maximum values during phase 5 (70–80%) with a local maximum (~55%) in the mid of phase 3. During phases 1, 2, and 4, the abundances are ~30%. Assemblage 4 has its most dominant appearance (~40%) at the mid of phase 4 and reaches a minor maximum (16–26%) at the beginning of phase 2. In all other phases, the values are around 8–15%.

The test densities (Fig. 3.5b) are highest during phase 5, reaching values of 7000 tests g^{-1}. During earlier phases (19–15 cal kyr BP), they show slightly increasing, but relatively low densities (<2500 tests g^{-1}). These densities are not influenced by the sedimentation rates (Fig. 3.5a) as can be seen in the BFARs (Fig. 3.5c). The only exception is found at ~19 cal kyr BP (phase 1), as there occurs an increase in the BFAR due to significantly higher sedimentation rates (~246 cm kyr^{-1}) than during all other phases (8–82 cm kyr^{-1}).

The richness of species per sample during phase 1 (Fig. 3.5d) is characterized by a steep increase of values from 23 to 30. During phase 2, the richness shows the most expressed undulations from almost the minimum (24) to the maximum value (33). Phase 3 shows a slight richness decrease, while a minimum of 23 is reached at the center of phase 4. Phase 5 shows a slight richness increase from 27 to 30.

J' (Fig. 3.5d) and H' (Fig. 3.5e) show similar trends throughout the investigated sedimentary sequence. Phase 1 is characterized by a steep increase in both values and by their maxima. During phase 2, J' reaches a 'plateau' around 0.7, while H' shows a slight undulation between 2.2 and 2.5. In the mid of phase 3, both parameters show a minimum, reaching again a local maximum value at the beginning of phase 4. During phase 4, a slight decrease occurs, while slight undulations follow during phase 5 with no evident long-term trend.

3.5.2. BFA properties indicative for paleoenvironmental conditions

The $\delta^{13}C$ values of the planktonic foraminifera *Globigerinoides ruber* are lowest (0.15–0.3) during phase 2 (Fig. 3.6g), being indicative for lower marine primary productivity in the ocean surface water. During other phases, the $\delta^{13}C$ values are higher, slightly undulating around 0.4.

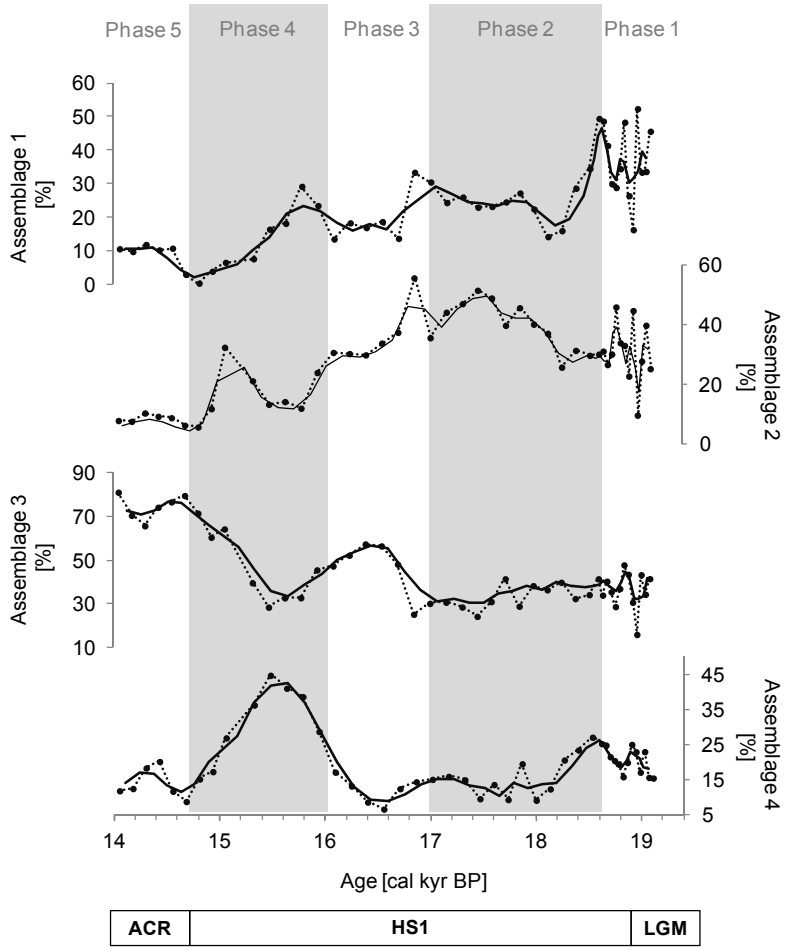

Fig. 3.4. Distinct benthic foraminiferal assemblage (BFA) derived from statistical cluster R-mode analysis (displayed in Fig. 3.3) and expressed as a percentage relative to total frequency of fauna per sample. The two vertical bars indicate five distinct paleoenvironmental phases. The horizontal bar divides the events Last Glacial Maximum (LGM), Heinrich Stadial 1 (HS1) and Antarctic Cold Reversal (ACR) as indicated in literature (e.g., Bard et al., 2000; Köhler et al., 2011; Stanford et al., 2011). Data are shown as dashed lines with dots. Three-point running averages are visualized by solid lines.

Relative abundances of BFAs defined as 'infauna' (e.g., *Globobulimina pacifica*), 'epifauna' (e.g., *Eponides repandus*), and 'epifauna-infauna' (e.g., *Brizalina subaenariensis*) are displayed in Fig. 3.6h. While the abundances of epifaunal BFA (0–10%) stay rather constant with time, the infaunal and the epifauna-infaunal BFA abundances stay relatively constant (both 35–50%) only during phases 1 and 2. During phase 3, the epifauna-infaunal BFAs continuously increase, reaching abundances of nearly 80% during phase 5. Simultaneously, the infaunal BFA abundances decrease, reaching minima of 10–20% during phase 5.

The Benthic Foraminifer High Productivity (BFHP) index (Fig. 3.6i) shows overall high values for the entire investigated sedimentary sequence. The BFHP index minima (~73%) during phase 1 increase and reach maxima (~93%) during phase 5.

The Benthic Foraminiferal Oxygen Index (BFOI) (Fig. 3.6j) shows main positive peaks (~8) at 18.8, 17.4, and 15 cal kyr BP. Besides those peaks, the BFOI mainly remains between 4 and 6. The lowest values (~2) are reached at ~19 and 16–15.3 cal kyr BP and during phase 5. Accordingly to the classification of Baas et al. (1998), the high values are indicative of an

Table 3.1.

Benthic Foraminiferal Assemblages (BFAs) valid for time sequence between 19 and 14 cal kyr BP of sediment core GeoB 6211-2 used as paleoenvironmental indicators based on main species and their characteristics according to Boltovskoy (1959), Corliss (1985), Caralp (1989), Murray (1991), Alve and Bernhard (1995), Jorissen et al. (1995), Thomas et al. (1995), Harloff and Mackensen (1996), Baas et al. (1998), Moodley et al. (1998), De Rijk et al. (2000), Kennet et al. (2000), Mercone et al. (2001), Fontanier et al. (2002), Kaminski et al. (2002), Polyzaak et al. (2002), Guilbault et al. (2003), Licari et al. (2003), Osterman (2003), Scott et al. (2003), Girardeau et al. (2004), Martins et al. (2004), Badawi et al. (2005), Duleba et al. (2005), Eberwein and Mackensen (2006), Langezaal et al. (2006), Sousa et al. (2006), Thibodeau et al. (2006), Martins et al. (2006, 2007), Kuhnt et al. (2007), Diz and Francés (2008), Eichler et al. (2008), Koho et al. (2008), Pascual et al. (2008), Riveiros and Patterson (2009), Basak et al. (2009), Milker et al. (2009), De and Gupta (2010), Zarries and Mackensen (2010), McCarthy (2011), and Van Hengstum and Scott (2011).

Assemblages	Main occurrence phases	Main species (Dominants and subdominants)	Secondary species (Accessories and rare)	Main characteristics of most important species
1	Between 19 and 18,6 cal kyr B.P., between ~18 and ~17 cal kyr B.P. and at ~16 cal kyr B.P.	*Bolivinellina translucens, Buliminella elegantissima, Globocassidulina crassa, Fursenkoina pontoni, Nonionella opima e Rutherfordoides rotundiformis*	*Bucella peruviana, Cancris sagra, Cibicides* spp., *Eponides repandus, Fissurina* spp., *Globocassidulina subglobosa, Lagena* spp., *Quinqueloculina lamarckiana, Quinqueloculina seminula, Pyrgo* spp., *Rosalina williamsoni, Uvigerina peregrina* and *Uvigerina striata*	Dysoxic, indicative of an environment with high O.M. accumulation, detritivorous, with precominance of epifauna-infauna species, proxies of fine sandy to muddy sediments. *R. rotundiformis* and *G. crassa* indicate cold waters. *G. crassa* is a *proxy* for the Malvinas Current. *B. translucens* and *N. opima* of stratified waters. *N. opima* is tolerant to anoxia. *B. elegantissima* indicates lower hydrodynamic energy of the environment.
2	Between 19 and ~16 cal kyr B.P. and at ~15 cal kyr B.P.	*Adelosina laevigata, Nonionella atlantica, Nonionoides grateloupi, Quinqueloculina atlantica, Quinqueloculina milletti* e *Stainforthia concava*	*Bolivina alata, Bucella peruviana, Cancris sagra, Cassidulina* spp., *Cibicides* spp., *Discorbis* spp., *Eponides repandus, Globocassidulina* spp., *Melonis barleeanus, Oolina* spp., *Poroeponides lateralis, Pseudononion pulchella, Pyrgo nasuta, Pyrgo ringens, Quinqueloculina lamarckiana, Quinqueloculina patagonica, Quinqueloculina seminula, Rubratella intermédia* and *Uvigerina* spp.	Species divided into 2 groups: i) infaunal, typical of high O.M. content and lower oxygenation rate of the environment, detritivorous or herbivorous, *proxies* of muddy sediments and lower hydrodynamic energy. ii) epifaunal, typical of high oxygenation rate of the environment and lower O.M. content, predominantly herbivorous, *proxies* of waters less stratified, with higher hydrodynamic energy. *N. atlantica* indicates hypoxia. *A. laevigata* can survive in a dysoxic environment with high O.M. contents. *Q. atlantica* and *Q. milleti* are intolerant to dysoxia. *S. concava* exists in sediments with high nitrogen and organic carbon contents and indicates cold waters (~3.4°C) and salinity of ~34.4‰.
3	Between ~17 and ~16 cal kyr B.P. and between ~15 and ~14 cal kyr B.P.	*Brizalina subaenariensis, Bulimina elongata, Cassidulinoides brasiliensis* e *Nonionellina labradorica*	*Bolivinellina translucens, Buliminella elegantissima, Cancris sagra, Cassidulina* spp., *Cibicides dispars, Cibicides kullenbergi, Cibicides refulgens, Eponides repandus, Fissurina* spp., *Gyroidina* spp., *Haynesina* spp., *Hopkinsina pacifica, Lagena* spp., *Lenticulina* spp., *Lobatula lobatula, Nonionella auris, Oridorsalis umbonatus, Rosalina williamsoni, Sigmoilopsis schlumbergeri* anc *Uvigerina striata*	Indicative of environments with lower oxygen and high O.M. contents. Mainly detritivorous, with a preference for labile O.M. Typical of upwelling regions of cold to temperate waters and with fine sandy to muddy sediments. *B. subaenariensis* reacts to the phytodetritus bloom with rapid growth and indicates more stratified waters and the presence of H_2S in the environment. *B. elongata* feeds on more refractory O.M. and indicates a lower hydrodynamic energy gradient and muddy sediments. *N. labradorica* indicates cold waters and can survive the dysoxia.
4	Between ~16 and ~15 cal kyr B.P.	*Bulimina marginata, Globobulimina pacifica, Melonis barleeanus, Uvigerina bifurcata* e *Uvigerina peregrina*	*Bolivinellinaa translucens, Buliminella elegantissima, Cancris sagra, Cassidulina* spp., *Cassidulinoides brasiliensis, Cibicides* spp., *Eponides repandus, Fissurina lucida, Fursenkoina pontoni, Globocassidulina* spp., *Gyroidina altiformis, Haynesina depressula, Hopkinsina pacifica, Lagena* spp., *lenticulina* spp., *Nonionella* spp., *Oridorsalis umbonatus, Pseudononion depressulum, Pseudononion pulchella, Quinqueloculina patagonica, Rosalina williamsoni, Sigmoilopsis schlumbergeri* anc *Uvigerina striata*	Typical of high O.M. contents and lower oxygenation rate in the environment. Mainly detritivorous, with a predominance of shallower infauna but able to occupy epifaunal niches if necessary. Typical of muddy sand to muddy sediments. *B. marginata* and *U. peregrina* indicate oxygen minimum zone. *B. marginata* recolonizes anoxic environments slowly, prefers labile O.M., is stenohaline and is related to La Plata River plume. It is typical of cold and stratified waters. *G. pacifica* and *M. barleeanus* indicate nitrate reduction zone. *G. pacifica* is medium to deep infaunal and indicates cold to temperate waters. *M. barleeanus* feeds on more refractory O.M. and is linked to denitrifying bacteria, to muddy sediments and to cold waters. *U. bifurcata* indicates high oceanic primary productivity and is typical of the AAIW and Malvinas Current. *U. peregrina* is favored by sedimentary carbon and indicates nutrients transported by the SACW. It tolerates more refractory concitions than O.M.

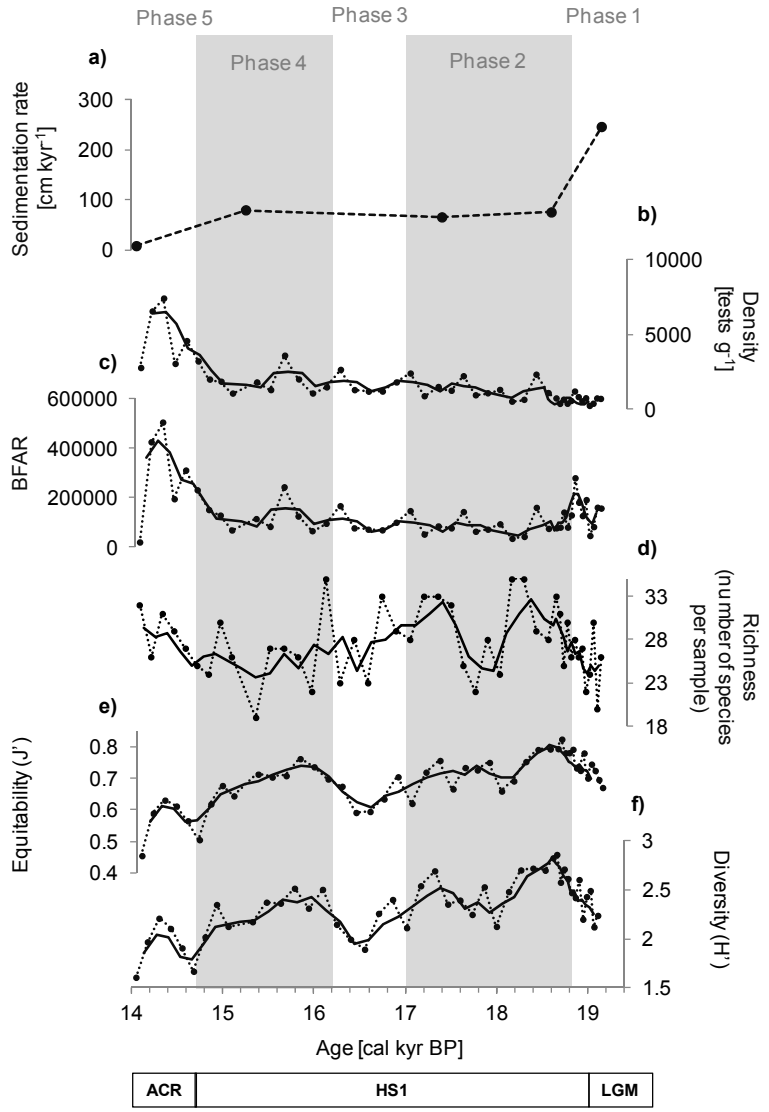

Fig. 3.5. Derived parameters from BFA data sets of the GeoB 6211-2 time sequence 19–14 cal kyr BP: (a) sedimentation rates; (b) tests density; (c) Benthic Foraminiferal Accumulation Rate (BFAR) index; (d) richness of species; (e) Pielou Equitability J'; and (f) Shannon-Wiener diversity H'. The two vertical bars indicate five paleoenvironmental phases defined as in Fig. 3.4. Obtained data are shown as dashed lines with dots. Three-point running averages are visualized by solid lines.

environment in which the dissolved oxygen content is high (>1.5 ml l^{-1} of O_2). Although the general trends of BFOI and BFHP appear to show no visible similarity, on the short-term basis increased oxygenation rate of the environment is inversely related to the O.M. accumulation in the Rio Grande Cone sediments. This indicates that the preservation of sedimentary O.M. decreased during conditions with higher oxygenation rates (Fig. 3.6i,j).

Specimens of the 'large' size (250–500 µm) are most common throughout the investigated sequence, reaching abundances of 30–60%. The maximum values are found at the mid of phase 2 (17.8 cal kyr BP) and during phase 4. 'Macro' is the second most common size (>500 µm) with values between 5% and 35%. Relatively high prevalence of 22–35% is reached during all phases except the minima at beginning of phase 2 and at the mid of phase 4. The 'small' size ranges also from 5% to 35%. However, it reaches maxima (>22%) just at 19–18 cal kyr BP and at 17.4–16.8 cal kyr BP. The at least abundant "medium" size reaches values of 0–20%.

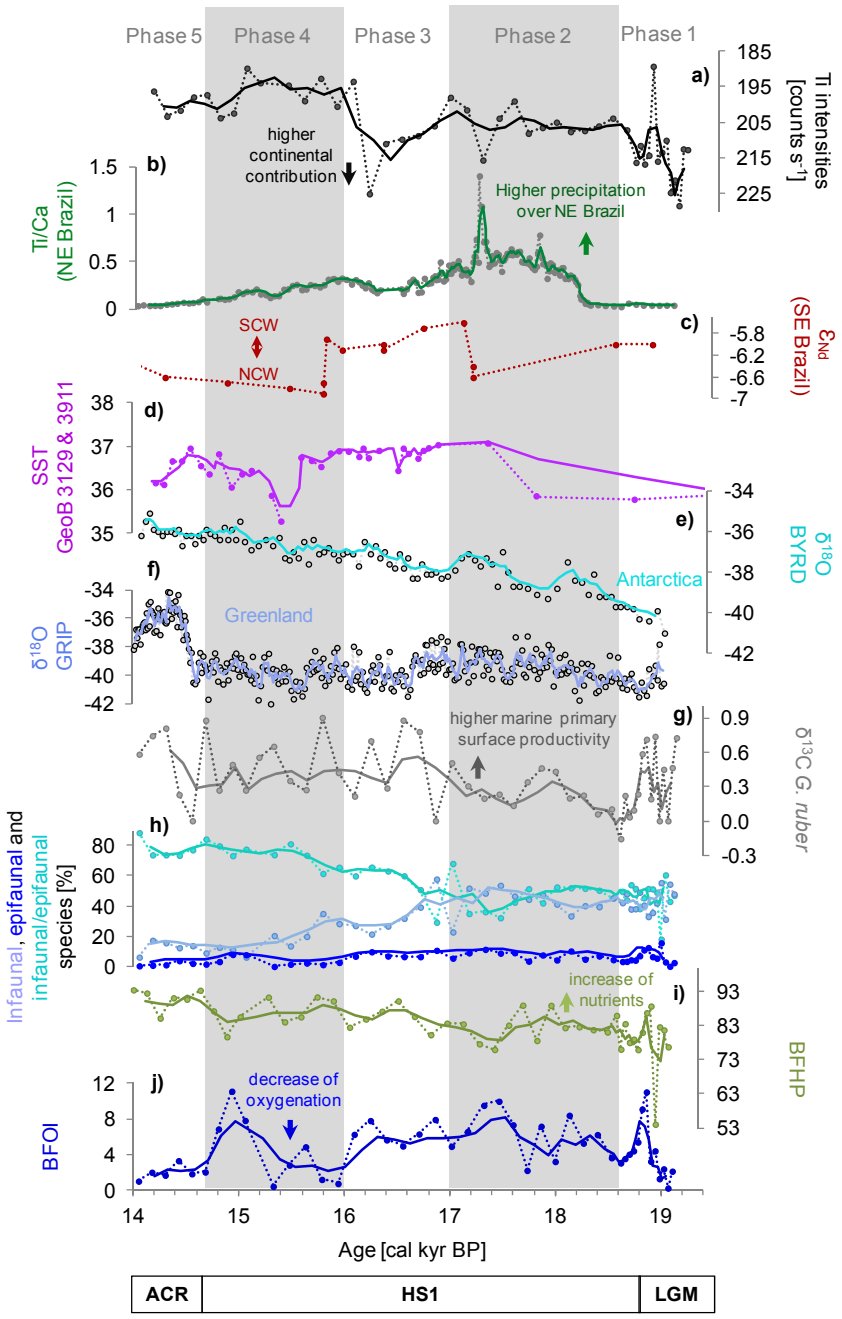

Fig. 3.6. Paleoclimatic changes between 19 and 14 cal kyr BP: (a) Titanium element intensity from core GeoB 6211-2 (Chiessi et al., 2009); (b) Ti/Ca ratio from core GeoB 3910-2 (Jaeschke et al., 2007); (c) ε_{Nd} from core KRN159-5-36GGC as proxy for Southern Component Water (SCW) and Northern Component Water (NCW) (Pahnke et al., 2008); (d) Sea-Surface Temperatures (SST) from cores GeoB 3129 / 3911 (Weldeab et al., 2006); (e) $\delta^{18}O$ from BYRD ice core (Blunier and Brook, 2001); (f) $\delta^{18}O$ from the NGRIP ice core (Blunier and Brook, 2001); (g) $\delta^{13}C$ of G. ruber from core GeoB 6211-2; (h) benthic foraminiferal species of epifauna, infauna, and epifauna-infauna from core GeoB 6211-2; (i) Benthic Foraminifer High Productivity (BFHP) index; and (j) Benthic Foraminiferal Oxygen Index (BFOI) derived from BFAs of core GeoB 6211-2, respectively. The two vertical bars indicate five paleoenvironmental phases defined as in Fig. 3.4. Obtained data are shown as dashed lines with dots. Three-point running averages are visualized as solid lines.

The maxima are found at 18.6–18.2 cal kyr BP and at 15.6–14.6 cal kyr BP.

White specimens (Fig. 3.7b) prevail throughout the analyzed period with values of 45–75%. They reach their maxima of 65–75% during phase 4. Golden specimens (impregnated with FeS_2), which are indicative of a highly reducing environment, reach abundances of 18–50%.

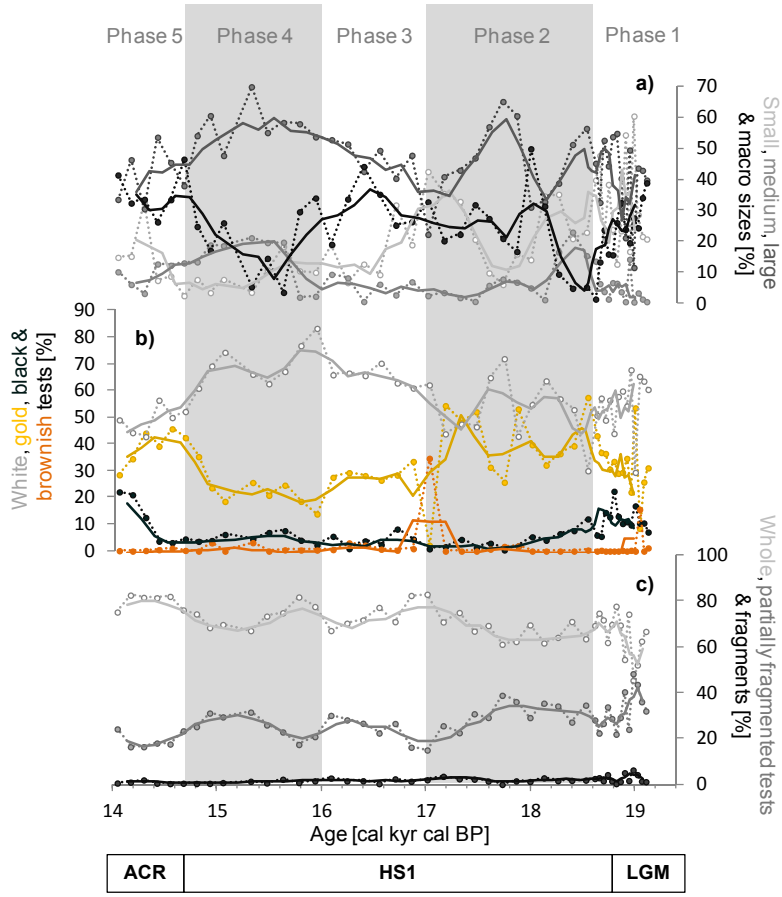

Fig. 3.7. Morphometric and taphonomic parameters derived from BFA data sets for time sequence 19–14 cal kyr BP of core GeoB 6211-2: (a) morphometry of samples; (b) colors of samples; and (c) fragmentation grades of samples. The two vertical bars indicate five paleoenvironmental phases defined as in Fig. 3.4. Obtained data are shown as dashed lines with dots. Three-point running averages are visualized by solid lines.

Values >30% are reached only during phase 2 and phase 5. Black specimens (impregnated with FeS; also indicative of reducing environment) lie between 0% and 18%, while they are significantly present only during phase 1 and during the second half of phase 5. Brownish specimens, which are indicative of oxidizing environments, occur only at beginning of phase 1 (~19 cal kyr BP) and at approximately the boundary between phase 2 and phase 3 (~17 cal kyr BP) (Fig. 3.7b). The latter are available as just two samples and occur during phases of low oxygenation rates (Fig. 3.6j). Thus, we can treat them as not meaningful and exclude them from subsequent interpretation.

3.5.3. BFA properties indicative for water current energies

Whole specimens (50–80%) prevailed throughout the studied time interval (Fig. 3.7c). Fragment frequency was very low (<2%) throughout the investigated core sequence (Fig. 3.7c). Both indicates that the analyzed BFA were not modified or not significantly compromised by wear or specimen transport and thus are interpretable in a paleoecological context. The frequencies of partially fragmented specimens (18–42%) undulate continuously with positive peaks at ~19, ~17.8, ~16.4, and ~15.8 cal kyr BP. These peaks are indicative of environments with greater stress. The analysis of SEM images (Fig. 3.8) enabled us to distinguish processes of abrasion (predominant), biotur-

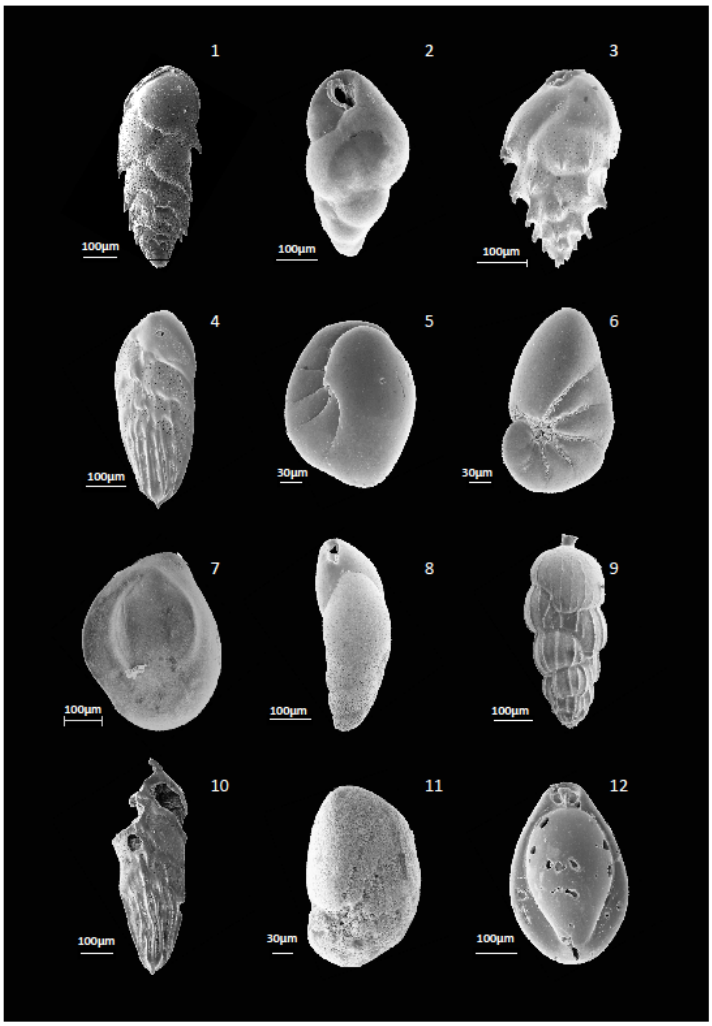

Fig. 3.8. Scanning Electron Microscopy images of benthic foraminiferal species found between 19 and 14 cal kyr BP of sediment core GeoB 6211-2. Shown are well preserved taphonomical examples and such being affected by postdepositional and diagenetic processes due to abrasion, corrosion, and bioturbation: **1.** *Bolivina alata*; **2.** *Bulimina elongata*; **3.** *Bulimina marginata*; **4.** *Brizalina subaenariensis*; **5.** *Nonionella opima*; **6.** *Nonionoides grateloupi*; **7.** *Quinqueloculina lamarckiana*; **8.** *Rutherfordoides rotundiformis*; **9.** *Uvigerina bifurcata*; **10.** *Brizalina subaenariensis* affected by abrasion and corrosion/dissolution; **11.** *Nonion sp.* affected by corrosion and/or dissolution; and **12.** *Pyrgo nasuta* affected by bioerosion and corrosion/dissolution.

bation and corrosion in partially fragmented tests. This leads to suggestions that most of the wear experienced on benthic foraminifera was caused by the increased hydrodynamic energy of bottom waters at the Rio Grande Cone.

3.5.4. Grain-size properties of the terrigenous fraction

Throughout the investigated sequence, the sand contents (Fig. 3.9a) show relatively low variations (2–15%) with time if compared with silt (55–75%) and clay (20–40%). During phases 1, 2, 3, and 5, the sand contents mainly lie between 5–10%. Phase 4 is characterized by highest changes in sand content from minima during its first half to maxima during its second half. Highest silt contents are found during phase 2, while the lowest are characteristic for phase 4. The clay contents show the inverted silt signal with minima during phase 2 and maxima during phase 4.

Silt maxima and clay minima cause the fine skewed signal (Fig. 3.9b) during phase 2. The

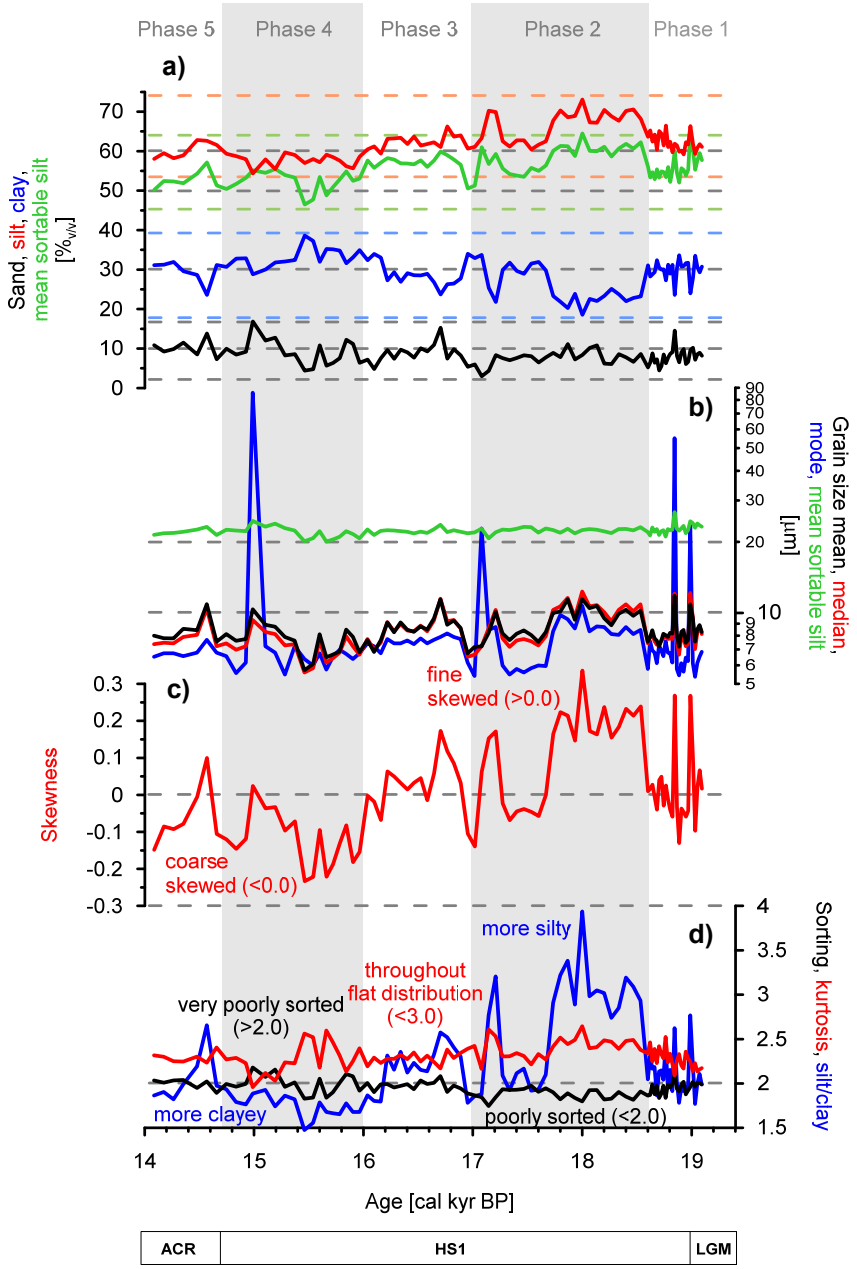

Fig. 3.9. Granulometric parameters of the terrigenous fraction for the time sequence 19–14 cal kyr BP of sediment core GeoB 6211-2: (a) concentrations of sand, silt (as well as sortable silt; 10–63 µm) and clay contents; (b) Grain size mean, median, and mode values, as well as mean sortable silt; (c) skewness; and (d) sorting, kurtosis, and slit/clay ratio. The two vertical bars indicate five paleoenvironmental phases defined as in Fig. 3.4.

contrary relation of silt to clay during phase 4 (Fig. 3.9a) is thus marked by a coarse skewed signal. The skewness trend is well resembled by the relation of silt/clay values (Fig. 3.9d). As the sortable silt concentrations (Fig. 3.9a) resemble the trend of the silt concentrations with no significant variations in the sortable-silt grain size (Fig. 3.9b), we deduce that changes in silt/clay values are mainly caused by changes in the clay content, while silt contents stay relatively constant. The decrease in clay content during phase 2 is further seen in the narrowing of the grain-size distributions, leading to a slightly better sorting (Fig. 3.9d) in contrast to phase 4.

As already mentioned for the mean, median and mode values, the higher clay contents during the second half of phase 4 are masked by the simultaneous input of sands. This leads to the

broadest distribution curve throughout the investtigated sediment sequence (kurtosis; Fig. 3.9d), very poor sorting and a change from coarse skewed to a normal distribution (Fig. 3.9c).

3.6. Discussion

During almost the entire period between 18.4 and 14.8 cal kyr BP (phases 2–4) at the Rio Grande Cone, high oxygenation rates (Fig. 3.6j) were accompanied by intensity changes in the AMOC (Stanford et al., 2011); while the Brazil Current experienced changes in hydrodynamics (Arz et al., 1999), the AAIW underwent changes in its formation process (Pahnke et al., 2008). Due to lower AMOC intensities between ~18.4 and 16.4 cal kyr BP (during phases 2–3), rainfall increased at the NE Brazilian margin (Fig. 3.6b) and at 17.4–14.8 cal kyr BP this also happened to sea-surface temperature as well as salinity (Fig. 3.6d) (Weldeab et al., 2006; Jaeschke et al., 2007). Exceptionally low oxygenation rates are found at 16–15.3 cal kyr BP (first half of phase 4), being connected to a drop in sea-surface temperatures at the NE Brazilian margin (Fig. 3.6d).

We suggest that phases of higher oxygenation rates in the Rio Grande Cone environment between 18.4 and 16 cal kyr BP (phases 2–3) were linked to a reduced AMOC (Bard et al., 2000; Stanford et al., 2006). With a reduced AMOC and lower NADW formation (Stanford et al., 2011), the strength and extension of the AAIW increased at intermediate depths of the Atlantic Ocean (Pahnke et al., 2008). Simultaneously, the Brazil Current intensity increased due to strengthening of the northeasterly trade winds, which in contrast weakened the North Brazilian Current (Arz et al., 1999). However, the substantial decrease in oxygenation rates (16–15.3 cal kyr BP) (Fig. 3.6j) during phase 4 was most likely linked to the AMOC restructuring (Stanford et al., 2011). On the one hand, the strengthened AMOC, and thus the intensified interhemispheric water-mass transport, together with weaker austral trade winds weakened the Brazil Current (Arz et al., 1999; Weldeab et al., 2006). On the other hand, at more or less the same time (15.3–15 cal kyr BP) there occurred the set-in of the Agulhas Leakage (Chiessi et al., 2009). This led to a change of chemo-physical signatures of the Atlantic intermediate waters and to increased hydrodynamics, including those of the Brazil Current (Chiessi et al., 2008). Pahnke et al. (2008) detected a decrease in the AAIW contribution at the SE Brazilian continental margin between 15.7 and 14.2 cal kyr BP (Fig. 3.6c).

This scenario bases upon three hypotheses, which are linked to each other and can be deduced as follows: The proposed hypothesis for increased oxygenation on the basis of strengthened northeasterly trade winds during HS1 (i.e., phases 2 and 3) is corroborated by findings of Arz et al. (1999). Consequently, the considered Brazil Current fortification most likely resulted in an increased hydrodynamic energy at the Rio Grande Cone. This scenario, leading to a greater environmental instability, can be verified by higher BFA diversities and higher amounts of mechanically damaged shells (Figs. 3.5d,e and 3.7c). In particular during the oxygenation maximum at 17.5–17.2 cal kyr BP, the Rio Grande Cone received temporarily high amounts of terrigenous silts (Fig. 3.9a), as detected by grain-size modes changing form 6 µm to 20 µm (Fig. 3.9b). But also relatively high clay contents could be deposited. This temporal coarsening led to poorer sorting and decrease of the kurtosis (Fig. 3.9d). In contrast (e.g., first half of phase 4), higher clay concentrations (Fig. 3.9a) are available during phases of lower oxygenation rates (Fig. 3.6j) and of better BFA shell preservation

(Fig. 3.7c), pointing to lower hydrodynamic energies. Higher hydrodynamic energy does not just have greater capacity to increase the oxygenation rate, but also to transport larger quantities of relatively light O.M. particles in the water column, thereby leaving the Rio Grande Cone with lower nutrition contents (Fig. 3.6i). The lower deposition of O.M. during phases 2 and 3 is further accompanied by low clay contents and thus high silt/clay values (Figs. 3.9a,d). Especially at the oxidation maximum around 17.4 cal kyr BP, higher oxygenation rates are clearly linked to drops in marine primary productivity at the ocean surface (Fig. 3.6g), confirming the increased influence of the warm and saline Brazil Current.

The second hypothesis regarding higher oxygenation rates during phases 2–4 bases on increased ventilation of the SACW already during its formation process. Stramma and England (1999) and Donners et al. (2005) considered that the SACW was partly composed of Subantarctic Mode Water *and* partly of water masses linked to the Agulhas Current, as well as to the Brazil Current (i.e., Light South Atlantic Central Water and South Atlantic Subtropical Mode Water). As the Subantarctic Mode Water was partially formed by subduction of shallow waters at the Subantarctic Front of the southern circumpolar region (Donners et al., 2005), the stronger upwelling of circumpolar waters during HS1 may have caused its already initially higher ventilation during phases 2 and 3 (Anderson et al., 2009). This second hypothesis, dealing with the already initially increased water ventilation, explains also very well the oxygenation peak at the initialization of the Agulhas Leakage at ~15 cal kyr BP (e.g., Chiessi et al., 2009). At this time, the water masses contributing to the formation of the SACW in the tropical South Atlantic (Stramma and England, 1999; Donners et al., 2005) most likely had changed the SACW chemo-physical signature. The renewed ventilation at the Rio Grande Cone due to the strengthened contribution of the Agulhas Current and the restructuring of the AMOC (weakening of the Brazil Current) during phase 4 can be followed by increased clay deposition (Fig. 3.9a) and lower silt/clay values (Fig. 3.9d), as well as by a short-termed deposition of sands at the initialization of the Agulhas Leakage itself (Fig. 3.9b). Sands with mode values of 90 µm are expected to be derived from the adjacent upper continental slope, which were likely mobilized due to sea-level transgression.

A third hypothesis supposes that during phases 2–4 there was a shallowing of the boundary between the SACW and the AAIW. Hence, the more ventilated AAIW (Tsuchiya et al., 1994) would have increased the oxygenation rate at the Rio Grande Cone independently from any changes in hydrodynamic energy or independently from ventilation changes during Subantarctic Mode Water formation. Accordingly to Pahnke et al. (2008), intensified AAIW formation during HS1 could have led to larger volume and bathymetrical extension of the AAIW. Thus, it would have been able to reach higher latitudes of the Atlantic and to vertically displace the SACW.

At the Rio Grande Cone (~32° S), the AAIW recently flows southward after recirculation in the subtropical gyre (Stramma and England, 1999; Silveira et al., 2000). At this latitude, it is unclear whether the AAIW should be considered as part of the Brazil Current or of the Intermediate Western Boundary Current (Silveira et al., 2000). If we suppose that the AAIW is part of the Brazil Current, its HS1 strengthening (Arz et al., 1999) would also have influenced the transport of the AAIW and led to higher hydrodynamic energies. This phenomenon together with the intensified AAIW formation during HS1 would have kept this water mass even more oxygenated than solely by

the effect of the SACW. This scenario is capable to link hypothesis 3 to hypothesis 1 during phases 2–4. However, in particular hypothesis 2 remains valid for the second half of phase 4.

Currently, the mid slope of the Rio Grande Cone, slightly above the boundary of the AAIW, is mainly under the influence of the SACW (Tsuchiya et al., 1994; Chiessi et al., 2008). Between 18.6 and 17 cal kyr BP, the sea level was 120–130 m below the modern one accor-dingly to Lambeck and Chappell (2001). Although the respective regionnal water column structure still has to be evaluated for the oxygenation peak at ~19 cal kyr BP, Chiessi et al. (2008) suggested a stronger impact by the AAIW due to a shallower SACW–AAIW boundary than at modern conditions.

When age-model uncertainties are considered, BFA changes found throughout the five defined paleoenvironmental phases of the Last Deglaciation (Figs. 3.4, 3.5, 3.6g–j, and 3.7) suggest links towards the paleoclimatic variations of the Antarctic and Greenlandic regions (Fig. 3.6e–j).

3.6.1. Phase 1 (19–18.6 cal kyr BP)

Moodley et al. (1998) reported that the presence of *Bulliminella elegantissima* is an indicator for the existence of sedimentary hydrogen sulfide (H_2S). In sediments containing H_2S, FeS occurs when there was insufficient time for its transformation into pyrite (FeS_2) under reducing sedimentary conditions (Berner, 1970). In phase 1, the frequency of *B. elegantissima* (Fig. 3.2o) and higher quantities of FeS and FeS_2 (Fig. 3.7b) at the Rio Grande Cone support the above mentioned suggestion: On the one hand, these reducing sedimentary conditions in the deeper sediment layers were caused by high sedimentation rates (~246 cm kyr^{-1}; Fig. 3.5a) found by Chiessi et al. (2008), which most likely caused a quick passing of the BFAs through the Taphonomically Active Zone (TAZ, from Davies et al., 1989), preventing the BFAs from *post mortem* processes under oxic and suboxic conditions (Berkeley et al., 1989). On the other hand, those high sedimentation rates increased the reducing sedimentary conditions due to simultaneous, relatively sudden inputs of O.M. (Fig. 3.6i) by the Plata River and coastal currents (Chiessi et al., 2009; Mahiques et al., 2010; Razik et al., 2013) under subaerial exposure of the continental shelf during a sea-level stand of 120–130 m below the modern one (Lambeck and Chappell, 2001).

At ~19 cal kyr BP, the relatively abruptly increasing sedimentation rates (Figs. 3.5a and 3.9b), leading to higher mechanical damage of foraminifera shells (Fig. 3.7c), together with high O.M. contents (Fig. 3.6i) and weaker Rio Grande Cone bottom currents (Fig. 3.9a,c,d) caused the lower oxygenation rate (Fig. 3.6j). At approximately 18.8 cal kyr BP, the rapid increase in the environment oxygenation (Fig. 3.6j), as well as the increase of whole and black samples (Fig. 3.7b,c) could have been caused by disturbances in the sedimentation rate or by first perturbation in the Rio Grande Cone hydrodynamics. The hydrodynamics was likely coupled to the changing AMOC intensities, which were ruled by the northern hemisphere's climate (Stanford et al., 2011).

3.6.2. Phase 2 (18.6–17 cal kyr BP)

Phase 2 may be subdivided into two sub-phases: (i) 18.6–17.7 cal kyr BP and (ii) 17.7–17 cal kyr BP according to the BFAs (Fig. 3.4) and the granulometric properties (Fig. 3.9). Both subphases were well-oxygenated (Fig. 3.6j), containing three strong oxygen pulses at 18.1, 17.8, and 17.4 cal kyr BP (Fig. 3.6j). These environmental oxygenation peaks follow the temperature variations in Antarctica and Greenland (Fig. 3.6e,f), as well as the rainfall peaks over NE Brazil

(Fig. 3.6b). They also most likely occurred simultaneously to the hydrodynamic energy increase at the Rio Grande Cone (Fig. 3.9a,c,d). At 17.4 cal kyr BP, in particular the higher peak of the oxygenation rate seems to be related to increased sea-surface temperatures (Fig. 3.6d) and salinities at the NE Brazilian margin (Arz et al., 1999; Weldeab et al., 2006).

During the first half of phase 2, increases in the environment oxygenation (Fig. 3.6j) occurred mainly at the water-sediment interface and in shallower sediment layers (Fig. 3.6h). The second half of phase 2 is mainly characterized by the oxygenation peak at ~17.4 cal kyr BP (Fig. 3.6j) reaching the shallow and deep sediment layers besides the water-sediment interface (Fig. 3.6h). Based on the oxygenation peaks and the various sedimentary oxygenation depths, we suppose that the weakening of the AMOC (Stanford et al., 2011) and the associated strengthening of the Brazil Current (Arz et al., 1999) occurred by discontinuous pulses at the Rio Grande Cone.

At ~17.6 cal kyr BP, the AMOC nearly collapsed (Fig. 3.9a,c,d) (Stanford et al., 2011), as the first greater deposition of Ice Rafted Debris occurred at the North Atlantic (Bard et al., 2000). We suppose that the high oxygenation rate of the environment at 17.5–17.2 cal kyr BP was caused by this AMOC weakening (heterogeneous Brazil Current strengthening). Since then, the hydrodynamic energy decreased (Figs. 3.9a,c,d and 3.7c) at the Rio Grande Cone, reducing the oxygenation grade of the environment (Fig. 3.6j).

Herbivorous species preferring labile O.M. (e.g., *Quinqueloculina* spp.) appear at high frequencies within epifaunal BFAs of phase 2 (Fig. 3.4; Table 3.1). Most of the *Quinqueloculina* genera species (Fig. 3.2k,t) support the high oxygenation rates (Fig. 3.6j) in the environment (Corliss, 1991; Duleba et al., 2005). However, these genera dominated the epifaunal assemblages even though other species (e.g., *Pyrgo* spp., *Eponides repandus*) were present, which prefer more degraded O.M. (Murray, 1991; De and Gupta, 2010). The O.M. export to the ocean floor is quite complex. However, in general terms, lower marine primary productivity (Fig. 3.6g) results in a lower accumulation of labile O.M. (Fig. 3.6i) (Rühlemann et al., 1999). Thus, we suppose that the labile O.M. reaching the Rio Grande Cone at phase 2 was mainly delivered by the SACW or AAIW.

3.6.3. Phase 3 (17–16 cal kyr BP)

Between 17 and 16 cal kyr BP, BFA 3 dominated the Rio Grande environment (Fig. 4), where equitability J' and diversity H' reached their local minima (Fig. 3.5e,f). Simultaneously, the decreasing hydrodynamic energy (Figs. 3.9a,c,d and 3.7c) must have caused the decreasing oxygenation rates (Fig. 3.6j) and the higher O.M. contents in the Rio Grande Cone sediments (Fig. 3.6i). The decreasing oxygenation rates of the environment may have forced infaunal species to adopt shallower sedimentary habitats (Fig. 3.6h), while leaving the former less reducing sedimentary environment (Fig. 3.7b).

We suggest that the decreasing hydrodynamic energy was caused by paleoclimatic changes which occurred in Antarctica at 17–16.2 cal kyr BP, when the sea ice had its smallest extension up to that time, as well as when the atmospheric CO_2 (Shemesh et al., 2002) and the atmospheric temperatures of the southern hemisphere increased (Fig. 3.6e). After approximately 200 years, there was a temporal oxygenation increase and the O.M. content in the Rio Grande Cone sediments decreased (Fig. 3.6i,j). In phase 3, two oxygenation peaks occurred at approximately 16.8 and 16.2 cal kyr BP, although

these peaks were less intense than those described for phase 2 (Fig. 3.6j). We suppose that this temporarily increased hydrodynamic energy (Figs. 3.9a,c,d and 3.7c) caused these peaks in the oxygenation rate. These peaks were most likely caused by a number of factors including a temporal strengthening of the Brazil Current (Arz et al., 1999; Weldeab et al., 2006), increased AAIW formation (Fig. 3.6) (Pahnke et al., 2008), increased ventilation of the AAIW and of the SACW (Anderson et al., 2009), climate changes in Antarctica (Fig. 3.6e) (Blunier and Brook, 2001; Shemesh et al., 2002), and the changes in the AMOC (Stanford et al., 2011). The AMOC remained collapsed until approximately 16.7 cal kyr BP, when it started to restructure (Stanford et al., 2011).

The highest frequencies of *Brizalina subaenariensis* during this phase occurred at approximately 16.5 cal kyr BP (Fig. 3.2d). This species is thought to quickly colonize stressed environments by responding to phytoplankton blooms with rapid growth (Langezaal et al., 2006). At approximately the same time, the highest O.M. values are seen in the Rio Grande Cone sediments (Fig. 3.6i), accompanied by a decrease of interstitial oxygenation (Fig. 3.6j) (Berner, 1970; Rühlemann et al., 1999). The presence of *B. subaenariensis* and the increased frequency of *Quinqueloculina* spp. (Fig. 3.2k,t), coupled with higher $\delta^{13}C$ values of *G. ruber* (Fig. 3.6g), attest the input of labile O.M..

Species that typify colder waters, such as *Bulimina marginata*, *Globocassidulina crassa*, *Stainforthia concava*, *Uvigerina bifurcata*, and *Uvigerina peregrina* (Murray, 1991; Badawi et al., 2005; Pascual *et al*., 2008) became more scarce or disappeared during phase 3 (Figs. 3.2 and 3.4; Table 3.1). In contrast, typical species for temperate waters and for more stratified oceanic conditions, such as *Bulimina elongata*, *Brizalina subaenariensis*, *Buliminella elegantissima*, *Nonionella atalntica*, and *Nonionella opima* (Murray, 1991; Kaminski et al., 2002; Martins et al., 2007) appeared at higher frequencies (Figs. 3.2 and 3.4; Table 1). These findings show that the oceanic water masses became warmer or more stratified at the Rio Grande Cone, if compared with earlier phases. This warming seems to be related to the increased atmospheric CO_2 concentrations and to a resultant warming of the southern hemisphere (Fig. 3.6e) (e.g., Shemesh et al., 2002).

3.6.4. Phase 4 (16–14.7 cal kyr BP)

Pronounced paleoenvironmental undulations in hydrodynamic energy (Figs. 3.9a,c,d and 3.7c) at the Rio Grande Cone are characteristic for phase 4. Hydrodynamic energy together with the oxygenation rate increase from their minima at 16 cal kyr BP to their maxima at 15 cal kyr BP (Fig. 3.6j). The continuous decrease of infaunal and the simultaneous increase of epifaunal-infaunal, as well as of epifaunal species (Fig. 3.6h) indicate that higher oxygenation rates were valid for the water-sediment interface and shallower sediment depths during the second half of phase 4.

At 16 cal kyr BP, the second greatest discharge of Ice Rafted Debris in the North Atlantic Ocean (Bard et al., 2000) caused changes in the AMOC (Stanford et al., 2011). These changes in turn produced temperature and salinity decreases (Fig. 3.6d) at the NE Brazilian margin during the first half of phase 4 due to increasing inter-hemispheric water-mass transport and strengthening of the AMOC (Weldeab et al., 2006; Stanford et al., 2011). We suppose that these hydrodynamic restructuring was also coupled to the atmospheric CO_2 increase in Antarctica (Shemesh et al., 2002), which reached the Rio

Grande Cone in pulses, initially reducing the hydrodynamic energy of the Brazil Current (Figs. 3.9a,c,d and 3.7c) and the oxygenation rates (Fig. 3.6j).

During the second half of phase 4 (15.3–15 cal kyr BP), we again observe peaks in the hydrodynamics (Fig. 3.9a,c,d) and oxygenation rates (Fig. 3.6j) at the Rio Grande Cone. However, as the Brazil Current weakened, these conditions could be caused by the restructuring of the Agulhas Leakage (Chiessi et al., 2009), leading to a change of chemo-physical signatures of the Atlantic intermediate waters, including those of the Brazil Current (Chiessi et al., 2008). After 15 cal kyr BP, decreasing oxygenation rates (Fig. 3.6j) and hydrodynamic energies (Figs. 3.9a–d and 3.7c), as well as increasing O.M. contents (Fig. 3.6i) appear to mark the transition between the HS1 and the ACR (Blunier et al., 1997; Stenni et al., 2001; Köhler et al., 2011). Increasing O.M. contents since ~15 cal kyr BP led to increased FeS_2 formation, which considerably increased the frequency of golden BFAs (Fig. 3.7b). Chiessi et al. (2008) and Razik et al. (2013) reported a considerable decrease in sedimentation rate since ~15 cal kyr BP on the Rio Grande Cone (Fig. 3.5a). Furthermore, Chiessi et al. (2008, 2009) described a simultaneous water-temperature increase. This temperature increase is in agreement with BFA trends between 16 and 14.7 cal kyr BP (Fig. 3.4; Table 3.1), as the bottom and interstitial waters gradually became warmer and less stratified (Kaminski et al., 2002; Scott et al., 2003; Eichler et al., 2008).

3.6.5. Phase 5 (14.7–14 cal kyr BP)

Phase 5 shows the lowest sedimentation rates of ~8 cm kyr^{-1} (Fig. 3.6a) at our study site (Chiessi et al., 2008; Razik et al., 2013), causing a significant disappearance of species being typical for lower sea-level stands (e.g., Fig. 3.2h,j). These BFAs (i.e., assemblages 2 and 4; Fig. 3.4) also indicate weakening of bottom water hydrodynamics (Figs. 3.9a,c,d and 3.7c) and higher sedimentary O.M. contents (Fig. 3.6i). Higher O.M. contents cause an increase of FeS_2 in the Rio Grande Cone sediments, as seen by a significant increase of golden foraminifera shells (Fig. 3.7b). Exclusively epifaunal and infaunal species (Fig. 3.6h) indicate weakened oxygenation of the sedimentary environment (Fig. 3.6j).

The lower Rio Grande Cone hydrodynamics and higher O.M. contents in the sediments created a better environment for the existence of benthic forms of epifauna in a shallow infaunal habitat with greater tolerance for less oxygenated environments (e.g., *Nonionella opima, Nonionellina labradorica, Brizalina subaenariensis, Bulimina elongata, Globocassidulina crassa*) (Figs. 3.2 and 3.4). The disappearance of BFAs during this phase (Figs. 3.2 and 3.4; Table 3.1) indicates slightly colder waters than those found in the previous phases (Murray, 1991; Martin and Gomes, 2004; Badawi et al., 2005), which mirrors the coldest period on the southern hemisphere during the Last Deglaciation (Blunier et al., 1997; Stenni et al., 2001; Köhler et al., 2011). We suppose that the reported changes throughout phase 5 were induced by the southern hemisphere's climate during the ACR.

3.7. Conclusions

With respect to the Last Deglaciation at the Rio Grande Cone off South Brazil, we differentiated five distinct paleoenvironmental phases by joint consideration of benthic foraminiferal assemblages and clastic granulometric parameters. These paleoenvironmental conditions are related to intensity changes of the Atlantic Meridional Overturning Circulation (AMOC), as well as to

climatic conditions of the North Atlantic and the Antarctic realms during Heinrich Stadial 1 and the Antarctic Cold Reversal, respectively.

Phase 1 (19–18.6 cal kyr BP) is characterized by high sedimentation rates (~246 cm kyr^{-1}) and by deposition highly variable clastic grain sizes. The deposits contain relatively high FeS and FeS_2 concentrations, which were fed by relatively sudden inputs of organic matter. Based on these sedimentary processes, the sedimentary environment was poorly oxygenated.

Phase 2 (18.6–17 cal kyr BP) has undergone two intervals; while both intervals were characterized by high oxygenation rates and hydrodynamic energies, the first showed higher sedimentary (labile) organic matter contents. Based on the conditions during the first interval, epifauna-infauna species were more dominant, which became valid for the infaunal ones during the second interval. The reason for this paleoenvironmental evolution was the discontinuous pulse-like increase of the Brazil Current's hydrographic energy as a result of the almost collapsed AMOC.

Phase 3 (17–16 cal kyr BP) is defined by more or less continuously weakening oxygenation and hydrodynamics, detected by increasing clay and organic matter deposition. This resulted in decreasing equability and diversity of benthic foraminiferal assemblages, where infaunal species populated shallower habitats in the sediments. We suggest that the decreasing hydrodynamic energy was reasoned by paleoclimatic changes in Antarctica at 17–16.2 cal kyr BP, causing the lowest sea-ice extension up to this time. This led to weakened AAIW formation, lower SACW ventilation, and warming of bottom waters at the Rio Grande Cone. This is detected by higher frequencies of benthic foraminiferal species typical for temperate waters and more stratified oceanic conditions.

Phase 4 (16–14.7 cal kyr BP) shows pronounced paleoenvironmental and hydrodynamic changes. The first half of this phase shows low hydrodynamics and oxygenations due to restructuring of the AMOC and strengthening of the interhemispheric water-mass transport (weakening of the Brazil Current), as seen by higher deposition of clays. During the second half of phase 4 (15.3–15 cal kyr BP), stronger hydrodynamics and oxygenations could be observed due to the set-in of the Agulhas Leakage affecting the Brazil Current. This led to a continuous increase of epifaunal-infaunal and epifaunal species, being indicative for higher oxygenation rates at especially the water-sediment interface and shallower sediment depths. After 15 cal kyr BP, weakening oxygenation and hydrodynamics, as well as increasing sedimentary organic matter contents marked the transition between Heinrich Stadial 1 and the Antarctic Cold Reversal. Increasing organic matter contents and decreasing sedimentation rates (~70 cm kyr^{-1}) under increasing temperatures of well-stratified water masses caused marked FeS_2 formation.

Phase 5 (14.7–14 cal kyr BP) shows the lowest sedimentation rates (~8 cm kyr^{-1}) due to a rising sea level and increasing shore-distance of the study site. This caused a significant disappearance of species being typical for sea-level lowstands. The weakening of the hydrodynamics led to higher deposition of organic matter and further increase of sedimentary FeS_2, while epifaunal and infaunal species indicate reduced oxygenation of the sedimentary environment. This phase offers the lowest bottom-water temperatures at the Rio Grande Cone with respect to the entire investigated time sequence. We suppose that the southern hemisphere's climate

during the Antarctic Cold Reversal was responsible for this temperature change of the bottom water.

The presented environmental and hydrodynamic results of this joint micropaleontologic and granulometric study performed at the Rio Grande Cone reveal that this study site is of over-regional importance with respect to ocean-wide paleoceanography. Conclusively, the obtained insights increase the knowledge regarding the paleoenvironmental changes in the western South Atlantic in particular, and contribute to a more robust overall understanding of the AMOC.

3.8. Acknowledgements

We thank the captains and crews of RV Meteor cruise M46/2, who played a vital part in the recovery of the investigated sediment core. We are grateful to Dr. Silvia Helena de Mello e Sousa (IO-USP), Dr. Andreas Mackensen (AWI-Bremerhaven), Dr. Maurício M. Mata (LEOC-FURG) and the students of Laboratório de Estudos dos Oceanos e Clima (LEOC-FURG) for their helpful comments. We acknowledge the financial support of the FAPESP (process 2008/57035-2) to this study. Financial support to S.R. was provided by the DFG through the European Graduate College 'Proxies in Earth History – EUROPROX'. The data reported in this paper will be archived in the PANGAEA database (www.pangaea.de).

3.9. References

Alve, E., Bernhard, M., 1995. Vertical migratory response of benthic foraminifera to controlled oxygen concentrations in an experimental mesocosm. Marine Ecology Progress Series 116, 137–151.

Anderson, R.F., Ali, S., Bradtmiller, L.I., Nielsen, S.H.H., Fleisher, M.Q., Anderson, B.E., Burckle, L.H., 2009. Wind-driven upwelling in the Southern Ocean and the deglacial rise in atmospheric CO2. Science 323, 1443–1448.

Arz, H.W., Pätzold, J., Wefer, G., 1999. The deglacial history of the western tropical Atlantic as inferred from high resolution stable isotope records of northeastern Brazil. Earth and Planetary Science Letters 167, 105–117.

Baas, J.H., Schönfeld, J., Zahn, R., 1998. Mid-depth oxygen drawdown during Heinrich Events: Evidence from benthic foraminiferal community structure, trace-fossil tiering, and benthic δ13C at the Portuguese margin. Marine Geology 152, 25–55.

Badawi, A., Schmiedl, G., Hemleben, C., 2005. Impact of Late Quaternary environmental changes on deep-sea benthic foraminiferal faunas of the Red Sea. Marine Micropaleontology 58, 13–30.

Bard, E., Rostek, F., Turon, J.-L., Gendreau, S., 2000. Hydrological impact of Heinrich Events in the subtropical northeast Atlantic. Science 289, 1321–1324.

Basak, C., Rathburn, A.E., Pérez, M.E., Martin, J.B., Kluesner, J.W., Levin, L.A., Deckker, P.D., Gieskes, J.M., Abrini, M., 2009. Carbon and oxygen isotope geochemistry of live (stained) benthic foraminifera from the Aleutian Margin and the Southern Australian Margin. Marine Micropaleontology 70, 89–101.

Berkeley, A., Perry, C.T., Smithers, S.G., Horton, B.P., Taylor, K.G., 2007. A review of the ecological and taphonomic controls on foraminiferal assemblage development in intertidal environments. Earth-Science Reviews 83, 205–230.

Berner, R.A., 1970. Sedimentary Pyrite formation. American Journal of Science 268, 1–23.

Blunier, T., Brook, E.J., 2001. Timing of millenial-scale climate change in Antarctica and Greenland during the Last Glacial Period. Science 291, 109–112.

Blunier, T., Schwander, J., Stauffer, B., Stocker, T., Dällenbach, A., Indermühle, A., Tschumi, J., Chapellaz, J., Raynaud, D., Barnola, J.-M., 1997. Timing of the Antarctic Cold Reversal and the atmospheric CO2 increase with respect to the Younger Dryas event. Geophysical Research Letters 24, 2683–2686.

Boltovskoy, E., 1959. Foraminifera as biological indicators in the study of ocean currents. Micropaleontology 5, 473–481.

Boltovskoy, E., Giussani, G., Watanabe, S., Wright, R., 1980. Atlas of benthic shelf foraminifera of the southwest Atlantic. The Hague, The Netherlands, 197 pp.

Brett, C.E., Baird, G.C., 1986. Comparative taphonomy: A key to paleoenvironment interpretation based on fossil preservation. Palaios 1, 207–227.

Caralp, M.H., 1989. Abundance of Bulimina exilis and Melonis barleeanum: Relationship to the quality of marine organic matter. Geo-Marine Letters 9, 37–43.

Castilho, L.L.A., Kazmierczak, T. de S., Chemale Jr., F., 2009. Rio Grande Cone tectono-stratigraphic model – Brazil: seismic sequences. Earth Sciences Research Journals 13, 40–53.

Chiessi, C.M., Mulitza, S., Paul, A., Pätzold, J., Groeneveld, J., Wefer, G., 2008. South Atlantic interocean exchange as the trigger for the Bølling warm event. Geology 36, 919—922.

Chiessi, C.M., Mulitza, S., Pätzold, J., Wefer, G., Marengo, J.A., 2009. Possible impact of the Atlantic Multidecadal Oscillation on the South American summer monsoon. Geophysical Research Letters 36, L21707.

Corliss, B.H., 1985. Microhabitats of benthic foraminifera within deep-sea sediments. Letters to Nature 31, 435–438.

Corliss, B.H., 1991. Morphology and microhabitat preferences of benthic foraminifera from the Northwest Atlantic Ocean. Marine Micropaleontology 17, 195–236.

Cortese, G., Abelmann, A., 2002. Radiolarian-based temperatures during the last 160 kyr at ODP Site 1089 (Southern Ocean, Atlantic Sector). Palaeogeography, Palaeoclimatology, Palaeoecology 182, 259–286.

Cruz Jr., F.W., Burns, S.J., Karmann, I., Sharp, W.D., Vuille, M., 2006. Reconstruction of regional atmospheric circulation features during the late Pleistocene in subtropical Brazil from oxygen isotope composition of speleothems. Earth and Planetary Science Letters 248, 495–507.

Davies, D.J., Powell, E.N., Stanton, R.J., 1989. Taphonomic signature as a function of environmental process: shell

and shell beds in a hurricane-influenced inlet in Texas coast. Palaeogeography, Palaeoclimatology, Palaeoecology 72, 317–356.

Dawson, A.G., 2013. Ice age Earth: Late Quaternary geology and climate. Routledge, 320 p.

De, S., Gupta, A.K., 2010. Deep-sea faunal provinces and their inferred environments in the Indian Ocean based on distribution of recent benthic foraminifera. Palaeogeography, Palaeoclimatology, Palaeoecology 291, 429–442.

Den Dulk, M., Reichart, G.J., van Heyst, S., Zachariasse, W.J., Van der Zwaan, G.J., 2000. Benthic foraminifera as proxies of organic matter flux and bottom water oxygenation? A case history from the northern Arabian Sea. Palaeogeography, Palaeoclimatology, Palaeoecology 161, 337–359.

De Rijk, S., Jorissen, F.J., Rohling, E., Troelstra, S.R., 2000. Organic flux control on bathymetric zonation of Mediterranean benthic foraminifera. Marine Micropaleontology 40, 151-166.

Diz, P., Francés, G., 2008. Distribution of live benthic foraminifera in the Ría de Vigo (NW Spain). Marine Micropaleontology 66, 165–191.

Donners, J., Drijfhout, S.S., Hazeleger, W., 2005. Water mass transformation and subduction in the South Atlantic. Journal of Physical Oceanography 35, 1841–1860.

Duleba, W., 1994. Interpretações paleoambientais obtidas a partir das variações na coloração das carapaças de foraminíferos da Enseada do Flamengo, SP. Boletim do Instituto Oceanográfico 42, 63–72.

Duleba, W., Coimbra, J.C., Petri, S., Barbosa, C.F., 2005. Foraminíferos, tecamebas e ostracodes recentes utilizados como bioindicadores em estudos ambientais brasileiros. In: Sousa, C.R.G., Kenitiro, S., Santos, M., Oliveira, P.E. (Eds.), Quaternário do Brasil. Associação Brasileira de Estudos do Quaternário, Ribeirão Preto: Holos Editora, pp. 176–210.

Eberwein, A., Mackensen, A, 2006. Regional primary productivity differences off Morocco (NW-Africa) recorded by modern benthic foraminifera and their stable carbon isotopic composition. Deep-Sea Research I 53, 1379–1405.

Eichler, P.P.B., Gupta, B.K.S., Eichler, B.B., Braga, E.S., Campos, E.J., 2008. Benthic foraminiferal assemblages of the South Brazil: Relationship to water masses and nutrient distributions. Continental Shelf Research 28, 1674–1686.

Everitt, B.S., Landau, S., Leese, M., Stahl, D., 2011. Cluster Analysis (5th ed.) Wiley Series in Probability and Statistics, New Jersey, USA, 346 pp.

Fontanier, C., Jorissen, F.J., Licari, L., Alexandre, A., Anschutz, P., Carbonel, P., 2002. Live benthic foraminiferal faunas from the Bay of Biscay: faunal density, composition, and microhabitats. Deep-Sea Research I 49, 751–785.

Frenz, M., Höppner, R., Stuut, J.-B.W., Wagner, T., Henrich, R., 2003. Surface sediment bulk geochemistry and grain-size composition related to the oceanic circulation along the South American continental margin in the Southwest Atlantic. In: Wefer, G., Mulitza, S., Ratmeyer, V., (Eds.), The South Atlantic in the Late Quaternary; Reconstruction of material budgets and current systems. Springer-Verlag, Berlin-Heidelberg-New York-Tokyo, pp. 347–373.

Girardeau, J., Jennings, A.E., Andrews, J.T., 2004. Timing and mechanisms of surface and intermediate water circulation changes in the Nordic Seas over the last 10,000 cal years: a view from the North Iceland shelf. Quaternary Science Reviews 23, 2127–2139.

Guilbault, J.P., Radi, T., Barrie, J.V., Conway, K., Lapointe, M., 2003. Paleoenvironments of the Strait of Georgia, British Columbia during the last deglaciation: Microfaunal and microfloral evidence. Quaternary Science Reviews 22, 839–857.

Harloff, J., Mackensen, A., 1996. Recent benthic foraminiferal associations and ecology of the Scotia Sea and Argentine Basin. Marine Micropaleontology 31, 1–29.

Herguera, J.C., Berger, W.H., 1991. Paleoproductivity from benthic foraminifera abundance: glacial to postglacial change in the westequatorial Pacific. Geology 19, 1173–1176.

Hewitt, G. 2000. The genetic legacy of the Quaternary ice ages. Nature 405(6789), 907–913.

Jaeschke, A., Rühlemann, C.R., Arz, H., Heil, G., Lohmann, G., 2007. Coupling of millennial-scale changes in sea surface temperature and precipitation off northeastern Brazil with high-latitude climate shifts during the last glacial period. Paleoceanography 22, PA4206.

Jorissen, F.J., De Stigter, H.C., Widmark, J.G.V., 1995. A conceptual model explaining benthic foraminiferal microhabitats. Marine Micropaleontology 22, 3–15.

Kaiho, K., 1991. Global changes of Paleogene aerobic/anaerobic benthic foraminifera and deep-sea circulation. Palaeogeography, Palaeoclimatology, Palaeoecology 83, 65–85.

Kaiho, K., 1994. Benthic foraminiferal dissolved-oxygen index and dissolved-oxygen levels in the modern ocean. Geology 22, 719–722.

Kaminski, M.A., Aksu, A., Box, M., Hiscott, R.N., Filipescu, S., Al-Salameen, M., 2002. Late Glacial to Holocene benthic foraminifera in the Marmara Sea: implications for Black Sea–Mediterranean Sea connections following the last deglaciation. Marine Geology 190, 165–202.

Kennet, J.P., Cannariato, K.G., Hendy, I.L., Behl, R.J., 2000. Carbon isotopic evidence for methane hydrate instability during Quaternary interstadials. Science 288, 128–133.

Köhler, P., Knorr, G., Buiron, D., Lourantou, A., Chappellaz, J., 2011. Abrupt rise in atmospheric CO2 at the onset of the Bølling/Allerød: in-situ ice core data versus true atmospheric signals. Climate of the Past 7, 473–486.

Koho, K.A., García, R., Stigter, H.C., Epping, E., Koning, E., Kouwenhoven, T.J., van der Zwaan, G.J., 2008. Sedimentary labile organic carbon and pore water redox control on species distribution of benthic foraminifera: A case study from Lisbon–Setúbal Canyon (southern Portugal). Progress in Oceanography 79, 55–82.

Kuhnt, T., Schmiedl, G., Ehmann, W., Hamann, Y., Hemleben, C., 2007. Deep-sea ecosystem variability of the Aegean Sea during the past 22 kyr as revealed by Benthic Foraminifera. Marine Micropaleontology 64, 141–162.

Lambeck, K., Chappell, J., 2001. Sea level change through the last glacial cycle. Science 292, 679–686.

Langezaal, A.M., Jorissen, F.J., Braun, B., Chaillou, G., Fontanier, C., Anschutz, P., van der Zwaan, G.J., 2006. The influence of seasonal processes on geochemical profiles and foraminiferal assemblages on the outer shelf of the Bay of Biscay. Continental Shelf Research 26, 1730–1755.

Lea, D.W., Pak, D.K., Peterson, L.C., Hughen, K.A., 2003. Synchroneity of tropical and high-latitude Atlantic temperatures over the last glacial termination. Science 301, 1361–1364.

Licari, L.N., Schumacher, S., Wenzhöfer, F., Zabel, M., Mackensen, A., 2003. Communities and microhabitats of living benthic foraminifera from the tropical east Atlantic: impact of different productivity regimes. Journal of Foraminiferal Research 33, 10–31.

Loeblich, A.R, Tappan, H., 1964. Protista. In: Moore, R.C. (Ed.), Treatise on invertebrate paleontology, Part C. The University Kansas Press, New York, v.1: 510 pp., v.2: 390 pp.

Loeblich, A.R., Tappan, H., 1988. Foraminiferal genera and their classification. Van Nostrand, New York, v.1, 970 pp.; v.2, 847 boards.

Lohmann, G., 2003. Atmospheric and oceanic freshwater transport during weak Atlantic overturning circulation. Tellus 55A, 438–449.

Mackensen, A., Schmiedl, G., Harloff, J., Giese, M., 1995. Deep-sea foraminifera in the South Atlantic Ocean: ecology and assemblage generation. Micropaleontology 41, 342–358.

Mahiques, M.M., Souza, S.H.M., Furtado, V.V., Tessler, M.G., Toledo, F.A.L., Burone, L.; Figueira, R.C.L., Klein, D.A., Martins, C.C., Alves, D.P.V., 2010. The southern Brazilian shelf: general characteristics, Quaternary evolution and sediment distribution. Brazilian Journal of Oceanography 58(special issue PGGM), 25–34.

Mangini, A., Godoy, J.M., Godoy, M.L., Kowsmann, R., Santos, G.M., Ruckelshausen, M., Schroeder-Ritzrau, A., Wacker, L., 2010. Deep sea corals off Brazil verify a poorly ventilated Southern Pacific Ocean during H2, H1 and the Younger Dryas. Earth and Planetary Science Letters 293, 269–276.

Martin, R.E., Liddell, W.D., 1991. The taphonomy of foraminifera in modern carbonate environments: implications for the formation of foraminiferal assemblages. In: Donovan, S.K. (Ed.), The Processes of Fossilization. Columbia University Press, New York, pp. 170–193.

Martins, M.V., Gomes, C.F., Gomes, V., 2004. Foraminíferos da Margem Continental NW Ibérica: Sistemática, Ecologia. Universidade de Aveiro, Aveiro, Portugal, 377 pp.

Martins, M.V., Jouanneau, J.-M., Weber, O., Rocha, F., 2006. Tracing the late Holocene evolution of the NW Iberian upwelling system. Marine Micropaleontology 59, 35–55.

Martins, V., Dubert, J., Jouanneau, J.-M., Weber, O., Silva, E.F., Patinha, C., Dias, J.M.A., Rocha, F., 2007. A multiproxy approach of the Holocene evolution of shelf-slope circulation on the NW Iberian Continental Shelf. Marine Geology 239, 1–18.

Mayklem, W.R., 1967. Black and brown speckled foraminiferal sand from the southern part of the Great Barrier Reef. Journal of Sedimentary Research 37, 1023–1030.

McCarthy, D.J., 2011. Late Quaternary ice-ocean interactions in central West Greenland. PhD Thesis, Durham University, England, 292 pp.

McCave, I N., 2008. Size sorting during transport and deposition of fine sediments: Sortable silt and flow speed. Contourites. Developments in Sedimentology 60. Elsevier, Amsterdam, pp. 121–142.

Mercone, D., Thompson, J., Abu-Zied, R.H., Croudace, I.W., Rohling, E.J., 2001. High-resolution geochemical and micropaleontological profiling of the most recent eastern Mediterranean sapropel. Marine Geology 177, 25–44.

Milker, Y., Schmiedl, G., Betzler, C., Römer, M., Jaramillo-Vogel, D., Siccha, M., 2009. Distribution of recent benthic foraminifera in shelf carbonate environments of the Western Mediterranean Sea. Marine Micropaleontology 73, 207–225.

Moodley, L., Schaub, B.E.M., Van der Zwaan, G.J., Herman, P.M.J., 1998. Tolerance of benthic foraminifera (Protista: Sarcodina) to hydrogen sulphide. Marine Ecology Progress Series 169, 77–86.

Murray, J.W., 1991. Ecology and paleoecology of benthic foraminifera. Longman Scientific and Technical, London, 397 pp.

Osterman, L.E., 2003. Benthic foraminifers from the continental shelf and slope of the Gulf of Mexico: An indicator of shelf hypoxia. Estuarine, Coastal and Shelf Science 58, 17–35.

Pahnke, K., Goldstein, S.L., Hemming, S.R., 2008. Abrupt changes in Antarctic Intermediate Water circulation over the past 25,000 years. Nature Geoscience 1, 870–874.

Pascual, A., Rodriguyez-Lazaro, J., Martín-Rubio, M., Jouanneau, J.-M., Weber, O., 2008. A survey of the benthic microfauna (foraminifera, Ostracoda) on the Basque shelf, southern Bay of Biscay. Journal of Marine Systems 72, 35–63.

Peterson, R., Stramma, L., 1991. Upper-level circulation in the South Atlantic Ocean. Progress in Oceanography 26, 1–73.

Pielou, E.C., 1969. Mathematical ecology. John Wiley and Sons, New York, 385 pp.

Polyak, L., Korsun, S., Febo, L., Stanovoy, V., Khusid, T., Mald, M., Paulsen, B.E., Lubinski, D.A., 2002. Benthic foraminiferal assemblages from the southern Kara Sea, a river-influenced arctic marine environment. Journal of Foraminiferal Research 32, 252–273.

Putman, A.E., Denton, G.H., Schaefer, J.M., Barrell, D.J.A., Andersen, B.G., Finkel, R.C., Schwartz, R., Doughty, A.M., Kaplan, M.R., Schlüchter, C., 2010. Glacier advance in southern middle-latitudes during the Antarctic Cold Reversal. Nature Geoscience 3, 700–704.

Rasmussen, S.O., Andersen, K.K., Svensson, A.M., Steffesen, J.P., Vinther, B.M., Clausen, H.B., Siggaard-Andersen, M.-L., Johnsen, S.J., Larsen, L.B., Dahl-Jensen, D., Bigler, M., Röthlisberger, R., Fisher, H., Goto-Azuma, K., Hansson, M.E., Ruth, U., 2006. A new Greenland ice core chronology for the last glacial termination. Journal of Geophysical Research 111, D06102.

Razik, S., Chiessi, C.M., Romero, O.E., von Dobeneck, T., 2013. Interaction of the South American Monsoon System and the Southern Westerly Wind Belt during the last 14 kyr. Palaeogeography, Palaeoclimatology, Palaeoecology 374, 28–40.

Riveiros, N.V., Patterson, R.T., 2009. Late Holocene paleoceanographic evidence of the influence of the Aleutian Low and North Pacific High on circulation in the Seymour-Belize Inlet Complex, British Columbia, Canada. Quaternary Science Reviews 28, 2833–2850.

Ruddiman, W.F., McIntyre, A., 1981. The North Atlantic Ocean during the last deglaciation. Palaeogeography, Palaeoclimatology, Palaeoecology 35, 145–214.

Rühlemann, C., Müller, P.J., Schneider, R.R., 1999. Organic Carbon and Carbonate as Paleoproductivity Proxies: Examples from High and Low Productivity Areas of the Tropical Atlantic. In: Fischer, G., Wefer, G. (Eds.), Use of Proxies in Paleoceanography: Examples from the South Atlantic. Springer-Verlag, Berlin - Heidelberg,, Germany, pp. 315–344.

Schmiedl, G., Mackensen, A., Müller, P.J., 1997. Recent benthic foraminifera from the eastern South Atlantic Ocean: dependence on food supply and water masses. Marine Micropaleontology 32, 249–287.

Schnitker, D., 1994. Deep-sea benthic foraminifers: food and bottom water masses. In: Zahn, R., Pedersen, T.F., Kaminski, M.A., Labeyrie, L. (Eds.), Carbon cycling in the glacial ocean: constraints on the ocean's role in global change. NATO ASI Series, vol. I 17. Springer-Verlag, Berlin, Germany, pp. 539–554.

Schröder, C.J., Scott, D.B., Medioli, F.S., 1987. Can smaller benthic foraminifera be ignored in paleoenviromental analyses? Journal of Foraminiferal Research 4, 101–110.

Schulz, H.D., Ayres Neto, A., Boetius, A., Enneking, A., Fabian, K., Feseker, T., Funk, J., Gorke, M., Heidersdorf, F., Hensen, C., Heuer, V., Hill, H.G., Hinrichs, S., Kasten, S., Klann, M., Lacerda de Souza, C., Martinez Briao, A., Meyer, S., Mulitza, S., Niebler, H.-S., Ochsenhirt, W.-T., Panteleit, B., Pfeifer, K., Schewe, F., Schwenk, T., Señorans, J.L., Siemer, S., Steinmetz, E., Wenzhöfer, F., 2001. Report and preliminary results of METEOR Cruise M46/2 Recife (Brazil) – Montevideo (Uruguay), 02.12.–29.12.1999. Berichte, Fachbereich Geowissenschaften, Universität Bremen vol. 01-1, 69 p.

Scott, G.A., Scourse, J.D., Austin, W.E.N., 2003. The distribution of benthic foraminifera in the Celtic Sea: the significance of seasonal stratification. Journal of Foraminiferal Research 33, 32–61.

Sen Gupta, B.K., Turner, R.E., Rabalais, N.N., 1996. Seasonal oxygen depletion in continental-shelf waters of Louisiana: Historical record of benthic foraminifers. Geology 24, 227–230.

Shannon, C., Weaver, W., 1949. The mathematical theory of communication. (5th ed.) University of Illinois Press, Illinois, pp. 379-423, 623–656.

Shemesh, A., Hodell, D., Crosta, X., Kanfoush, S., Charles, C., Guilderson, T., 2002. Sequence of events during the last deglaciation in Southern Ocean sediments and Antarctic ice cores. Paleoceanography 17, 1056–1062.

Silveira, I.C.A., Schmidt, A.C.K., Campos, E.J.D., Godoi, S.S., Ikeda, Y., 2000. A Corrente do Brasil ao Largo da Costa Leste Brasileira. Revista Brasileira de Oceanografia 48, 171–183.

Silveira, D.P., Machado, M.A.P., 2004. Bacias sedimentares brasileiras: Bacia de Pelotas. Boletim Informativo da Fundação Paleontológica Phoenix, Ano 6, n. 63.

Smart, C.W., 2008. Abssal NE Atlantic benthic foraminifera during the last 15 kyr: relation to variations in seasonality of productivity. Marine Micropaleontology 69, 193–211.

Sousa, S.H.M., Passos, R.F., Fukumoto, M., Silveira, I.C., Figueira, R.L., Koutsoukos, E.A.M., Mahiques, M.M., Rezende, C.E., 2006. Mid-lower bathyal benthic foraminifera of the Campos Basin, Southeastern Brazilian margin: Biotopes and controlling ecological factors. Marine Micropaleontology 61, 40–57.

Stanford, J.D., Rohling, E.J., Hunter, S.E., Roberts, A.P., Rasmussen, S.O., Bard, E., McManus, J., Fairbanks, R.G., 2006. Timing of meltwater pulse 1a and climate responses to meltwater injections. Paleoceanography 21, PA4103.

Stanford, J.D., Rohling, E.J., Bacon, S., Roberts, A.P., Grousset, F.E., Bolshaw, M., 2011. A new concept for the paleoceanographic evolution of Heinrich event 1 in the North Atlantic. Quaternary Science Reviews 30, 1047–1066.

Stenni, B., Mason-Delmotte, V., Johnsen, S., Jouzel, J., Longinelli, A., Monnin, E., Röthlisberger, R., Selmo, E., 2001. An Oceanic Cold Reversal During the Last Deglaciation. Science 293, 2074-2077.

Stramma, L., England, M., 1999. On the water masses and mean circulation of the South Atlantic Ocean. Journal of Geophysical Ressearch 104, 863–883.

Thibodeau, B., Vernal, A., Mucci, A., 2006. Recent eutrophication and consequent hypoxia in the bottom waters of the Lower St. Lawrence Estuary: Micropaleontological and geochemical evidence. Marine Geology 231, 37–50.

Thomas, E., Booth, L., Maslin, M., Shackleton, N.J., 1995. Northeastern Atlantic benthic foraminifera during the last 45,000 years: Changes in productivity seen from the bottom up. Paleoceanography 10, 545–562.

Toledo, F.A.L., Cachão, M., Costa, K.B., Pivel, M.A.G., 2007. Planktonic foraminifera, calcareous nannoplankton and ascidian variations during the last 25 kyr in the Southwestern Atlantic: A paleoproductivity signature? Marine Micropaleontology 64, 67–79.

Tsuchiya, M., Talley, L.D., McCartney, M.S., 1994. Water-mass distributions in the western South Atlantic: a section from South Georgia Island (54S) northward across the Equator. Journal of Marine Research 52, 55–81.

Tucker, M. 1996. Methoden der Sedimentologie. Ferdinand Enke Verlag, Stuttgart, 366 p.

Urien, C.M., Ewing, M., 1974. Recent sediments and environment of southern Brazil, Uruguay, Buenos Aires, and Rio Negro continental shelf. In: Burk, C.A., Drake, C.L., (Eds.), The geology of continental margins. Springer, Berlin, pp.157–177.

Van Hengstum, P.J., Scott, D.B., 2011. Ecology of foraminifera and habitat variability in an underwater cave: distinguishing anchialine versus submarine cave environments. Journal of Foraminiferal Research 41, 201–229.

Weldeab, S., Schneider, R.R., Kölling, M., 2006. Deglacial sea surface temperature and salinity increase in the western tropical Atlantic in synchrony with high latitude climate instabilities. Earth and Planetary Science Letters 241, 699–706.

Wentworth, C.R., 1922. A scale of grade and class terms for clastic sediments. Journal of Geology 30, 377–392.

Zarries, M., Mackensen, A., 2010. The tropical rainbelt and productivity changes off northwest Africa: A 31,000-year high-resolution record. Marine Micropaleontology 76, 76–91.

3.10. Scientific background and individual contributions

The study ‘Paleoenvironmental evolution and hydrodynamics of the Rio Grande Cone: Insights from benthic foraminiferal and terrigenous granulometric properties from Last Deglacial sediments off South Brazil’ is based to a large extent on the PhD thesis of Dr. Juliana Braga Silva. Since her thesis was mainly focused on the Last Deglacial (14–19 cal kyr BP) sequence of the gravity core GeoB 6211-2, her preliminary investigatory work could be amplified by data sets not published earlier in the study ‘Interaction of the South American Monsoon System and the Southern Westerly Wind Belt during the last 14 kyr’ (see chapter 2). The cooperation was launched in the mid of 2012, while investigations of benthic foraminiferal assemblages were supplemented by clastic granulometric

parameters, which strengthened the interpretations regarding the Brazil Current paleointensities with clues on water-mass ventilation and oxygenation.

The design of the study was carried out by Dr. Cristiano M. Chiessi and Prof. Dr. Wania Duleba. Counting of benthic forams was done by Dr. Juliana Braga Silva and Dr. Cristiano M. Chiessi. The stable isotope analyses on planktic forams were performed by Dr. Cristiano M. Chiessi. Grain-size distributions of the terrigenous sediment fraction and derived granulometric parameters were provided by Sebastian Razik. All authors contributed to the interpretation of the respective data sets to deepen the understanding of the paleoceanography and the marine paleoenvironment as a whole with equal contributions regarding the writing of this manuscript.

Chapter 4: Identification of terrigenous sediment provinces at the continental margin of SE South America

Sebastian Razik [a], Aline Govin [b], Cristiano M. Chiessi [c] and Tilo von Dobeneck [a,b]

[a] Department of Geosciences, University of Bremen, Klagenfurter Straße, 28359 Bremen, Germany

[b] MARUM – Center for Marine Environmental Sciences, University of Bremen, Leobener Straße, D-28359 Bremen, Germany

[c] Escola de Artes, Ciências e Humanidades, Universidade de São Paulo, Av. Arlindo Béttio 1000, CEP03828-000 São Paulo SP, Brazil

Under revision at Marine Geology

4.1. Abstract

The continental margin of SE South America receives sediments from various terrigenous sources, each conveying specific magnetic mineral assemblages and major-element signatures due to prevailing source-rock petrology and influencing climatic (weathering) conditions. Here, we aim at identifying the sources of terrigenous sediments deposited along the SE South American continental margin (20°–55° S), investigating rock-magnetic and major-element ratios, as well as clastic grain-size distributions of 25 surface-sediment samples obtained between 16 and 1805 m water depth. A set of five ratios (i.e., χ_{fd}%, ARM/IRM, $S_{0.3T}$, SIRM/Fe and Fe/K) was used as input parameters for fuzzy c-means cluster analysis and non-linear mapping to depict and unmix sediment-province characteristics. This multivariate approach yields three regionally coherent clusters representing petrologically and climatically distinct source regions. Cluster 1 is composed of sediments from the Plata Drainage Basin. These sediments are tropically weathered clayey silts with the highest proportions of fine magnetite, which were distributed with the Plata Plume Water up to ~24° S. Cluster 2 consists of Pampean loessoidal sands (highest hematite and goethite proportions) delivered to the Pampean shelf by westerly winds and coastal wave erosion. During sea-level lowstands, these sands were widely distributed along the outer shelf and are recently being admixed to Plata-sourced sediments on the slope off SE Brazil during up- / downwelling events. Cluster 3 is entirely restricted to the Pampean slope and has been identified as relict contouritic sand (prevalence of coarse magnetite and lowest proportion of Fe-bearing clays). Their direct transport to the slope was enabled by Colorado and Negro River meltwaters under deglacial sea-level lowstand conditions. This study corroborates the usefulness of the performed approach as a sensitive and efficient tool to access sediment sources in regions with complex sediment dynamics and multiple sediment sources.

4.2. Introduction

The SE South American continental margin (ca. 20°–55° S; Fig. 4.1) presents complex sedimentary distribution patterns due to multiple terrestrial sediment contributions and an intricate oceanographic setting. This continental margin is supplied with terrigenous sediments from the Plata Drainage Basin (PDB), the Pampas and Patagonia. Fluvial sediments are mainly delivered by the Plata River (~35° S) (Urien and Ewing, 1974; Laborde, 1997; Violante and

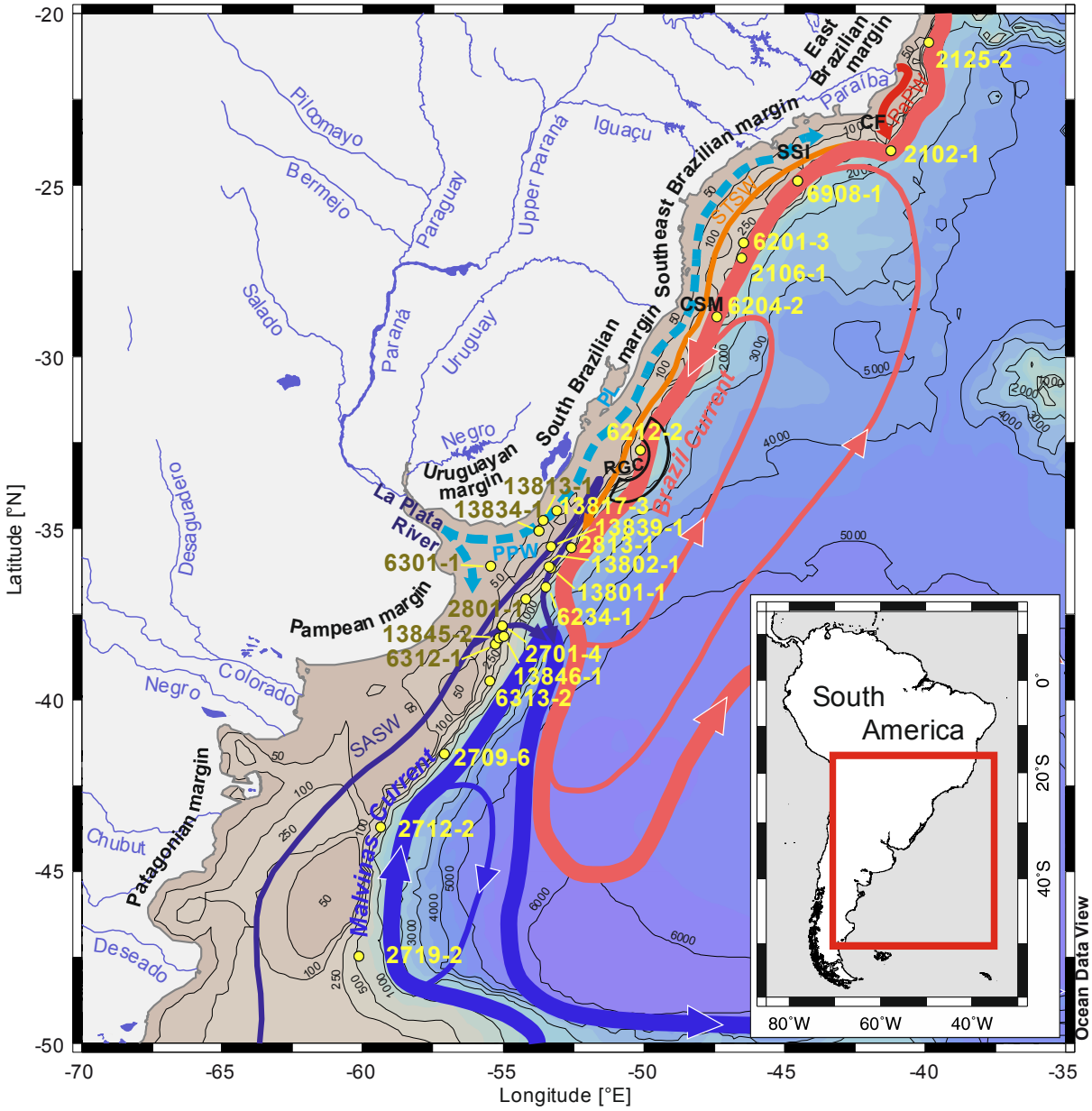

Fig. 4.1. Location map of (GeoB) surface sediment samples and ocean currents (Subantarctic Shelf Water, SASW; Subtropical Shelf Water, STSW; Plata Plume Water, PPW) at the SE South American continental margin (Cape Frio, CF; Cape Santa Marta, CSM; Patos Lagoon, PL; Rio Grande Cone, RGC; São Sebastião Island, SSI). Surface water circulation was compiled and redrawn after Stramma and England (1999), Piola and Matano (2001) and Piola et al. (2005).

Parker, 2004; Lantzsch et al., 2014), with minor amounts carried by the Paraíba do Sul (21.5° S), Colorado (40° S), and Negro (41° S) Rivers (Fig. 4.1) (Martin et al., 1985; Gaiero et al., 2003; Bernardes et al., 2012; Oliveira et al., 2012). The eolian input by the southern westerly winds is relevant off the Pampas and Patagonia (e.g., Gaiero et al., 2003 and references therein). Subsequent sediment distribution and mixing on the continental margin are conducted by the slope-parallel northward-flowing Malvinas Current and southward-flowing Brazil Current, as well as by their respective shelf components and countercurrents (e.g., Piola et al., 2000, 2005; Möller et al., 2008; Palma et al., 2008).

Only a limited number of studies aimed at identifying the terrestrial sources and related transport paths of these marine sediments (e.g., Urien and Ewing, 1974; Martins et al., 2005;

Nagai et al., 2013). Covering a broad range of geoscientific methods, these studies focused on the northward transport of coarse Argentinean shelf and fine Plata plume sediments. The most extensive study was undertaken by Mahiques et al. (2008) using Pb- and Nd-isotopes. They showed that Plata plume sediments reach Cape Santa Marta (~28° S) (Fig. 4.1). However, multi-proxy studies of Mahiques et al. (2004, 2009), Gyllencreutz et al. (2010), and the enviro-magnetic investigation of Mathias et al. (2014) could detect the presence of Plata plume sediments up to São Sebastião Island (~24° S; Fig. 4.1). Besides that, Argentinean shelf sediments in surface deposits could only be tracked up to the Subtropical Shelf Front (STSF) at 34°–36° S (Fig. 4.1) based on clay- and heavy-mineral investigations of Campos et al. (2008) and Corrêa et al. (2008), respectively. Both studies are generally in agreement with the results of Mahiques et al. (2008), while in addition the clay- and heavy-mineral assemblages revealed that deposits to the south of the STST underwent little alteration due to weathering. In contrast, to its north the deposits show well advanced weathering, hinting at the presence of relict deposits.

At the Rio Grande Cone (31°–34° S; Fig. 4.1), Razik et al. (2013) were able to identify the deposition of predominantly fine sands originating from the Argentinean shelf during the Mid Holocene, while Plata plume silts and clays represented a minor sediment portion. Razik et al. (2013) were able to distinguish between these two sediment provinces based on rock-magnetics, major elements and grain-size distributions of bulk sediments. However, Nd-isotope investigations performed on bulk material from the same sediment core mainly reflected the properties of the fine Plata plume sediments during the Mid Holocene, with a slight shift towards Argentinean shelf values (Lantzsch et al., 2014). Thus, the recent northward transport of Argentinean shelf sediments still remains unclear. As Nd is a heavy element with the most frequent abundance in ores as monazite and bastnäsite, it tends to be enriched in the clay fraction of riverine and marine sediments (e.g., Revel et al., 1996; Innocent et al., 2000). This raises the question of whether Nd-isotopic values measured on bulk sediments might over-represent the properties of fine fractions and mask those of coarser ones, even if these predominate.

Magnetic mineral diagnostics provide a range of sedimentary parameters to (i) determine source areas, (ii) identify pathways of aeolian, fluvial and marine sediments, and (iii) detect authigenic Fe-minerals formed by biomineralization, abiotic precipitation and diagenetic processes (e.g., Liu et al., 2012). Although magnetic Fe-oxide and Fe-sulfide minerals are relatively low in species number and concentration, even trace contents [ppm] can be quantified by rock-magnetic methods evidencing their magmatic, meta-morphic, pedogenic, biogenic, or diagenetic origin (e.g., Maher, 1986; Franke et al., 2007). Sedimentary major-element signatures can yield complementary information on terrestrial climate (i.e., weathering) conditions. Govin et al. (2012) suggest that Fe/K is a suitable marker to distinguish between less chemically weathered sediments from arid (subtropical) regions and more weathered ones from humid (tropical) areas in SE South America.

Here, we aim at identifying the sources and the mixing degree of terrigenous sediments depo-sited at the SE South American continental margin. For the first time rock-magnetic and major-element properties of sediments from 20°

to 48° S off SE South America are investigated and compared with clastic grain-size distributions. Rock-magnetic parameters and major-element concentrations are used to calculate five concentration-independent interparametric ratios (χ_{fd}%, ARM/IRM, $S_{0.3T}$, SIRM/Fe, and Fe/K). They serve as input data for fuzzy c-means (FCM) cluster analysis and non-linear mapping (NLM) to detect regionally coherent clusters representing petrologically and climatically distinct sedimentary provinces and transport pathways.

4.3. Environmental and sedimentary setting

4.3.1. Hydrography off SE South America

The SE South American continental margin (ca. 20°–55° S) is under the influence of tropical and extratropical oceanographic regimes (Fig. 4.1). Its southern sector (38°–55° S) is affected by the cold northward-flowing Malvinas Current, while its northern sector (20°–38° S) is affected by the warm southward-flowing Brazil Current (Palma et al., 2008). Both currents converge at the Brazil-Malvinas Confluence Zone. As a continuation of this confluence on the shelf, the north-south oriented STSF divides the cold and relatively fresh Subantarctic Shelf Water from the warm and more saline Subtropical Shelf Water (Piola et al., 2000, 2005; Möller et al., 2008). The STSF is created by the dynamic effect of an arrested topographic wave (Csanady, 1978), which is set up by a cross-shelf pressure gradient imposed by the Malvinas Current and acts as an export path of shelf waters to the slope (Piola et al., 2008). To the south of the STSF, the PDB discharges large amounts of freshwater (710 km^3 yr^{-1}) at the Plata estuary (e.g., Bernardes et al., 2012 and references therein). The northeastward-directed Brazilian Coastal Current carries this Plata Plume Water at the inner continental shelf along the Uruguayan coast towards South Brazil (Souza and Robinson, 2004). The Plata Plume Water frequently reaches 24° S during austral fall and winter (Piola et al., 2008; Palma et al., 2008), sporadically reaching as far north as 22° S (Fig. 4.1) (Stevenson et al., 1998). The Plata Plume Water mainly consists of Plata River water with a minor contribution from the Patos Lagoon (63 km^3 yr^{-1}) (Campos et al., 2013 and references therein), while riverine runoff between 22° and 34° S is negligible under modern conditions (Campos et al., 2008; Corrêa et al., 2008).

The southern sector (south of 38° S; Fig. 4.1) of the study area is overflowed by the Subantarctic Shelf Water at its shallowest levels (0–100 m). It mainly originates from water masses entering the Atlantic via the Magellan Strait at ~52° S and is mixed with local coastal freshwater inputs along its way, as well as with water masses entering at the shelf break (Palma et al., 2008). The outer continental shelf and the slope are influenced by the Malvinas Current (Palma et al., 2008; Preu et al., 2013), which transports the Subantarctic Water (100–500 m), the Antarctic Intermediate Water (500–1000 m), and the Circumpolar Deep Water (1000–4000 m). All of them enter the Atlantic via the Drake Passage at ~55° S. The Argentinean basin below 4000 m is under influence of the Antarctic Bottom Water mainly originating from the Weddell Sea (Piola and Matano, 2001).

The northern sector (20°–38° S; Fig. 4.1) of the study area is overflowed by the Subtropical Shelf Water streaming southward from Cape Frio (~24° S) on the mid shelf. It is formed by mixing of Tropical Water with South Atlantic Central Water, and subordinately with Plata Plume Water (Palma et al., 2008). At lower water depths, the outer shelf and the slope are affected by the Brazil Current (Stramma and Peterson, 1989;

Boebel et al., 1999; Palma et al., 2008). The Brazil Current is generated at the slope between 10° and 15° S due to bifurcation of the westward-flowing South Equatorial Current (Stramma and England, 1999; Piola and Matano, 2001). The Brazil Current's upper layer consists of the Tropical Water and South Atlantic Central Water (at least 0–1000 m). At intermediate depths, the bifurcation of the South Equatorial Current shifts south to ~24° S, while the southward-flowing branch of the recirculated Antarctic Intermediate Water (1000–1500 m) merges with the Brazil Current (e.g., Boebel et al., 1999; Preu et al., 2013). In contrast, the northern branch of the Antarctic Intermediate Water together with a portion of the South Atlantic Central Water flows northwards along the East Brazilian slope (intermediate counter current at depths of 400–1500 m). At lower water depths (1500–3500 m), the southward-flowing western boundary undercurrent transports the North Atlantic Deep Water originating from high latitudes of the North Atlantic.

4.3.2. Sedimentology off SE South America

The continental shelf and slope off the Pampas (south of 36° S; Fig. 4.1) are covered with fine siliciclastic sands (Urien and Ewing, 1974; Parker et al., 1997; Frenz et al., 2003; Martins et al., 2005). Minor contents of very fine and medium sand, and occasionally even gravel and mud, are found off the Plata estuary and at contourite terraces of the mid and lower slope (Frenz et al., 2003; Hernández-Molina et al., 2009; Bozzano et al., 2011; Preu et al., 2013). These sands contain high concentrations of igneous detritus (Potter, 1984, 1986; Bozzano et al., 2011) and were mainly deposited as coastline sediments under sea-level lowstand conditions, being later reworked by coastal processes under a predominantly northward along-shore transport.

The continental margin off Uruguay and South Brazil up to Cape Santa Marta (29°–36° S; Fig. 4.1) shows a more heterogeneous sedimentary pattern. Along the inner shelf (0–50 m water depth), siliciclastic sands constitute ~50% of the surface sediments (Urien and Ewing, 1974; Potter, 1984, 1986). On the outer shelf (100–160 m water depth) relict sands make up to 75% of the total sediment (Urien and Ewing, 1974; Franco-Fraguas et al., 2014; Lantzsch et al., 2014). Generally, the upper and mid continental slope is composed of sandy (<50%) and silty (50–65%) deposits. However, the mid shelf (50–100 m; in particular the Plata mudbelt, a recently filled lowstand paleo-valley of the Plata River to the northeast of the Plata estuary; e.g., Lantzsch et al., 2014) and the continental slope of the Rio Grande Cone (31°–34° S) constitute exceptional sediment compositions: Their shelf deposits are characterized by coarse silts or even finer sediments (Urien and Ewing, 1974; Laborde, 1997; Violante and Parker, 2004; Lantzsch et al., 2014), which turn into silty to clayey muds at the upper and mid slope (Frenz et al., 2003). Those fine deposits were described as magnetite-rich sediments transported with the Plata Plume Water and as being deflected off-shelf at the STSF (Razik et al., 2013 and references therein). Further to the north, clay content increases and reaches 60% at the slope off Cape Santa Marta (Frenz et al., 2003).

The continental margin off SE Brazil between Cape Santa Marta and Cape Frio (23°–29° S; Fig. 4.1) exposes the coarsest deposits (125–500 µm) at the inner shelf, which decrease in grain-size towards the mid shelf. There, they show very 'patchy' depositional patterns being locally identified as coarse, medium, or fine silts

(Mahiques et al., 2004; Gyllencreutz et al., 2010; Reis et al., 2013). Towards the outer shelf and the slope, sediments coarsen and are characterized as coarse sands (Reis et al., 2013). These 'patchy' distributions are an effect of intensive sediment remobilization and redistribution due to frequent up- and downwelling. Eddies and vertical movements in the water column are generated by the meandering Brazil Current (Campos et al., 2000; Silveira et al., 2008; Calado et al., 2010).

The investigated continental margin off East Brazil to the north of Cape Frio is confined to 20°–23° S (Fig. 4.1). The continental shelf to the north of the Paraíba do Sul River shows the coarsest sediments in this part of the study area (i.e., coarse sands) (Reis et al., 2013). At the inner and the mid shelf southward of the Paraíba do Sul River mouth, sediments become finer (i.e., medium sands) and change to fine sands to the northeast of Cape Frio. Directly southward of Cape Frio, surface deposits are identified as muds. This fining pattern is caused by the southward-directed transport of the Brazil Current (Oliveira et al., 2012). The upper slope (200–400 m) is primarily covered with medium to coarse sandy contouritic deposits (Viana, 2002). The middle slope (400–1500 m) is characterized by erosional surfaces, while the lower slope (1500–3500 m) serves as a deposition center for fine to medium sandy patches and separated plastered contouritic drifts.

4.4. Materials and methods

4.4.1. Materials

This study is based on 25 surface sediment samples (uppermost 1.5 cm) collected at the continental margin of SE South America during RV Meteor cruises M23/2 (Bleil et al., 1994), M29/1+2 (Schulz et al., 1999), M46/2+3 (Schulz et al., 2001; Bleil et al., 2001), M49/3 (Bleil et al., 2002), and M78/3a+b (Krastel and Wefer, 2011) (Fig. 4.1; Table 4.1). They were obtained with box and multicorers from water depths between 16 and 1805 m. The sediments on the continental slopes off Argentina and Uruguay are mainly composed of olive and olive gray very fine to medium sands. The respective shelf deposits are similar in grain size, displaying colors as dark grayish brown, dark olive brown, and very pale brown in addition to the previously mentioned ones. The clayey silts, deposited at the mid continental shelf off Uruguay and the mid continental slope off South Brazil, are brown and grayish brown. Silty sands at the eastern and southeastern Brazilian continental margin display the broadest color diversity, ranging from light brownish gray over grayish brown to pale brown.

Each sample was subsampled for enviromagnetic and major-element powder analyses. The grain-size distributions of the terrigenous fractions were determined on the same material as used for the enviromagnetic investigation (standard 6.2 cm^3 plastic cubes). The 1.5-cm thick surface-sediment samples used in this study comprise a varying time span of roughly 40–150 years, when common shelf and slope sedimentation rates of 10–40 cm kyr^{-1} are expected (e.g., Chiessi et al., 2007). As box and multicorers are suitable to obtain unconsolidated, little viscous surface sediments, one can presume that neither material loss nor stratigraphic disturbances occurred during core recovery.

4.4.2. Methods

4.4.2.1. Grain-size distributions of the terrigenous fraction

The grain-size distributions of the terrigenous sediment fraction were determined by laser

Table 4.1

Surface-sediment samples from the continental margin off SE South America analyzed in this study.

Surface sample (GeoB)	Latitude [°]	Longitude [°]	Water depth [m]	RV METEOR cruise	Recovery method
2102-1	-24.0	-41.2	1805	M23/2	MUC
2106-1	-27.1	-46.5	502	M23/2	MUC
2125-2	-20.8	-39.9	1542	M23/2	MUC
2701-4	-37.8	-55.0	576	M29/1	MUC
2709-6	-41.5	-57.1	1087	M29/1	MUC
2712-2	-43.7	-59.3	1228	M29/1	MUC
2719-2	-47.4	-60.1	684	M29/1	MUC
2801-1	-37.0	-54.2	490	M29/2	MUC
2813-1	-35.5	-52.6	508	M29/2	MUC
6201-3	-26.7	-46.4	473	M46/2	MUC
6204-2	-28.7	-47.4	578	M46/2	MUC
6212-2	-32.7	-50.1	1009	M46/2	MUC
6234-1	-36.7	-53.5	1140	M46/2	MUC
6301-1	-36.1	-55.4	30	M46/3	MUC
6312-1	-38.4	-55.3	435	M46/3	MUC
6313-2	-39.4	-55.4	733	M46/3	MUC
6908-1	-24.9	-44.5	500	M49/3	MUC
13801-1	-36.1	-53.3	244	M78/3a	MUC
13802-1	-36.1	-53.3	141	M78/3a	GBC
13813-1	-34.7	-53.6	58	M78/3a	GBC
13817-3	-34.5	-53.1	62	M78/3a	GBC
13834-1	-35.1	-53.7	16	M78/3a	GBC
13839-2	-35.5	-53.3	67	M78/3a	GBC
13845-2	-38.2	-55.1	550	M78/3b	MUC
13846-1	-38.1	-55.0	637	M78/3b	MUC

MUC = Multi Corer GBC = Giant Box Corer

particle sizing after chemical removal of organic carbon, calcium carbonate ($CaCO_3$), and biogenic opal. For this purpose, samples of 2–4 g were consecutively treated with 10 ml H_2O_2 (35%$_{v/v}$), 10 ml HCl (10%$_{v/v}$), and 6 g NaOH-pellets in 100 ml aquatic solutions as described by Mulitza et al. (2008). Between every chemical reaction, samples were washed with demineralized water. To avoid clay-mineral aggregation, ~300 mg of $Na_4P_2O_7 \cdot 10(H_2O)$ was added to the sediment solutions before analysis.

The analyses were performed using a BECKMANN-COULTER LS200 laser particle sizer coupled to a water demineralization and degassing device at the *MARUM – Center for Marine Environmental Sciences in Bremen (Germany)*. The grain-size detection range of the equipment is specified as 0.04–2000 µm. Due to the sediment pre-treatment and its settling properties, abundances of particles <2 µm might be underrepresented. For data processing the BECKMANN-COULTER Particle Characterization software v.3.01 was used.

4.4.2.2. Major-element concentrations

Major-element (i.e., Al, Ca, Fe, K, Si, and Ti) concentrations were detected by energy dispersive polarization X-ray fluorescence (EDP-

XRF). 3–6 ml per bulk-sediment sample (~0.5–5 g of dry sediment) were freeze-dried, then powdered and homogenized with an agate mortar, and loosely packed into plastic sample holders with bottoms of Ultralene® X-ray transmission foil. EDP-XRF spectroscopy was performed on a SPECTRO XEPOS instrument at the *MARUM*, as described in Wien et al. (2005) and Tjallingii et al. (2007). The device was operated with the Spectro X-Lab Pro v.2.4 software following the Turboquant method of Schramm and Heckel (1998). The analytical quality of the measurements was assessed by repeated analyses of the certified standard reference material MAG-1 (Govindaraju, 1994). The measured values were within 1% of accepted values. The root mean square deviation of replicated samples is ~2%. In the following, we focus on the Fe/K values.

4.4.2.3. Magnetic susceptibility and remanence measurements

Magnetic frequency-dependent susceptibility χ_{fd}% was measured on a BARTINGTON MS2 unit with a B-type sensor operating at frequencies of 0.46 kHz and 4.6 kHz. The resolution of this sensor is set to 1.0×10^{-6} SI, while each sample was measured 3 times with subsequent background-measurements after each remeasurement. The measurement sequence for a sample was restarted when the difference between remeasured values exceeded the sensor resolution. This procedure avoids impacts on the highly sensitive χ_{fd}% measurements, which can be caused by changing room and equipment temperatures, as well as by electronic system drifts. As the volume susceptibility κ values (not shown here) were all above 130×10^{-6} SI (reaching 3500×10^{-6} SI), the χ_{fd}% values can be treated as reliable (e.g., Dunlop and Özdemir, 2001).

Measurements of the anhysteretic and isothermal remanent magnetizations (ARM and IRM, respectively) were performed with a fully automated 2G ENTERPRISES 755R DC-SQUID pass-through magnetometer at the *Marine Geophysics Section, University of Bremen (Germany)*. The sensitivity of this equipment is 1.0×10^{-12} Am^2 corresponding to 0.1613×10^{-6} A m^{-1} for a sample of 6.2 cm^3.

During ARM measurement, the fractions were magnetized in a 0.1 T alternating magnetic field (biasing direct field of 40 µT) followed by demagnetization at 11 steps. IRM was acquired at 22 steps from 0 to 700 mT in an internal pulse coil and at 5 more steps up to 2.6 T in an external pulse coil. After reaching the external pulse-coil maximum field of 2.6 T, the samples were treated as magnetically saturated and the corresponding IRM is labeled SIRM. Although the saturations of hematite and goethite are not complete (pure hematite and goethite require saturation fields of 1–5 T and 10 T, respectively; e.g., Dunlop and Özdemir, 2001), the SIRM values are sufficient for the relative quantification purposes of the present study. The magnetic remanence data was used to calculate interparametric ratios like ARM/IRM obtained in respective fields of 0.1 T, as well as the saturation ratio ($S_{0.3T}$) being a ratio between the remanences acquired at 0.3 T and 2.6 T direct fields. These ratios were accomplished by χ_{fd}%, SIRM/Fe and Fe/K.

4.4.2.4. Fuzzy c-means cluster analysis and non-linear mapping

Cluster analysis is a multivariate technique to discern similarities among multi-parametric data sets. Applied to sediment properties, it can detect groupings and their relations representing possible sediment sources and mixing, which may not be evident from univariate or bivariate analyses (Dekkers et al, 1994; Schmidt et al.,

1999; Urbat et al., 1999; Watkins and Maher, 2003; Watkins et al., 2007; Köhler et al., 2008).

In FCM cluster analysis (Bezdek, 1981), likeness or similarity of a sample with respect to a cluster center is indicated by a continuous function between 0 (completely different) and 1 (exactly the same). The memberships of one sample to all clusters sum up to 1. Hence, FCM cluster analysis allows gradual membership changes between clusters, while intermediate cases can be recognized by similarly close memberships to multiple clusters. NLM basically determines a 2- or 3-dimensional image of a multi-dimensional data cloud, such that the interdata distances are minimally distorted during an iterative process (e.g., Vriend et al., 1988; Urbat et al., 1999). A great advantage of NLM, as an independent evaluation technique for FCM cluster analysis, is that no presumptions about the number of clusters or even the existence of subgroups are required.

In this study, for the FCM cluster analysis we used the 'Fuzzy Logic Toolbox' of the software MATHWORKS Matlab R12 applying the FCM algorithm of Bezdek (1981). The same software was used for NLM, based on the algorithm of Sammon (1969), and for calculation of Euclidean distances between cluster-center positions in a multi-dimensional parameter space. Prior to FCM cluster analysis and NLM, all data values were standardized (i.e., normalized to a mean of 0 and a standard deviation of 1), avoiding over-representation of sediment characteristics due to large parameter values or high variability. Subsequently, the 'Komolgorov-Smirnov test' for a significance level of α = 0.02 (two-tailed) (e.g., Davis, 1986) was successfully applied to evaluate the data sets for normal or log-normal distributions (Fig. 4.2). Knowledge of this statistical parameter is crucial for the characterization of sediment populations and for the applicability of multivariate analyses (Dekkers et al, 1994; Schmidt et al., 1999; Urbat et al., 1999; Watkins and Maher, 2003; Watkins et al., 2007; Köhler et al., 2008). Although our data sets contain 3 outliers deviating from the mean value by >3σ (χ_{fd}% of GeoB 13813-7 and 138171-1, Fig. 4.2a; $S_{0.3T}$ of GeoB 13834-1, Fig. 4.2b), we decided not to exclude them from the analysis as they carry meaningful petrologic information. Further, FCM cluster and NLM results performed with and without the outliers did not show any significant change in the definition of the cluster centers (not shown here).

Input parameters for the FCM cluster analysis and NLM were carefully chosen considering that a parameter must have a clear interpretation and does not represent the same property as another parameter. Further, only concentration-independent interparametric ratios were used to differentiate the sediment-provenance signal from transport signatures and to avoid magnetic dilution by diamagnetic phases (e.g., quartz and $CaCO_3$). Transport usually leads to sorting and mineral enrichment or depletion as a function of the transporting medium's flow energy. Due to a relatively high similarity between the investigated samples and due to the bimodal parameter-frequency distributions (Fig. 4.2b–e), the Pearson's correlation coefficient could not exclude a linear dependence between all of the interparametric ratios. An initial series of FCM cluster analyses was therefore performed with various 4–8 interparametric ratios per run (not shown here). From these trials, we selected a crucial minimum of five interparametric ratios (i.e., χ_{fd}%, ARM/IRM, $S_{0.3T}$, SIRM/Fe, and Fe/K) and excluded others due to negligible influence on clustering. Their simplified environmental interpretation is summarized in Table 4.2.

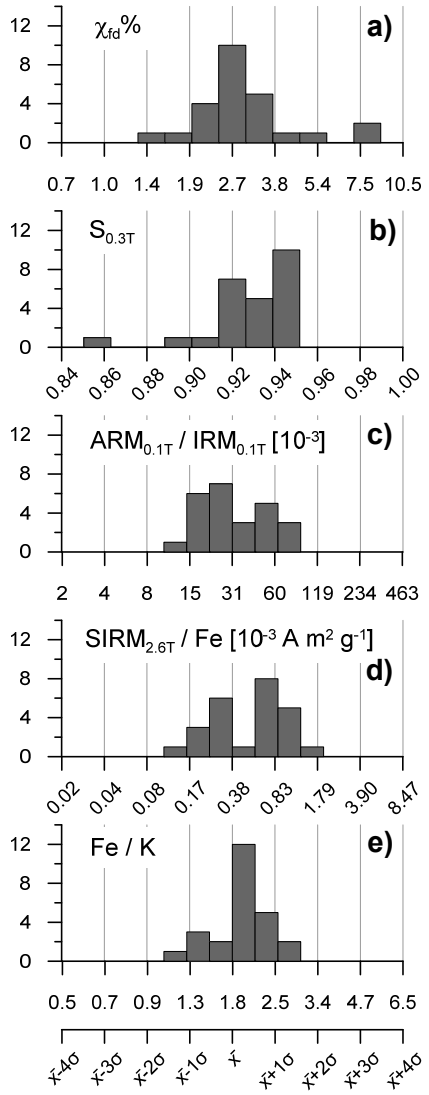

Fig. 4.2. Parameter-frequency distributions after standardization prior to fuzzy c-means cluster analysis: (a) frequency-dependent susceptibility (χ_{fd}%); (b) saturation-ratio ($S_{0.3T}$); (c) ratio of anhysteretic remanent magnetization and isothermal remanent magnetization ($ARM_{0.1T}/IRM_{0.1T}$); (d) ratio of saturation IRM and iron ($SIRM_{2.6T}$/Fe); and (e) iron-potassium ratio (Fe/K).

The interparametric ratios χ_{fd}% and ARM/IRM describe the magnetic grain size (domain state) of magnetite in various ranges from (i) superparamagnetic (SP; <20 nm) over (ii) single-domain (SD; 20–100 nm) to (iii) multi-domain (MD; >10 µm) (Table 4.2). Magnetogranulometry must not be confused with clastic grain sizes, because small magnetic particles can be contained within larger (carbonate, quartz, and feldspar) so-called 'host' grains, which mainly mirrors the origin or genesis (e.g., Hounslow and Maher, 1996; Otofuji et al., 2000; Hounslow and Morton, 2004). $S_{0.3T}$ and SIRM/Fe report the relative influences of magnetically 'soft' (magnetite and maghemite) and 'hard' (hematite and goethite) minerals, as well as paramagnetic Fe-bearing clay minerals (Table 4.2). Fe/K marks the difference between less and more chemically weathered sediments from arid or humid areas, respectively. Those five interparamagnetic ratios are influenced by petrological characteristics of the source rock and by the climate in the sediment-source area affecting weathering processes (e.g., magnetic mineral dissolution and neoformation).

The selected input parameters for FCM cluster analysis and NLM are able to: (i) determine source areas; (ii) identify pathways of eolian, fluvial and marine sediments; and (iii) detect authigenic Fe-minerals formed by biomineralization, abiotic precipitation and diagenetic processes. For detailed explanations on rock and enviromagnetic properties, please refer to Liu et al. (2012). The obtained magnetic data are suitable for a provenance study since diagenetically formed greigites could be excluded by the absence of gyro-remanence (data not shown) after ARM-demagnetization. Due to throughout strong magnetic signals, post-depositional diagenetic alteration of Fe-oxides is unlikely. Potential bias of source-rock signals by paramagnetic Fe-sulfides (e.g., pyrite) is bypassed by avoiding absolute magnetic susceptibility values.

4.5. Results

Sediment dynamics at continental margins is generally mirrored by clastic grain-size distributions. As this dynamics has to be taken into account prior to the identification of sediment-source properties, results of the grain-size

Table 4.2

Interparametric ratios based on rock-magnetic and major-element properties listed together with their environmental interpretations (e.g., Dunlop and Özdemir, 2001; Evans and Heller, 2003; Liu et al., 2012; Govin et al., 2012) and used as input parameters for fuzzy c-means cluster analysis and non-linear mapping.

Input parameter	'Simplified' interpretation of fuzzy c-means cluster analysis
χ_{fd}%	input of ultrafine (<20 nm) igneous or pedogenic superparamagnetic particles (mainly magnetite and maghemite); related to source-rock petrology or climate / soil weathering
$S_{0.3T}$	ratio between magnetization carried by 'soft' magnetic particles (magnetite and maghemite) and 'hard' magnetic particles (hematite and goethite); related to source-rock petrology and pedogenesis
$ARM_{0.1T}$ / $IRM_{0.1T}$	ratio between mainly single-domain (20–100 nm) and multi-domain (>10 μm) particles of magnetite (or maghemite); related to source-rock petrology and pedogenesis
$SIRM_{2.6T}$ / Fe	relation between all remanence carrying minerals (e.g. magnetite / maghemite, hematite and goethite) and the entire sedimentary iron (mainly contained within paramagnetic clay minerals); related to source-rock petrology and climate / soil weathering
Fe / K	ratio between sedimentary iron and potassium; related to source-rock petrology and soil weathering

analysis are shown first (Fig. 4.3). Subsequently, outcomes of the FCM cluster analysis and NLM are presented (Fig. 4.4).

4.5.1. Clastic grain-size distributions

Surface sediments found at the continental slope of Patagonia, the Pampas, and Uruguay (Fig. 4.3a) are mainly composed of very fine to medium sands with only subordinate amounts of medium to coarse silts. Even finer particles are only sporadically admixed in small amounts. The mode values are located between 100–200 μm. The southernmost sample of our study area (GeoB 2719-2; Fig. 4.1) shows an exceptionally coarse bimodal distribution in the 100–300 μm range. The Pampean and Uruguayan shelf sediments are exclusively composed of very fine to fine sands with mode values ranging from 100 to 200 μm (Fig. 4.3b). The shallowest sample in this study (GeoB 13834-1; Table 4.1) from a water depth of 16 m has a slightly coarser mode of ~250 μm likely due to grain-size sorting by strong surface currents. Samples from the mid shelf off Uruguay (i.e., Plata mudbelt) and from the Rio Grande Cone off South Brazil contain no sands and display mode values of ~6 μm (Fig. 4.3c). Surface sediments from the East and SE Brazilian margins exhibit a bimodal grain-size distribution (Fig. 4.3d), with a very fine silty mode at 4–8 μm and a coarser silty to very fine sandy mode at 40–90 μm. Solely based on grain-size distributions, the slope samples off SE Brazil are not distinguishable from those off East Brazil. The abundances of particles around 1000 μm, present in some of the distributions, show no systematic pattern and seem to be stochastic. It is assumed that they are generated by sporadically coarse, local debris and are not taken into further consideration in the subsequent interpretation chapter.

4.5.2. Clusters of terrigenous sediment provinces

Since the most appropriate number of clusters is not *a priori* known, FCM cluster solutions were calculated for cluster numbers ranging between 2 and 5. The best solution was chosen by comparing the results from a sedimentological and geological perspective, as well as from a numerical viewpoint by calculating the partition coefficient *F* (should be highest) and the classi-

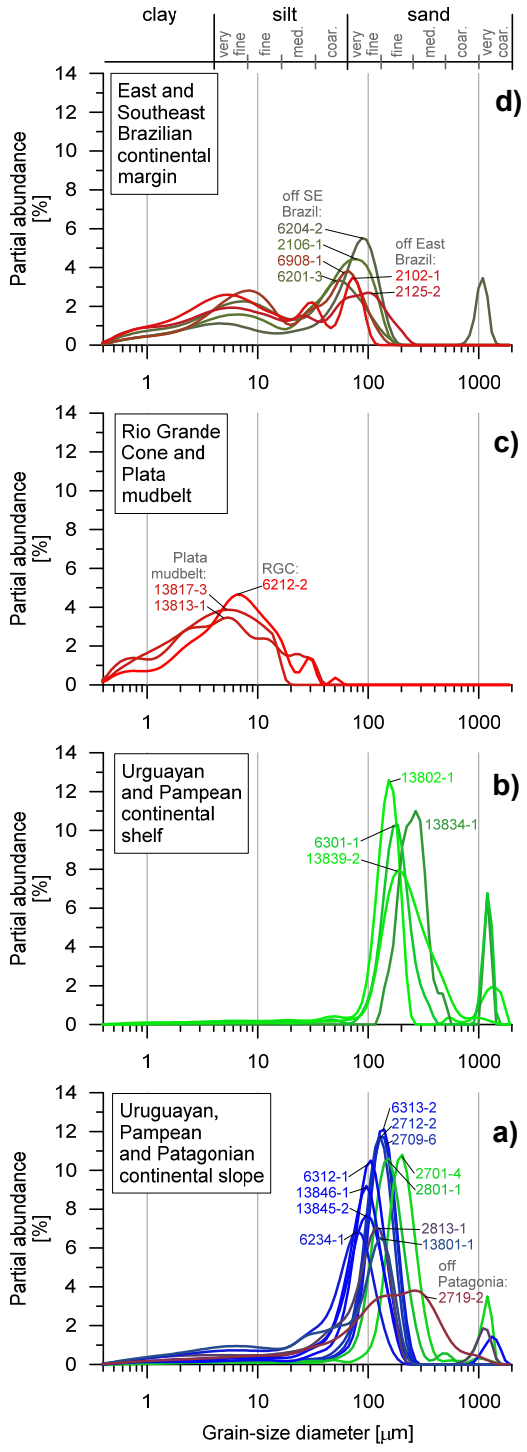

Fig. 4.3. Grain-size distributions of the terrigenous fractions from (a) Patagonian, Pampean, and Uruguayan slope; (b) Pampean and Uruguayan shelf; (c) Plata mudbelt at the Uruguayan inner shelf and Rio Grande Cone (RGC) at the South Brazilian slope; and from (d) the Southeast and East Brazilian slope. Data grouping refers to the samples' presence on the slope or shelf, as well to their geographic location. Colors refer to cluster memberships as in Fig. 4.4.

fication entropy *H* (should be lowest) (Bezdek et al., 1984). The values of *F* and *H* are given in Table 4.3 for all tested FCM cluster solutions. Although *F* and *H* point towards the 2-cluster solution, the 3-cluster solution was chosen because it shows a more specific solution from a sedimentological and geological perspec-tive, while having the second highest *F* and the second lowest *H*. In addition, the 3-cluster solution inherits the 2-cluster solution. Thus in the following, only the most insightful 3-cluster solution will be shown.

The 3 sediment clusters defined by FCM cluster analysis (Fig. 4.4a) were named after their prevailing geographic occurrences as follows: (i) cluster 1 – 'Plata plume'; (ii) cluster 2 – 'Pampean shelf'; and (iii) cluster 3 – 'Pampean slope'. Cluster center 1 is characterized by the highest χ_{fd}%, ARM/IRM and Fe/K values and the lowest SIRM/Fe values (Table 4.4). Cluster center 2 is defined by rather intermediate values for almost all ratios, except for the lowest $S_{0.3T}$ and Fe/K values. Cluster center 3 is defined by the highest values of $S_{0.3T}$ and SIRM/Fe. The Euclidean distances between the cluster centers (Table 4.5) reveal that cluster 1 is the most distant from the other cluster centers in the 5-dimensional parameter space. This result implies that cluster 1 is more dissimilar from clusters 2 and 3, which are closer to each other. It is important to note that

Table 4.3

Partition coefficient *F* (should be highest) and classification entropy *H* (should be lowest) used for cluster number assessment. Although *F* and *H* suggest a 2-cluster solution, the chosen 3-cluster solution delivers more conclusive results in terms of terrigenous sediment provenance (see text for details).

n clusters	*F*	*H*
2	0.689	0.209
3	0.637	0.282
4	0.633	0.318
5	0.576	0.384

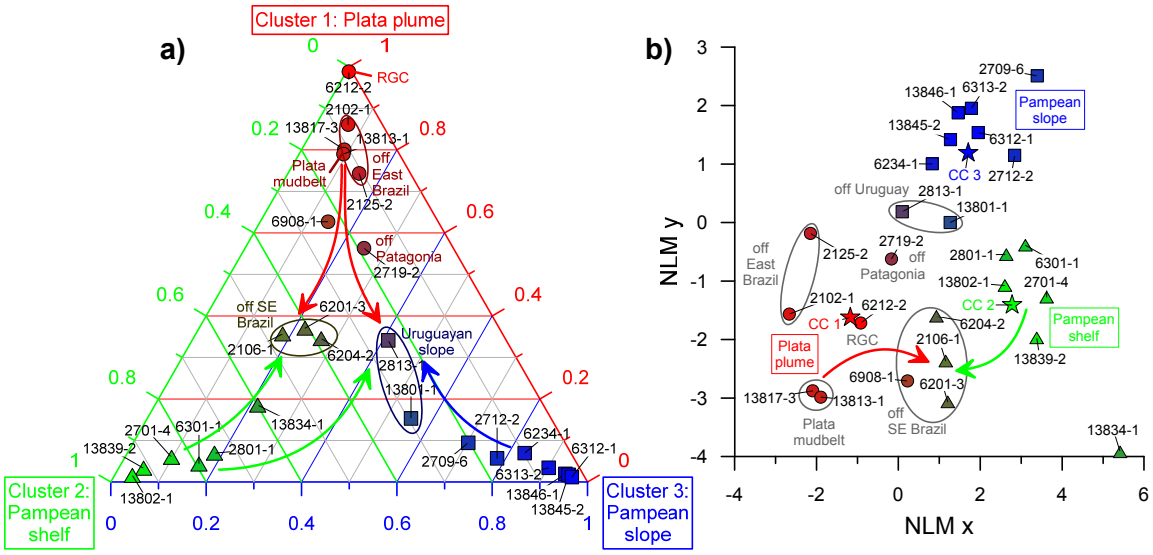

Fig. 4.4. Results of the fuzzy c-means cluster analysis showing 25 samples and their memberships to the 3 cluster centers (CC) in (a) a ternary diagram, and (b) after transformation from the 5-dimensional parameter space to a 2-dimensional plane by non-linear mapping (NLM; axes have no units). The cluster centers are located at the corners of the ternary diagram in panel (a) and represented as stars in panel (b). CC 1 is displayed in red (RGB: 255 0 0), CC 2 in green (RGB: 0 255 0), and CC 3 in blue (RGB: 0 0 255). Samples associated to multiple clusters are displayed in the color of accordingly interpolated RGB values.

the samples from the slope off SE Brazil present a mixed composition of clusters 1 and 2 (Fig. 4.4a), while the shallowest slope samples off Uruguay show contributions from all three clusters. Sample GeoB 2719-2 from the Patagonian slope differs significantly from the Pampean slope sediments further to the north and is accounted to cluster 1.

Almost the same cluster arrangement and mixing is independently achieved by NLM (Fig. 4.4b), supporting the choice of the 3-cluster solution. The robustness of the NLM results is assessed from the 'Sammon's error', which reaches here 0.007 (Sammon, 1969). This very low value reveals almost no distortion of the data projection from the 5-dimensional parameter space into the 2-dimensional plane. The cluster distribution derived from NLM is also in agreement with the Euclidean distances between the cluster centers (Table 4.5). However, NLM does not only serve as an evaluation tool for FCM cluster analysis. NLM allocates cluster centers within their respective data clouds (Fig. 4.4b) rather than at extreme corners, as it is the case for the ternary diagram (Fig. 4.4a), providing additional information on terrigenous sediment provinces. For example, the sample from the Rio Grande Cone (i.e., GeoB 6212-2), located at the uppermost corner of the ternary diagram (RGC; Fig. 4.4a), does not represent a specific sediment source. Its properties are just the most similar to those of cluster center 1 as seen in NLM (Fig. 4.4b). Beyond that, the northernmost sample (GeoB 6908-1) from the slope off SE Brazil is grouped closer to other SE Brazilian slope samples in NLM (Fig. 4.4b) than it can be inferred from the ternary diagram representation between sample GeoB 6908-1 and other SE Brazilian samples.

The presented concentration-independent inter-parametric ratios are suitable to highlight the provenance- and climate-related sediment signatures, while avoiding a significant bias by transport-induced properties (i.e., magnetite enrichment with fining grain size due to its relatively high density). As transport usually leads to particle sorting with respect to the flow velocity, it is mainly mirrored in the grain-size distributions

Table 4.4

Properties of the three cluster centers (CC) calculated by fuzzy c-means cluster analysis.

	CC 1: Plata plume	CC 2: Pampean shelf	CC 3: Pampean slope
χ_{fd}%	5.17	2.64	1.94
$S_{0.3T}$	0.926	0.893	0.936
$ARM_{0.1T}$ / $IRM_{0.1T}$ [10^{-3}]	63.5	25.5	17.6
$SIRM_{2.6T}$ / Fe [10^{-3} A m^2 g^{-1}]	0.177	0.460	0.774
Fe / K	2.42	1.26	1.82

(Fig. 4.3). However, each of the three clusters reveals individual data trends with respect to the clastic grain size (Fig. 4.5). Thus, the inter-parametric ratios are mainly independent from the clastic grain size and contain the 'primary' source-derived signatures targeted in this study. Sedimentary magnetic properties being mainly governed by transport processes would be evident by consistent interparametric trends throughout the entire grain-size range, which however contradicts our observations (Fig. 4.5).

Table 4.5

Euclidean distances of the 3 cluster centers (CC) in the 5-dimensional parameter space. These are graphically displayed in the NLM plane in Fig. 4.4b.

	CC 1: Plata Plume	CC 2: Pampean shelf	CC 3: Pampean slope
CC 1	–	3.77	4.07
CC 2	3.77	–	2.77
CC 3	4.07	2.77	–
Mean distance	3.92	3.27	3.42

4.6. Discussion

Beginning with the geographic distribution of the cluster centers, as well as their jointly considered magnetic and major-element properties, the three indentified sediment provinces of the SE South American continental margin are characterized sequentially. Subsequently, potential terrigenous sediment provenances and transport processes are discussed in relation to previous studies. This section is finished by the discussion of subordinate, but petrologically independent, as well as mixed sediment populations located at the rims of the major sediment provinces.

4.6.1. Plata plume sediment province

Samples with the highest memberships to cluster center 1 are mainly located to the north of the Plata estuary (Fig. 4.6a). The largest of the Plata plume subgroupings (Fig. 4.4b) is constituted by silts deposited within the Plata mudbelt off Uruguay and on the Rio Grande Cone off South Brazil (Fig. 4.3c). These clayey silts are characterized by high proportions of ultra-fine (SP) and fine (SD) magnetite, indicated by high χ_{fd}% and ARM/IRM values, respectively (Fig. 4.5a,c; Tables 4.2 and 4.4). The SD magnetite may represent inclusions in igneous host rocks and the SP magnetite likely reflects pedogenically formed Fe-oxide particles attached to clay minerals. In contrast, SIRM/Fe values are low (Fig. 4.5d). Because magnetosomes provide high SIRM by concurrent low Fe concentrations, such low SIRM/Fe values indicate that bacterial magnetite is unlikely to be the main source for SD magnetite (e.g., Dunlop and Özdemir, 2001; Evans and Heller, 2003; Liu et al., 2012 and

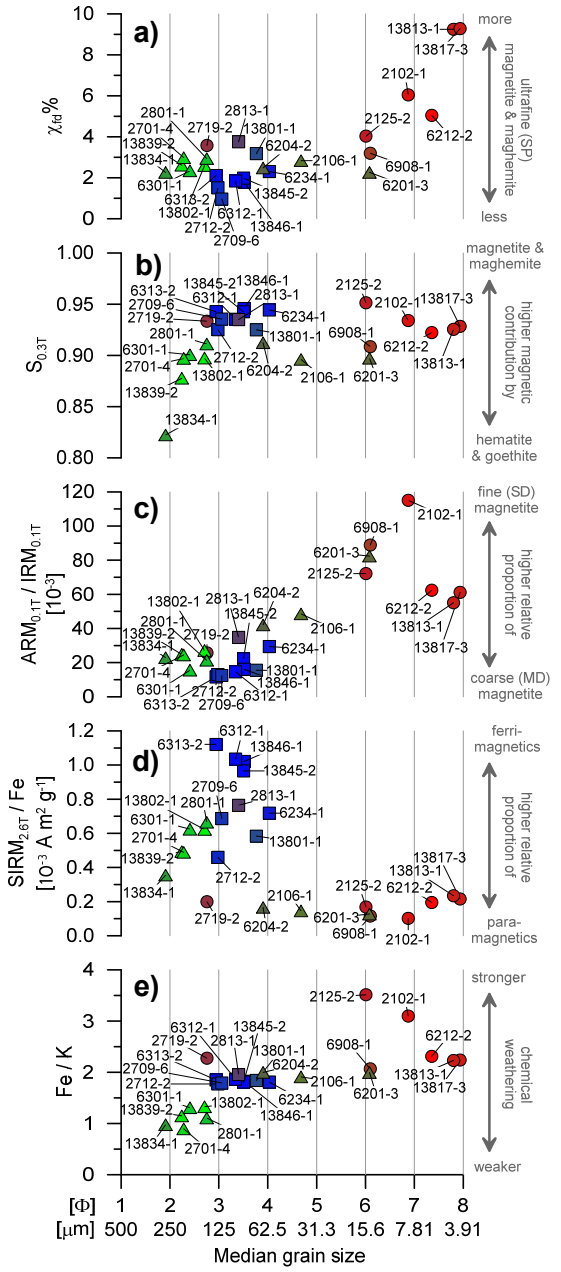

Fig. 4.5. Rock-magnetic and major-element ratios plotted versus the median of clastic grain-size: (a) frequency-dependent susceptibility (χ_{fd}%); (b) saturation-ratio ($S_{0.3T}$); (c) ratio of anhysteretic remanent magnetization and isothermal remanent magnetization ($ARM_{0.1T}/IRM_{0.1T}$); (d) ratio of saturation IRM and iron ($SIRM_{2.6T}$/Fe); and (e) iron-potassium ratio (Fe/K). Colors refer to cluster memberships as in Fig. 4.4. The abbreviations stand for domain states of magnetite and are characterized as superparamagnetic (SP), single-domain (SD), and multi-domain (MD) in respect to particle diameter in Table 4.2.

references therein). In addition, these relatively low SIRM/Fe values likely reflect the large proportion of sedimentary Fe mainly contained in paramagnetic clay minerals rather than in the trace contents of ferrimagnetic Fe-minerals originating from igneous source rocks (e.g., Rumble, 1976; Maher, 1986, 1998; Schwertmann and Taylor, 1989). This result suggests more pronounced chemical weathering of tropical and subtropical soils with a high content of sedimentary Fe. The intense chemical weathering is also supported by high Fe/K values (Fig. 4.5e) (Mulitza et al., 2008; Govin et al., 2012).

Based on these properties, the PDB can be confirmed as the source for these distinctly magnetic sediments. These sediments show relatively high concentrations of magnetic minerals, as their major portion is derived from the Upper Paraná catchment area (Fig. 4.1), where flood basalts and intrusive felsic rocks crop out (Peate, 1997). Both generally show the highest ferrimagnetic Fe-(Ti)-oxide concentrations of all natural rocks (e.g., Rumble, 1976; Evans and Heller, 2003 and references therein). Due to an intense weathering of mainly mafic source rocks (e.g., Allan et al., 1989), these relatively weathering-resistant primary magnetic minerals are common as residual particles in subtropical and tropical soils of SE South America (Schwertmann and Taylor, 1989). The Bermejo River (Fig. 4.1) is the main sediment contributor to the Plata estuary due to the former's steep topographic gradient through unconsolidated Chaco Plain sedimentary deposits (Orfeo and Stevaux, 2002). However, these sediments of Andean origin contain primarily diamagnetic quartz and feldspars (Zárate, 2003). Thus, they should have very limited influence on the rock-magnetic properties of the PDB sediments (e.g., Dunlop and Özdemir, 2001; Evans and Heller, 2003).

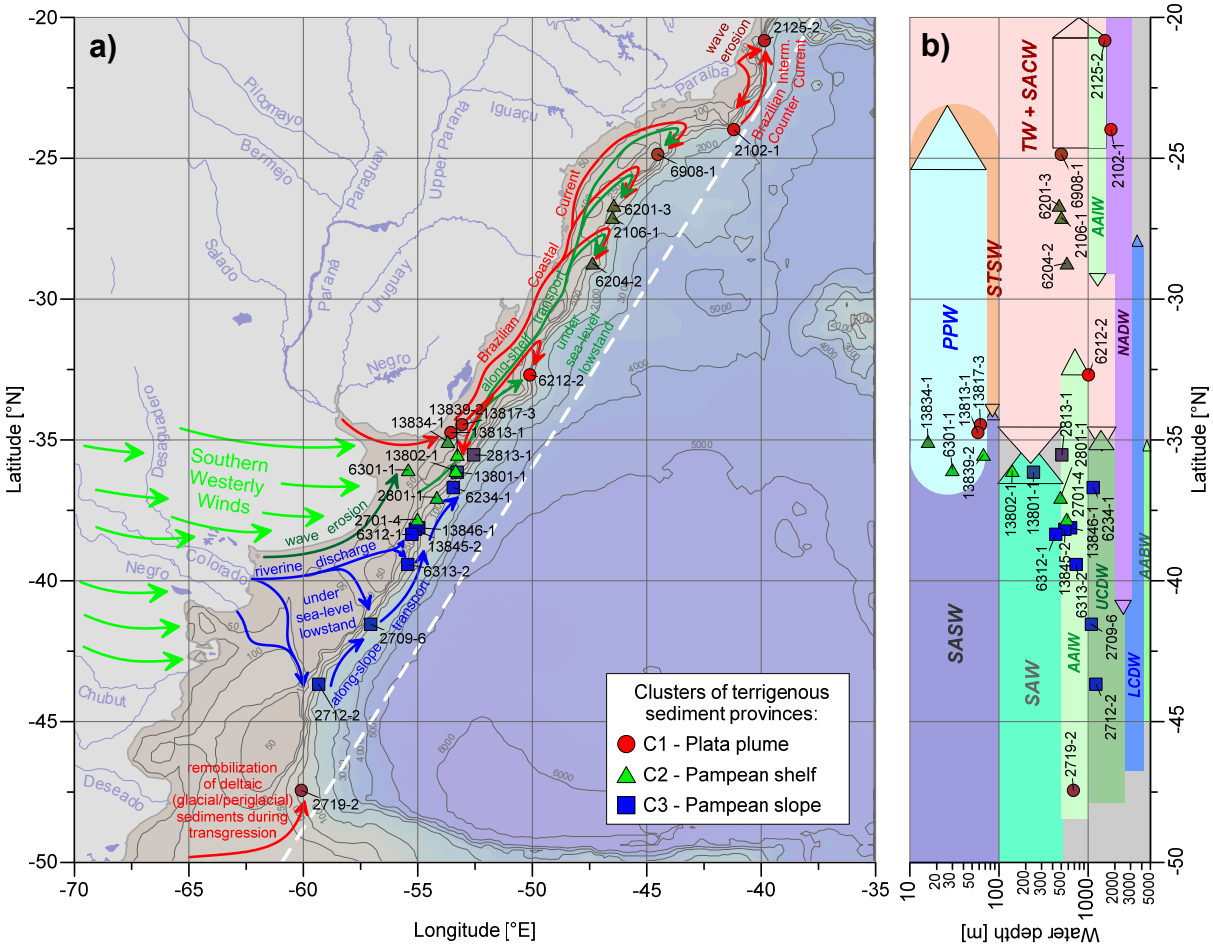

Fig. 4.6. Eolian, fluvial, and ocean-current sediment transport to the SE South American continental margin displayed in (a) geographic map, and (b) oceanographic section. Colors of sample locations and clusters (C1, C2, and C3) refer to Fig. 4.4. All relevant water masses in contact with the sample locations, allocated between the white dashed profile line in (a) and the coast line, are displayed in a simplified way: Antarctic Bottom Water (AABW); Antarctic Intermediate Water (AAIW); Lower Circumpolar Deep Water (LCDW); North Atlantic Deep Water (NADW); South Atlantic Central Water (SACW); Subantarctic Shelf Water (SASW); Subtropical Shelf Water (STSW); Tropical Water (TW); and Upper Circumpolar Deep Water (UCDW) (compiled after Stramma and England, 1999; Piola and Matano, 2001; Viana, 2002 and references therein; Piola et al., 2005; Preu et al., 2013; Reis et al., 2013).

Off Uruguay and South Brazil (Figs. 4.1 and 4.6a), the Plata River is the major deliverer of terrigenous sediments with ~92 × 10^6 t yr^{-1} of mainly silty to clayey sediments (Bernardes et al., 2012 and references therein). At the Plata estuary, these fine sediments are almost entirely deflected to the northeast together with the Plata Plume Water and deposited in paleo-channels at the northeastern side of the Plata estuary, creating the Plata mudbelt. However, silt-dominated Plata plume sediments are also found at other places of the mid shelf (Urien and Ewing, 1974; Laborde, 1997; Violante and Parker, 2004; Lantzsch et al., 2014). Additionally, Razik et al. (2013) showed that Late Holocene Plata plume silts were also deposited at the Rio Grande Cone in water depths below 500 m. At the location of the STSF and further to the north (Figs. 4.1 and 4.6b), the sediment transport from the mid shelf to the upper slope takes place together with the Subantarctic Shelf Water and the Subtropical Shelf Water, respectively (Piola et al., 2008). At the slope (Fig. 4.6b), southward transport together with the Tropical and South Atlantic Central Water of the Brazil Current are possible under modern conditions. Thus, the modern hydrodynamics is capable to explain the observed sediment distribution of the Plata plume

sediment province off Uruguay and South Brazil (Fig. 4.6a).

4.6.2. Pampean shelf sediment province

The Pampean shelf sediments posses the highest memberships to cluster center 2 and were mainly detected to the east of the Pampas, as well as off the Plata estuary (Fig. 4.6a). They are composed of fine sands (mode values of 150–250 µm; Fig. 4.3b) and are characterized by the highest antiferromagnetic (hematite and goethite) over ferrimagnetic (magnetite and maghemite) proportions, as it can be deduced from low $S_{0.3T}$ values (Fig. 4.5b; Tables 4.2 and 4.4). In Pampean loessoidal deposits (Zárate and Blasi, 1993; Zárate, 2003), hematite and goethite are vastly found as pedogenically formed minerals during intermittently humid and arid seasons, as observed in Chinese, Siberian, and Alaskan loess deposits (e.g., Heller and Tung-sheng, 1986; Maher and Thompson, 1991; Maher, 1998; Evans and Rutter, 1998). The well drained, intermittently wet and dry soils of the Chinese loess plateau show magnetic enhancement with respect to associated Chinese loess deposits (e.g., Heller and Tung-sheng, 1986; Maher and Thompson, 1991; Maher, 1998). In contrast to Chinese soils derived from loess deposits, Pampean, as well as Siberian and Alaskan soils are mainly depleted in fine ferrimagnets with respect to the underlying loessoidal deposits (e.g., Maher, 1998). The dissolution of ferrmagnets in Pampean soils may be strengthened by relatively high organic carbon concentrations and cation-exchange capacity. But also higher clay contents, and thus associated waterlogging, may play a significant role on magnetite and maghemite dissolution. Additionally, under excessively arid, waterlogged or acid conditions, just low amounts of pedogenic ferrimagnets can be formed. The dissolution scenario seems to be valid for the Pampas explaining the relative high proportion of antiferromagnets in the Pampean shelf samples (Fig. 4.5b). This result is corroborated by relatively low ARM/IRM and χ_{fd}% values, if compared with PDB sediments (GeoB 6212-2, 13813-1, and 13817-3; Fig. 4.5a,c), which suggest the favored dissolution of ultra-fine (SP) and fine (SD) magnetite particles, leading to a relative higher proportion of coarse (MD) magnetite. Although the Pampean soils seem to be frequently exposed to waterlogging, the Pampean humid season is significantly less pronounced than that of the PDB (e.g., Garreaud et al., 2009), as confirmed by the lowest Fe/K values here (Fig. 4.5e).

Terrestrial deposits, with grain-size distributions and petrological characteristics resembling those of the Pampean shelf sands (Fig. 4.3b), are found in the southern Pampas as loessoidal sands (Zárate and Blasi, 1993; Zárate, 2003). The loessoidal sands of the Pampas and the adjacent fluvial sands of the Colorado River originate from the Andean Cordillera between 32° and 42° S (e.g., Zárate and Blasi, 1993), where mafic and intermediate effusive rocks, as well as felsic intrusive and eruptive bodies are extensively exposed (Deruelle, 1982; Drake et al., 1982). Such igneous rocks contain significant amounts of magnetic minerals (Rumble, 1976). The total eolian sediment off-shore export from Patagonia and the Pampas is estimated to be ~29 × 10^6 t yr^{-1} (Pierce and Siegel, 1979; Gaiero et al., 2003 and references therein). However, most dust particles (86 ± 4% of mass) have diameters <10 µm, mainly ranging between 5 and 20 µm. Consequently, the largest part of modern eolian dust derived from Patagonia and the Pampas is not deposited on the shelf, where we observe sandy sediments with grain-size diameters >100 µm (Fig. 4.3b), but in the deep

Argentine Basin (e.g., Sachs and Ellwood, 1988). The total estimated fluvial sediment export from Patagonia and the Pampas (~2.0 × 10^6 t yr^{-1}) is small compared to the eolian (Gaiero et al., 2003). Thus, recent sandy shelf deposits are likely supplied by cliff erosion accounting for a contribution of ~39 × 10^6 t yr^{-1} (Gaiero et al., 2003 and references therein), which are subsequently redistributed by northward-directed shelf currents.

4.6.3. Pampean slope sediment province

The Pampean slope deposits (Fig. 4.6a) show the highest memberships to cluster center 3 and their geographic distribution is restricted to the Pampean continental slope, mainly to the east and northeast of the Colorado and Negro Rivers. These slope sediments have mode values between 70 and 140 µm (Fig. 4.3a) and are characterized by the highest magnetite and maghemite proportions with respect to hematite and goethite, as reflected by the highest $S_{0.3T}$ values (Fig. 4.5b; Tables 4.2 and 4.4). They also present the coarsest magnetite grain size of all sediment provinces (Fig. 4.5c). Coarse magnetite grain size in combination with highest SIRM/Fe values (Fig. 4.5d) suggests the presence of unaltered Fe-oxides particles, which were not much exposed to subaerial chemical weathering and are more typical of fluvial than eolian sediments. The recent minor sediment load of the largest Patagonian rivers and simultaneously the most adjacent ones to our survey site (Colorado and Negro) is neither sufficient to constitute vast layers at the Pampean continental slope, nor able to reach the slope due to the strong northward shelf currents (Urien and Ewing, 1974; Martins et al., 2005; Bozzano et al., 2011). However, this was likely possible during deglacial phases of sea-level lowstand, when the shore line was closer to the shelf break. Thus, both rivers were able to transport enhanced sediment loads with meltwaters from the Andes more directly to the upper continental slope. Passing the shelf break, these fluvial sediments were distributed northwards by the Malvinas Current (Fig. 4.6b), which created a series of erosive and depositional features on the slope (Hernández-Molina et al., 2009; Preu et al., 2013). The most exten-sive bodies are terraces at different water depths covered by slope-parallel contouritic drift deposits, which were described by Bozzano et al. (2011). Our provenance-related findings corroborate the suggestions of Bozzano et al. (2011) concerning the fluvial material of Andean origin, as the countourite drift deposits were identified as highly magnetic sands and silts. Gravel-rich facies were only found in contourite channels and moats, while muddy facies have a limited distribution at outer rims of the terraces. Lithic fragments of the gravel-rich facies were microscopically investigated under cross-polarized light and attributed to relict gravels, most likely derived from the submerged delta system of the Colorado River (Bozzano et al., 2011). Redistribution was assumed by winnowing and along-slope processes. All finer deposits were assigned to eolian input by westerly winds from Patagonia, the Pampas, or from the glacially exposed shelf during sea-level lowstands.

The deposition of Pampean shelf sediments (GeoB 2701-4 and 2801-1) at the continental slope off the Pampas at ~38° S (Figs. 4.1, 4.3a, and 4.6a,b) is exceptional and noteworthy, since it cannot be detected further to the south. This depositional pattern is in accordance with the modern off-shelf deflection of the Subantarctic Shelf Water at the respective latitude (Fig. 4.1). An analogous mixing of sediment provinces can be detected at the Uruguayan slope at 36°–37° S (GeoB 2813-1 and 13801-1; Figs. 4.1, 4.4a,b, and 4.6a,b). The off-shelf deflection of the

southward-flowing, recirculated Subantarctic Shelf Water mirrors the simultaneous admixture of Plata plume and Pampean shelf sediments to those of the Pampean slope.

The southernmost sample (GeoB 2719-2) investtigated in this study (Fig. 4.6a; Table 4.1) shows mixed magnetic and geochemical properties of cluster centers 1 and 3 (Fig. 4.4a,b). Although it resembles some properties of the adjacent Pampean shelf sediments (Fig. 4.5a,c) and some from the Pampean slope (Fig. 4.5b,c), it significantly differs from both sediment provinces by higher proportions of Fe (Fig. 4.5d,e). Based on the similarities towards both Pampean sediment provinces (Fig. 4.4), the Andean Cordillera remains a potential sediment provenance for core site GeoB 2719-2. However, due to the differences, the Pampas become questionable as a gateway for Andean sediments on their way towards this location. On the other side, there is no evidence for neither a recent nor a past transport process, which would be able to carry PDB sediments that far southward. Conclusively, the PDB can also be excluded as a potential source. The closest individual source for poorly sorted sands (and gravels) of igneous origin are the post-glacial deltas of the Chico, Cruz, and Gallegos Rivers draining South Patagonia (49°–55° S) (Martins et al., 2005). Accordingly, the Patagonian slope sample GeoB 2719-2 is constituted by the coarsest and broadest grain-size distribution (poor sorting of glacial and periglacial deposits) of all samples in this study (Fig. 4.3a).

4.6.4. Terrigenous sediments of the East Brazilian continental margin

The East Brazilian slope samples (GeoB 2102-1 and 2125-2; Fig. 4.6a) show similar properties to the PDB sediments deposited within the Plata mudbelt and on the Rio Grande Cone (Figs. 4.4 and 4.5). Thus, all of them show a high membership to cluster center 1 (Fig. 4.4b). However, NLM exhibits a relatively high multi-dimensional heterogeneity for cluster 1 (Fig. 4.4b) with distinct subgroupings for East Brazilian samples, as well as for Plata mudbelt and Rio Grande Cone samples, respectively. In particular, the East Brazilian slope sediments show lower proportions of ultra-fine (SP) magnetite (Fig. 4.5a; Table 4.2), but higher proportions of fine (SD) magnetite (Fig. 4.5c) and higher Fe/K values (Fig. 4.5e) than the PDB sediments. This is likely due to different source-rock petrology and pedogenesis, as well as weathering patterns present at each respective sediment-catchment area. The closest terrestrial sediment source, supplying the East Brazilian continental margin, is the Serra do Mar coastal mountain range. The Serra do Mar is mainly drained by the Paraíba do Sul River, which is the most important supplier to this part of the continental margin with a sediment load of ~4.2×10^6 t yr^{-1} (Bernardes et al., 2012). These mountains are characterized by Pre-Cambrian crystalline basement rocks with extensive exposures of Paleozoic granites and gneisses, as well as of other metamorphic rocks of igneous origin (De Almeida et al., 1981; Anjos et al., 2006). Besides basalts, granites are also significant natural source rocks for magnetic minerals (e.g., Rumble, 1976; Evans and Heller, 2003 and references therein). Granitic rocks can even be found as outcrops directly on the continental shelf and slope to the east of the Paraíba do Sul River mouth (Viana, 2002). In coastal areas, felsic igneous and metamorphic rocks are locally dissected by Mesozoic basaltic dykes. Quarternary lowland sediments and coastal plains to the north and to the south of the Paraíba do Sul River mouth are mainly composed of weathering products from igneous and metamorphic rocks (medium to very fine sands). They are described as light yellow to brown or reddish, resembling

eolian sands and being enriched by clays, as well as by ferruginous oxides (Anjos et al., 2006). Based on the properties of the East Brazilian slope sediments (Fig. 4.5), the igneous and metamorphic rocks of the Serra do Mar coastal mountain range can be considered as a locally dominant and independent sediment source.

In addition to the fluvial delivery of sediments, wave erosion of the sandy coastal plains to the north of the Paraíba do Sul River mouth may play a significant if not major role as deliverer of coarse sediments to the East Brazilian continental shelf (Martin et al., 1985). As the East Brazilian slope samples show a bimodal grain-size distribution (Fig. 4.3d) with modes of ~5 µm and 60–100 µm, we argue that the finer mode was transported directly by the Paraíba do Sul River, while the coarser mode is derived from the outer shelf and upper slope sands (Viana, 2002). Finally, north- and southward-directed surface-ocean currents (depending on the direction of seasonal winds), the southward-flowing Brazil Current and the Brazilian Intermediate Counter Current at mid-slope water levels (Fig. 4.6b) (Viana, 2002 and references therein; Oliveira et al., 2012) are responsible for the distribution of the terrigenous material, which reaches the slope.

4.6.5. Terrigenous sediments of the SE Brazilian continental margin

The SE Brazilian slope sediments (GeoB 6204-2, 2106-1, 6908-1, and 6201-3; Fig. 4.6a) show mixed magnetic and geochemical properties of clusters 1 and 2 (Fig. 4.4a,b). This feature is in accordance with the bimodal grain-size distributions (4–8 µm and 40–90 µm) of these samples (Fig. 4.3d), which also roughly resembles mixing between the respective modes of the Pampean shelf and Plata plume sediment provinces (Fig. 4.3b,c). Although grouped to cluster 1, the northernmost sample from off SE Brazil (GeoB 6908-1) is not related to East Brazilian samples. NLM rather shows that properties of SE Brazilian slope samples (Fig. 4.4b) fall on a straight mixing line between those of the Plata mudbelt and Rio Grande Cone (i.e., PDB sediments), on the one hand, and those properties of the Pampean shelf samples, on the other hand. In contrast, East Brazilian samples lie apart from a direct mixing path and are therefore ruled out as a provenance for SE Brazilian slope sediments. The reason for the expressed similarity of sample GeoB 6908-1 to cluster center 1, compared to other SE Brazilian samples (Figs. 4.4b and 4.6a), is the decreasing contribution of the sandy Pampean shelf province (cluster 2) with increasing distance to the north. This explanation is supported by decreasing relative proportions of coarse (MD) magnetite with increasing transport distance (Fig. 4.5c). For example, the two northernmost SE Brazilian samples (GeoB 6908-1 and 6201-3; Fig. 4.5c) show the lowest proportions of coarse (MD) magnetite in this region of the continental margin.

The continental margin off SE Brazil between Cape Santa Marta and Cape Frio (23°–29° S) is starved from terrigenous input under recent conditions, because of the absence of pro-nounced river mouths (e.g., Reis et al., 2013 and references therein). Over the past 2000 years, the only significant contributor of fine sediments to this area has been the Plata River (Mahiques et al., 2009; Gyllencreutz et al., 2010; Mathias et al., 2014). As the Plata Plume Water can frequently reach 24° S (Palma et al., 2008; Piola et al., 2008) and sporadically even 22° S, passing the São Sebastião Island (Stevenson et al., 1998), we suggest that fine PDB sediments can reach all SE Brazilian sample locations (Fig. 4.6a,b). Because this region of the conti-nental margin is also affected by the meandering Brazil Current

leading to the formation of eddies and vertical movements of the upper water column (Campos et al., 2000; Silveira et al., 2008; Calado et al., 2010), we argue that suspended PDB and remobilized shelf sediments can reach the deeper Tropical and South Atlantic Central Water, leading to a southward recirculation of these sediments and hence to their deposition on the slope at our sample locations (Fig. 4.6b).

4.6.6. Implications for isotopic-based provenance studies on multimodal sediments

The provenance study of Mahiques et al. (2008) based on Nd- and Pd-isotopes was able to track surface sediments from the Argentinean shelf as far north as the Plata estuary (~35° S). Owing to our study, this is the first time that Pampean shelf sediments could be tracked in surface sediments north of the modern STSF position (~34°–36° S) (Fig. 4.1), reaching SE Brazil (Fig. 4.6a,b). Although SE Brazilian coastal sands cannot be entirely ruled out as contributor to the observed coarser mode (Fig. 4.3d), they are unlikely the major source, as the entire SE Brazilian coast is characterized by felsic granites and gneisses (De Almeida et al., 1981; Anjos et al., 2006; Bernardes et al., 2012 and references therein). Sands with felsic origin would mirror magnetic and major-element properties of the East Brazilian samples, which contradicts our observations (Figs. 4.4a,b and 4.5).

We assume that the signature of the Pampean shelf sediments could not be detected north of the STSF by e.g. the Nd-isotope values in the study of Mahiques et al. (2008) due to mixing of two sediment sources with different grain-size modes. As Nd is a heavy element, it commonly occurs in fine particles in the marine realm and is therefore enriched in the clay fraction. This causes a grain-size dependence of isotopic values as shown by Revel et al. (1996) and Innocent et al. (2000). Thus, a small amount of relatively clay-enriched PDB sediment may contain a larger absolute concentration of Nd than a large amount of Pampean shelf sand. In this scenario, the Nd-isotopic signature of clay-enriched PDB silts will mask the Nd-isotopic signature of Pampean shelf sand, even if the latter constitutes the major component. This seems to be the case, when bimodal Mid Holocene grain-size distributions (Razik et al., 2013; Fig. 5a–e therein) are compared with Nd-isotope values (Lantzsch et al., 2014; Fig. 8B therein) from the same sediment core. This grain-size dependence obviously could not be detected by Mahiques et al. (2008), as all measurements were performed on bulk sediments and the obtained values were only displayed against clay concentrations (see Fig. 7 therein). Since the clay fraction dominates the bulk Nd-isotopic signature, these values remain more or less constant independently from the clay concentration, as far as the clays are derived from the same source. Consequently, the comparison of Nd-isotopic signatures versus clay concentration just pretends grain-size independence for sediments deposited at the margin of SE South America.

However, under modern oceanographic conditions, there are no realistic transport scenarios for such relatively coarse sediments to overcome the distance of 1300–2000 km between the Pampean and the SE Brazilian shelves. Thus, the Pampean shelf sediments were likely transported along the outer shelf and upper slope by northward coastal currents during multiple sea-level transgression-regression cycles. This low-stand scenario is in accordance with findings from sedimentological studies of the Uruguayan shelf and slope, where this sandy facies was described (Franco-Fraguas et al., 2014; Lantzsch et al., 2014). Nowadays, the Pampean sands are remobilized at the outer SE Brazilian shelf and

swept off the shelf break by the Brazil Current during frequent upwelling and downwelling events (Campos et al., 2000; Silveira et al., 2008; Calado et al., 2010).

4.7. Conclusions

Applying FCM cluster analysis and NLM to rock-magnetic and element data, we identified three major sources and associated transport pathways for terrigenous particles deposited on the SE South American continental margin. Therefor, five concentration-independent interparametric ratios were used, which bear information about source-rock petrology and climate-related weathering conditions.

Cluster 1 (clayey silt) originates from the PDB and is transported with the Plata Plume Water from the Plata estuary up to ~24° S. These sediments are characterized by the highest proportions of ultra-fine (SP) and fine (SD), likely pedogenic magnetite, together with prominent proportions of Fe-bearing clay minerals in respect to magnetic Fe-oxides. The pronounced chemical weathering of the PDB's mafic source rocks is supported by the highest Fe/K values, reflecting highly weathered material derived under humid conditions. Cluster 2 (fine to medium sand) predominates at the continental shelf off the Pampas. It originates from the Pampean coastal loessoidal deposits, which are characterized by the highest hematite and goethite proportions. In Pampean soils, both minerals occur widely as pedogenically formed minerals. They are supplied to the inner shelf by westerly winds or by coastal wave erosion. Subsequent shelf-wide redistribution and off-shelf transport is performed by the northward-flowing shelf current. For the first time Pampean shelf sediments were tracked as far north as ~24° S. Accordingly, SE Brazilian slope deposits show mixed magnetic and geochemical properties of clusters 1 and 2, as well as corresponding bimodal grain-size distributions. While the finer mode is composed of recent PDB sediments, the coarser mode consists of Pampean loessoidal sediments delivered by along-shelf transport during Pleistocene sea-level transgression and regression cycles. Under modern conditions, both sediment modes are swept off-shelf by the Brazil Current in combination with upwelling and downwelling events. Cluster 3 (contouritic sand) is entirely restricted to the Pampean slope. It is characterized by the highest proportions of magnetite and the coarsest magnetogranulometry. Coarse (MD) magnetite together with highest SIRM/Fe values hint at the presence of unaltered Fe-oxides, which were less exposed to subaerial chemical weathering than the sediments of the two other provinves. The Pampean slope sand originates from the Andes and was more directly delivered by the Colorado and Negro Rivers together with meltwaters at deglacial sea-level lowstands.

East Brazilian slope sediments are distinct from PDB sediments due to differences in magnetogranulometry and Fe/K values. These sediments originate from the Serra do Mar coastal mountain range and inherit significant detritus from felsic rocks. The Paraíba do Sul River and coastal erosion are the main deliverers of these sediments. The presented insights also reveal that FCM cluster analysis and NLM, applied to joint enviromagnetic and major-element properties, constitute a sensitive and efficient approach for provenance studies in regions with complex sediment dynamics and multiple sediment sources.

4.8. Acknowledgements

We thank the captains and crews of RV Meteor cruises M23, M29, M46, M49, and M78 who played a vital part in the

recovery of the investigated sediments. Sample material has been provided by the GeoB Core Repository at the MARUM – Center for Marine Environmental Sciences, University of Bremen, Germany. Financial support for this study was provided to S.R. by the DFG through the European Graduate College 'Proxies in Earth History – EUROPROX' and to A.G. by the DFG-Research Center / Cluster of Excellence 'The Ocean in the Earth System', and within the Special Priority Program INTERDYNAMIC (EndLIG project). C.M.C. acknowledges financial support from FAPESP (grant 2012/17517-3). This work contributes to MARUM Research Area Sediment Dynamics project SD2 – Climatic control on large-scale sedimentary structures. The data reported in this paper will be archived in the PANGAEA database (www.pangaea.de).

4.9. References

Allen, J.R.L., 1965. A review of the origin and characteristics of recent alluvial sediments. Sedimentology 5, 89–191.

Anjos, R.M., Veiga, R., Macario, K., Carvalho, C., Sanches, N., Bastos, J., Gomes, P.R.S., 2006. Radiometric analysis of Quaternary deposits from the southeastern Brazilian coast. Marine Geology 229, 29–43.

Bernardes, M.C., Knoppers, B.A., Rezende, C.E., Souza, W.F.L., Ovalle, A.R.C., 2012. Land-sea interface features of four estuaries on the South America Atlantic coast. Brazilian Journal of Biology 72, 761–774.

Bezdek, J.C., 1981. Pattern recognition with fuzzy objective function algorithms. Plenum New York, 256 p.

Bezdek, J.C., Ehrlich, R., Full, W., 1984. FCM: the fuzzy c-means clustering algorithm. Computers and Geosciences 10, 191–203.

Bleil, U., Spieß, V., Wefer, G., 1994. Report and preliminary results of METEOR Cruise M23. Berichte, Fachbereich Geowissenschaften, Universität Bremen vol. 94-1, 261 p.

Bleil, U., Alin, A., Bickert, T., Böke, W., Breitzke, M., Drachenberg, S., Eades, E., Frederichs, T., Frenz, M., Heuer, V., Hilgenfeld, C., Hopfauf, V., de Leon, A., von Lom-Keil, H., Michels, K., Pfeifer, K., Rosiak, U., Rühlemann, C., Segl, M., Spieß, V., Violante, R., Watanabe, S., Westerhold, T., Zatloukal, N., 2001. Report and preliminary results of METEOR Cruise M46/3, Montevideo (Uruguay) – Mar del Plata (Argentina), 04.01.–07.02.2000. Berichte, Fachbereich Geowissenschaften, Universtät Bremen vol. 01-1, 89 p.

Bleil, U., Albrecht, N., Breitzke, M., Brüning, M., Dehning, K., Diekamp, K., Domingues, J.M., Donner, B., Franke, P., Gerdes, A., Klann, M., Krastel, S., Krüger, D., von Lom-Keil, H., Martins Lima, L., Mulitza, S., Quental, S., Rudolf, T., Rühlemann, C., Santiago Grossmann, G., Steinborn, W., Thiele, J., Truscheit, T., 2002. Report and preliminary results of METEOR Cruise M49/3, Montevideo (Uruguay) – Salvador (Brazil), 09.03.–01.04.2001. Berichte, Fachbereich Geowissenschaften, Universtät Bremen vol. 02-1, 62 p.

Bozzano, G., Violante, R., Cerredo, M.E., 2011. Middle slope contourite deposits and associated sedimentary facies off NE Argentina. Geo-Marine Letters 31, 495–507.

Calado, L., da Silveira, I.C.A., Gangopadhyay, A., de Castro, B.M., 2010. Eddy-induced upwelling off Cape São Tomé (22 S, Brazil). Continental Shelf Research 30, 1181–1188.

Campos, E.J., Velhote, D., da Silveira, I.C., 2000. Shelf break upwelling driven by Brazil Current cyclonic meanders. Geophysical Research Letters 27, 751–754.

Campos, E.J.D., Mulkherjee, S., Piola, A.R., de Carvalho, F.M.S., 2008. A note on a mineralogical analysis of the sediments associated with the Plata River and Patos Lagoon outflows. Continental Shelf Research 28, 1687–1691.

Campos, P.C., Möller, O.O., Piola, A.R., Palma, E.D., 2013. Seasonal variability and coastal upwelling near Cape Santa Marta (Brazil). Journal of Geophysical Research: Oceans 118, 1420–1433.

Chiessi, C.M., Ulrich, S., Mulitza, S., Pätzold, J., Wefer, G., 2007. Signature of the Brazil-Malvinas Confluence (Argentine Basin) in the isotopic composition of planktonic foraminifera from surface sediments. Marine Micropaleontology 64, 52–66.

Corrêa, I.C.S., Ayoup-Zouain, R.N., Weschenfelder, J., Tomazelli, L.J., 2008. Áreas fontes dos minerais pesados e sua distribução sobra a plataforma continental sul-brasileira, uruguaya e norte-argentina. Revista Pesquisas em Geosciências 35, 137–150.

Csanady, G.T., 1978. The arrested topographic wave. Journal of Physical Oceanography 8, 47–62.

Davis, J.C., 1986. Statistics and data analysis in Geology. John Wiley, New York, 646 p.

De Almeida, F.F.M., Hasui, Y., de Brito Neves, B.B., Fuck, R.A., 1981. Brazilian structural provinces: an introduction. Earth-Science Reviews 17, 1–29.

Dekkers, M.J., Langereis, C.G., Vriend, S.P., van Santvoort, P.J.M., DeLange, G.J., 1994. Fuzzy c-means cluster analysis of early diagenetic effects on natural remanent magnetization acquisition in a 1.1 Myr piston core from the Central Mediterranean. Physics of the Earth and Planetary Interiors 85, 155–171.

Deruelle, B., 1982. Petrology of the Plio-Quaternary volcanism of the South-Central and Meridional Andes. Journal of Volcanology and Geothermal Research 14, 77–124.

Drake, R., Vergara, M., Munizaga, F., Vicente, J.C., 1982. Geochronology of Mesozoic-Cenozoic magmatism in Central Chile, Lat. 31°-36°S. Earth-Science Reviews 18, 353–363.

Dunlop, D.J., Özdemir, Ö., 2001. Rock Magnetism: Fundamentals and Frontiers (Cambridge Studies in Magnetism). Cambridge University Press, 573 p.

Evans, M.E., Rutter, N.W., 1998. A magnetic investigation of a Late Quaternary loess/palaeosol record in Siberia. Geophysical Journal International 132, 128–132.

Evans, M.E., Heller, F., 2003. Environmental magnetism - principles and applications of enviromagnetics. Academic Press, Amsterdam, 299 p.

Franco-Fraguas, P., Burone, L., Mahiques, M., Ortega, L., Urien, C., Muñoz, A., López, G., Marin, Y., Carranza, A., Lahuerta, N., de Mello, A., 2014. Hydrodynamic and geomorphological controls on surface sedimentation at the Subtropical Shelf Front / Brazil–Malvinas Confluence transition off Uruguay (Southwestern Atlantic Continental Margin). Marine Geology 349, 24–36.

Franke, C., von Dobeneck, T., Drury, M.R., Meeldijk, J.D., Dekkers, M.J., 2007. Magnetic petrology of equatorial Atlantic sediments: Electron microscopic results and their environmental magnetic implications. Paleoceanography 22, PA4207, 1–23.

Frenz, M., Höppner, R., Stuut, J.-B.W., Wagner, T., Henrich, R., 2003. Surface sediment bulk geochemistry and grain-size composition related to the oceanic circulation along the South American continental margin in the Southwest Atlantic. In: Wefer, G., Mulitza, S., Ratmeyer, V., (Eds.), The South Atlantic in the Late

Quaternary; Reconstruction of material budgets and current systems. Springer-Verlag, Berlin-Heidelberg-New York-Tokyo, pp. 347–373.

Gaiero, D.M., Probst, J.-L., Depetris, P.J., Bidart, S.M., Leleyter, L., 2003. Iron and other transition metals in Patagonian riverborne and windborne materials: Geochemical control and transport to the southern South Atlantic Ocean. Geochimica et Cosmochimica Acta 67, 3603–3623.

Garreaud, R.D., Vuille, M., Compagnucci, R., Marengo, J., 2009. Present-day South American climate. Palaeogeography, Palaeoclimatology, Palaeoecology 281, 180–195.

Govin, A., Holzwarth, U., Heslop, D., Ford Keeling, L., Zabel, M., Mulitza, S., Chiessi, C.M., 2012. Distribution of major elements in Atlantic surface sediments (36 N–49 S): Imprint of terrigenous input and continental weathering. Geochemistry, Geophysics, Geosystems 13, 1–23.

Govindaraju, K., 1994. 1994 compilation of working values and sample description for 383 geostandards. Geostandards Newsletter 18, 1–158.

Gyllencreutz, R., Mahiques, M.M., Alves, D.V.P., Wainer, I.K.C., 2010. Mid- to late-Holocene paleoceanographic changes on the southeastern Brazilian shelf based on grain size records. The Holocene 20, 863–875.

Heller, F., Tung-sheng, L., 1986. Palaeoclimatic and sedimentary history from magnetic susceptibility of loess in China. Geophysical Research Letters 13, 1169–1172.

Hernández-Molina, F.J., Paterlini, M., Violante, R., Marshall, P., de Isasi, M., Somoza, L., Rebesco, M., 2009. Contourite depositional system on the Argentine slope: an exceptional record of the influence of Antarctic water masses. Geology 37, 507–510.

Hounslow, M.W., Maher, B.A., 1996. Quantitative extraction and analysis of carriers of magnetization in sediments. Geophysical Journal International 124, 57–74.

Hounslow, M.W., Morton, A.C., 2004. Evaluation of sediment provenance using magnetic mineral inclusions in clastic silicates, comparison with heavy mineral analysis. Sedimentary Geology 171, 13–36.

Innocent, C., Fagel, N., Hillaire-Marcel, C., 2000. Sm–Nd isotope systematics in deep-sea sediments: clay-size versus coarser fractions. Marine Geology 168, 79–87.

Kim, W., Doh, S.J., Yu, Y., Lee, Y.I., 2013. Magnetic evaluation of sediment provenance in the northern East China Sea using fuzzy c-means cluster analysis. Marine Geology 337, 9–19.

Köhler, C.M., Heslop, D., Dekkers, M.J., Krijgsman, W., van Hinsbergen, D.J.J., von Dobeneck, T., 2008. Tracking provenance change during the late Miocene in the eastern Mediterranean using geochemical and environmental parameters. Geochemistry, Geophysics, Geosystems 9, Q12018.

Krastel, S., Wefer, G., 2011. RV METEOR Cruise Report M78/3a+b, Sediment transport off Uruguay and Argentina: From the shelf to the deep sea. Deutsche Forschungsgesellschaft, Senatskommission für Ozeanographie vol. 11–8, 59 p.

Laborde, J.L., 1997. Geomorphological and geological setting of the Río de la Plata. In: Wells, P.G., Daborn, G.R (Eds.), The Río de la Plata – An environmental overview. Dalhousie University, Halifax, pp. 1–16.

Lantzsch, H., Hanebuth, T.J.J., Chiessi, C.M., Schwenk, T., Violante, R.A., 2014. The high-supply, current-dominated continental margin of southeastern South America during the late Quaternary. Quaternary Research 81, 339–354.

Liu, Q.S., Roberts, A.P., Larrasoaña, J.C., Banerjee, S.K., Guyodo, Y., Tauxe, L., Oldfield, F., 2012. Environmental magnetism: Principles and applications. Reviews of Geophysics 50, RG4002, 1–50.

Maher, B.A., 1986. Characterisation of soils by mineral magnetic measurements. Physics of the Earth and Planetary Interiors 42, 76–92.

Maher, B.A., 1998. Magnetic properties of modern soils and Quaternary loessic paleosols: paleoclimatic implications. Palaeogeography, Palaeoclimatology, Palaeoecology 137, 25–54.

Maher, B.A., Thompson, R., 1991. Mineral magnetic record of the Chinese loess and paleosols. Geology 19, 3–6.

Maher, B.A., Watkins, S.J., Brunskill, G., Alexander, J., Fielding,C.R., 2009. Sediment provenance in a tropical fluvial and marine context by magnetic 'fingerprinting' of transportable sand fractions. Sedimentology 56, 841–861.

Mahiques, M.M., Tessler, M.G., Ciotti, A.M., da Silveira, I.C.A., Sousa, S.H.M., Figueira, R.C.L., Tassinari, C.C.G., Furtado, V.V., Passos, R.F., 2004. Hydrodynamically driven patterns of recent sedimentation in the shelf and upper slope off Southeast Brazil. Continental Shelf Research 24, 1685–1697.

Mahiques, M.M., Tassinari, C.C.G., Marcolini, S., Violante, R.A., Figueira, R.C.L., Silveira, I.C.A., Burone, L., Sousa, S.H.M., 2008. Nd and Pb isotope signatures on the southeastern South American upper margin: Implications for sediment transport and source rocks. Marine Geology 250, 51–63.

Mahiques, M.M., Klein, I., Wainer, C., Burone, L., Nagai, R., Sousa, S.H.M., Figueira, R.C.L., Silveira, I.C.A., Bícego, M.C., Alves, D.P.V., Hammer, Ø. , 2009. A high-resolution Holocene record on the Southern Brazilian shelf: Paleoenvironmental implications. Quaternary International 206, 52–61.

Martin, L., Suguio, K., Flexor, J.M., Tessler, M., Eichler, B.B., 1985. Roundness in Holocene sands of the Paraíba do Sul coastal plain, Rio de Janeiro, Brazil. Journal of Coastal Research 1, 343–351.

Martins, L.R., Urien, C.M., Martins, I.R., 2005. Gênese dos sedimentos da plataforma continental atlântica entre o Rio Grande do Sul (Brasil) e Tierra del Fuego (Argentina). Gravel 3, 85–102.

Mathias, G.L., Nagai, R.H., Trindade, R.I., de Mahiques, M.M., 2014. Magnetic fingerprint of the late Holocene inception of the Río de la Plata plume onto the southeast Brazilian shelf. Palaeogeography, Palaeoclimatology, Palaeoecology 415, 183–196.

Möller, O.O., Piola, A.R., Freitas, A.C., Campos, E.J.D., 2008. The effects of river discharge and seasonal winds on the shelf off southeastern South America. Continental Shelf Research 28, 1607–1624.

Mulitza, S., Prange, M., Stuut, J.-B., Zabel, M., von Dobeneck, T., Itambi, A.C., Nizou, J., Schulz, M., Wefer, G., 2008. Sahel megadroughts triggered by glacial slowdowns of Atlantic meridional overturning. Paleoceanography 23, PA4206.

Nagai, R.H., Ferreira, P.A.L., Mulkherjee, S., Martins, M.V., Figueira, R.C.L., Sousa, S.H.M., Mahiques, M.M., 2013. Hydrodynamic controls on the distribution of surface sediments from the southeast South American continental shelf between 23° S and 38° S. Continental Shelf Research 89, 51–60.

Oliveira, E.N.D., Knoppers, B.A., Lorenzzetti, J.A., Medeiros, P.R.P., Carneiro, M.E., Souza, W.F.L.D., 2012. A satellite view of riverine turbidity plumes on the NE-E Brazilian coastal zone. Brazilian Journal of Oceanography 60, 283–298.

Orfeo, O., Stevaux, J., 2002. Hydraulic and morphological characteristics of middle and upper reaches of the Paraná River (Argentina and Brazil). Geomorphology 44, 309–322.

Otofuji, Y., Uno, K., Higashi, T., Ichikawa, T., Ueno, T., Mishima, T., Matsuda T., 2000. Secondary remanent magnetization carried by magnetite inclusions in silicates: a comparative study of unremagnetized and remagnetized granites. Earth and Planetary Science Letters 180, 271–285.

Palma, E.D., Matano, R.P., Piola, A.R., 2008. A numerical study of the southwestern Atlantic shelf circulation: Stratified ocean response to local and offshore forcing. Journal of Geophysical Research 113, C11010.

Parker, G., Paterlini, C.M., Violante, R.A., 1997. El fondo marino. In: Boschi, E. (Ed.), El Mar argentino y sus Recursos Marinos. INIDEP, Mar del Plata 1, pp. 65–87.

Peate, D.W., 1997. The Paraná-Etendeka province. In: Mahoney, J.J., Coffin, M.F. (Eds.), Large Igneous Provinces. Continental, Oceanic, and Planetary Flood Volcanism. American Geophysical Union, pp. 217–245.

Pierce, J.W., Siegel, F.R., 1979. Suspended particulate matter on the southern Argentine shelf. Marine Geology 29, 73–91.

Piola, A.R., Matano, R.P., 2001. Brazil and Falklands (Malvinas) currents. Ocean Currents. A Derivative of the Encyclopedia of Ocean Sciences, 35–43.

Piola, A.R., Campos, E.J.D., Möller, O.O., Charo, M., Martinez, C., 2000. Subtropical shelf front off eastern South America. Journal of Geophysical Research 105, 6565–6578.

Piola, A.R., Matano, R.P., Palma, E.D., Möller, O.O., Campos, E.J.D., 2005. The influence of the Plata River discharge on the western South Atlantic shelf. Geophysical Research Letters 32, L01603.

Potter, P. E., 1984. South American modern beach sand and plate tectonics. Nature 311, 645–648.

Potter, P. E., 1986. South America and a few grains of sand: Part 1, beach sands. Journal of Geology 94, 301–319.

Preu, B., Hernández-Molina, F.J., Violante, R., Piola, A.R., Paterlini, C.M., Schwenk, T., Voigt, I., Krastel, S., Spiess, V., 2013. Morphosedimentary and hydrographic features of the northern Argentine margin: The interplay between erosive, depositional and gravitational processes and its conceptual implications. Deep Sea Research Part I 75,157–174.

Razik, S., Chiessi, C.M., Romero, O.E., von Dobeneck, T., 2013. Interaction of the South American Monsoon System and the Southern Westerly Wind Belt during the last 14 kyr. Palaeogeography, Palaeoclimatology, Palaeoecology 374, 28–40.

Reis, A.T., Maia, R.M.C., Silva, C.G., Rabineau, M., Guerra J.V., Corini, C., Ayres, A., Arantes-Oliveira, R., Benabdellouahed, M., Simões, I., Tardin, R., 2013. Origin of step-like and lobate seafloor features along the continental shelf off Rio de Janeiro State, Santos basin-Brazil. Geomorphology 203, 25–45.

Revel, M., Cremer, M., Grousset, F.E., Labeyrie, L., 1996. Grain-size and Sr–Nd isotopes as tracer of paleo-bottom current strength, Northeast Atlantic Ocean. Marine Geology 131, 233–249.

Rumble, D., 1976. Oxide Minerals - Short Course Notes Volume 3. Mineralogical Society of America, 706 p.

Sachs, S.D., Ellwood, B.B., 1988. Controls on magnetic grain-size variations and concentration in the Argentine Basin, South Atlantic Ocean. Deep Sea Research Part A. Oceanographic Research Papers 35, 929–942.

Sammon, J.W., 1969. A nonlinear mapping for data structure analysis. IEEE Transactions on Computers C18, 401–409.

Schmidt, A.M., von Dobeneck, T., Bleil, U., 1999. Magnetic characterization of Holocene sedimentation in the South Atlantic. Paleoceanography 14, 465–481.

Schramm, R., Heckel, J., 1998. Fast analysis of traces and major elements with ED(P)XRF using polarized X-rays: TURBOQUANT. Journal de Physique IV France 8, 335–342.

Schulz, H.D., Bleil, U., Henrich, R., Segl, M., 1995. Report and preliminary results of METEOR Cruise M29. Berichte, Fachbereich Geowissenschaften, Universität Bremen vol. 95-2, 323 p.

Schulz, H.D., Ayres Neto, A., Boetius, A., Enneking, A., Fabian, K., Feseker, T., Funk, J., Gorke, M., Heidersdorf, F., Hensen, C., Heuer, V., Hill, H.G., Hinrichs, S., Kasten, S., Klann, M., Lacerda de Souza, C., Martinez Briao, A., Meyer, S., Mulitza, S., Niebler, H.-S., Ochsenhirt, W.-T., Panteleit, B., Pfeifer, K., Schewe, F., Schwenk, T., Señorans, J.L., Siemer, S., Steinmetz, E., Wenzhöfer, F., 2001. Report and preliminary results of METEOR Cruise M46/2 Recife (Brazil) – Montevideo (Uruguay), 02.12.–29.12.1999. Berichte, Fachbereich Geowissenschaften, Universität Bremen vol. 01-1, 69 p.

Schwertmann, U., Taylor, R.M., 1989. Iron Oxides. In: Dixon, J.B., Weed, S.B., Dinauer, R.C. (Eds), Minerals in soil environments. Soil Scientific Society of America, pp. 379–435.

Silveira, I., Lima, J., Schmidt, A., Ceccopieri, W., Sartori, A., Francisco, C., Fontes, R., 2008. Is the meander growth in the Brazil Current system off Southeast Brazil due to baroclinic instability?. Dynamics of Atmospheres and Oceans 45, 187–207.

Souza, R.B., Robinson, I.S., 2004. Lagrangian and satellite observations of the Brazilian Coastal Current. Continental Shelf Research 24, 241– 262.

Stevenson, M.R., Dias-Brito, D., Stech, J.L., Kampel, M., 1998. How do cold water biota arrive in a tropical bay near Rio de Janeiro, Brazil? Continental Shelf Research 18, 1595–1612.

Stramma, L., England, M., 1999. On the water masses and mean circulation of the South Atlantic Ocean. Journal of Geophysical Research 104, 20863–20883.

Tjallingii, R., Röhl, U., Kölling, M., Bickert, T., 2007. Influence of the water content on X-ray fluorescence core-scanning measurements in soft marine sediments. Geochemistry, Geophysics, Geosystems 8, Q02004.

Urbat, M., Dekkers, M.J., Vriend, S.P., 1999. The isolation of diagenic groups in marine sediments using fuzzy c-means cluster analysis. In: Tarling, D.H., Turner, P. (Eds.), Palaeomagnetism and Diagenesis in Sediments 151, Geological Society, London, pp. 85–93.

Urien, C.M., Ewing, M., 1974. Recent sediments and environment of southern Brazil, Uruguay, Buenos Aires, and Rio Negro continental shelf. In: Burk, C.A., Drake, C.L., (Eds.), The geology of continental margins. Springer, Berlin, pp.157–177.

Viana, A.R., 2002. Seismic expression of shallow- to deep-water contourites along the south–eastern Brazilian margin. In: Rebesco, M., Stow, D.A.V. (Eds.), Seismic Expression of Contourites and Related Deposits 22 (5–6). Marine and Geophysical Researches, Special Issue, pp. 509–521.

Violante, R.A., Parker, G., 2004. The post-last glacial maximum transgression in the de la Plata River and adjacent inner continental shelf, Argentina. Quaternary International 114, 167–181.

Vriend, S.P., van Gaans, P.F.M., Middelburg, J.J., de Nijs, A., 1988. The application of fuzzy c-means cluster analysis and non-linear mapping to geochemical datasets: examples from Portugal. Applied Geochemistry 3, 213–224.

Watkins, S.J., Maher, B.A., 2003. Magnetic characterisation of present-day deep-sea sediments and sources in the North Atlantic. Earth and Planetary Science Letters 214, 379–394.

Watkins, S.J., Maher, B.A., Bigg, G.R., 2007. Ocean circulation at the Last Glacial Maximum: a combined modelling and magnetic proxy-based study. Paleoceanography 22, 1–20.

Wien, K., Wissmann, D., Kölling, M., Schulz, H.D., 2005. Fast application of X-ray fluorescence spectrometry aboard ship: How good is the new portable Spectro Xepos analyser? Geo-Marine Letters 25, 248–264.

Zárate, M.A., 2003. Loess of southern South America. Quaternary Science Reviews 22, 1987–2006.

Zárate, M.A. Blasi, A., 1993. Late Pleistocene-Holocene eolian deposits of the southern Buenos Aires Province, Argentina: A preliminary model. Quaternary International 17, 15–20.

4.10. Scientific background and individual contributions

The study 'Identification of terrigenous sediment provinces at the continental margin of SE South America' was launched as a continuation of the 'paleo'-study 'The South American Monsoon System and the Southern Westerly Wind Belt during the last 14 kyr' (see chapter 2). The aim was to investigate the spatial distribution of various terrigenous sediments and to describe for the first time their magnetic properties, which was not realizable within the context of the foregoing study. In addition to the here used marine surface-sediment samples from off SE South America, also terrestrial samples from the major river catchments were investigated, providing direct information about source-rock properties. These sediments were obtained in cooperations with Prof. Dr. Mario L. Assine (Rio Clara, Brazil) and Prof. Dr. Elírio E. Toldo Jr. (Porto Allegre, Brazil), who provided samples from the Paraguay and the Patos Lagoon catchment areas, respectively. The cooperations were built during a stay abroad of Sebastian Razik at the University of São Paulo in 2010, while oral presentations were given at two congresses: 'The AGU Meeting of the Americas' in Foz do Iguaçu, Brazil and 'The 18th International Sedimentological Congress' in Mendoza, Argentina. Although the terrestrial samples were investigated, they were not included into this study, as the sampling coverage and sampling density appeared to be insufficient. Thus, the described study was restricted to marine sediments only, keeping the terrestrial data sets for future studies aimed at investigation of terrestrial sediment sources.

The design of the study was carried out by Sebastian Razik and Dr. Cristiano M. Chiessi. The sets of rock and enviromagnetic parameters, as well as clastic grain-size data were provided by Sebastian Razik. Dr. Aline Govin measured the major-element concentrations. Essential interpretation of the results and writing of the paper was carried out by Sebastian Razik. Constructive comments on the manuscript's shape and the contents were made by Prof. Dr. Tilo von Dobeneck, Dr. Aline Govin and Dr. Cristiano M. Chiessi.

Chapter 5: How environmental magnetism can enhance the interpretational value of grain-size analysis: A time-slice study on sediment export to the NW African margin in Heinrich Stadial 1 and Mid Holocene

Sebastian Razik [a], Mark J. Dekkers [b] and Tilo von Dobeneck [a,c]

[a] Department of Geosciences, University of Bremen, Klagenfurter Straße, 28359 Bremen, Germany

[b] Department of Earth Sciences, Utrecht University, Budapestlaan 17, 3584 CD Utrecht, The Netherlands

[c] MARUM – Center for Marine Environmental Sciences, University of Bremen, Leobener Straße, 28359 Bremen, Germany

Palaeogeography, Palaeoclimatology, Palaeoecology 406 (2014) 33–48
(reprinted with permission from Elsevier)

5.1. Abstract

Sediment dynamics in limnic, fluvial, and marine environments can be assessed by granulometric and rock-magnetic methodologies. While classical grain-size analysis by sieving or settling mainly bears information on composition and transport, the magnetic mineral assemblages reflect to a larger extent the petrology and weathering conditions in the sediment-source areas. Here, we combine both methods to investigate Late Quaternary marine sediments from five cores along a transect across the continental slope off Senegal. This region near the modern summer Intertropical Convergence Zone is particularly sensitive to climate change and receives sediments from several aeolian, fluvial, and marine sources. From each of the investigated five GeoB sediment cores (494–2956 m water depth) two time slices were processed which represent contrasting climatic conditions: the arid Heinrich Stadial 1 (~15 kyr BP) and the humid Mid Holocene (~6 kyr BP). Each sediment sample was split into 16 grain-size fractions ranging from 1.6 to 500 μm. Concentration and grain-size indicative magnetic parameters (susceptibility, SIRM, HIRM, ARM and ARM/IRM) were determined at room temperature for each of these fractions. The joint consideration of whole sediment and magnetic mineral grain-size distributions allows to address several important issues: (i) distinction of two aeolian sediment fractions, one carried by the north-easterly trade winds (40–63 μm) and the other by the overlying easterly Harmattan wind (10–20 μm), as well as a fluvial fraction assigned to the Senegal River (<10 μm); (ii) identification of three terrigenous sediment source areas: southern Sahara and Sahel dust (low fine-grained magnetite amounts and a comparatively high haematite content), dust from Senegalese coastal dunes (intermediate fine-grained magnetite and haematite contents), and soils from the upper reaches of the Senegal River (high fine-grained magnetite content); (iii) detection of partial diagenetic dissolution of fine magnetite particles as a function of organic input and shore distance; (iv) analysis of magnetic properties of marine carbonates dominating the grain-size fractions 63–500 μm.

5.2. Introduction

The Northwest African realm is particularly sensitive to climate change as it is located off the Sahel, a transition zone between the humid tropics and the arid subtropics (White, 1983). Changes in precipitation as well as in direction and intensity of low- and high-altitude winds have large impact on the origin and properties of sediments deposited off Northwest Africa (Fig. 5.1). The region is also intriguing as it is under the influence of two aeolian transport systems, the north-easterly trade winds and the overlying easterly Harmattan, as well as one fluvial transport system, the Senegal River. As the predominant climatic factors and sediment transport mechanisms are essentially understood thanks to earlier palaeoclimatic studies (e.g., Koopmann, 1981; Sarnthein et al., 1981: Mulitza et al., 2008; Itambi et al., 2009; Just et al., 2012a), this study area is very appropriate to test whether grain-size specific enviromagnetic analysis has the potential to deliver further insights.

Sediment grain-size distribution analyses provide important information to reconstruct past and present sediment transport dynamics and depositional conditions. Grain-size methods have been successfully applied in a vast number of sedimentological studies covering all climate zones and settings (Allen, 1965; Folk, 1966; Holland and Elmore, 2008; Poizot et al., 2008). In contrast, sediment provenance as well as pedogenic and post-depositional alteration state are primarily derived from sediment petrological observations. Environmental magnetism is in principle an efficient lithostratigraphic method to explore these questions; it is based on the marker potential of sedimentary magnetic minerals and the variation of magnetic properties through time and space (e.g., Liu et al., 2012). The approach is particularly useful to reconstruct weathering conditions in sediment source areas (e.g., Maher, 1986; Lyons et al., 2010) and to detect syn- or post-depositional Fe-mineral diagenetic alteration (e.g., Karlin and Levi, 1985; Hesse, 1994; Robinson et al., 2000; Fu et al., 2008). Magnetic Fe-oxide and sulphide minerals are relatively low in species number and concentration. However, even trace contents (ppm level) can be quantified by rock-magnetic methods and provide clues as to their magmatic, metamorphic, pedogenic, biogenic, or diagenetic origin (e.g., Franke et al., 2007).

Like other proxies of sediment composition, grain-size and rock-magnetic records reflect the combined impact of multiple sediment sources and transport modes. Provenance and transport vary as function of changing climatic and weathering conditions. These convolved contributions are the rule in many “palaeostudies”; individual contributions can only be made visible by separating transport, source, and climate signatures – a nearly hopeless task if only bulk sediment properties are known. Rock-magnetic properties are dependent on the mineralogy of the magnetic particles and on their concentration, but also on their grain size. Therefore, grain-size fractionation prior to rock-magnetic analysis enables constraining magnetic mineralogy and concentration effects to certain grain-size fractions while enhancing their diagnostic potential.

So far, enviromagnetic methods have been rarely utilised in the analysis of sieved sediment grain-size fractions. Previous studies mainly dealt with riverine and coastal environments (e.g., Maher et al., 2009). The magnetic characterisation of soils from different tributaries plays an important role in demonstrating changing land-use patterns or to detect variations in precipitation and surface

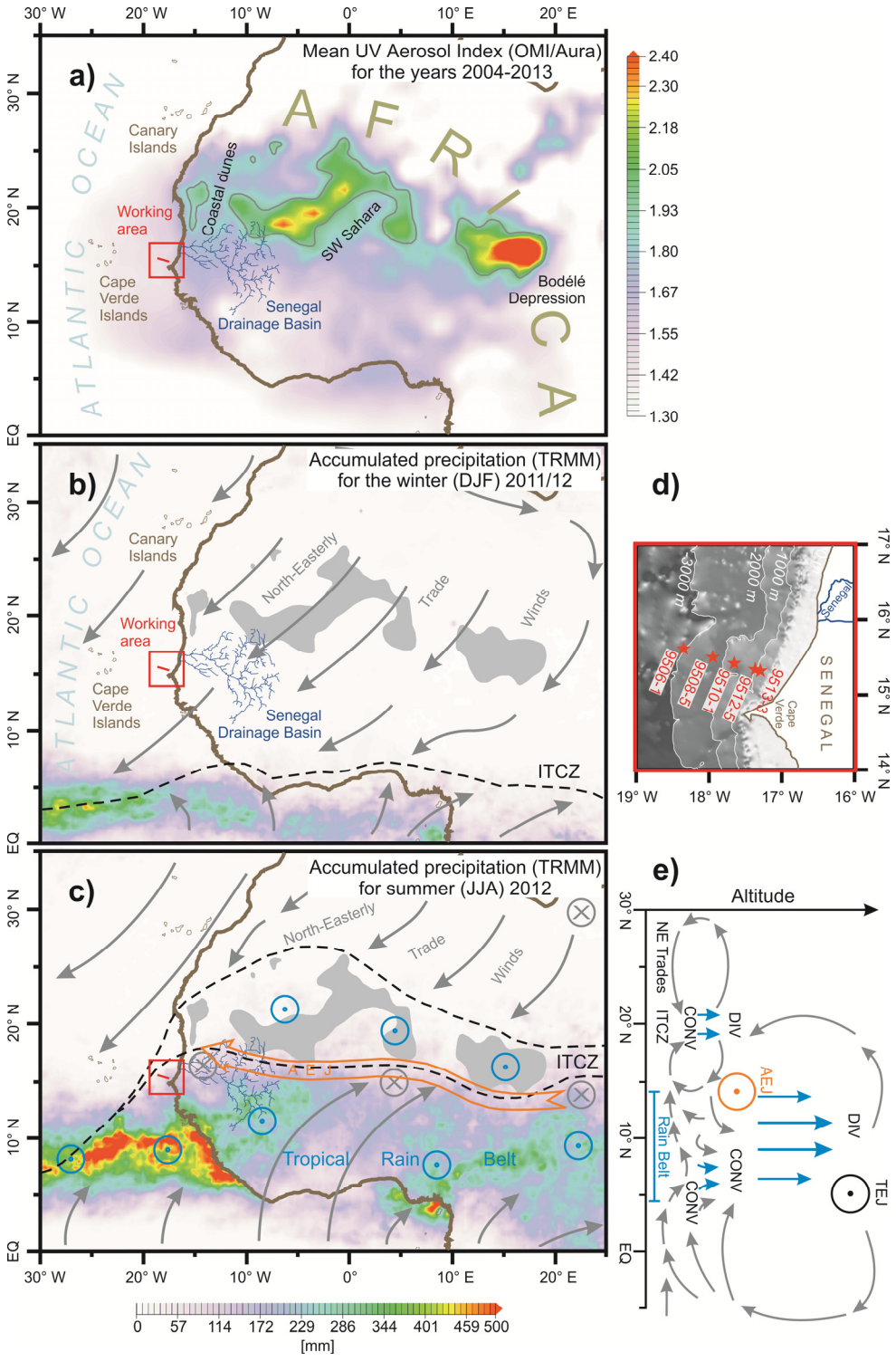

Fig. 5.1. Set of maps showing the study area under the modern climate of Northwest Africa and the adjacent Atlantic with main terrigenous sediment sources and transport systems (aeolian / fluvial): (a) Mean Aerosol Index (non-dimensional) for the years 2006–2013 (freely available OMI/AURA data from http://mirador.gsfc.nasa.gov/), values >2.0 mark areas with frequent sand and dust storm events due to convection of air masses; (b) Accumulated precipitation for boreal winter (December-January-February; DJF) of the year 2011/12 (freely available TRMM data from http://mirador.gsfc.nasa.gov/), the approximate location of the Intertropical Convergence Zone (ITCZ) is shown in a simplified way as dashed black line with the tropical rain belt being located to its south over land, north-easterly and south-easterly trade winds are shown as grey arrows (compiled and drawn after Ruddiman, 2001), the main aeolian dust sources in map (a) are displayed as grey areas; (c) Accumulated precipitation for boreal summer (June-July-August; JJA) of the year 2012, the tropospheric circulation is displayed schematically to visualise the

mechanism of dust uplift from main sources of NW Africa (after Nicholson, 2009), the ITCZ (area between dashed black lines) and the tropical rain belt are quasi-independent features, areas of air convection are marked by blue circles with a central dot, areas of air subsidence are marked by grey crossed circles, the African Easterly Jet (AEJ) above the convection cell of the ITCZ is shown as broad orange arrow; (d) Bathymetry (GEBCO 0.5 min grid) and locations of 5 gravity cores obtained during the METEOR research-cruise M65/1 (Mulitza et al., 2006) and sampled within this project; (e) Vertical cross-section of the tropospheric circulation cells averaged for 10° W to 10° E during boreal summer (drawn after Nicholson, 2009), the latitudinal scale is identical to (c), AEJ and the Tropical Easterly Jet (TEJ) are symbolised by orange and black circles, the convergence (CONV) and the convection of air at the ITCZ and the tropical rain belt are shown as blue arrows, the flow of the trade winds and air subsidence after divergence (DIV) are marked by grey arrows.

erosion (Oldfield et al., 1985; Hatfield and Maher, 2009). A coastal magnetic study by Oldfield and Yu (1994) was able to separate magnetic provenance signals in the coarse silt and sand fractions from a bacterial magnetite signal associated to the clay fraction. Magnetic provenance "fingerprinting" has been used to describe along- and across-shelf sediment dynamics (e.g., Hatfield et al., 2010). In their extensive magnetogranulometric study on modern North Atlantic sediments, Hatfield et al. (2013) could distinguish Greenlandic and Icelandic terrestrial provenances. Both deliver magnetite particles of similar sizes but with different abundances within the clastic grain-size spectrum. These results illustrate the well-known rock-magnetic phenomenon that clastic and magnetogranulometric grain sizes often differ substantially as many magnetite particles are inclusions in larger silicate host grains (Hounslow and Maher, 1996; Otofuji et al., 2000; Hounslow and Morton, 2004).

Our time-slice study intends to lead somewhat further: By testing a grain-size specific rock-magnetic approach in (i) a glacial arid and (ii) a post-glacial humid climate, we aim to resolve the impacts of individual sediment sources as well as of various transport systems. In particular, we examine whether or not magnetic particles are being enriched or depleted in specific grain-size ranges by these afore-mentioned factors. It is also essential to test whether or not the grain sizes of magnetic particles co-vary with clastic grain size and, if so, how strong this link is for various magnetic mineral associations and provenances. We will also try to derive palaeoclimatic information from the preservation of fine magnetic particles and pinpoint magnetite dissolution throughout the clastic grain-size range.

Therefore, we have resampled five well-studied Late Quaternary sediment gravity cores from a depth transect across the continental slope off Senegal (Fig. 5.1a,d). For each core, we identified the stratigraphic position of the arid Heinrich Stadial 1 (HS1, ~15 kyr BP) and of the Mid Holocene (MH, ~6 kyr BP) at the end of the African Humid Period (Mulitza et al., 2008). The arid HS1 at Northwest Africa was caused by the slowdown of the Atlantic Meridional Overturning Circulation (e.g., Mulitza et al., 2008 and references therein). This slowdown, due to inputs of large amounts of melt water from the high-latitude continental ice shields, led to cooling of the North Atlantic and increased the temperature gradient between the higher and lower latitudes. This in turn shifted the tropical rain belt south-wards and amplified the north-easterly trade winds. In contrast, the MH (and the entire African Humid Period) was characterised by weakened trade winds and by a more northern position of the tropical rain belt compared to today. A gradual increase in boreal summer insolation led to high precipitation over the Sahara which was almost entirely vegetated in those times (e.g., deMenocal et al., 2000).

The sediment samples of both time slices from the five cores were separated into 16, on average ~0.5 Φ wide, grain-size fractions ranging from 1.6

to 500 µm. This yielded 160 grain-size fractions of which a set of rock-magnetic parameters was determined at room temperature. Subsequently, we interpreted grain-size dependent trends in the magnetic susceptibility as well as in isothermal, anhysteretic, and high-field magnetic remanence intensities and compared them to values obtained for the bulk samples.

5.3. Sedimentary and environmental setting

5.3.1. Tropospheric circulation of Northwest Africa

The scene of this study, the northern part of the Sahel, is a savannah landscape and semi-desert experiencing yearly precipitations from 0 to 500 mm (Li et al., 2004). While annual and seasonal precipitation controls weathering at terrestrial sediment sources, wind intensities and seasonally predominant wind directions determine the main transport systems. All of them experience systematic climate-driven changes as shown by the marine archives off-coast Senegal (Michel, 1973 and references therein; Diester-Haass, 1976; Mulitza et al., 2008; Itambi et al., 2009).

Some traditional, but rather simplified explanations for seasonal precipitation and wind patterns of Northwest Africa (e.g., Dettwiller, 1965; Germain, 1968), however, are still prevailing. As the tropospheric circulation is of palaeoclimatic relevance for the interpretation of the HS1 and MH data, we give a short introduction to modern views based on the seminal work of Nicholson (2009). Further, a review paper by Zhang et al. (2006) on this topic is interesting reading.

During boreal winter (December-January-February; DJF), Northwest Africa and the northern Senegalese continental margin are under influence of boreal north-easterly trade winds (Fig. 5.1b). These winds are directed from the North-Saharan high-pressure cell towards the tropical low-pressure trough (Intertropical Convergence Zone; ITCZ) located at around 5° N over the Atlantic and central Africa (e.g., Sultan and Janicot, 2003 and references therein). At the ITCZ, the north-easterly trade winds from the Sahara and Sahel converge with austral south-easterly trade winds transporting oceanic moisture. Their joint updraft leads to cooling at higher tropospheric levels and to abundant daily rainfalls (Parker et al., 2005).

During boreal summer (June-July-August; JJA) the area of maximum insolation shifts northwards (Fig. 5.1c). At low-tropospheric levels, the austral south-easterly trade winds arise at the equatorward side of the South Atlantic high-pressure cell and cross over the equator. They are deflected northeast-wards by Coriolis forces and by the enhanced surface low-pressure cell (ITCZ) over Northwest Africa (Xie and Saiki, 1999). Although a significant part of the moisture for precipitation comes from the Atlantic Ocean (African coast between 5° and 10° N; Fig. 5.1c), the main portion of the moisture for convection and on-land precipitation is derived from local evaporation (Nicholson, 2009). The responsible force for the convection of air masses within the “tropical rain belt” over land (the zone of maximum summer precipitation, mainly at 5–15° N; Fig. 5.1c,e) is the cross-equatorial pressure gradient. The intensity of this deep convection is primarily influenced by the dynamics of the African Easterly Jet (AEJ) and the Tropical Easterly Jet (TEJ) rather than by wind or moisture convection (Nicholson, 2009). Simultaneously with the northward shift of the tropical rain belt, the ITCZ shifts northward to 15°–23° N at the surface, reaching the latitudes of the northern Sahel and southern Sahara (Tetzlaff and Peters, 1986; Sultan and

Janicot, 2003; Nicholson, 2009). At the ITCZ, the south-westerly monsoon winds merge with the north-easterly trade winds and the overlying easterly Harmattan (Fig. 5.1c,e; latter not marked here for clarity) (Sultan and Janicot, 2003; Nicholson, 2009), also referred to as "Saharan Air Layer" in literature (Tetzlaff and Peters, 1986; Middleton and Goudie, 2001: Stuut et al., 2005 and references therein). This rather shallow air-convection cell is responsible for precipitation over the northern Sahel and southernmost Sahara particularly during wet years, being quasi-independent from the tropical rain belt (Nicholson, 2009).

5.3.2. Aeolian transport systems and related terrestrial sediment sources

As the ITCZ creates little precipitation during mean boreal summers, the concerned area provides the largest source for aeolian dust worldwide (Fig. 5.1a,c) (e.g., Mahowald et al., 2006; Roberts et al., 2011). During boreal winter conditions, the north-easterly trade winds as well as the overlying easterly Harmattan are the major suppliers of aeolian dust towards the Senegalese continental margin. The north-easterly trade winds pick up relatively coarse particles from dunes of the western Sahara (Table 5.1) and transport them at low-tropospheric levels of up to 1000–1500 m (Fig. 5.1a,b) (Koopmann, 1981: Sarnthein et al., 1981; Grousset et al., 1998; Middleton and Goudie, 2001). These particle distributions have modal values between 40 and 70 µm (Grousset et al., 1998); only ca. 5–13% of the grains are covered with haematite (Koopmann, 1981 and references therein).

The north-easterly trade winds are overlain by the easterly Harmattan, which is strongest during summer months due to an enhanced AEJ (Fig. 5.1c,e). The Harmattan and AEJ transport the largest part of aeolian sediments from Sahel and southern Sahara to the Atlantic (e.g., Middleton and Goudie, 2001; Caquineau et al., 2002; Holz et al., 2004; Stuut et al., 2005). Both climatic features are located at mid-tropospheric levels (1500–5500 m) with highest aeolian dust concentrations at ~3000 m (Tetzlaff and Peters, 1986). The dust is mainly picked up from southern Sahara and Sahel Zone dry lands (Fig. 5.1a) by vertical atmospheric turbulence, i.e. dust outbreaks (Fig. 5.1e) (e.g., Holz et al., 2004; Stuut et al., 2005). Main aeolian sediment sources are the Bodélé Depression in Chad (Fig. 5.1a), the Southern Sahara of Algeria, northern Mali, and western Morocco (Middleton and Goudie, 2001; Caquineau et al., 2002 and references therein). Sahel dust sources between 10° and 16° N are the second most important sources (Tetzlaff and Peters, 1986).

Although these southern Sahara and northern Sahel sediment sources show loessoidal characteristics with grain-size modes between 16 and 60 µm, the transported aeolian dust is typically between 10 and 30 µm (Table 5.1) (Koopmann, 1981 and references therein; Holz et al., 2004; Stuut et al., 2005; Lyons et al., 2012). Particles >30 µm fall out after few tens of kilometres, creating residual Sahara and Sahel sediment covers (Lyons et al., 2010, 2012). Aeolian dust particles <16 µm can be created by crumbling of coarser particles during saltation. Between 35% and 75% of the Harmattan and AEJ sediments are haematite-coated (Table 5.1) (Koopmann, 1981 and references therein). Besides abundant haematite coatings, these sediments also contain high amounts of pedogenically formed maghaemite. This makes them more strongly magnetic than the northern and north-western Sahara sediments. These important insights were established with the help of grain-size based rock and environmental magnetic studies of Lyons et al. (2010, 2012),

Table 5.1

Properties of terrigenous source sediments relevant for our grain-size based rock-magnetic study off Senegal (from earlier studies mentioned in sections 5.3.2 and 5.3.3: Koopmann, 1981: Sarnthein et al., 1981; Grousset et al., 1998; Middleton and Goudie, 2001; Lyons et al., 2010, 2012).

Sediment source	Transport system	Mode size carried to NW Africa	Magnetite / maghaemite		Haematite	
			Main appearance as	Rate	Main appearance as	Rate
Western Sahara	NE trade winds	40-70 µm	inclusions in host grains	+/-	coatings on quartz grains	+/-
Southern Sahara / Sahel	Harmattan	10-30 µm	pedeogenic individual grains	+	coatings on quartz grains	++
Fouta Djallon / Manding Plateaus	Senegal River	~6 µm	pedogenic / igneous individual grains	++	coatings on quartz grains and clays	+

+/- rare + common ++ very common

which were performed on dust samples collected along north-south trending transects across the whole Sahara and Sahel.

In the coastal region, the lower zone of the Harmattan shows increased turbulence with the underlying moist and cool north-easterly trade winds. This leads to a marked and relatively abrupt gravitational fall-out of its coarsest dust grains with sizes >40 µm (Koopmann, 1981) originating from coastal dunes. The grain size of these aeolian sediments decreases with shore distance. Particles <12 µm can reach as far as the Caribbean (Prospero et al., 1981; Middleton, 1985; Swap et al., 1996), but fine aeolian particles can also be found in significant concentrations at the continental margin off Senegal (Koopmann, 1981: Sarnthein et al., 1981; Grousset et al., 1998; Middleton and Goudie, 2001). These particles act as nuclei for moisture condensation and are easily washed out by rain. Clay particles often aggregate already in the air column. Aggregation is even more intense after the saline sea surface is reached. The settling process within the ocean can further be enhanced by suspension feeders digesting the aggregates and bonding them to larger faecal particles. Such aggregates obtain settling characteristics of fine sandy quartz and can reach the ocean floor within a few days to weeks (Koopmann, 1981 and references therein; Grousset et al., 1998 and references therein), where they disintegrate. This sedimentation process is therefore relatively fast and the grain-size distributions along our sediment core transect (Fig. 5.1a,d) should mainly mirror these aeolian transport dynamics and not be biased by ocean currents at the continental slope (Koopmann, 1981; Sarnthein et al., 1981; Mulitza et al., 2008; Itambi et al., 2009).

5.3.3. Fluvial transport system and related terrestrial sediment sources

A major contributor of silty to clayey sediments to the northern Senegalese continental margin is the Senegal River (Fig. 5.1a–d; Table 5.1) (Michel, 1973; Lesack et al., 1984; Nizou et al., 2010 and references therein). Its average yearly runoff is 641 $m^3 s^{-1}$, with a yearly sediment load between 1.2 and 2.8 Mt yr^{-1} and a mean suspended solid concentration of 196–252 mg l^{-1} (Gac and Kane, 1986). The Senegal drainage

basin contains the oldest rocks at its upper reaches, the Fouta Djallon and Manding Plateaus, which constitute the strongly magnetic Precambrian basement rocks of the West African Shield. They are overlain by Palaeozoic schists and quartzites, sedimentary sandstones together with few schists and dolomites, as well as basalts and rhyolites intersected by diorite and granite intrusions.

The middle and lower reaches of the Senegal drainage basin consist mainly of Mesozoic-Tertiary sandstone formations. Only the Senegal River delta is covered by Quaternary alluvial deposits. From an enviromagnetic view, the igneous rocks of the upper drainage reaches are the most important source for weathering products like ferruginous and ferralitic soils that contain high concentrations of ferrimagnetic and antiferromagnetic Fe-oxides. The upper drainage reaches of the Senegal River in Mali also appear to be a prominent source for fine-grained, pedogenically formed, magnetite and maghaemite (Lyons et al., 2010). Their concentrations in the soils increase southwards with higher precipitation (Lyons et al., 2010). When the river reaches the saline ocean water, the suspended particles settle and the dissolved Fe-complexes precipitate. The availability of such syn-sedi-mentary precipitates results in the formation of olive-green to grey Fe-rich and strongly paramagnetic marine clay deposits (Odin, 1988; Itambi et al., 2009).

5.3.4. Hydrography and sedimentology at the continental margin off northern Senegal

The continental margin off northern Senegal and Mauritania between Cape Verde and Cape Blanc (15–21° N) is characterised by a relatively narrow continental shelf of 40–60 km width (Fig. 5.1a,d) and a 100–200 m deep shelf break (McMaster and Lachance, 1969; Wynn et al., 2000). The continental slope has a width of ~80 km and descends at an angle of ~1.5° down to 2500 m water depth.

The oceanography at the continental margin between Cape Verde and Cape Blanc has been described by Hagen (2001) and Stramma et al. (2005). During boreal summer, the inner and middle parts of the continental shelf (0–100 m) are under influence of the Tropical Surface Water from a northward-flowing coastal counter current driven by south-westerly monsoon winds. Simultaneously, the northward-flowing South Atlantic Central Water overflows the outer shelf and the upper slope (100–500 m). During boreal winter, this subsurface water is upwelling onto the entire shelf and driven southwards by the north-easterly trade winds, displacing the Tropical Surface Water southwards. This seasonally clockwise or anti-clockwise circulating shelf waters have a significant influence on the sediment transport to the slope (e.g., Nizou et al., 2010 and references therein). During boreal summer, coastal currents transport sediments to the north up to Cape Blanc and then down-slope and partially backward to the south (Koopmann, 1981 and references therein). Thus, the shelf and upper continental slope between the Senegal River mouth and Cape Blanc are generally free of silty and clayey sediments, which are then found in higher concentrations at the continental rise (Barusseau et al., 1988; Nizou et al., 2010). This part of the continental shelf is mainly covered with medium or fine (aeolian) sands (>75% of sediment composition) with less than 10% of silt and 10% of clay (McMaster and Lachance, 1969 and references therein).

Between the Senegal River mouth and Cape Verde to its south (Fig. 5.1d), a high proportion of very fine fluvial material (Barusseau et al., 1988; Nizou et al., 2010) is deposited besides coarser

Table 5.2
Locations and water depths of five sampled GeoB gravity cores recovered from the continental slope off Senegal, Northwest Africa.

Core (GeoB)	Latitude	Longitude	Water depth	Shore distance
9506-1	15°36.60'N	18°21.01'W	2956 m	163 km
9508-5	15°29.90'N	17°56.88'W	2378 m	118 km
9510-1	15°25.00'N	17°39.20'W	1566 m	85 km
9512-5	15°20.21'N	17°22.02'W	795 m	53 km
9513-3	15°19.11'N	17°17.64'W	494 m	45 km

quartz particles during boreal winter. As these sediments do not reach areas south of Cape Verde, they must be diverted off-shelf and down-slope toward our sediment core transect. Here, the inner shelf deposits (0–50 m water depth) show the largest grain-size range and most heterogeneous distributions of the shelf deposits (Lézine and Chateauneuf, 1991; Nizou et al., 2010). Locally, they are described as sands, muddy sands, or sandy muds. The mid shelf (50–100 m) is mainly covered with sandy muds and the outer shelf (100–200 m) with muddy sands. The surface sediments of the adjacent continental slope (200–2500 m) consist of muddy silts (silt composes 40% of terrigenous fraction with minor amounts of sandy and clayey grains) and the sediments of the continental rise (2500–4500 m) are composed of clayey muds to muddy clays (Koopmann, 1981).

5.4. Materials and methods

5.4.1. Materials

This study is based on five sediment gravity cores collected at the continental margin off northern Senegal during Meteor cruise M65/1 (Mulitza et al., 2006). These are GeoB 9513-3, 9512-5, 9510-1, 9508-5, and 9506-1 (from shallow to deep, Fig. 5.1a,d; Table 5.2) and come from water depths between 494 m and 2956 m following an ESE-WNW trending transect across the slope. Each core was sampled at two levels (20–30 ml each) corresponding to the time slices HS1 (~15 kyr BP) and the MH (~6 kyr BP).

The age model of the deepest core GeoB 9506-1 was based on a benthic $\delta^{18}O$ curve and correlated to the already dated cores GeoB 9516-4 (Itambi et al., 2009) and MD 95-2042 (Shackleton et al., 2004). Core GeoB 9508-5 has its independent ^{14}C age model (Mulitza et al., 2008). The HS1 and MH time slices of the remaining three sediment cores were defined by correlation of rock-magnetic, element and colour data to the GeoB 9506-1 age model (Itambi et al., 2009). In all cores, the arid HS1 level is represented by reddish-brown sandy muds of distinctly aeolian origin (Just et al., 2012a). The colour is due to haematite coatings on quartz particles and clay minerals. During the African Humid Period of the MH, climate conditions enabled the deposition of dark-green silty muds, containing an important contribution from fine-grained Senegal River sediments (e.g., Odin, 1988).

5.4.2. Methods

5.4.2.1. Wet sieving

Before sieving, the samples were freeze-dried to determine their dry bulk masses of 18–52 g while avoiding alteration and aggregation. About 20% of the dry sediment was removed for bulk sediment measurements. The other 80% of the

Table 5.3

Grain-size fractions obtained by wet sieving and settling listed by their maximum and main grain size based on the density of quartz. Shown are settling times for first and second runs. The main grain size was assumed by calculating the most abundant grain size with respect to finer grains being previously caught in coarser fractions.

	Maximum-grain size [µm]	Main grain size [µm]	1. run time		2. run time	
			minutes	hours	minutes	hours
Sieving	500	500	10	0.17	-	-
	355	355				
	250	250				
	180	180				
	125	125				
	90	90				
	80	80				
	63	63				
	40	40				
	20	20				
Settling	14	11.1	18.7	0.31	3.7	0.06
	10	7.9	36.6	0.61	7.3	0.12
	6.3	5.0	92.3	1.54	18.5	0.31
	4	3.2	229.1	3.82	45.8	0.76
	2.8	2.2	467.5	7.79	93.5	1.56
	2	1.6	916.2	15.27	183.2	3.05

dry bulk sample were suspended in 100 ml of demineralised water. 3.5 g of tetra-sodium-diphosphate was added to prevent creation of aggregates in the clay fraction (following e.g. Barbanti and Bothner, 1993). The sediment was then further diluted with 200 ml demineralised water and ultrasonically dispersed in a BRANSON Sonifier 450 homogeniser for 3–5 minutes.

Wet sieving was performed with the sifting machine FRITSCH analysette 3 with ISO-3310 sieves. The maximum water discharge of the glands was ~1.5 l per minute at ~2 bar water pressure. Sieving was done with vibration amplitude of 2.0 mm. The sieving time was 10 minutes in total with shake intervals of 3 s, being followed by a pause of 1 s. Ten grain-size fractions from >500 µm to >20 µm (Table 5.3) were obtained using 10 stacked sieves.

5.4.2.2. Settling method

A settling method served to partition the <20 µm effluent into 6 further fractions (Table 5.3). The settling times for each targeted fraction (i.e., maximum diameter) were calculated from Stokes' law as shown by Oldfield and Yu (1994) and Lamb (2006) assuming a sediment density equal to that of quartz. Two sequential runs per settled grain-size fraction were performed (Table 5.3) to reduce contamination by finer particles which settle simultaneously with the larger target-size particles from the starting suspension.

The settling was started with retention of the coarsest particles to obtain as much mass as possible from each fraction. Hence, settling of particles finer than the target grain size is a disadvantage of this separation method and leads to an underestimation of the finer grain-size fractions obtained later. Therefore, a more repre-

sentative (main) grain size was calculated, which was qualitatively defined by the largest mass proportion within each settled fraction applying again Stokes' law to mathematically simulate the two settling runs. Target (maximum) and corresponding main grain sizes are listed in Table 5.3.

The calculated main grain sizes were validated by incident light microscopy on a set of selected grain-size fractions. In the following, we show grain-size distributions with respect to the main grain size of quartz as most dominant mineral in terms of mass. The rock-magnetic parameters are also shown against quartz equivalent grain size to facilitate comparison of the entire range of measured parameters within this study. As the individual sieve fractions vary extremely in volume, it was more practical to normalise susceptibility and remanences by sample mass.

5.4.2.3. Sample preparation for magnetic measurements

To enable meaningful low-field magnetic susceptibility (MS) and remanence measurements, all fractions with their widely varying mass (Tables 5.4 and 5.5) were set either in molten paraffin that was moulded into spherules, or fixated in gelatine capsules. This prevents grain rotation in the applied magnetic fields and centres the small amounts of material in the standard 6.2 cm^3 plastic sample cubes. Both procedures yielded measurement results of comparable quality. We favoured the gelatine capsule method, since it is faster and also more convenient for further analyses (e.g., microscopy). Hard-gelatine capsules of size "00" (length 23.3 mm; Ø 8.2 mm) of high purity were used. To avoid grain rotation, the sediment in one half of the capsule was firmly compressed with the outside of the reversely inserted second half. Both halves were fixated with Scotch Tape and slid into a drinking straw of an appropriate diameter. To centre the sediment in the standard 6.2 cm^3 plastic cubes, the drinking straw was trimmed to the necessary length. The mass of each individual gelatine capsule was measured to subtract its diamagnetic contribution from the measured MS.

5.4.2.4. Magnetic susceptibility and remanence measurements

MS measurements were performed at 920 Hz and 320 A m^{-1} rms-field strength using a KAPPABRIDGE KLY-2 instrument with a sensitivity of 0.04×10^{-6} SI. All measurements were corrected for sample holder, casing, and stabiliser effects.

Measurements of the anhysteretic and isothermal remanent magnetisations (ARM and IRM respectively) were performed with a fully automated 2G ENTERPRISES 755R DC-SQUID passthrough magnetometer at the *Marine Geophysics Section, University of Bremen (Germany)*. The sensitivity of this equipment is 1.0×10^{-12} Am^2 corresponding to 0.1613 µA m^{-1} for a sample of 6.2 cm^3.

During ARM measurement, the fractions were magnetised in a 0.1 T alternating magnetic field (biasing direct field of 40 µT) followed by demagnetisation in 15 steps. IRMs were measured after application of incrementally stronger direct current pulse fields up to 0.7 T in 21 steps. After reaching the internal pulse-coil maximum field of 0.7 T, the samples were treated as magnetically saturated and the corresponding IRM is labelled SIRM. Although the saturation of haematite is not complete (pure haematite requires saturation fields of 1–5 T), it was sufficient for the relative quantification purposes of the present study.

Table 5.4

Masses and relative abundances of grain-size fractions from the Heinrich Stadial 1 time slice.

Sediment core	GeoB 9506-1			GeoB 9508-5			GeoB 9510-1			GeoB 9512-5			GeoB 9513-3			Heinrich Stadial 1
Sediment depth	120-125 cm			270-725 cm			155-160 cm			300-305 cm			165-170 cm			
Grain size [μm]	Mass [g]	Mass [%]	Cum. sum [%]	Mass [g]	Mass [%]	Cum. sum [%]	Mass [g]	Mass [%]	Cum. sum [%]	Mass [g]	Mass [%]	Cum. sum [%]	Mass [g]	Mass [%]	Cum. sum [%]	
initial	35.3652	100.0	-	31.6829	100.0	-	49.5571	100.0	-	49.4491	100.0	-	41.8745	100.0	-	
500	0.0047	0.0	0.0	0.0053	0.0	0.0	0.0053	0.0	0.0	0.0079	0.0	0.0	0.2158	0.5	0.5	
355	0.0260	0.1	0.1	0.0174	0.1	0.1	0.0250	0.1	0.1	0.0068	0.0	0.0	0.0868	0.2	0.7	
250	0.1157	0.4	0.5	0.0334	0.1	0.2	0.0514	0.1	0.2	0.0118	0.0	0.1	0.1403	0.3	1.0	
180	0.1275	0.4	0.9	0.0362	0.2	0.4	0.0615	0.2	0.4	0.0162	0.0	0.1	0.2108	0.5	1.5	
125	0.0903	0.3	1.2	0.0335	0.1	0.5	0.0772	0.2	0.6	0.0260	0.1	0.2	0.2793	0.6	2.1	
90	0.0869	0.3	1.5	0.0393	0.2	0.7	0.0853	0.2	0.8	0.1714	0.4	0.6	0.5083	1.2	3.3	
80	0.0300	0.1	1.6	0.0245	0.1	0.8	0.1497	0.4	1.2	0.4432	1.1	1.6	0.6723	1.5	4.8	
63	0.6050	2.0	3.7	0.4541	1.9	2.7	2.4894	6.5	7.7	6.3862	15.2	16.8	7.6410	17.4	22.3	
40	5.5020	18.6	22.2	7.4406	31.0	33.7	13.5659	35.3	42.9	16.5413	39.3	56.0	17.6144	40.2	62.5	
20	7.9043	26.7	48.9	5.9553	24.8	58.5	9.5850	24.9	67.9	6.7230	16.0	72.0	9.5076	21.7	84.1	
11.1	5.1316	17.3	66.3	2.9419	12.3	70.8	3.3905	8.8	76.7	2.7758	6.6	78.6	1.5824	3.6	87.8	
7.9	0.6003	2.0	68.3	0.4245	1.8	72.6	0.5550	1.4	78.1	0.4941	1.2	79.7	0.2960	0.7	88.4	
5.0	0.5415	1.8	70.1	0.3781	1.6	74.2	0.4786	1.2	79.4	0.3744	0.9	80.6	0.2738	0.6	89.1	
3.2	0.5038	1.7	71.8	0.3016	1.3	75.4	0.3936	1.0	80.4	0.2999	0.7	81.3	0.2570	0.6	89.6	
2.2	0.4707	1.6	73.4	0.2987	1.2	76.7	0.4126	1.1	81.5	0.2446	0.6	81.9	0.2942	0.7	90.3	
1.6	0.5277	1.8	75.2	0.3226	1.3	78.0	0.4414	1.1	82.6	0.2199	0.5	82.4	0.2837	0.6	91.0	

Table 5.5

Masses and relative abundances of grain-size fractions from the Mid Holocene time slice.

Sediment core	GeoB 9506-1			GeoB 9508-5			GeoB 9510-1			GeoB 9512-5			GeoB 9513-3			Mid Holocene
Sediment depth	30-35 cm			60-70 cm			25-30 cm			40-45 cm			50-55 cm			
Grain size [μm]	Mass [g]	Mass [%]	Cum. sum [%]	Mass [g]	Mass [%]	Cum. sum [%]	Mass [g]	Mass [%]	Cum. sum [%]	Mass [g]	Mass [%]	Cum. sum [%]	Mass [g]	Mass [%]	Cum. sum [%]	
initial	23.2449	100.0	-	20.5728	100.0	-	27.5040	100.0	-	24.7665	100.0	-	52.1601	100.0	-	
500	0.0445	0.2	0.2	0.0487	0.3	0.3	0.0047	0.0	0.0	0.0157	0.1	0.1	0.1113	0.3	0.3	
355	0.1054	0.5	0.8	0.0826	0.6	0.9	0.0361	0.2	0.2	0.0440	0.2	0.3	0.0820	0.2	0.6	
250	0.1493	0.8	1.5	0.0857	0.6	1.5	0.0565	0.3	0.5	0.0289	0.2	0.5	0.1902	0.5	1.1	
180	0.1994	1.0	2.6	0.0833	0.6	2.0	0.0838	0.4	0.8	0.0377	0.2	0.7	0.2498	0.7	1.8	
125	0.4320	2.2	4.8	0.0701	0.5	2.5	0.1228	0.6	1.4	0.0816	0.4	1.1	0.3364	1.0	2.8	
90	0.2803	1.5	6.3	0.0852	0.6	3.1	0.1312	0.6	2.0	0.1330	0.7	1.8	0.8900	2.6	5.4	
80	0.1348	0.7	7.0	0.0345	0.2	3.3	0.0869	0.4	2.4	0.0813	0.4	2.2	1.5145	4.4	9.7	
63	0.4344	2.2	9.2	0.1233	0.8	4.1	0.3288	1.5	4.0	0.6677	3.5	5.7	9.6866	27.9	37.6	
40	0.8609	4.5	13.7	0.3814	2.6	6.7	1.5335	7.2	11.1	2.4922	13.0	18.7	10.6436	30.6	68.3	
20	0.8696	4.5	18.2	0.6318	4.2	10.9	2.2858	10.7	21.8	2.0722	10.8	29.6	3.3822	9.7	78.0	
11.1	3.0094	15.6	33.7	2.7508	18.5	29.4	2.4936	11.6	33.5	1.8984	9.9	39.5	1.0210	2.9	80.9	
7.9	0.3339	1.7	35.5	0.2547	1.7	31.1	0.9120	4.3	37.7	0.3320	1.7	41.2	0.2599	0.7	81.7	
5.0	0.3616	1.9	37.3	0.2847	1.9	33.0	1.5968	7.5	45.2	0.3463	1.8	43.0	0.2332	0.7	82.4	
3.2	0.3864	2.0	39.3	0.2604	1.7	34.8	0.9459	4.4	49.6	0.4249	2.2	45.3	0.1912	0.6	82.9	
2.2	0.4259	2.2	41.6	0.3481	2.3	37.1	0.8626	4.0	53.6	0.4745	2.5	47.7	0.2163	0.6	83.5	
1.6	0.4753	2.5	44.0	0.4162	2.8	39.9	0.8505	4.0	57.6	0.4700	2.5	50.2	0.2033	0.6	84.1	

The enviromagnetic methodology provides a range of sedimentary parameters to: (i) mark source areas; (ii) identify pathways of aeolian, fluvial and marine sediments and (iii) detect authigenic Fe-minerals formed by biomineralisation, abiotic precipitation and diagenetic processes. In this study, we mainly focus on the properties of magnetite and haematite, as the first has the strongest impact on the magnetic properties of the sediment and the second is the most abundant Fe-mineral by mass in our research area. The rock-magnetic parameters

Table 5.6

Set of commonly applied rock and environmental magnetic parameters (e.g., Liu et al., 2012) used in this study.

χ	*Magnetic susceptibility* as mass-specific (χ) or volume-specific (κ): ratio between induced magnetisation of a material and the applied magnetic field; measure for (relative) concentration of ferrimagnetic, antiferromagnetic, paramagnetic and diamagnetic minerals.
IRM	*Isothermal Remanent Magnetisation*: magnetisation applied stepwise in direct magnetic fields at constant room temperature.
SIRM	*Saturation IRM*: IRM acquired (in this study) at a 700 mT magnetic field, above which no remanence acquisition takes place due to maximum possible magnetisation; measure for (relative) joint concentration of ferrimagnetic magnetite and antiferromagnetic haematite.
HIRM	*High-coercive IRM*: difference between SIRM and remanence acquired at a 300 mT field; measure for (relative) concentration of magnetically high-coercive haematite.
S-ratio	*Saturation ratio*: remanence obtained in a 300 mT direct field related to SIRM; measure for contribution of pure magnetite to entire sediment magnetisation; under reductive diagenetic alteration the value decreases.
ARM	*Anhysteretic Remanent Magnetisation*: applied in 40 μT direct field; based on relatively low intensity of the applied field and its fast parallel / anti-parallel alternation, ARM is dominantly carried by Single Domain magnetite particles (0.02-0.1 µm).
ARM/IRM	Ratio between remanences acquired in alternating and direct fields of 100 mT; measure for (relative) concentration of fine magnetite particles in relation to coarse; ratio increases with fining particles; with coarsening particles and under reductive diagenetic alteration of magnetite the ratio decreases.

selected for our study and their interpretation is listed in Table 5.6. For detailed explanations, several review papers are available; the most recent review is Liu et al. (2012).

5.5. Results

Grain-size specific mass distribution curves and magnetic parameters for each sediment core and time slice are shown in joint displays in Fig. 5.2a–h. The HS1 curves are always blue hatched and the MH curves green solid. Bulk property values (where shown) are visualised by red triangles (HS1) and circles (MH) for comparison. Due to inconsistent settling and quasi-permanent abeyance of light clay minerals (due to electrostatic interactions), we decided not to analyse fractions <1.6 µm. As we do not expect any sediment-source signal being exclusively contained within that grain-size range, exploring the range between 1.6 and 500 µm is considered representative for the provenance and palaeoclimate related targets of our study.

5.5.1. Grain-size distributions of total sediment and of magnetic minerals

The grain-size distribution curves (Fig. 5.2a) of both time slices illustrate that most particles have grain sizes of 10–70 µm. HS1 sediments show distributions peaking between 40 and 70 µm, strongly skewed towards finer grain sizes. MH grain-size distributions tend to be more bimodal over the coarse silt (40–70 µm) and fine silt (10–20 µm) range. In HS1, the 40–70 µm mode remains dominant over the entire transect, while in MH the 10–20 µm mode becomes more prominent with shore distance and is dominant at the distal locations. Contrasting with the varying amounts of the 40–70 µm mode, the 10–20 µm mode shows no obvious changes between the two time slices. The MH grain-size distributions are also characterised by a higher content of fine particles (<10 µm), in particular at the deeper locations. Cumulative recoveries for the HS1 range from 75% at the deepest to 91% at the shallowest location (Table 5.4). For the MH

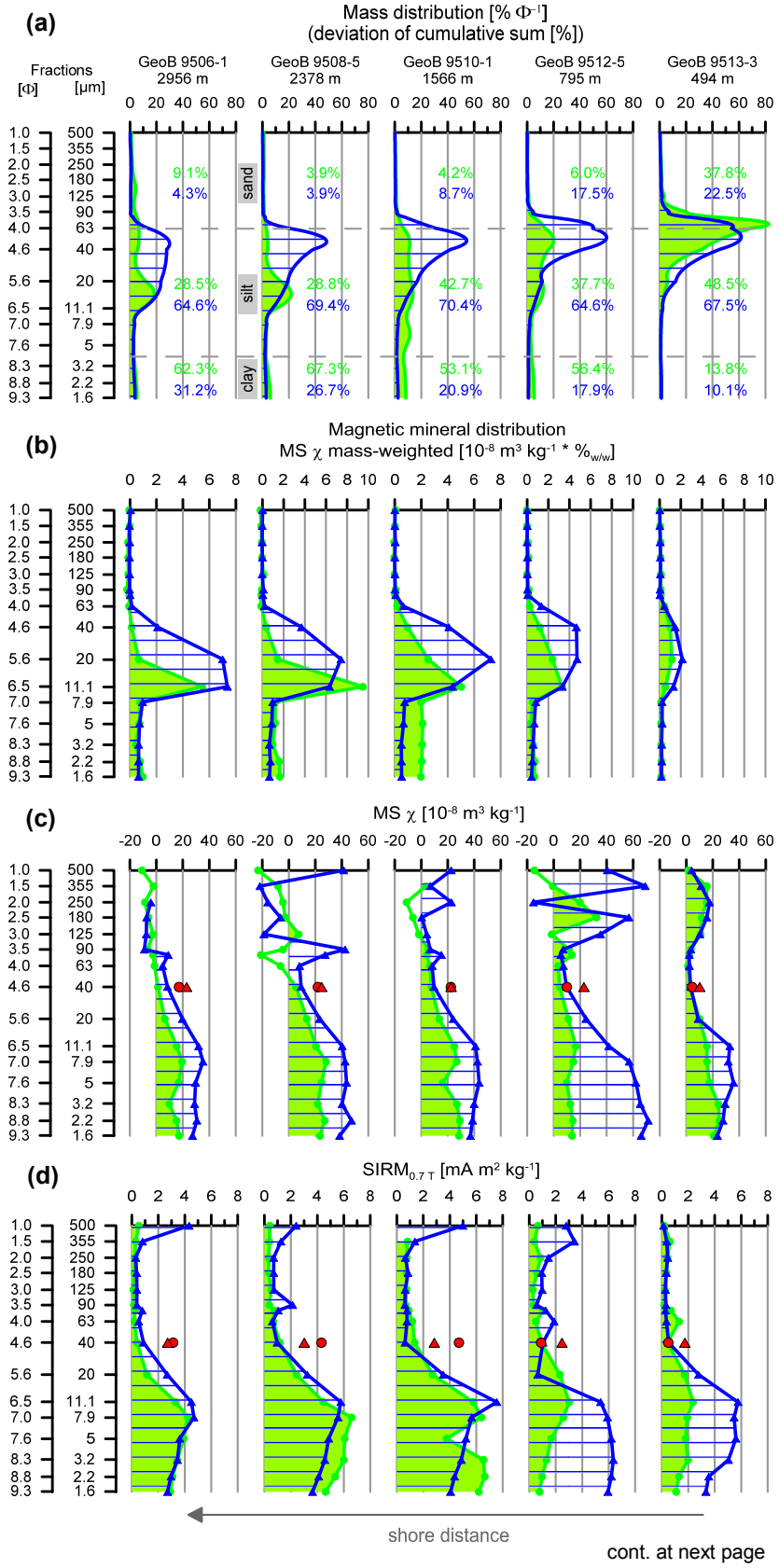

Fig. 5.2. The measured parameters for each grain-size fraction of the core transect are displayed for the Heinrich Stadial 1 (HS1) or Mid Holocene (MH) by blue triangle-marked lines with horizontal hatching or by green dotted lines with solid background, respectively. Bulk sample values are shown as red triangles (HS1) or red dots (MH): (a) Grain-size mass distributions are shown as the cumulative sum derivative (spline of second order) of sieved and settled fractions; (b) Mass-weighted susceptibility (representing mineral grain-size distribution) of both time slices was obtained by multiplying

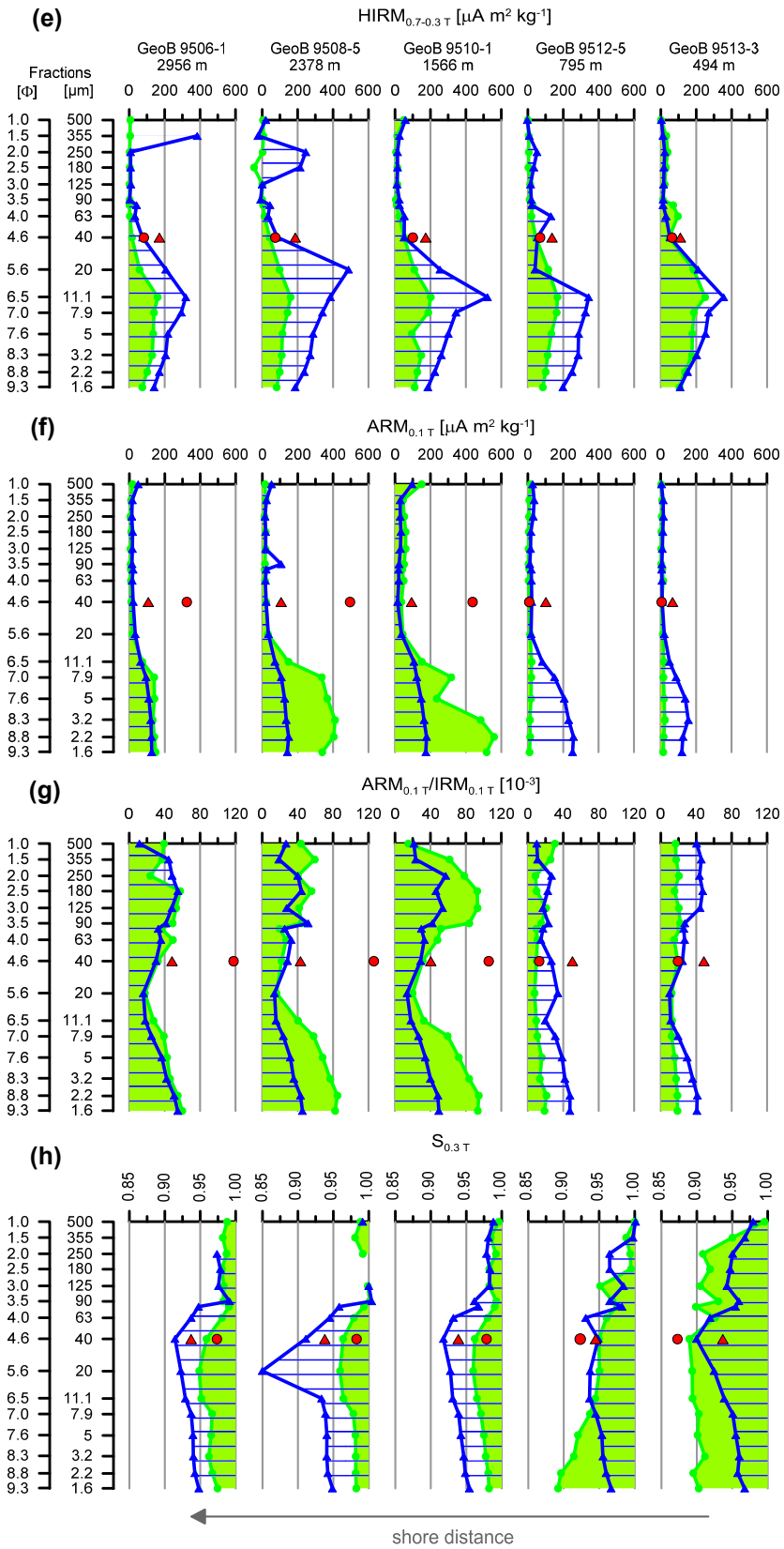

susceptibility χ with the mass portion of the respective grain-size fraction (relative to the cumulative recovered mass ≥1.6 µm); (c) MS χ, (d) $SIRM_{0.7\,T}$, (e) $ARM_{0.1\,T}$ and (f) $HIRM_{0.7–0.3\,T}$ are all shown on a mass-specific basis; (g) Magnetogranulometric $ARM_{0.1\,T}/IRM_{0.1\,T}$ ratio compares relative particle size of magnetite with clastic particle size; (h) $S_{0.3\,T}$ displayed as indicator of magnetite to haematite content. A few values of coarse fractions lie outside the data range and are not displayed for better clarity.

slices, the cumulative recoveries (40–84%) were lower due to the much higher clay contents (14–67% instead of 10–31%) (Table 5.5).

First assumptions about corresponding magnetic mineral grain-size distributions (Fig. 5.2b) were obtained by multiplying the mass-specific susceptibility χ of every grain-size fraction with its respective mass portion (Tables 5.4 and 5.5) and hereafter named as "mass-weighted". Within the investigated grain-size range, the bulk MS resides mainly in fractions of 10–40 µm during HS1 and 10–20 µm during MH; finer fractions down to 1.6 µm also have noticeable influence. Fractions ≥63 µm do not appear to have significant impact on the bulk MS in both time slices. Similar findings are also observed for mass-weighted $ARM_{0.1\,T}$ and $SIRM_{0.7\,T}$ grain-size distribution curves, which are not shown here. All these distributions primarily reflect the behaviour of the mineral magnetite due to its prominent MS.

5.5.2. Grain-size specific magnetic mineral concentrations

If MS χ is displayed without relation to fraction mass (Fig. 5.2c), it represents the magnetic mineral proportion in each grain-size fraction for the given location and time slice. For grain sizes >40 µm, the MS values appear to be quite irregularly distributed. From 40 µm down to 10 µm grain size, MS increases systematically. For even finer grain sizes, the MS values tend to level off and decrease slightly. MS is systematically lower in all MH fractions, averaging ~20×10^{-8} $m^3\,kg^{-1}$, while HS1 values double or even triple. In HS1 fractions, MS slightly decreases with shore distance, while no such trend is observed for MH.

Likewise for both time slices, mass-specific SIRM values (Fig. 5.2d) are very low above 40 µm, except for the coarsest HS1 fractions (355–500 µm). SIRM takes much higher values below 40 µm and reaches its maximum at ~10 µm. At the three distal locations, the differences between MH and HS1 time slices are small, but a decline with shore distance can be observed. The two most proximal cores GeoB 9512-5 and 9513-3 show similar SIRM distributions during HS1 as in the other cores. However, their MH SIRM values are anomalously low in comparison to these outer cores. Fig. 5.2c,d shows similar trends which indicate that MS behaviour is governed by magnetic minerals. SIRM is not affected by paramagnetism and diamagnetism, but reflects magnetic particle size, i.e. domain state.

HIRM values (Fig. 5.2e) are low above 40 µm and increase sharply below that grain size, reaching maxima in the 10–20 µm fractions. They are about two times higher in HS1 as in MH. HIRM values >40 µm are low and irregularly distributed as in the case of MS. No trend with shore distance can be observed for the whole grain-size range.

ARM values (Fig. 5.2f) in grain-size fractions >40 µm are very low. Interestingly ARM values increase only in the <20 µm fractions. For HS1, ARM behaviour does not change much as function of shore distance. In contrast, MH trends differ vastly: At the two most proximal locations, fine magnetite particles seem to be nearly absent, while in the central core GeoB 95010-1 MH values are times those of HS1.

The HS1 bulk values of MS, SIRM, HIRM, and ARM are in most cases about half of the fractions' maximum values. For MH, however, bulk values resemble more the high values of the finest fractions collected. As the masses of MH fractions <1.6 µm are larger than those of HS1 (cf., Tables 5.4 and 5.5), the formers have consequently a stronger magnetic influence on the bulk values. We are aware that a portion of fine magnetic particles was lost in the grain-size extraction

procedure. Although fractions <1.6 µm may have a considerable influence on the bulk signal, in the present study they can be neglected, as it is unlikely that they contain information about a separate sediment source not being already represented by the properties of coarser fractions.

5.5.3. Grain-size specific magnetic granulometry and mineralogy

Through all MH fractions, the two most proximal cores show rather constant and low ARM/IRM values, pointing towards diagenetic depletion of fine magnetite grains. Interestingly for the other cores, the magnetogranulometric proxy parameter ARM/IRM (Fig. 5.2g) does not show the anticipated linear grain-size dependence, but prominent bimodal characteristics. With one exception, all distribution curves have minima at 20 µm marking the coarsest magnetite crystal sizes. Towards finer and coarser clastic grain-sizes, ARM/IRM increases systematically in both time slices. The largest increase is observed in the MH sample of the central core GeoB 9510-1. No trend with shore distance is visible in HS1. The MH fractions of the three outer cores show a smaller ARM/IRM increase with shore distance.

S-ratio values (Fig. 5.2h) are relatively low, i.e. more haematite-dominated, between 10 and 63 µm and reach nearly 1.00, i.e. magnetite-dominated, for the coarser (>63 µm) fractions. The relative magnetite proportion also increases towards finer grain sizes below 10 µm. At the three most distal core locations, the MH fractions show less haematite predominance than the HS1 fractions. At the two most proximal core locations, MH grain-size fraction values indicate selective magnetite depletion with respect to haematite. For both time slices, there is no obvious trend with shore distance.

5.6. Interpretation and discussion

Before we can interpret measured trends in terms of provenance and palaeoclimate, we need to consider potential biasing factors of magnetic properties such as diagenetic dissolution of magnetite and dilution by biogenic carbonates. Afterwards, we aim to distinguish the two relevant aeolian transport systems (north-easterly trade winds and Harmattan) and deduce palaeoclimatic changes from sediment flux variations. Finally, we will draw attention to the sediment contributions by the Senegal River.

5.6.1. Diagenetic dissolution of fine-grained magnetite

Grain-size fractionation clearly facilitates to demonstrate the known effects of reduction and dissolution of sedimentary Fe-oxides during organic matter degradation and remineralisation (Karlin and Levi, 1983; Canfield and Berner, 1987; Canfield et al., 1992; Tarduno, 1994; Smirnov and Tarduno, 2000; Fu et al., 2008; Rowan et al., 2009). Magnetite reduction occurs primarily during the MH at the two proximal sites as documented by unusually low SIRM, ARM, and ARM/IRM values (Fig. 5.2d,f,g). The two inner core sites are closer to the Senegal River mouth and receive a higher input of fresh terrestrial organic matter (Zarriess and Mackensen, 2010). Magnetite reduction primarily affects fine isolated grains due to their much larger specific surface (Karlin and Levi, 1985; Robinson et al., 2000). Especially core GeoB 9512-5 shows increaseing diagenetic alteration (lower SIRM, ARM, and S-ratio) towards finer grain sizes (Fig. 5.2d,f,h). This effect is not occurring at the three more distal locations of the MH, nor along the entire transect during the HS1.

The impact of grain-size selective diagenesis on the magnetic characteristics is even better shown

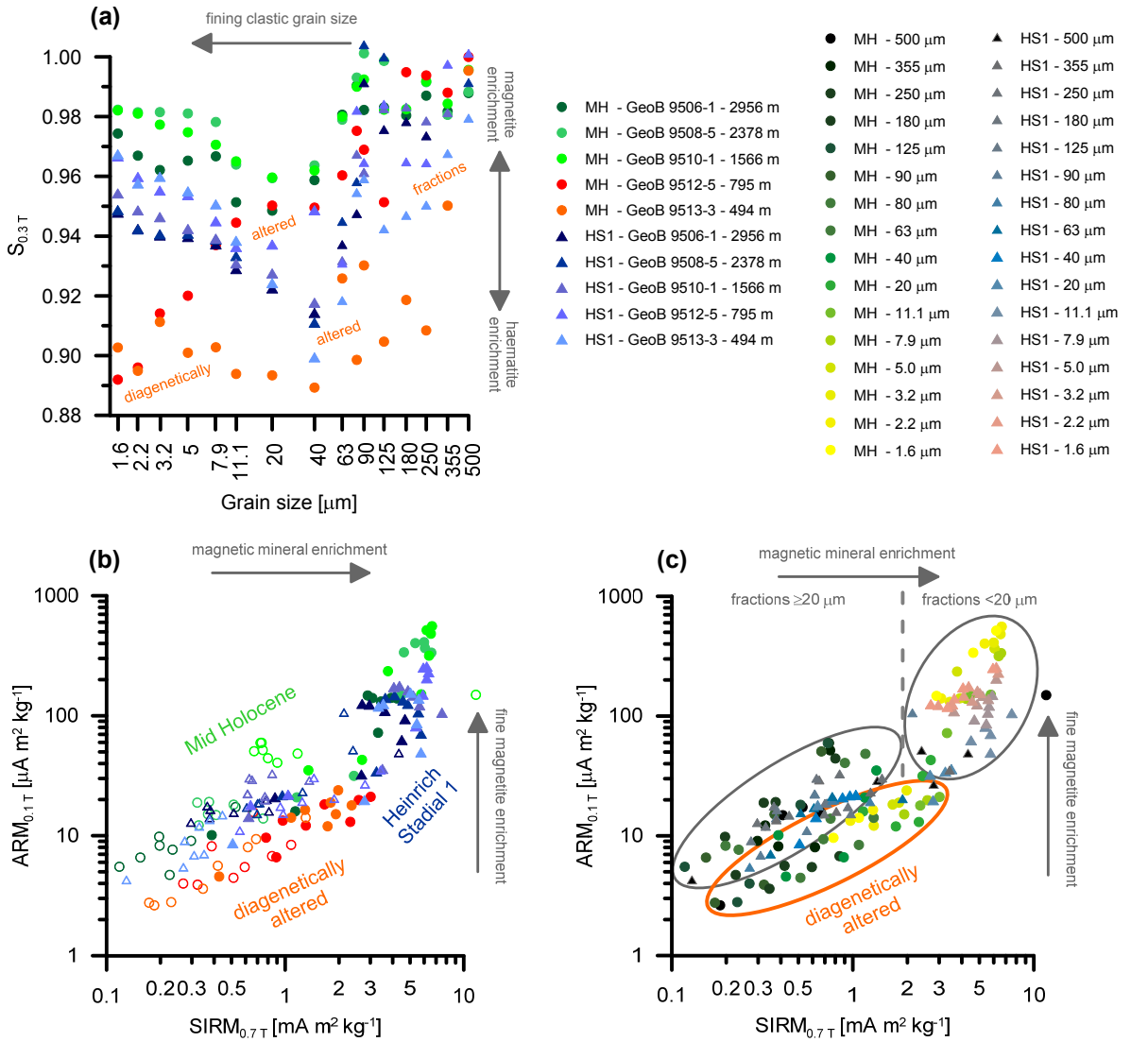

Fig. 5.3. $S_{0.3\,T}$ vs. grain size plot (a) summarises Fig. 5.2h and displays the intensification of magnetite dissolution particularly in fine grain-size fractions. $ARM_{0.1\,T}$ vs. $SIRM_{0.7\,T}$ plot (b) shows magnetic property trends of individual grain-size fractions in response to the environmental conditions in Heinrich Stadial 1 (HS1; bluish triangles) and Mid Holocene (MH; greenish dots). Fractions ≥63 µm are displayed as empty circles of the respective colours. Diagram (c) shows the same data as (b) but highlights the grain-size trends in black-blue-pink colours for HS1 and black-green-yellow colours for MH. Fractions have been grouped for better interpretability.

in crossplots in Fig. 5.3: While (a) highlights the intensity of diagenetic magnetite depletion within the clastic grain-size fractions, (b) points out the different magnetic "palaeoclimate trends" of MH and HS1, where the magnetite-depleted MH grain-size fractions resemble more the characteristics of the HS1 fractions than those of unaltered MH fractions. Finally, Fig. 5.3c points out that selective diagenesis biases magnetogranulometric information.

5.6.2. Dilution by marine carbonates

Besides the gradual concentration increase of fine magnetite particles in fining clastic grain-size fractions <20 µm (Fig. 5.4a), fractions ≥63 µm show an enrichment of fine magnetite particles with no consistent trend. These unexpected magnetogranulometric ARM/IRM trends ≥63 µm have three potential reasons: (i) autochthonous benthic and planktonic foraminifera fragments occur

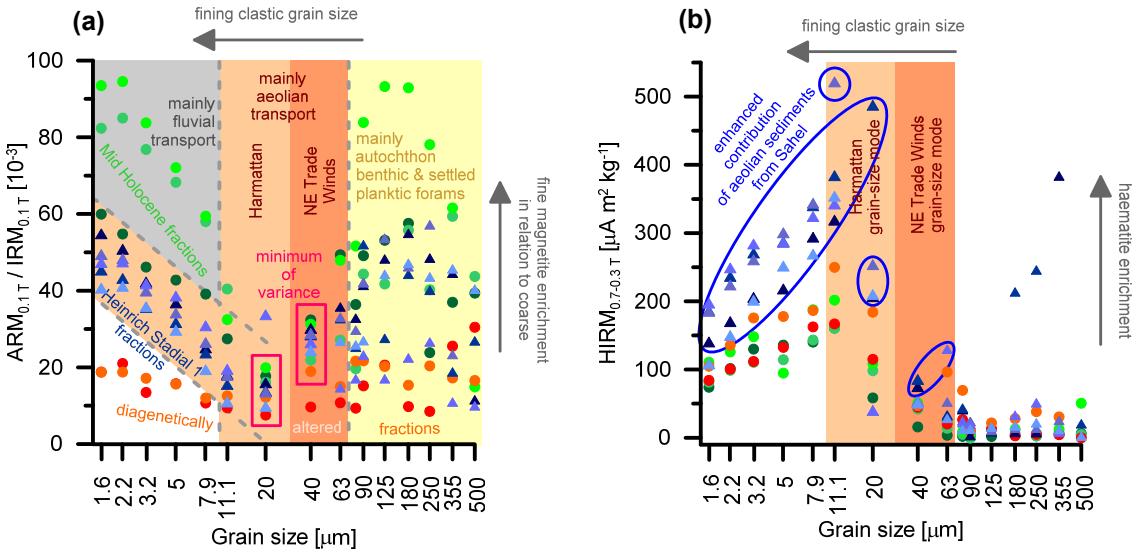

Fig. 5.4. (a) Magnetogranulometry ($ARM_{0.1\,T}/IRM_{0.1\,T}$) vs. clastic grain size plot encloses the appearance of fine magnetite particles and magnetic inclusions. Based on the magnetogranulometric trends between adjacent grain-size fractions and variances within distinct grain-size fraction, different transport processes and sources can be visualised. (b) $HIRM_{0.7–0.3\,T}$ vs. clastic grain size visualises the enhanced content in haematite-coated particles (emphasised by blue ellipses) during the HS1 with respect to the MH data. The colour key is identical to Fig. 5.3a,b.

as individual particles within this grain-size range. As these hollow carbonate shells are fragile, it is conceivable that fine-grained magnetites may have entered their interior during burial; (ii) fine-grained magnetic particles often occur as inclusions in large clastic particles of igneous origin (Hounslow and Maher, 1996; Otofuji et al., 2000; Hounslow and Morton, 2004); (iii) as magnetites are heavy minerals, they are rarely found in deep marine sediments as individual terrigenous particles of ≥63 µm. Due to their higher density, fine heavy minerals are often incorporated into shells of agglutinated benthic foraminifera, which makes them less prone to current drifts (e.g., Makled and Langer, 2010).

As we observe diagenetic dissolution of magnetite throughout the entire MH grain-size range (Figs. 5.3 and 5.4a) at the two shallowest locations, only hypothesis (i) reasonably explains the inconsistent relative enrichment of fine magnetites versus coarse magnetites in fractions ≥63 µm. While fragile foraminifera can contain fine magnetites, they do not protect them from dissolution. Explanations (ii) and (iii) are still possible, but are likely of minor importance. Terrigenous quartz of igneous origin with particles of 63–500 µm is rarely transported to the continental slope and rise by either aeolian or fluvial systems. Agglutinating benthic foraminifera would be more appropriate, as they explain at least the minor magnetic peaks at 63–90 µm (Fig. 5.2c–f). However, fine-grained magnetite inclusions in quartz grains or in agglutinating benthic foraminifera would be protected from selective diagenetic dissolution, while even coarser individual magnetites could be dissolved. Under such protection, fine inclusions would lead to an increase of the granulometric proxy ARM/IRM, which contradicts our observation throughout all altered grain-size fractions (Fig. 5.4a). Therefore, in the next sections, these relatively small fractions ≥63 µm will be considered as less relevant, as well as less significant for the reconstruction of sediment sources and palaeoclimatic changes.

5.6.3. Aeolian sediment fluxes and sources

To carry out magnetic fingerprinting of distinct Northwest African dust species, we begin with

identifying grain-size ranges with characteristic haematite-magnetite proportions. Dust particles transported by north-easterly trade winds should be found in the 40–63 µm mode (Table 5.1), where intermediate proportions of haematite-coated particles with respect to fractions >63 µm and <40 µm are observed (Fig. 5.4b). Particles transported by the Harmattan would be expected in the 10–20 µm mode, which contains the highest proportion of haematite and lowest of fine-grained magnetite in respect to other fractions (Fig. 5.4a). Although haematites occur as coatings on particles particularly in the Harmattan mode (Fig. 5.4b), it is likely that haematite particles in the <10 µm fractions were also mainly transported by the Harmattan. The notion that the <10 µm fractions are an extension of the Harmattan 10–20 µm mode is most clearly supported by the steady ARM/IRM trend between 1.6 and 20 µm in the HS1 time slice (Fig. 5.4a). The consistent fining of clastic and magnetic grain sizes indicates that fine magnetite grains seem to exist as individual particles unlike the haematite coatings. The ARM/IRM values of the trade-wind mode (40–63 µm) lie outside this trend. The ARM/IRM vs. SIRM cross-plots (Fig. 5.5a,b) also show that the magnetic characteristics of the coarse end of the Harmattan fraction (~20 µm) are very similar to those of the <20 µm dust. The 10 µm Harmattan fraction is indistinguishable from the properties of the <10 µm fractions, while the trade-wind fraction of 40 µm clearly differs magnetically.

The Harmattan sediment load originates from the Sahel Zone (Fig. 5.1a), as it resembles the properties of the strongly magnetic Sahelian surface sediments (Figs. 5.4a,b and 5.5a,b; Table 5.1) (Koopmann, 1981; Lyons et al., 2010, 2012). Their haematite coatings are created by pedogenic processes during successive arid and humid seasons (Kämpf and Schwertmann, 1983; Schwertmann and Taylor, 1989). Consequently, the quartz grains of the arid southern and western Sahara show lower concentrations of haematite-coatings. Their magnetic properties (Figs. 5.4a,b and 5.5a,b) resemble those being transported by the north-easterly trade winds. More distal sediment sources for the trade-wind mode (40–63 µm) than the white coastal Senegalese dunes can be excluded, as particles with grain sizes of 40–63 µm can only be transported over 20–100 km (Koopmann, 1981 and references therein; Grousset et al., 1998).

Based on the grain-size distributions (Fig. 5.2a), as well as on the magnetomineralogy (Fig. 5.4b) and magnetogranulometry (Figs. 5.4a and 5.5a,b), we are now able to reconstruct palaeoclimatic impacts on the transport dynamics: During the arid HS1 in respect to the humid MH, the north-easterly trade winds were strengthened, as seen in the higher portion of the 40–63 µm mode (Fig. 5.2b). While the sediments carried by the trade winds (40–63 µm) do not show any strong change neither in ARM/IRM (Fig. 5.4a) nor in HIRM (Fig. 5.4b) from HS1 to MH, there is a clearly visible shift in the Harmattan mode (10–20 µm). As, however, the 10–20 µm grain-size mode (Fig. 5.2a) does not shift or increase in proportion, we deduce that the Harmattan at these latitudes was not stronger during HS1 than during MH. Stronger HS1 trade winds and the rather constant wind velocities of the Harmattan are in agreement with earlier studies (e.g., Koopmann, 1981; Sarnthein et al., 1981; Mulitza et al., 2008; Tjallingii et al., 2008; Itambi et al., 2009; Zarriess and Mackensen, 2010). Both together produced at least 2–5 times higher accumulation rates of aeolian sediments off-coast Northwest Africa than today (Koopmann, 1981; Sarnthein et al., 1981;

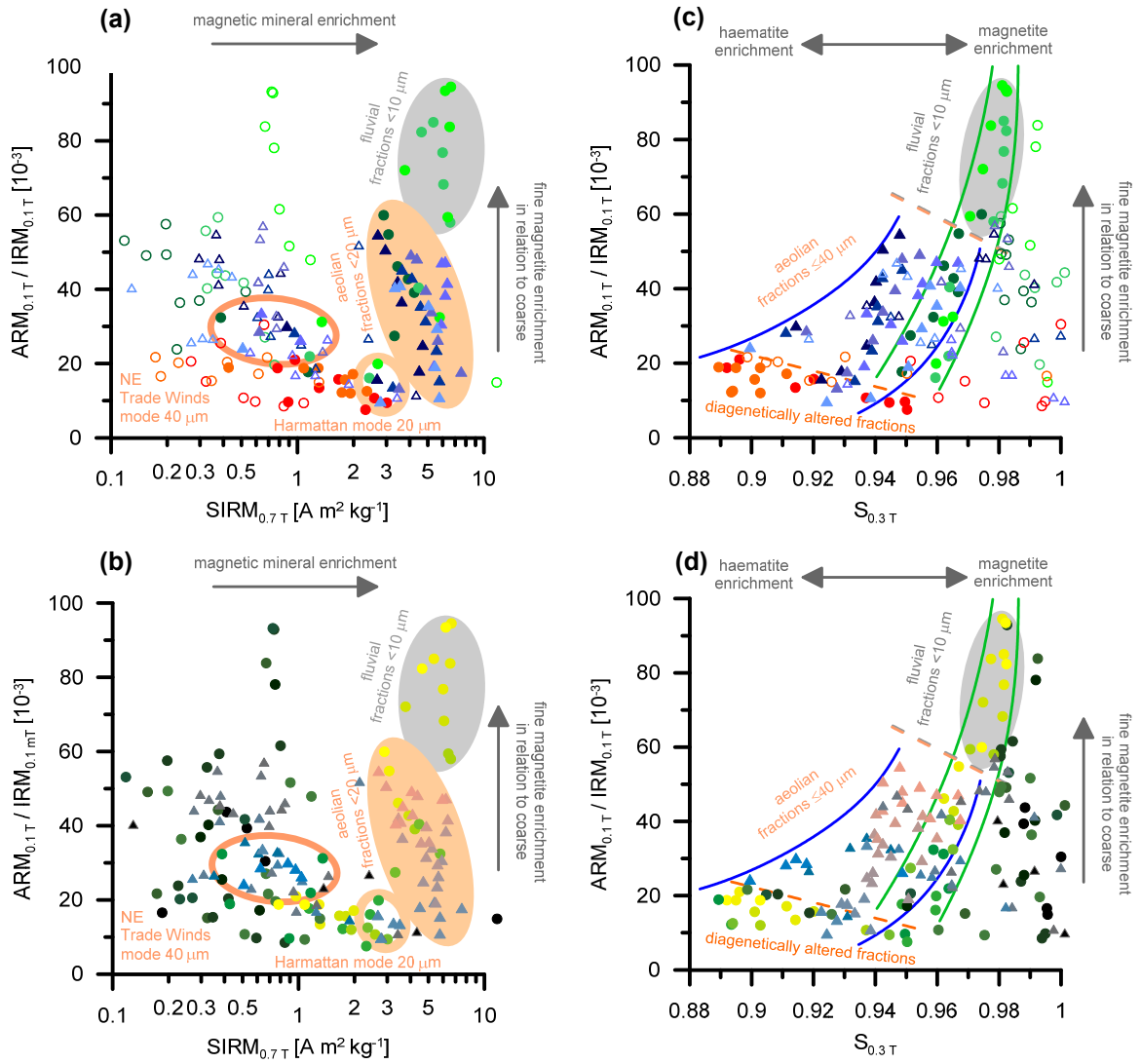

Fig. 5.5. (a,b) $ARM_{0.1\,T}/IRM_{0.1\,T}$ vs. $SIRM_{0.7\,T}$ plot highlights the differences between each of the two aeolian sediment sources as well as of the fluvial one. Colouring in (a) focuses on the climate phases, that in (b) on grain-size fractions. (c,d) $ARM_{0.1\,T}/IRM_{0.1\,T}$ vs. $S_{0.3\,T}$ plot indicates different magnetic properties of aeolian and fluvial sediments with (c) climate, and (d) grain-size interpretational aspects highlighted. The colour keys are identical to Fig. 5.3, while fractions ≥63 µm are displayed as circles.

deMenocal et al., 2000; Kohfeld and Harrison, 2001; Mulitza et al., 2008; Tjallingii et al., 2008; Itambi et al., 2009) or even 40–120 times higher ones (Just et al., 2012b). The enhanced HS1 accumulation rates could additionally be favoured by the ~100 m lower sea level than during the MH (Faure et al., 1980; Barusseau et al., 1988; Fleming et al., 1998; Lambeck and Chappell, 2001, updated 2007; Waelbroeck et al., 2002), moving the shore line 25–30 km closer to the transect.

The increased haematite proportions during the arid HS1 (Fig. 5.4b) suggest that more highly magnetic Sahelian sediments have been transported during Heinrich Stadials even without intensification of the easterly Harmattan at these latitudes. This larger dust export could have been enabled by a sparser or even any vegetation cover in the Sahel during HS1 (e.g., Nicholson and Flohn, 1980; deMenocal et al., 2000; Tjallingii et al., 2008). During the MH, the Sahel Zone and the southern Sahara had a dense vegetation cover (denser than today's) inhibiting

haematite-coated particles from being uplifted by winds. This would raise the relative proportion of haematite-poor sediments from the southern Sahara within the Harmattan dust flux.

5.6.4. Fluvial sediment flux and sources

During the arid HS1, large parts of the shelf were subaerially exposed and covered by coast-line parallel dune fields acting as barriers for the Senegal River (Nicholson and Flohn, 1980; Koopmann, 1981; Nizou et al., 2010). Senegal River sediments with typical grain sizes of <10 µm (e.g. Koopmann, 1981) were therefore not exported to the Northwest African continental slope (Nicholson and Flohn, 1980; Koopmann, 1981; Gasse and Campo, 1994; Gasse, 2000; Mulitza et al., 2008; Nizou et al., 2010). Terrigenous particles <10 µm (Fig. 5.2a) deposited at the northern Senegalese continental slope during this time, can consequently not be directly linked to the fluvial transport system. Although the continental slope underwent strong upwelling by intensified north-easterly trade winds during HS1 (e.g., Zarriess and Mackensen, 2010; Just et al., 2012a), we can exclude resuspension of former fluvial silts and clays at the upper continental slope and shelf. Remobilised silts would show a down-slope directed concentration increase (defined as sortable silt of 10–63 µm; e.g., McCave et al., 1995), as they are easiest to be remobilised by currents after deposition. This scenario can be ruled out, as no distortion of a consistent shore-distance (down-slope) trend is detectable in the grain-size distributions (Fig. 5.2a).

In contrast, due to the increased precipitation during the African Humid Period, the MH sediment export by the Senegal River became significant (Nicholson and Flohn, 1980; Koopmann, 1981; Gasse and Campo, 1994; Gasse, 2000; Mulitza et al., 2008; Nizou et al., 2010). This change in the fluvial contribution between the HS1 and MH slices is most distinct at the location of GeoB 9510-1 (Figs. 5.1d and 5.2a). There, the fine sediment is trapped at the eastern (upper) flank of a sea-mount, acting as a down-slope transport barrier (Mulitza et al., 2006). However, if the grain-size distributions are being considered only (Fig. 5.2a), the change in fluvial contribution between HS1 and MH can only vaguely be detected at other locations of the transect. The change in the relative clay abundances seems to be more evident, as these values double or even triple from HS1 to MH (Fig. 5.2a; Tables 5.4 and 5.5). However, the increase in clay content might reflect a weakened MH dust flux in the 40–63 µm grain-size mode.

This ambiguity can be resolved by magnetics, as the presence of fluvial sediments during MH is clearly revealed by the magnetogranulometric parameters in Figs. 5.4a and 5.5a,b. Fluvial sediments contain a higher fine-grained magnetite content in comparison to <10 µm fractions from the HS1 time slice. The concentration of fine-grained fluvial magnetite also decreases faster with shore-distance than the aeolian contributions, as expressed by the much steeper ARM/IRM vs. grain-size gradient in the 1.6–20 µm range (Fig. 5.4a). Fine-grained magnetite is also present in the HS1 grain-size fractions (Fig. 5.4a), but the variation with shore-distance (especially within the two aeolian modes at 10–20 µm and 40–63 µm) is much lower, pointing to the extensive dust transport by the Harmattan. In cross-plot Fig. 5.5c,d, magnetogranulometry and magnetomineralogy are combined. Here, the fluvial contribution during MH is also differentiated from the aeolian by a higher fine-grained magnetite proportion and by a lower haematite-magnetite proportion. This cross-plot visualises

that the haematite-rich trend of HS1 does lack the fluvial component.

We argue that this fine fluvial magnetite is either of igneous origin from the nowadays semi-humid upper reaches of the Senegal River or pedogenically formed in the overlain soils, which are very common there (Lyons et al., 2010 and references therein). A biogenic origin for very fine-grained magnetite must always be considered as an alternative explanation for stronger sediment magnetic properties. Fossilised magnetosomes (very crystalline particles of 0.02–0.1 µm) created by magnetotactic bacteria are very common in marine surface sediments (e.g., Petersen et al., 1986; Just et al., 2012a). Additionally, Oldfield et al. (2009) showed by means of grain-size based rock-magnetism on various terrigenous samples that magnetosomes tend to settle mainly in fractions of 2–4 µm. This was explained by their clustering to chains and aggregation to clay minerals. However, in a magnetic end-member study on sediment cores from the continental slope off the Gambia River, Just et al. (2012a) found that higher sedimentary magnetosome concentrations were linked to higher MH riverine input of fresh terrestrial organic matter (Zarriess and Mackensen, 2010). Thus, even if the higher magnetisation with fining clastic grain-size is due to biogenic magnetite, the latter is valid to be used as indirect marker for stronger riverine input in our study area and fully supports our palaeoclimatic and transport-related interpretations.

Since budgeting of aeolian and fluvial sediment fluxes is beyond the scope of our study, we deal only with relative concentrations (Fig. 5.2a; Tables 5.4 and 5.5) and not with accumulation rates. A quantification of the fluvial sediment flux would require determination of sedimentation rates from more precise age models and a sediment volume calibration of magnetic markers as described by Just et al. (2012b). However, by combining magnetogranulometric (Figs. 5.4a and 5.5a,b) with magnetomineralogical (Figs. 5.4b and 5.5c,d) parameters from two contrasting climate situations, we seem to be able to distinguish between fluvial and aeolian sediments in the fine 1.6–10 µm grain-size range. This is interesting, as foregoing studies in this area could not untangle the “mixed” fluvio-aeolian <10 µm sediment fraction (e.g., Koopmann, 1981; Grousset et al., 1998; Itambi et al., 2009). These findings were possible primarily because of the additional gain of grain-size specific information, which goes further beyond those obtained from exclusive bulk investigations. In particular, the magnetogranulometric parameter ARM/IRM on a grain-size specific basis appears to be sensitive in detecting selective magnetite dissolution, while it also contributes to a more robust provenance study.

5.7. Conclusions

The simultaneous action of multiple environmental processes, ranging from sediment dynamics to climate-related weathering of source rocks, defines grain-size distributions of terrigenous marine sediments. Unravelling these processes from proxy records is a non-trivial task. This pilot study returned to the well-studied continental slope sediments off northern Senegal as an application study to fathom the potential of integrated grain-size and enviromagnetic analyses. By applying rock-magnetic measurements not just to bulk samples, but to a wide range of well-defined grain-size fractions obtained by wet sieving and settling methods, many new interpretational options arise. Since this approach also distinctly enlarges the number of processed samples, it is not feasible to deploy a continuous

high-resolution record. Therefore, we decided to focus on two contrasting Northwest African climate phases, the arid Heinrich Stadial 1 and the humid Mid Holocene.

The joint consideration of sedimentological and magnetogranulometric parameters appears to be a sensitive and powerful approach for a differentiated understanding of source and transport mechanisms. The insights would not be achievable solely from an interpretation of grain-size distributions and bulk-magnetic measurements. Especially, the magnetogranulometric parameter ARM/IRM on a grain-size specific basis appears to be sensitive in detecting selective magnetite dissolution.

We departed from the assumption of two "aeolian" grain-size modes of 40–63 µm (north-easterly trade winds) and 10–20 µm (Harmattan) and were able to verify that these grain-size modes contain different proportions of fine (as inclusions) and coarse (separate) magnetite particles. The trade wind and Harmattan modes occur in the sediments with different haematite to magnetite proportions. Haematite occurs as fine-grained coatings on larger quartz particles and clay minerals. Beyond distinguishing transport systems, these magnetogranulometric "fingerprints" mirror the formation conditions of the magnetic particles at their respective sediment source (trade winds: Senegalese coastal dunes – Harmattan: southern Sahara and Sahel). Palaeoclimatic variations in aeolian transport dynamics could hence be identified by their peculiar grain-size modes. Changes in the palaeoclimatic conditions of the Sahel could be detected by changing proportions of haematite-coatings within the Harmattan sediment mode. Fluvial and aeolian sediments in the 1.6–10 µm grain-size range could be differentiated by the higher fine-grained magnetite content of the former. Fluvial fractions show a much greater shore-distance dependency as aeolian fractions.

Particles in the 63–500 µm range were identified as autochthonous benthic foraminifera and planktonic foraminifera settling from the surface waters above and probably being filled with fine magnetite-bearing sediment during burial. This was hinted at by the absence of consistent magnetogranulometric trends and the occasionally negative diamagnetic susceptibility values of these fractions.

We could show by comparing standard magnetic bulk-sediment measurements with those of individual grain-size fractions that it is not straightforward to tie bulk magnetic properties to certain grain-size fractions. This can become error-prone, particularly when sedimentological and enviromagnetic investigations would be launched in areas, where no constraints are possible concerning the distribution, concentration and origin of magnetic minerals. In such cases, however, it would seem insightful to check also the grain-size dependency of magnetic properties, at least for a few selected test samples. Once the fractions containing the magnetic mineral concentration-peaks are detected, the fractionation approach can be simplified and limited to just a few fractions of interest. Hence, the presented approach can improve the understanding of sediment transport processes, enable budgeting of sediment fluxes at complex depositional centres, facilitate provenance studies and thereby strengthen future palaeoclimatic and palaeoceanographic investigations.

5.8. Acknowledgements

The authors would like to thank the reviewers for their constructive comments which greatly improved the paper. We acknowledge Dr. A. Cletus Itambi for stimulating discussions and comments on the manuscript at an early stage. We thank

the captain and crew of R/V METEOR cruise M65 who played a vital part in the recovery of the investigated sediment cores. Financial support for this study was provided to S.R. by the DFG through the European Graduate College “Proxies in Earth History” EUROPROX. This work contributes to MARUM Research Area Sediment Dynamics project SD2 – Climatic control on large-scale sedimentary structures. Data presented in this study are available at the PANGAEA database (http://www.pangaea.de).

5.9. References

Allen, J.R.L., 1965. A review of the origin and characteristics of recent alluvial sediments. Sedimentology 5, 89─191.

Barbanti, A., Bothner, M.H., 1993. A procedure for partitioning bulk sediments into distinct grain-size fractions for geochemical analysis. Environmental Geology 21, 3–13.

Barusseau, J.P., Giresse, P., Faure, H., Lézine, A.M., Masse, J.P., 1988. Marine sedimentary environments on some parts of the tropical and equatorial Atlantic margins of Africa during the Late Quaternary. Continental Shelf Research 8, 1–21.

Canfield, D.E., Berner, R.A., 1987. Dissolution and pyritization of magnetite in anoxic marine sediments. Geochimica et Cosmochimica Acta 51, 645–659.

Canfield, D.E., Raiswell, R., Bottrell, S., 1992. The reactivity of sedimentary iron minerals toward sulfide. American Journal of Science 292, 659–683.

Caquineau, S., Gaudichet, A., Gomes, L., Legrand, M., 2002. Mineralogy of Saharan dust transported over northwestern tropical Atlantic Ocean in relation to source regions. Journal of Geophysical Research 107, D15, 4251, 12 pp.

deMenocal, P., Ortiz, J., Guilderson, T., Adkins, J., Sarnthein, M., Baker, L., Yarusinsky, M., 2000. Abrupt onset and termination of the African Humid Period: rapid climate responses to gradual insolation forcing. Quaternary Science Reviews 19, 347–361.

Dettwiller, J., 1965. Note sur la structure du front intertropical boréal sur le Nord-Ouest de l’Afrique. Météorologie 6, 337–347.

Diester-Haass, L., 1976. Late Quaternary climatic variations in northwest Africa deduced from East Atlantic sediment cores. Quaternary Research 6, 299–314.

Faure, H., Fontes, J.C., Hebrard, L., Monteillet, J., Pirazzoli, P.A., 1980. Geoidal change and shore-level tilt along Holocene estuaries: Sénégal River Area, West Africa. Science 210, 421–423.

Fleming, K., Johnston, P., Zwartz, D., Yokoyama, Y., Lambeck, K., Chappell, J., 1998. Refining the eustatic sea level curve since the Last Glacial Maximum using far- and intermediate-field sites. Earth and Planetary Science Letters 163, 327–342.

Folk, R.L., 1966. A review of grain-size parameters. Sedimentology 6, 73–93.

Franke, C., von Dobeneck, T., Drury, M.R., Meeldijk, J.D., Dekkers, M.J., 2007. Magnetic petrology of equatorial Atlantic sediments: Electron microscopic results and their environmental magnetic implications. Paleoceanography 22, PA4207, pp. 23.

Fu, Y., von Dobeneck, T., Franke, C., Heslop, D., Kasten, S., 2008. Rock magnetic identification and geochemical process models of greigite formation in Quaternary marine sediments from the Gulf of Mexico (IODP Hole U1319A). Earth and Planetary Science Letters 275, 233–245.

Gac, J.Y., Kane, A. 1986. Le fleuve Sénégal / I : Bilan hydrologique et flux continentaux de matières particulaires a l’embouchure. Sciences Géologiques Bulletin 39, pp. 99–130.

Gasse, F. 2000. Hydrological changes in the African tropics since the Last Glacial Maximum. Quaternary Science Reviews 19, 189–211.

Gasse, F., van Campo, E., 1994. Abrupt post-glacial climate events in West Asia and North Africa monsoon domains. Earth and Planetary Science Letters 126, 435–456.

Germain, H., 1968. Météorologie dynamique et climatologie; application au régime des pluies au Sénégal. ASECNA, Direction de l’Exploitation Météorologique, Dakar, Sénégal, 15 p.

Grousset, F.E., Parra, M., Bory, A., Martinez, P., Bertrand, P., Shimmeld, G., Ellam, R.M., 1998. Saharan wind regimes traced by the Sr–Nd isotopic composition of subtropical Atlantic sediments: Last Glacial Maximum vs today. Quaternary Science Reviews 17, 395–409.

Hagen, E., 2001. Northwest African upwelling scenario. Oceanologica Acta 24 – Supplement, 113–128.

Hatfield, R.G., Maher, B.A., 2009. Fingerprinting upland sediment sources: particle size-specific magnetic linkages between soils, lake sediments and suspended sediments. Earth Surface Processes and Landforms 34, 1359–1373.

Hatfield, R.G., Cioppa, M.T., Trenhaile, A.S., 2010. Sediment sorting and beach erosion along a coastal foreland: Magnetic measurements in Point Pelee National Park, Ontario, Canada. Sedimentary Geology 231, 63–73.

Hatfield, R.G., Stoner, J.S., Carlson, A.E., Reyes, A.V., Housen, B.A., 2013. Source as a controlling factor on the quality and interpretation of sediment magnetic records from the northern North Atlantic. Earth and Planetary Science Letters 368, 69–77.

Hesse, P.P., 1994. Evidence for bacterial palaeoecological origin of mineral magnetic cycles in oxic and sub-oxic Tasman Sea sediments. Marine Geology 117, 1–17.

Holland, K.T., Elmore, P.A., 2008. A review of heterogeneous sediments in coastal environments. Earth-Science Reviews 89, 116–134.

Holz, C. Stuut, J.-B., Henrich, R., 2004. Terrigenous sedimentation processes along the continental margin off NW Africa: implications from grain-size analysis of seabed sediments. Sedimentology 51, 1145–1154.

Hounslow, M.W., Maher, B.A., 1996. Quantitative extraction and analysis of carriers of magnetization in sediments. Geophysical Journal International 124, 57–74.

Hounslow, M.W., Morton, A.C., 2004. Evaluation of sediment provenance using magnetic mineral inclusions in clastic silicates, comparison with heavy mineral analysis. Sedimentary Geology 171, 13–36.

Itambi, A.C., von Dobeneck, T., Mulitza, S., Bickert, T., Heslop, D., 2009. Millennial-scale northwest African droughts related to Heinrich events and Dansgaard-Oeschger cycles: Evidence in marine sediments from offshore Senegal. Paleoceanography 24, 1205–1220.

Just, J., Dekkers, M.J., von Dobeneck, T., van Hoesel, A., Bickert, T., 2012a. Signatures and significance of aeolian, fluvial, bacterial and diagenetic magnetic mineral fractions in Late Quaternary marine sediments off Gambia, NW Africa, Geochemistry, Geophysics, Geosystems 13, Q0AO02, 23 p.

Just, J., Heslop, D., von Dobeneck, T., Dekkers, M.J., Frederichs, T., Meyer, I., Zabel, M., 2012b. Multi-proxy characterization and budgeting of terrigenous end-

members at the NW African continental margin. Geochemistry, Geophysics, Geosystems 13, Q0AO01, 18 p.

Kämpf, N., Schwertmann, U., 1983. Goethite and hematite in a climosequence in southern Brazil and their application in classification of kaolinitic soils. Geoderma 29, 27–39.

Karlin, R., Levi, S., 1983. Diagenesis of magnetic minerals in recent haemipelagc sediments. Nature 303, 327–330.

Karlin, R., Levi, S., 1985. Geochemical and sedimentological control of the magnetic properties of hemipelagic sediments. Journal of Geophysical Research 90, 10373–10392.

Kohfeld, K.E., Harrison, S.P., 2001. DIRTMAP: the geological record of dust. Earth-Science Reviews 54, 81–114.

Koopmann, B. 1981. Sedimentation von Saharastaub im subtropischen Nordatlantik während der letzten 25.000 Jahre. “Meteor”-Forschungs-Ergebnisse Reihe C, 35: 23–59.

Lamb, H., 2006. Hydrodynamics. Cambridge Univ. Press, London, 737 pp.

Lambeck, K., Chappell, J., 2001. Sea level change through the last glacial cycle. Science 292, 679–686.

Lesack, L.F.W., Hecky, R.E., Melack, J.M., 1984. Transport of carbon, nitrogen, phosphorus, and major solutes in the Gambia River, West Africa. Limnology and Oceanography 29, 816–830.

Lézine, A.-M., Chateauneuf, J.-J., 1991. Peat in the "Niayes" of Senegal: depositional environment and Holocene evolution. Journal of African Earth Sciences 12, 171–179.

Li, J., Lewis, J., Rowland, J., Tappan, G., Tieszen, L., 2004. Evaluation of land performance in Senegal using multi-temporal NDVI and rainfall series. Journal of Arid Environments 59, 463–480.

Liu, Q.S., Roberts, A.P., Larrasoaña, J.C., Banerjee, S.K., Guyodo, Y., Tauxe, L., Oldfield, F., 2012. Environmental magnetism: Principles and applications. Reviews of Geophysics 50, RG4002, pp. 1–50.

Lyons, R., Oldfield, F., Williams, E., 2010. Mineral magnetic properties of surface soils and sands across four North African transects and links to climatic gradients. Geochemistry Geophysics Geosystems 11, Q08023, 22 pp.

Lyons, R., Oldfield, F., Williams, E., 2012. The possible role of magnetic measurements in the discrimination of Sahara/Sahel dust sources. Earth Surface Processes and Landforms 37, 594–606.

Maher, B.A., 1986. Characterisation of soils by mineral magnetic measurements. Physics of the Earth and Planetary Interiors 42, 76–92.

Maher, B.A., Watkins, S.J., Brunskill, G., Alexander, J., Fielding, C.R., 2009. Sediment provenance in a tropical fluvial and marine context by magnetic ‘fingerprinting’ of transportable sand fractions. Sedimentology 56, 841–861.

Mahowald, N.M., Muhs, D.R., Levis, S., Rasch, P.J., Yoshioka, M., Zender, C.S., Luo, C., 2006. Change in atmospheric mineral aerosols in response to climate: Last glacial period, preindustrial, modern, and doubled carbon dioxide climates. Journal of Geophysical Research 111, D10202, 22 p.

Makled, W.A., Langer, M.R., 2010. Preferential selection of titanium-bearing minerals in agglutinated Foraminifera: Ilmenite (FeTiO3) in Textularia hauerii d’Orbigny from the Bazaruto Archipelago, Mozambique. Revue de Micropaléontologie 53, 163–173.

McCave, I.N., Manighetti, B., Robinson, S.G., 1995. Sortable silt and fine sediment size/composition slicing: parameters for palaeocurrent speed and palaeoceanography. Paleoceanography 10, 593–610.

McMaster, R.L., Lachance, T.P., 1969. Northwestern African continental shelf sediments. Marine Geology 7, 57–67.

Middleton, N.J., 1985. Effect of drought on dust production in the Sahel. Nature 316, 431-434.

Middleton, N.J., Goudie, A.S., 2001. Saharan dust: sources and trajectories. Transactions of the Institute of British Geographers 26, 165–181.

Michel, P. 1973. Les Bassins des fleuves Sénégal et Gambie. Étude Géomorphologique, ORSTOM, Paris, 792 pp.

Mulitza, S., Bouimetarhan, I., Bruening, M., Freesemann, A., Gussone, N., Filipsson, H., Heil, G., Hessler, S., Jaeschke, A., Johnstone, H., Klann, M., Klein, F., Kuester, K., Maerz, C., McGregor, H., Minning, M., Mueller, H., Ochsenhirt, W.-T., Paul, A., Pokorna, M., Schewe, F., Schulz, M., Steinloechner, J., Stuut, J.-B., Tjallingii, R., von Dobeneck, T., Wiesmaier, S., Zabel, M., Zonneveld, C., 2006. Report and preliminary results of Meteor-Cruise M65/1 Dakar–Dakar, 11.06.-01.07.2005. Bremen, 149 pp.

Mulitza, S., Prange, M., Stuut, J.B., Zabel, M., von Dobeneck, T., Itambi, A.C., Nizou, J., Schulz, M., Wefer, G., 2008. Sahel megadroughts triggered by glacial slowdowns of Atlantic meridional overturning. Paleoceanography 23, PA4206, 11 pp.

Nicholson, N., Flohn, H., 1980. African environmental and climatic changes and the general atmospheric circulation in Late Pleistocene and Holocene. Climatic Change 2, 313–348.

Nicholson, S.E., 2009. A revised picture of the structure of the “monsoon” and land ITCZ over West Africa. Climate Dynamics 32, 1155–1171.

Nizou, J., Hanebuth, T.J.J., Heslop, D., Schwenk, T., Palamenghi, L., Stuut, J.-B., Henrich, R., 2010. The Senegal River mud belt: A high-resolution archive of paleoclimatic change and coastal evolution. Marine Geology 278, 150–164.

Odin, G.S. (ed), 1988. Green marine clays: Oolitic ironstone facies, glaucony facies and caledonite-bearing facies – A comparative study. Developments in Sedimentology 45, Elsevier, Amsterdam, pp. 445.

Oldfield, F., Yu, L., 1994. The influence of particle size variations on the magnetic properties of sediments from the north-eastern Irish Sea. Sedimentology 41, 1093–1108.

Oldfield, F., Maher, B.A., Donoghue, J., Pierce, J., 1985. Particle-size related, mineral magnetic source sediment linkages in the Rhode River catchment, Maryland, USA. Journal of the Geological Society 142, 1035–1046.

Oldfield, F., Hao, Q., Bloemendal, J., Gibbs-Eggar, Z., Patil, S., Guo, Z., 2009. Links between particle size and magnetic grain size: General observations and some implications for Chinese loess studies. Sedimentology 56, 2091–2106.

Otofuji, Y., Uno, K., Higashi, T., Ichikawa, T., Ueno, T., Mishima, T., Matsuda T., 2000. Secondary remanent magnetization carried by magnetite inclusions in silicates: a comparative study of unremagnetized and remagnetized granites. Earth and Planetary Science Letters 180, 271–285.

Parker, D.J., Burton, R.R., Niang, A.D., Ellis, R.J., Felton, M., Taylor, C.M., Thorncroft, C.D., Bessemoulin, P., Tompkins, A.M., 2005. The diurnal cycle of the West African monsoon circulation. Quarterly Journal of the Royal Meteorological Society 131, 2839–2860.

Petersen, N., von Dobeneck, T., Vali, H., 1986. Fossil bacterial magnetite in deep-sea sediments from the South Atlantic Ocean. Nature 320, 611–615.

Poizot, E., Méar, Y., Biscara, L., 2008. Sediment trend analysis through the variation of granulometric

parameters: A review of theories and applications. Earth-Science Reviews 86, 15–41.

Prospero, J.M., Glaccum, R.A., Nees, R.T., 1981. Atmospheric transport of soil dust from Africa to South America. Nature 289, 570–572.

Roberts, A.P., Rohling, E.J., Grant, K.M., Larrasoaña, J.C., Liu, Q., 2011. Atmospheric dust variability from Arabia and China over the last 500,000 years. Quaternary Science Reviews 30, 3537–3541.

Robinson, S.G., Sahota, J.T.S., Oldfield, F., 2000. Early diagenesis in North Atlantic abyssal plain sediments characterized by rock-magnetic and geochemical indices. Marine Geology 163, 77–107.

Rowan, C.J., Roberts, A.P., Broadbent, T., 2009. Reductive diagenesis, magnetite dissolution, greigite growth and paleomagnetic smoothing in marine sediments: A new view. Earth and Planetary Science Letters 277, 223–235.

Ruddiman, W.F., 2001. Earth's Climate – Past and Future. W. H. Freeman and Company, New York, 465 pp.

Sarnthein, M., Tetzlaff, G., Koopmann, B., Wolter, K., Pfaumann, U., 1981. Glacial and interglacial wind regimes over the eastern subtropical Atlantic and North-West Africa. Nature 293, 193–196.

Schwertmann, U., Taylor, R.M., 1989. Iron Oxides, in: Dixon, J.B., Weed, S.B., Dinauer, R.C. (Eds), Minerals in soil environments. Soil Scientific Society of America, pp. 379-439.

Shackleton, N.J., Fairbanks, R.G., Chiu, T., Parrenin, F., 2004. Absolute calibration of the Greenland time scale: Implications for Antarctic time scales and for 14C. Quaternary Science Reviews 23, 1513–1522.

Smirnov, A.V., Tarduno, J.A., 2000. Low-temperature magnetic properties of pelagic sediments (Ocean Drilling Program Site 805C): Tracers of maghemitization and magnetic mineral reduction. Journal of Geophysical Research 105, 16457–16471.

Stramma, L., Hüttl, S., Schafstall, J., 2005. Water masses and currents in the upper tropical northeast Atlantic off northwest Africa. Journal of Geophysical Research 110, C12006, 18 pp.

Stuut, J.-B., Zabel, M., Ratmeyer, V., Helmke, P., Schefuß, E., Lavik, G., Schneider, R., 2005. Provenance of present-day eolian dust collected off NW Africa. Journal of Geophysical Research 110, D04202, 14 pp.

Sultan, B., Janicot, S., 2003. The West African Monsoon Dynamics. Part II: The ''Preonset'' and ''Onset'' of the Summer Monsoon. Journal of Climate 16, 3407–3427.

Swap, R., Ulanski, S., Cobbett, M., Garstang, M., 1996. Temporal and spatial characteristics of Saharan dust outbreaks. Journal of Geophysical Research 101, 4205–4220.

Tarduno, J.A., 1994. Temporal trends of magnetic dissolution in the pelagic realm: Gauging paleoproductivity? Earth and Planetary Science Letters 123, 39–48.

Tetzlaff, G., Peters, M., 1986. Deep-Sea sediments in the eastern equatorial Atlantic off the African coast and meteorological flow patterns over the Sahel. Geologische Rundschau 75, 71–79.

Tjallingii, R., Claussen, M., Stuut, J.-B., Fohlmeister, J., Jahn, A., Bickert, T., Lamy, F., Rohl, U., 2008. Coherent high- and low-latitude control of the northwest African hydrological balance. Nature Geoscience 1, 670–675.

Waelbroeck, C., Labeyrie, L., Michel, L., Duplessy, J.C., McManus, J.F., Lambeck, K., Balbon, E., Labracherie, M., 2002. Sea-level and deep water temperature changes derived from benthic foraminifera isotopic records. Quaternary Science Reviews 21, 295–305.

White, F., 1983. The vegetation of Africa, a descriptive memoir to accompany the UNESCO/AETFAT/UNSO vegetation map of Africa. United Nations Educational, Scientific, and Cultural Organization, Paris, 356 pp.

Wynn, R.B., Masson, D.G., Stow, D.A., Weaver, P.P.E., 2000. The Northwest African slope apron: a modern analogue for deep-water systems with complex seafloor topography. Marine and Petroleum Geology 17, 253–265.

Xie, S.P., Saiki, N., 1999. Abrupt onset and slow seasonal evolution of summer monsoon in an idealized GCM simulation. Journal of the Meteorological Society of Japan 77, 949–968.

Zarriess, M., Mackensen, A., 2010. The tropical rain belt and productivity changes off northwest Africa: A 31,000-year high-resolution record. Marine Micropaleontology 76, 76–91.

Zhang, C., Woodworth, P., Gu, G.J., 2006. The seasonal cycle in the lower troposphere over West Africa from sounding observations. Quarterly Journal of the Royal Meteorological Society 132, 2561–2584.

5.10. Scientific background and individual contributions

The study 'How environmental magnetism can enhance the interpretational value of grain-size analysis: A time-slice study on sediment export to the NW African margin in Heinrich Stadial 1 and Mid Holocene' returned to the well-studied site off northern Senegal. This published study builds upon the preliminary results of the Bachelor thesis of Sebastian Razik, while the insights were further deepened in the context of this dissertation. As this study site is located at the proximity to the summer position of the Intertropical Convergence Zone, being also under the influence of two eolian and one fluvial sediment source, it represents a challenging sedimentary setting for provenance studies. The aim of this provenance study was to fathom the potential of grain-size based magnetic properties at a study site, where rock- and environmental magnetic measurements of terrestrial source sediments are available for direct comparison with marine deposits. Preliminary results and interpretations of this study were demonstrated during an oral presentation entitled 'Rock-magnetic parameters of sediment fractions obtained from gravity cores drilled off NW Africa' at the IAGA 11th assembly in Sopron

(Hungary) in August 2009. In the future, this approach (as a whole or just in parts) may be used in the realm of SE South America, where no insights about magnetic properties of terrestrial source rocks are available.

The design of the study was carried out by Sebastian Razik and Prof. Dr. Tilo von Dobeneck. The sets of rock- and environmental magnetic parameters on a grain-size specific basis were measured by Sebastian Razik. Essential interpretation of the results and writing of the paper were realized by Sebastian Razik. Constructive comments on the manuscript's shape and the contents were made by Prof. Dr. Tilo von Dobeneck and Dr. Mark J. Dekkers.

Chapter 6: Synthesis and outlook

Enviromagnetism provides a range of expedient sedimentary parameters to (1) mark terrigenous sediment source areas, (2) identify transport processes, i.e. pathways of eolian, fluvial, and marine sediments, as well as (3) detect authigenic Fe-minerals formed by biomineralization, abiotic precipitation, and diagenetic processes. Although magnetic Fe-oxide, Fe-hydroxide, and Fe-sulfide minerals are relatively low in species number and concentration in natural soils and sediments, even trace contents can be quantified by rock-magnetic methods and raise evidence for their magmatic, metamorphic, pedogenic, biogenic, and diagenetic origin. As the factors (1)–(3) usually jointly influence the sediments' magnetic properties, the general focus of this thesis was to differentiate between them by means of multiple enviromagnetic approaches, each with a different emphasis. These approaches provide access to the understanding of paleoceanographic and paleoclimatic issues at regional, as well as over-regional scales and were conducted as: (i) A multi-proxy study focusing on paleoclimate and surface-ocean paleocirculation during the last 14 cal kyr, complemented by a study on deep-ocean paleocirculation during the Last Deglaciation at 14–19 cal kyr BP; (ii) a provenance study targeting at surface sediments using multivariate analyses; and (iii) a grain-size specific study taking it up with all aforementioned influencing environmental factors at once, while being independent on other non-magnetic methods.

In the following, the advantages of the single studies performed off SE South America and NW Africa are depicted in a more overarching way. This is done with respect to the detection of temporal changes of terrestrial and marine environments in the view of specific magnetic and non-magnetic properties of terrigenous sediments. The synthesis is completed by an outlook considering each study's individual outcomes and adjusting them to a consistent course with respect to succeeding scientific challenges.

6.1. Magnetomineralogy

Magnetomineralogical parameters mainly bear information about igneous source-rock petrology and weathering conditions of the respective terrestrial source area. Especially mafic rocks contain high concentrations of magnetite. However, magnetite and maghemite are also formed during pedogenesis in response to intermittently humid and arid seasons and sufficient soil temperatures of the South American, as well as North African tropics and subtropics. Abundant pedogenic mineral neoformation refers also to hematite and goethite during more arid or humid climatic conditions, respectively. Thus, magnetomineralogical aspects were considered off SE South America and NW Africa to identify the main terrestrial sources and to detect significant paleoclimatic influences. Different proportions of ferrimagnets (i.e., magnetite and maghemite) versus antiferromagnets (i.e., hematite and goethite) are mirrored by the parameter $S_{0.3T}$. Varying sedimentary contribution by ferri- and antiferomagnets versus paramagnets (e.g., Fe-bearing clay minerals and pyrite) are detectable by changes in SIRM/Fe. Relative concentrations of all magnetic minerals (ferri-, antiferro-, and paramagnets) can be detected

by χ, while relative concentrations of more specific assemblages can be detected by SIRM (ferri- and antiferromagnets) and HIRM (antiferromagnets).

Conclusively, it could be displayed that the continental margin of SE South America is supplied by the Plata River. The transported sediments originate from the Plata Drainage Basin (see chapters 2 and 4), which drains the Brazilian Highlands and the Andean Cordillera. The Argentinean Colorado and Negro Rivers deliver subordinate amounts of terrestrial sediment, which is significant off the Pampas. The Pampean material is additionally transported to the continental shelf by winds and coastal wave erosion. Pampean shelf sediments originate from the Pampas and contain higher proportions of antiferromagnets than the Plata sediments.

The continental margin of NW Africa is supplied by eolian dust from the Sahel Zone, from the southern Sahara and from Senegalese coastal dunes (see chapter 5). While the Sahel dust contains the highest amount of hematite, the fluvial sediment originating from the upper reaches of the Senegal River is characterized by the highest proportions of magnetite. More arid conditions over SE South America (Mid Holocene) and NW Africa (Heinrich Stadial 1) were mirrored by decreased deposition of fluvial ferrimagnets at both continental margins. Humid conditions (Late or Mid Holocene, respectively) were mirrored by opposite sedimentary signatures and dynamics.

6.2. Magnetogranulometry

Magnetogranulometry combined with clastic grain-size distributions provide information on sediment sources, transport systems, and transport paths. While clastic grain-size distributions mainly mirror sediment transport dynamics due to particle sorting, the grain size (domain state) of magnetic minerals (reflected in χ_{fd}% and $ARM_{0.1T}/IRM_{0.1T}$) mainly bears information about source-rock petrology and climatic (weathering) conditions of the respective area. These relations were shown in two ways; by (i) comparison of bulk-magnetic properties with clastic grain-size distributions, and by (ii) magnetic investigations of individual grain-size fractions.

Approach (i) performed off SE South America was able to delineate the distribution of Pampean sand with high proportions of coarse magnetite with respect to the Plata clay and silt (see chapters 2 and 4). The latter are characterized by the highest proportions of fine (single-domain) and ultra-fine (super-paramagnetic) magnetite. While the Pampean sand is mainly found on the Pampean shelf and slope, the Plata clay and silt are deflected northeastwards from the Plata estuary and distributed mainly on the mid and outer shelf reaching as far as ~24° S. Based on the magnetogranulometric characteristics and grain-size distributions, temporal changes of sediment-transport intensities could be detected (see chapter 2). Thus, for the first time relative meridional shifts of the Subtropical Shelf Front were revealed and assumptions were made about the related position of the Brazil-Malvinas Confluence for the last 14 cal kyr. In addition, insights were gained about changes of the Brazil Current intensity during the Last Deglacial with clues on the Atlantic Meridional Overturning Circulation (see chapter 3).

Approach (ii) performed off Northwest Africa was capable to reveal the highest proportions of coarse (multi-domain) magnetite in the grain-size fractions transported by the Harmattan winds (10–20 µm), while fractions mainly transported by the trade winds (40–63 µm) and the Senegal River (<10 µm)

were characterized by higher proportions of fine magnetite (see chapter 5). In particular, $ARM_{0.1T}/IRM_{0.1T}$ on a grain-size specific basis is very sensitive to highlight differences in eolian and fluvial off-shore transport. This ratio for fluvial sediments indicates rapid magnetite fining with increasing shore-distance, while dust shows a less distance-dependent magnetogranulometric trend. Additionally, grain-size specific $ARM_{0.1T}/IRM_{0.1T}$ values are sensitive towards selective dissolution of magnetite, which would not be easily detectable considering solely bulk-magnetic properties. Thus, magnetite dissolution could be linked to enhanced riverine input of organic matter close to the Senegal River mouth during the climatic conditions of the African Humid Period during the Mid Holocene.

The studies performed in the realm of South America and West Africa reveal that the obtained insights based on magnetomineralogy are enriched and underpinned by magnetogranulometric parameters. In particular, the magnetic approach on a grain-size specific basis bears the potential to provide more explicit information regarding terrestrial source-rock properties than bulk-magnetic investigations alone. Thus, this approach is predestinated to be applied to regions lacking terrestrial rock-magnetic data for direct comparison with marine samples.

6.3. Enviromagnetism supported by non-magnetic parameters

Bulk-magnetic investigations can be rewardingly supplemented by consideration of terrigenous grain-size distributions, bulk porosity, major-element and $CaCO_3$ concentrations, as well as micropaleontologic data (see chapter 2). As the measured magnetic properties (e.g., χ_{cof}, $SIRM_{2.6T\,cof}$, and SIRM/Fe) represent the characteristics of the terrigenous sediment portion, they mainly bear information concerning the source-rock petrology and terrestrial climatic (weathering) conditions. On the other side, the marine sediment portion mainly provides information about the characteristics of specific water masses; like their temperature, salinity, nutrient content etc. (represented by $CaCO_3$- and TOC-concentrations, abundances of siliceous diatoms and benthic foraminifera, as well as derived oxygen- and carbon-isotopic values), and the water mass sediment-transport abilities (represented by e.g. the deposited particle size).

The combined investigation of terrigenous and marine sediment portions obtained from continental margin deposits revealed insights about climatic conditions over the South American continent. For the first time, past variations in intensities and latitudinal extents of the South American Monsoon System and of the Southern Westerly Wind Belt were jointly considered for the last 14 cal kyr. Their past interactions were revealed with respect to precipitation over land, as well as with respect to their collective impact on surface-ocean circulation of the western South Atlantic. Thus, while the South American Monsoon System significantly intensified during the humid Late Holocene over SE Brazil, the Subtropical Shelf Water could extend further southward than during the Mid and Early Holocene. Simultaneously, the Southern Westerly Wind Belt extended to the north in the course of the Holocene accompanied by an intensity decrease at its core zone around 50°–55° S. This progression led to the northernmost penetration of the Subantarctic Shelf Water during the relatively arid Mid Holocene in the realm of SE South America, resulting in the northernmost position of the Subtropical Shelf Front. In conclusion, one of the most striking advantages of this enviromagnetic-weighted multi-proxy approach

is the capacity to tag intercoupled terrestrial and marine processes, as well as to differentiate between them. This achievement would be hardly possible by studies focusing solely on one of the involved methods described in chapter 2.

6.4. Enviromagnetism supported by multivariate analysis

Fuzzy c-means cluster analysis and non-linear mapping are suited to discern similarities among multi-parametric data groups and thus to highlight even small differences between prevalent sediment provinces, as well as to depict their mixing portions (see chapter 4). Small differences between sediment provinces (e.g., due to the same igneous source-rock signature but different weathering conditions or transport paths) are usually hardly detectable by univariate or bivariate analyses of magnetomineralogical and magnetogranulometric sedimentary properties. Thus, a set of inter-parametric ratios (χ_{fd}%, $S_{0.3T}$, $ARM_{0.1T}/IRM_{0.1T}$, $SIRM_{2.6T}$/Fe, and Fe/K) was used as input data. On the one hand, χ_{fd}% and $ARM_{0.1T}/IRM_{0.1T}$ reflect the magnetogranulometry being valid for detection of superparamagnetic (<20 nm), single-domain (20–100 nm), and multi-domain (>10 µm) states, respectively. On the other hand, $S_{0.3T}$ and SIRM/Fe mirror the magnetomineralogy being indicative for relative influences of ferrimagnets versus antiferromagnets, as well as for relative influences of ferrimagnets versus paramagnets (e.g., Fe-bearing clay minerals), respectively.

While using this concentration-independent interparametric ratios, information from bulk sediments could be extracted regarding changing source-rock petrology and the prevailing humid or arid climate, which affects related soil-forming processes (i.e., magnetic mineral dissolution or neoformation) in SE South America. Simultaneously, significant biasing impacts on magnetic signatures could be avoided, which may be caused by diamagnetic dilution due to marine bioproductivity, or by magnetic mineral enrichment in the clay fraction due to particle sorting during transport.

For the first time Pampean shelf and slope sediments, both originating from the Andean Cordillera, could be distinguished based on different alteration states of their magnetic assemblages. While the Pampean shelf sediments are derived from the Pampean loessoidal deposits delivered to the shelf mainly by coastal wave erosion, the slope sediments are constituted of riverine sediments, which show an original igneous magnetic signature being less pedogenically altered. Silty sediments derived from the Plata Drainage Basin were detected between the Plata estuary and SE Brazil. For the first time Pampean shelf sand could be tracked up to ~24° S, which is being admixed to the Plata clay and silt at the SE Brazilian continental slope. Conclusively, this sensitive and effective multivariate approach is favorable for provenance studies in regions prone to complex sediment dynamics and multiple sediment sources.

6.5. Outlook

The multi-proxy and grain-size based enviromagnetic approaches performed in this thesis reveal suitable strategies to approximate aims with different emphases on e.g., paleoclimate, paleoceanography, and sediment provenance. The performed studies yield robust insights concerning the geographical distributions of terrigenous sediment provinces on the SE South American and NW

African continental margins, with meaningful conclusions on the respective terrestrial sediment sources. Additionally, clues about marine environmental conditions were drawn, highlighting the links to over-regional tropospheric circulation systems of both continents.

Nonetheless, there still remain open questions and ambiguities: In particular, the detection of absolute paleopositions of the Subtropical Shelf Front requires further down-core studies towards the north and the south of the Rio Grande Cone off South Brazil and Uruguay. Besides that, the here presented studies of terrigenous sediment provinces provide first assumptions about the magnetic properties of corresponding terrestrial source rocks. A direct comparison of available marine sediment properties with terrestrial source-rock properties was not possible due to only a very limited number of rock-magnetic studies performed on the South American continent. As the Plata Drainage Basin is the second largest drainage basin of South America, its western rivers drain petrologically different sedimentary deposits originating from the Andes than the eastern ones draining the flood basalts of the Brazilian Highlands. Above all, the Andean Bermejo River contributes the majority of unconsolidated sediments to the entire sediment load transported towards the Plata estuary. However, so far there are no rock-magnetic investigations which budget the magnetic relevance of the Bermejo River sediments in relation to those of the Upper Paraná River, for instance. Knowledge about the individual riverine contributions of magnetic minerals would facilitate future magnetic-based provenance studies and enable farther-reaching clues on terrestrial climatic conditions responsible for source-rock weathering, erosion, and discharge towards the continental shelf.

As the sample material from the continental shelf of Patagonia (40°–55° S), as well as of SE (22°–28° S) and East (20°–22° S) Brazil was limited to few surface samples, future identification of the respective sediment provinces could be verified and even deepened by selected source and sink sampling. In particular, the differentiation between South Patagonian glacial and periglacial deltaic deposits, on the one hand, as well as of ice-rafted debris originating from Antarctica, on the other hand, would be worthwhile. Both sediment assemblages are vastly found at the Patagonian and Pampean continental margin and have not been investigated by a profound rock-magnetic methodology so far. The latter provides large potential for future provenance studies and related identification of sediment distribution paths in this region.

The study performed off NW Africa, dealing with provenance- and paleoclimate-related issues, is located at the modern boreal summer position of the Intertropical Convergence Zone. Thus, this location is markedly sensitive towards climate change. However, this site obtains eolian sediments from the western Sahara, from the southern Sahara and the Sahel Zone, as well as fluvial material from the Senegal River. It would be worthwhile to extend the study site to the north and to the south. Thus, future rock and environmental magnetic investigations of continental margin sediments could delineate the extent of the terrigenous sediment provinces and, hence, also detect the influence of the aforementioned individual terrestrial sediment sources.

These future aims can be reached by a combination of the enviromagnetic-weighted multi-proxy approaches described in this thesis, which were supported by multivariate analyses (i.e., fuzzy c-means cluster analysis and non-linear mapping). As the continental margins of SE South America and NW Africa provide sediments originating from various terrestrial sediment sources with different grain-

size ranges, the grain-size specific enviromagnetic approach carried out on distinct grain-size fractions is most promising to obtain convincing and original provenance- and transport-related insights. It appears to be worthwhile to evaluate the grain-size dependency of magnetic properties for at least a few selected test samples from different marine and terrestrial regions of the continental margins. Once the fractions containing the magnetic mineral concentration-peaks are detected, the fractionation approach can be simplified and limited to just a few fractions of interest to focus on the targeted scientific issues. Following this rationale, new meaningful insights can be obtained about environmental conditions in the marine and terrestrial realms of South America and West Africa, with rewarding inferences about global recent and past oceanic, as well as climatic processes.

Acknowledgements

First and foremost, my thanks go to my supervisor, Prof. Dr. Tilo von Dobeneck. This PhD thesis would not have been possible without his helpful and instructive comments on the performed studies, on the one hand. On the other hand, I am very thankful for his trust and his patience, as well as his humane and amicable nature.

A very special ‘thank you’ goes to Dr. Cristiano M. Chiessi for his critical but very inspiring discussions on our corporate studies’ results. After some serious draw-backs during the first year, the confidable cooperation with him gave this PhD thesis a positive and constructive turn. Accordingly, the new focus enabled a stay abroad, which created in me a deep personal relation to South America in general and to Brazil in particular.

I would like to gratefully acknowledge my coauthors Dr. Aline Govin and Dr. Oscar E. Romero. Their specific geoscientific skills and essential contributions to the multi-proxy approaches enriched the value of rock- and environmental magnetism within the framework of this thesis.

On top of this, I am very glad to have had the possibility to work in the Marine Geophysics section of the Geosciences Faculty at Bremen University. During the past years, the entire crew was always endeavored to enable a smooth scientific routine. Thus, their individual experiences and personal contributions – in the view of running the technical equipment and the logistics, as well as giving competent advice – have contributed to the quality of this thesis.

As a doctoral thesis never is apart from other aspects of life, I would like to thank all the people I have met for their companionship. I am very thankful for all positive and negative experiences so far, as they have been very enriching and made me learn a lot. I am happy that this thesis may contribute to a general understanding of the world’s processes.